Measurement of the Neutron Magnetic Form Factor at Large Momentum Transfer Using the Super-Bigbite Apparatus in Jefferson Lab Hall-A

Anuruddha Dilshan Rathnayake Mudiyanselage
Kandy, Sri Lanka

B.Sc. Special Degree in Physics, University of Peradeniya, 2016

A Dissertation presented to the Graduate Faculty of the University of Virginia in Candidacy for the Degree of Doctor of Philosophy

Department of Physics

University of Virginia
September, 2024

Abstract

The nucleon elastic electromagnetic form factors help us study the electromagnetic structure of the nucleon, benchmark theoretical models, and improve our understanding of non-perturbative quantum chromodynamics and confinement. The Nobel Prize-winning electron-nucleon scattering experiments by Robert Hofstadter and collaborators in the 1950s at Stanford High Energy Physics Lab were the first nucleon form factor measurements performed using leptonic probes. The Super Bigbite Spectrometer (SBS) program at Hall-A of Jefferson Lab represents the latest efforts to measure nucleon form factors. This ambitious program aims to significantly extend the current data set in terms of square momentum transfer (Q^2) with high precision. The advent of novel detector technologies, like Gas Electron Multipliers (GEM), which provide excellent position resolution (< 100 μm) while withstanding high background particle rates (several hundred MHz/cm^2) over a large active area, has paved the way for open-geometry, moderate solid angle spectrometers, which are central to all form factor experiments in the SBS program. The first experimental run group in SBS ran successfully between September 2021 and February 2022, collecting data for the measurement of the magnetic form factor of the neutron G_M^n at five squared momentum-transfer values: 3.0, 4.5, 7.5, 9.8, and 13.5 $(GeV/c)^2$. This extends the existing high-precision data for G_M^n by about a factor of four. The ratio technique was used, which involved the simultaneous measurement of exclusive quasielastic scattering of D(e,e′n)p and D(e,e′p)n from a deuterium target. Pre-preliminary results for D(e,e′n)p and D(e,e′p)n quasi-elastic ratio, and the neutron magnetic form factor G_M^n, for Q^2 points 3.0, 9.8, and 13.5 $(GeV/c)^2$ are presented.

Acknowledgments

" *We are like dwarfs on the shoulders of giants. We see more, and things that are more distant, than they did, not because our sight is superior or because we are taller than they, but because they raise us up, and by their great stature add to ours.* "

— Bernard of Chartres

I was able to pursue my dream of getting a PhD because of the support I received from many individuals. If it were not for their generous support, I would not have succeeded. It would be impossible to list each and every one, and I apologize in advance for any possible omissions.

I would like to start by thanking my parents, my mother Pamodha Abeysinghe and father Hemantha Ratnayake. Your love, motivation, commitment, and continued guidance have made this all possible. It is hard to express in words all the support both of you have given me. My mother always made sure I was safe and on track. My father's knack for science and technology shaped my mind from an early age to think along those lines.

I extend a warm thank you to my advisor, Nilanga Liyanage. You have been an excellent mentor to me over the past six years, and I feel privileged to have had your support. I began my PhD journey with very little knowledge about this field, and you gracefully guided me to gain knowledge and skills over time. You entrusted me with the safety and well-being of a large number of valuable and delicate GEM detectors at the beginning of my research career, and that helped me in many ways. Your calm and caring nature is greatly appreciated, and it has allowed me to grow freely.

A big thank you to all the present and past members of the University of Virginia detector group. Kondo Gnanvo was my first mentor besides Nilanga. Most of my knowledge about GEM detectors came from working closely with him during the GEM commissioning work at JLab. It seemed like there was absolutely nothing he did not know about GEM detectors, and he always knew the right answer or solution when a GEM detector misbehaved. Huong Nguyen taught me how to assemble a GEM detector "from scratch." Thanks to her meticulous assembly process and impressive touch, our GEM detectors have been very successful. I am very grateful for all the support and guidance in GEM hardware, software, and analysis work from Xinzhan Bai. You have generously helped me with your knowledge on countless occasions. John Boyd has been my friend, classmate, and lab mate for the longest time, and the

work we have done together over the last seven years is enormous. I will always cherish that partnership. The knowledge and support we shared—whether it was homework, qual-prep, GEM work, or analysis—were invaluable in this PhD journey. Sean Jeffas was my lab mate for five years, and roommate for about two years. We spent a lot of time together working on GEMs at JLab and getting the experiments ready and running. I think we can be proud of how we managed to make a very complicated and delicate detector subsystem work! Sean also took the initiative in organizing many fun events within the SBS students, and his efforts made the stressful times easier, for which I am thankful. The past senior students in our group, Danning Di, John Matter, and Siyu Jian, have also helped me a lot with their impressive knowledge and expertise. I warmly thank Minh Dao, Vimukthi Gamage, Bhasitha Dharmasena, Asar Ahmed, Jacob McMurtry, and Mihitha Maithripala. I know the future of GEMs is in safe and competent hands.

I gratefully acknowledge the hard work and dedication of Zeke Wertz, Holly Szumila-Vance, Ben Rydo, Malinga Rathnayake, Thir Gautam, Chuck Long, and Bryan Moffit. All your efforts were central to the successful operation of GEMs at JLab, and I enjoyed and learned a lot from working with each and every one of you.

I also want to thank the wider SBS collaboration for their efforts and collaboration over the years. I would especially like to thank Bogdan Wojtsekhowski, Mark Jones, Andrew Puckett, Eric Fucey, Brian Quinn, Alexandre Camsonne, Arun Tadepalli, Gordon Cates, Brad Sawatzky, and Evaristo Cisbani.

The fellow GMn/nTPE thesis students made a great team, and it was a great pleasure to have worked with each and every one of you. I thank Provakar Datta, Sebastian Seeds, Zeke Wertz, Maria Satnik, John Boyd, Ralph Marinaro, and Nathaniel Lashley. The Monday student analysis meetings were a great opportunity for all of us to share knowledge and learn from each other. A special thanks goes to Zeke for running those meetings for over two and a half years. The teamwork between the GMn/nTPE thesis students certainly led to the rapid development of both the students and the wider GMn/nTPE analysis.

I also want to thank my PhD committee members, Kent Paschke, Donal Day, and David Cafiso. I appreciate all the time you put into reading my thesis, providing feedback, and asking thoughtful questions. All of that helped me improve my dissertation immensely.

I want to thank all my dear friends in Charlottesville and Newport News. The very first friends I met in Charlottesville, when I first came to the US and UVA, helped me in many ways to settle and feel at home. They helped me overcome many challenges one faces when they first arrive in a completely new environment. For the majority of my PhD student career, I was stationed at JLab in Newport News. The friends in Newport News were like family away from home to me. Together, we got through the challenging COVID-19 pandemic by keeping each other company. The many parties we had and trips we took are some of my favorite memories, and I thank you all for being such wonderful friends.

There are many people back home in Sri Lanka who helped me get to the point of starting a PhD, and continue to provide me with support and guidance. I would like to thank all the teachers and friends at Dharmaraja College, Kandy. My passion for

science was first conceived there, and I am grateful for all the amazing teachers I've had. I also want to thank all my lecturers and friends from the Faculty of Science at the University of Peradeniya. I extend a warm thank you to my grandparents, relatives, and friends from Sri Lanka. You all gave me love, care, and support, and I am very grateful for that.

Finally, I want to say a big thank you to my loving wife, Chathuranika Imiya (Imii). You gave me a lot of love and support over the last few years. Getting a PhD is a challenging and time-consuming task. I greatly appreciate your patience and understanding when I had to put in a lot of time and energy into my work while being engaged on a PhD journey of your own. I look forward to supporting you and watching us grow together.

Contents

List of Figures

List of Tables

Chapter 1

Introduction

The investigation and characterization of the structure of the nucleon have been central areas of study in nuclear and hadronic physics for nearly a century. In 1933, Otto Stern measured the proton's magnetic moment and found it to be approximately 2.8 times larger than expected for a spin-$\frac{1}{2}$ Dirac particle (a point-like particle with no structure) [8], providing the earliest evidence for the proton's deviation from a point-like charge and magnetic moment. In the 1950s, Robert Hofstadter and collaborators led the way in using leptonic probes to study nucleon structure via electron-nucleon scattering with electron beam energies up to 550 MeV [9]. They demonstrated a deviation of the electron-proton scattering cross section from that of point-like particles and also performed the first direct measurement of the proton's charge and magnetic radii. According to the standard model of particle physics, leptons such as electrons do not possess an internal structure, making the theoretical interpretation of experimental results from electron-nucleon scattering relatively straightforward. This process remains one of the simplest and most commonly used to study nucleon structure.

1.1 Electron-Nucleon Scattering within the QED Framework

The leading-order term contributing to the cross-section of elastic electron-nucleon (eN) scattering is the one-photon-exchange (OPE) term. The OPE approximation is also commonly referred to as the Born approximation in the literature. Figure 1.1 depicts the Feynman diagram for this process. The vast majority of past and present elastic eN scattering experiments are performed using high-energy electron

beams incident on nucleon or nucleon bound-state targets. In Figure 1.1, an incident electron interacts/scatters from a nucleon at rest in the lab frame via the exchange of a *single virtual photon*.

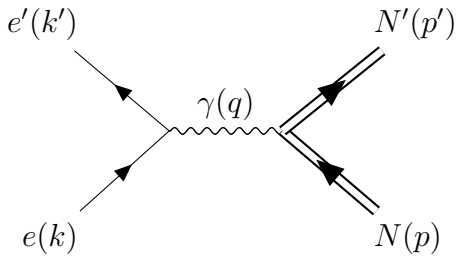

Figure 1.1: Feynman diagram for elastic eN scattering under the one-photon-exchange approximation.

The four-momenta of the pre-scattering (eN) and post-scattering ($e'N'$) electron and nucleon can be defined as:

- The incident electron four-momentum, $k = (E_e, \vec{k})$; where E_e is the electron beam energy.
- The target nucleon four-momentum, $p = (E_N, \vec{P}) = (M, 0)$; where M is the rest mass energy of the nucleon.
- The scattered electron four-momentum, $k' = (E'_e, \vec{k'})$.
- The recoiled nucleon four-momentum, $p' = (E'_N, \vec{p'})$.

The electron beam energies used in the experiment discussed in this dissertation are in the many GeV range, and hence the ultrarelativistic approximation ($E_e \gg m_e$, with m_e being the rest mass energy of the electron) can be safely applied. This gives rise to $|\vec{k}| = E_e, |\vec{k'}| = E'_e$, and $k^2 = k'^2 = 0$. The four-momentum transfer to the nucleon from the electron is $q = k - k'$, which can also be interpreted as the four-momentum of the virtual photon. The energy-momentum conservation of this two-body scattering reaction yields,

$$k + p = k' + p' \rightarrow p' = q + p = (E_e - E'_e + M, \vec{k} - \vec{k'}) \tag{1.1}$$

By taking the Lorentz invariant dot product of the right-hand side equation, we get the invariant mass of the virtual photon-nucleon system (W), $p'^2 = W^2$. Elastic scattering requires $W = M$. Along with this requirement, the kinematics of elastic eN scattering can be defined by the electron scattering polar angle (θ_e) and the incoming

beam energy. Since $q = k - k'$ is spacelike with q^2 being negative, the invariant squared-momentum-transfer is defined as $Q^2 = -q^2$, which is a critical quantity in the cross-section calculation of the elastic eN process, described below.

The most general form (electrons and nucleons have spin-$\frac{1}{2}$, nucleons have structure and an anomalous magnetic moment, relativistic treatment included, and nucleon recoil considered) of the Lorentz invariant elastic eN scattering OPE amplitude $\mathcal{M}$ according to the Feynman rules of QED can be written as (using the natural unit system, $\hbar = c = 1$):

$$\mathcal{M} = 4\pi\alpha\bar{u}(k')\gamma^{\mu}u(k)\left(\frac{g_{\mu\nu}}{q^2}\right)\bar{u}(p')\Gamma^{\nu}u(p) \tag{1.2}$$

where:

- $\alpha = \frac{e^2}{4\pi}$ is the fine structure constant.
- $\bar{u}$ and u represent the free-particle Dirac spinors for the incoming and outgoing particles, respectively.
- $\bar{u}(k')\gamma^{\mu}u(k)$: Represents the electron current. It describes the interaction of the incoming and outgoing electrons with the virtual photon. Here, γ^{μ} is a Dirac γ matrix.
- $\frac{g_{\mu\nu}}{q^2}$: The photon propagator in Feynman gauge, describing the propagation of the virtual photon with four-momentum transfer q. Here, $g_{\mu\nu}$ is the Minkowski metric tensor.
- $\bar{u}(p')\Gamma^{\nu}u(p)$: Represents the nucleon current. It describes the interaction of the incoming and outgoing nucleons with the virtual photon.
- Γ^{μ} is the vertex function that accounts for the internal structure of the nucleon and its interaction with the photon. This term contains all the "unknown" information about the nucleon structure that we intend to investigate from electron scattering.

The photon-nucleon vertex function Γ^{μ} is given by:

$$\Gamma^{\nu} = F_1(q^2)\gamma^{\mu} + \frac{i\sigma^{\mu\nu}q_{\nu}}{2M}F_2(q^2) \tag{1.3}$$

where $\sigma^{\mu\nu} \equiv \frac{i}{2}[\gamma^{\mu}, \gamma^{\nu}]$. The *form factors* F_1 and F_2 are real-valued functions of q^2, and they are the only independent scalar variables on which this vertex function

depends. Together, they fully parameterize the eN scattering with respect to the charge and magnetization distribution of the nucleon (for a given q^2). $F_1(q^2)$ depends on the nucleon's charge and point-like magnetic moment (Dirac particle's magnetic moment) distributions, and is hence also known as the *Dirac form factor*. $F_2(q^2)$ depends on the nucleon's anomalous magnetic moment distribution and is also referred to as the *Pauli form factor*.

1.2 Sach's Form Factors and Rosenbluth Formula

The interpretation of experimental results becomes more convenient by formulating the so-called Sach's form factors as linear combinations of F_1 and F_2 [10]. With $\tau = \frac{Q^2}{4M^2}$, the Sachs electric form factor (G_E) and the magnetic form factor (G_M) are defined as follows:

$$G_E = F_1 - \tau F_2 \tag{1.4}$$

$$G_M = F_1 + F_2 \tag{1.5}$$

The Rosenbluth formula gives the eN scattering differential cross section under the OPE approximation:

$$\frac{d\sigma}{d\Omega_e} = \left(\frac{d\sigma}{d\Omega_e}\right)_{Mott} \frac{1}{(1+\tau)}(G_E^2 + \frac{\tau}{\epsilon}G_M^2) \tag{1.6}$$

Here, the Mott cross-section, $\left(\frac{d\sigma}{d\Omega_e}\right)_{Mott}$, is the ultrarelativistic electron scattering cross section from a point-like target with charge Ze, no spin, and no magnetic moment. The target recoil is considered in this particular version of the Mott cross-section. Following the same variable naming convention already introduced, the Mott differential cross section is given by:

$$\left(\frac{d\sigma}{d\Omega_e}\right)_{Mott} = \frac{Z\alpha^2 E_e' \cos^2\left(\frac{\theta_e}{2}\right)}{4E_e^3 \sin^4\left(\frac{\theta_e}{2}\right)} \tag{1.7}$$

ϵ can be interpreted as the *longitudinal polarization of the virtual photon* and is given by:

$$\epsilon = \left[1 + 2(1+\tau)\tan^2\left(\frac{\theta_e}{2}\right)\right]^{-1} \tag{1.8}$$

The Sachs form factors allow for a separation of contributions between the electric

and magnetic components of the nucleon current distributions to the eN differential cross section. By using various kinds of eN scattering, including unpolarized electron and unpolarized nucleon, polarized electron and unpolarized nucleon, and polarized electron and polarized nucleon, Sachs form factors are relatively straightforward to extract by measuring cross section ratios and cross section asymmetries. The Rosenbluth formula in Eq 1.6 represents unpolarized eN scattering, and this process is used in the experimental technique discussed in this dissertation.

At extremely low squared four-momentum transfer ($Q^2 \to 0$), the wavelength of the virtual photon is not small enough to resolve the fine structure of the nucleon, and the scattering is equivalent to that from a point-like charged particle. Hence, the nucleon current term should be reduced to that of a point particle, however with an anomalous magnetic moment intrinsic to the isospin state of the nucleon. Then for the proton with charge $Z = +1$, the Dirac and Pauli form factors should be:

$$F_1^p(0) = 1, F_2^p(0) = \kappa_p \tag{1.9}$$

and for the neutron with zero charge:

$$F_1^n(0) = 0, F_2^n(0) = \kappa_n \tag{1.10}$$

where κ_p and κ_n represent the anomalous magnetic moments of the proton and the neutron respectively. Then the Sachs form factors for the respective nucleon isospin states can be written as:

$$G_E^p(0) = 1, G_M^p(0) = 1 + \kappa_p = \mu_p \tag{1.11}$$

$$G_E^n(0) = 0, G_M^n(0) = 0 + \kappa_n = \mu_n \tag{1.12}$$

where μ_p and μ_n represent the total magnetic moments of the proton and neutron respectively, in the units of nuclear magnetons ($\mu_N = \frac{e}{2M}$). From this point onward in this dissertation, by the phrase "form factors" we will refer to the Sachs form factors unless otherwise stated.

1.3 Theoretical Importance of Nucleon Elastic Electromagnetic Form Factors

Naturally, the very first electron-nucleon scattering experiments involved relatively low-energy electron scattering (a few hundred MeV) and very small Q^2. We will first focus on the interpretation and use-cases of form factors in this regime.

Let's consider a relatively simple case of electron scattering from a static charge distribution $\rho(\vec{r})$ of total charge Ze within the OPE approximation:

$$\left(\frac{d\sigma}{d\Omega_e}\right) = \left(\frac{d\sigma}{d\Omega_e}\right)_{Mott} |F(\vec{q})|^2 \tag{1.13}$$

where $F(\vec{q})$ is known as the *form factor* for electron scattering, which is the Fourier transform of the charge distribution $\rho(\vec{r})$:

$$F(\vec{q}) = \int \rho(\vec{r}) e^{i\vec{q}\cdot\vec{r}} d^3\vec{r} \tag{1.14}$$

with $\vec{q} = \vec{k} - \vec{k'}$ being the counterpart spatial vectors of the four-momenta defined in Section 1.1. Now, if we consider the case of extremely low squared momentum transfer electron scattering ($Q^2 \to 0$), the Rosenbluth equation (Eq. 1.6) reduces to:

$$\left(\frac{d\sigma}{d\Omega_e}\right) \approx \left(\frac{d\sigma}{d\Omega_e}\right)_{Mott} G_E^2 \tag{1.15}$$

Thus, at very low energy electron scattering, the Sachs electric form factor G_E can be interpreted as the Fourier transform of the electric charge density, and similarly, the Sachs magnetic form factor G_M can be identified as the Fourier transform of the magnetization density. However, this simple and direct interpretation of EEFF gets complicated by relativistic effects at larger Q^2. Also, very importantly, very low Q^2 form factors can be used to extract nucleon charge and magnetization radii. By expanding the integrand in Eq. 1.14 in terms of powers of q^2 and doing a coordinate transformation into the spherical coordinate system, we get:

$$G_E = \int \rho(r) \left\{1 - \frac{1}{2}(qr)^2 \cos^2\theta + \ldots\right\} r^2 \sin\theta dr d\theta d\phi \tag{1.16}$$

By taking the derivative with respect to q^2 and taking the limit $q^2 \to 0$, we can obtain the mean square charge radius of the nucleon:

$$\langle r_e^2 \rangle = -6 \left.\frac{dG_E}{dq^2}\right|_{q^2\to 0} \tag{1.17}$$

The high Q^2 form factors from modern experiments are particularly useful for constraining the Generalized Parton Distributions (GPDs), and form factor data is required for the analysis of experiments to measure GPDs from Deeply Virtual Compton Scattering (DVCS) processes. GPDs provide a "three-dimensional picture" of the nucleon by offering information about the longitudinal momentum distribution and the transverse spatial distribution of partons (quarks and gluons), thereby broadening our understanding of QCD.

Lattice QCD is the only method for calculating physical observables such as form factors using the first principles of QCD. Even though recent improvements in computational power allow for more accurate and realistic calculations, these calculations have still not reached a level where they can be directly compared with experimental data with the required rigor and accuracy, especially at large energy/momentum transfer.

1.4 Current Status of Nucleon EEFF Data

To get a comprehensive understanding of the nucleon, both the electric and magnetic form factors of the two isospin states, proton and neutron, must be measured. An up-to-date detailed review of the current status of nucleon EEFF measurements is provided in reference [1]. We will denote the proton electric and magnetic form factors as G_E^p and G_M^p, respectively, and for the neutron as G_E^n and G_M^n.

A target made with molecular hydrogen (${}^1_1H_2$) can be effectively used as a free proton target. The nucleus of the (${}^1_1H$) atom is a single unbound proton and therefore gaseous or liquid/cryogenic hydrogen targets provide the cleanest possible elastic scattering with no smearing effects due to the Fermi motion or changes in cross sections due to nuclear effects such as final state interactions and nuclear binding. Additionally, the proton is charged and therefore can be detected easily. On the other hand, the neutron is not a stable particle and it decays with a mean lifetime of about 880 seconds. Stable neutrons only exist as bound states within atomic nuclei. Therefore, *quasi-elastic* scattering from weakly bound nuclei such as deuteron (${}^2_1H$) and helium-3 (${}^3_2He$) is commonly used to study the neutron form factors. This invariably complicates the measurement and data analysis process. The neutron does not carry an overall electric charge, making it difficult to detect as it only interacts with matter via strong interactions to the extent that creates measurable signals within existing nuclear and high energy physics detectors. For absolute cross-section measurements, the final results will have to heavily rely on the nuclear wave

function models in order to unfold the nuclear effects such as Fermi motion, binding energy, final state interactions, and so on. Due to these reasons, the number of measurements, Q^2 range, and precision of neutron form factor data are currently smaller in comparison to the proton form factor data.

When representing the EEFF data, in order to remove the strong Q^2 dependence, it is customary to normalize the true values with respect to the so-called dipole form given by:

$$G_D(Q^2) = \frac{1}{\left(1 + \frac{Q^2}{\Lambda^2}\right)^2} \tag{1.18}$$

where $\Lambda^2 = 0.71\,(GeV/c)^2$. This represents a particular standardized dipole. It has been found that the proton electric and magnetic form factors, and also the neutron magnetic form factor, can be quite accurately described in the relatively low Q^2 regime (about below 2.0 $(GeV/c)^2$) by scaling this dipole form as given by:

$$\begin{aligned} G_E^p &= G_D \\ G_M^p &= \mu_p G_D \\ G_M^n &= \mu_n G_D \end{aligned} \tag{1.19}$$

However, due to the zero charge of the neutron, G_E^n is not well represented by this dipole scaling method.

Rearranging Eq 1.6, we can obtain the *reduced cross section* σ_R,

$$\sigma_R = \frac{\left(\frac{d\sigma}{d\Omega_e}\right)_{Measured}}{\left(\frac{d\sigma}{d\Omega_e}\right)_{Mott}} \epsilon(1+\tau) = (\epsilon G_E^2 + \tau G_M^2) \tag{1.20}$$

For proton form factor measurements, one of the earlier widely used techniques was the Rosenbluth separation or the Longitudinal/Transverse (L/T) separation technique. This technique involves measuring the scattered electron $(e, e')p$ differential cross section from a hydrogen target at two (or more) different ϵ values while keeping the Q^2 constant. As it can be seen from Eq 1.20, the reduced cross section is linear in ϵ with the slope being G_E^2 and the intercept τG_M^2. The Q^2 is kept constant by changing the electron beam energy and the polar scattering angle of the electron spectrometer (thus changing ϵ as per Eq 1.8). At low Q^2 reasonably good results could be obtained from this technique, but as Q^2 increases the τG_M^2 term dominates the total cross section and the sensitivity for ϵG_E^2 term goes down. This makes it difficult to extract G_E^p from this technique at larger Q^2 values.

With the advancement of electron beam spin polarization and target spin polarization techniques, several methods have been developed that relate form factors to polarization observables. These techniques show much higher sensitivity to the smaller electric form-factor (both G_E^p and G_E^n) at larger Q^2 values, and most modern experiments use these techniques. An in-depth review of the use of polarization observables for form factor measurements is out of scope for this discussion.

Figure 1.2 summarizes the current status of the proton form factor world data measurements. The G_M^p measurements are relatively straightforward to perform as it dominates the elastic scattering cross section and high precision data exists going up to very large Q^2 ($\approx$30 $(GeV/c)^2$). For G_E^p, high precision Q^2 range stops around 10 $(GeV/c)^2$ and almost all of the modern data come from the techniques involved with observing polarization observables rather than direct cross section measurements. One very important feature in the G_E^p world data is the apparent disagreement between the trends of the world data from polarization observables (shown in filled circles) and the direct L/T separation or the Rosenbluth technique (shown by empty circles). Starting in the early 2000s, this led to massive efforts in both theoretical and experimental fronts to explain and validate these observations and increased interest in the study of nucleon form factors. The leading explanation for this effect is, polarization observables are relatively insensitive to the modification of the total cross section due to Two-Photon-Exchange (TPE) effects. TPE effects are also predicted to depend strongly on ϵ, and hence the Rosenbluth technique is much more sensitive to it up to the point that the smaller G_E^p at large Q^2 is comparable to this effect [11].

Figure 1.3 summarizes the current status of the neutron form factor world data. With the neutron electric form factor going to zero as $Q^2 \to 0$ (see Eq 1.12), the contribution of G_E^n to the elastic scattering cross section for the entire Q^2 range is dominated by G_M^n. The entire set of world data presented in Figure 1.3b represents data obtained from experimental techniques that use polarization observables. It should be noted that G_E^n is the most difficult to measure out of the four nucleon form factors and this is represented by the smaller Q^2 range and smaller number of data points in the world data plot.

The analysis of this dissertation focuses on extracting G_M^n at the highest Q^2 and precision to date, and an overview of the past and present efforts to extract the neutron magnetic form factor will be presented in Section 1.5.

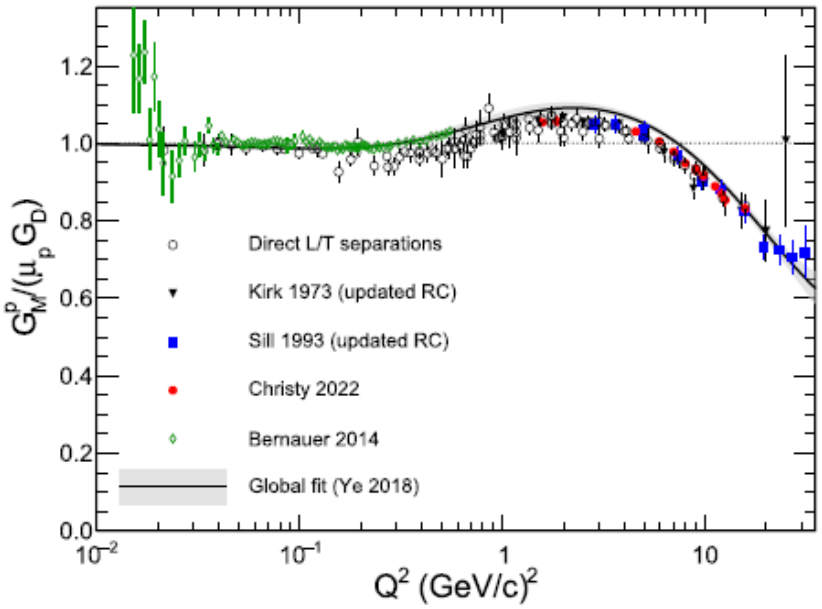

(a) G_M^p world data. The points shown with empty shapes are extracted from the L/T separation or the Rosenbluth technique. The points shown with filled shapes are single point cross section measurements.

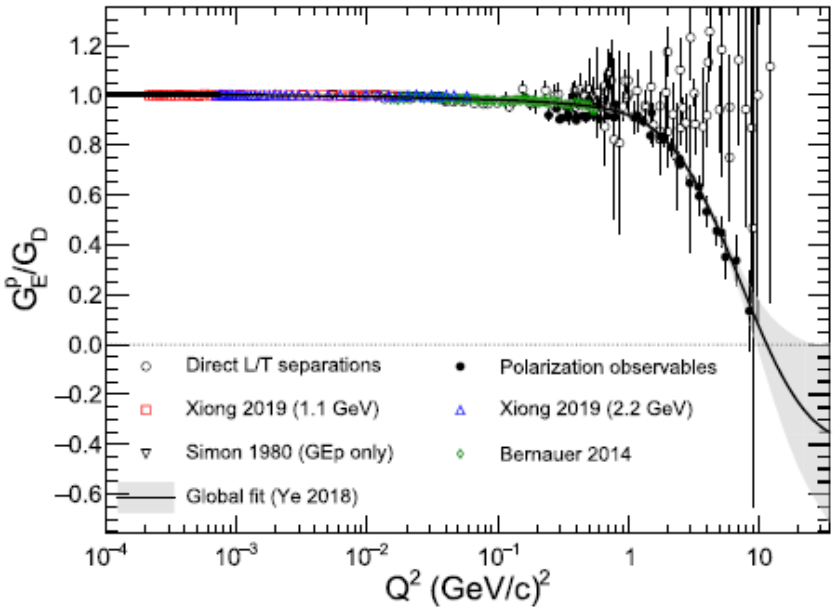

(b) G_E^p world data. The points shown with empty shapes are extracted from the L/T separation or the Rosenbluth technique. The points shown with filled shapes are extracted from polarization observables.

Figure 1.2: Proton form factors world data. Plots reproduced from [1]. Global fits are produced using the parameterization given in [2].

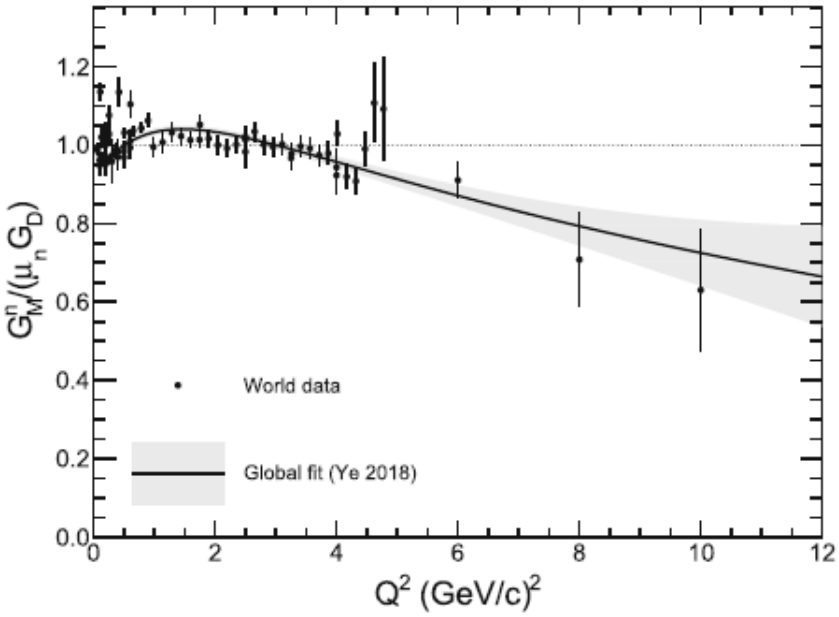

(a) G_M^n world data.

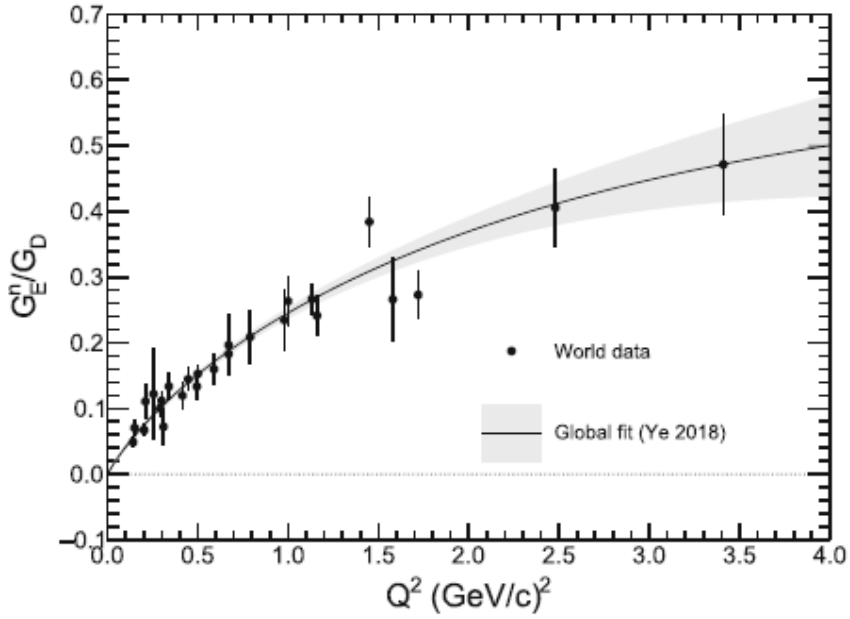

(b) G_E^n world data.

Figure 1.3: Neutron form factors world data. Plots reproduced from [1]. Global fits are produced using the parameterization given in [2].

1.5 Previous G_M^n Measurements

Several different experimental techniques have been employed for G_M^n measurements. All of these experimental techniques revolve around overcoming the difficulties asso-

ciated with the lack of free-neutron targets and reliable neutron detection.

The inclusive electron-deuteron scattering $D(e, e')$ was used in references [12], [13], [14], [15], and [16]. These are single-arm measurements of the scattered electron, which incorporate the Rosenbluth technique for the L-T separation. Proton cross section is subtracted using the known proton form factor data, and deuteron wave function models must be used to account for the various nuclear effects. This introduces an inherent model bias. Also, this technique suffers from increased error from error propagation when the large proton cross section is subtracted. Since the scattered nucleon is not detected, coincidence requirements cannot be applied, which is very useful for inelastic event rejection, especially at large Q^2.

The error due to proton subtraction can be avoided when the neutron from the inclusive $D(e, e'n)p$ reaction is measured in coincidence with the electron. This method still relies on deuteron wave function models to account for nuclear effects. References [17], [18], and [19] use this technique. In this technique, the neutron detection efficiency is a key component in the systematic error budget. The requirement of theory-based corrections for nuclear effects could be outlined as the most challenging aspect of this technique.

Another technique that has been employed in the past is the so-called "anti-coincidence" (as opposed to the "coincidence" technique previously described) or the "proton-tagging" technique. This technique relies on the fact that protons are easier to detect compared to neutrons. The events $D(e, e'NOT - p)$, or in other words, the events where there is no scattered proton detected in coincidence with the scattered electrons are ascribed to be neutron events. References [20] and [21] have used this technique. This technique also suffers from the model dependence errors as in the previous two techniques, and since the scattered neutron is not detected, electron-nucleon coincidence criteria cannot be applied for inelastic event rejection, which makes this technique impossible to be used at large Q^2.

Measuring the ratio of inclusive quasielastic scattering cross section ratio of tritium $^3H(e, e')$ and helium-3 $^3He(e, e')$ mirror nuclei has also been used to extract G_M^n [22][23]. Many systematic experimental uncertainties cancel out in this ratio, especially the nuclear effects of the tritium and helium-3 mirror nuclei (with ground-state wavefunctions of the two nuclei being very similar), leading to only requiring small nuclear corrections. Since two different targets are used, the differences in target densities, especially from beam heating, must be accounted for carefully. The very recent publication from JLab in reference [23] has extracted G_M^n in the Q^2 region of 0.6 - 2.9 $(GeV/c)^2$ using this method. However, just like some of the previous techniques, this

method being a single-arm technique does not detect the scattered nucleon, which would allow the suppression of very large inelastic background contamination at large Q^2.

A completely unique technique that has been used for G_M^n extraction in the low Q^2 regime (0 - 0.6 $(GeV/c)^2$) is the use of polarization observables (transverse asymmetry A_T) of inclusive quasi-elastic scattering of spin-polarized ^3He and electrons $^3\vec{H}e(\vec{e},e')$. This technique is governed by an entirely different set of systematic uncertainties and has been used to verify some disagreements of G_M^n measurements from other techniques at $Q^2 < 1(GeV/c)^2$ [24][25][26][27]. However, the extraction of G_M^n from this technique relies on theoretical modeling of the ^3He nucleus, and these calculations are not accurate enough to be used at large Q^2 values.

The "ratio method" [28] (or the Durand technique) is widely considered the most superior among the existing measurement techniques for the extraction of G_M^n. It can be distinguished from the other techniques described above by its minimal dependence on deuteron wave-function models and nuclear effects, inherent ability to reject inelastic background events, and the cancellation of many systematic uncertainties related to beam conditions, target, and electron detection. Especially for the modern G_M^n measurements at large momentum transfer values such as the published results from reference [29], and the data currently being analyzed from JLab E12-07-104 and E12-09-019 (this dissertation), all employ the ratio method. In addition, the past experiments [30], [31], [32], and [33] used the ratio method. A detailed description of the ratio method is provided in the following Section 1.6.

1.6 Ratio Method of G_M^n Extraction

The ratio method is used for the experiment E12-09-019, for G_M^n extraction from the quasi-elastic electron scattering on the deuteron. As indicated by the name, in this technique the D(e,e′n)p and D(e,e′p)n *differential cross section ratio* is the primary physics observable:

$$R' = \frac{\left(\frac{d\sigma}{d\Omega}\right)_{D(e,e'n)}}{\left(\frac{d\sigma}{d\Omega}\right)_{D(e,e'p)}} \tag{1.21}$$

This involves the simultaneous measurement of *neutron-tagged*, D(e,e′n)p, and *proton-tagged*, D(e,e′p)n, quasi-elastic scattering from a deuteron target. The scattered nucleon is detected in coincidence with the scattered electron, and the kinematics of the scattered electron is used for elastic event selection and the reconstruction

of the $\vec{q}$ vector, which is used for the "tagging" of the nucleon. Electron trigger efficiency, tracking efficiency, event reconstruction efficiency, electron acceptance, data acquisition live time, target thickness, target density, beam intensity, and beam energy are some of the critical systematic uncertainties that completely cancel in the ratio. The coincidence detection of both the proton and the neutron allows for the application of coincidence constraints between the electron arm and the hadron arm, which will be extremely helpful in eliminating inelastic contamination dominant at larger Q^2. The main systematic uncertainty inherent to this technique is the neutron and proton detection efficiency. However, with controlled inelastic contamination and well-understood neutron and proton detection efficiencies, this technique results in the smallest systematic error among the available methods, as many other systematic uncertainties cancel when forming the ratio as explained above.

The quantity that is directly comparable with nucleon elastic electromagnetic form factors would be the elastic n(e,e′) and p(e,e′) differential cross section ratio:

$$R = \frac{\left(\frac{d\sigma}{d\Omega}\right)_{n(e,e')}}{\left(\frac{d\sigma}{d\Omega}\right)_{p(e,e')}} \tag{1.22}$$

From the quasi-elastic cross section ratio to obtain the elastic cross section ratio, *nuclear corrections* must be applied to correct for the modification of elastic scattering cross sections due to the nuclear binding energy, final state interactions, and other nuclear effects. However, these corrections are almost identical between the neutron and the proton and hence they cancel out in the ratio, with a small correction ϵ_{nuc} surviving due to small effects such as the mass difference between the neutron and the proton.

$$R = \frac{R'}{1 + \epsilon_{nuc}} \tag{1.23}$$

This residual nuclear correction has been found to be less than 0.1% for the Q^2 regime (3.0 - 13.5 $(GeV/c)^2$) being considered in this experiment [34]. A deuteron wave function model built into the Monte-Carlo (MC) simulation machinery used for the data analysis of this experiment accounts for the nuclear effects, and the real data and MC generated data comparison technique employed (that will be described in Chapter 4) allows for a direct extraction of elastic cross section ratio R without having to implement it manually.

Now we can write the ratio R in terms of the electromagnetic form factors from the one photon exchange approximation,

$$R = \frac{\left(\frac{1}{1+\tau_n}\right)\left((G_E^n)^2 + \frac{\tau_n}{\epsilon_n}(G_M^n)^2\right)}{\left(\frac{1}{1+\tau_p}\right)\left((G_E^p)^2 + \frac{\tau_p}{\epsilon_p}(G_M^p)^2\right)} \tag{1.24}$$

Where τ and ϵ are defined above for the general case of electron-nucleon elastic scattering and the subscripts indicate the value for the corresponding nucleon obtained by substituting the correct rest mass. Now solving for G_M^n yields,

$$G_M^n = \sqrt{\left[R\frac{1+\tau_n}{1+\tau_p}\left((G_E^p)^2 + \frac{\tau_p}{\epsilon_p}(G_M^p)^2\right) - (G_E^n)^2\right]\frac{\epsilon_n}{\tau_n}} \tag{1.25}$$

This expression could be further simplified by re-writing it in terms of proton's reduced cross section $\sigma_{R,p}$ (defined in Eq 1.20) instead of the form factors,

$$G_M^n = \sqrt{\left[R\left(\frac{1+\tau_n}{1+\tau_p}\right)\frac{\sigma_{R,p}}{\epsilon_p} - (G_E^n)^2\right]\frac{\epsilon_n}{\tau_n}} \tag{1.26}$$

The proton cross section and the from factors have been measured with high-precision at Q^2 values extending much further than the range we intend to extract G_M^n from this experiment. The neutron electric form factor G_E^n is small and expected to contribute minimally at the Q^2 region of interest to us. We will use the latest proton form factor and G_E^n parameterizations for our final extractions.

Chapter 2

Description of the Experiment

The SBS GMn experiment (E12-09-019) setup in Hall-A, from September 2021 to February 2022, is shown in Figure 2.1. A high-energy electron beam (3.7 GeV - 9.91 GeV) was provided by Jefferson Lab's CEBAF accelerator. Hall-A's standard cryogenic target system was used, with the liquid deuterium target being the production target, and the liquid hydrogen, optics, and carbon hole targets being used for calibration purposes. Two spectrometer arms were used for the coincidence measurement of D(e,e′n)p and D(e,e′p)n quasi-elastic scattering reactions. The electron arm provided the trigger for the experiment, and data from its detector package was used for the $\vec{q}$ vector (momentum transferred by the virtual photon) reconstruction for the scattering events. The hadron arm was used to detect neutrons and protons from quasi-elastic scattering.

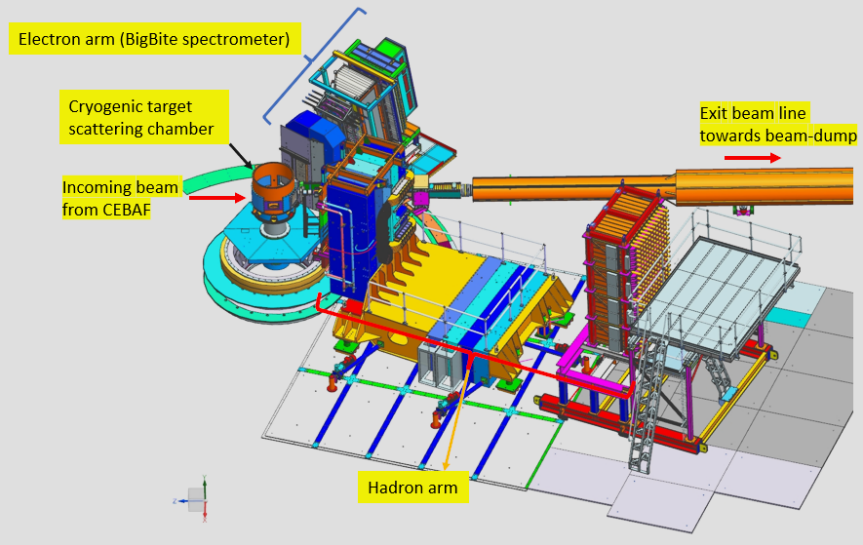

Figure 2.1: GMn experiment setup CAD diagram

GMn was the first experiment to run in the SuperBigbite program. The majority of the detector package was brand new, and it was during the GMn experiment that they were commissioned and used in an experiment for the first time.

This chapter provides an overview of the entire GMn experiment, starting with a brief description of the CEBAF accelerator.

2.1 CEBAF

The Continuous Electron Beam Accelerator Facility (CEBAF) [35], a unique electron accelerator capable of producing electron beams with high energy, high duty factor (continuous wave), high intensity, and high polarization, is central for carrying out nuclear physics research at the Jefferson Lab. See Figure 2.2 for a schematic overview of CEBAF.

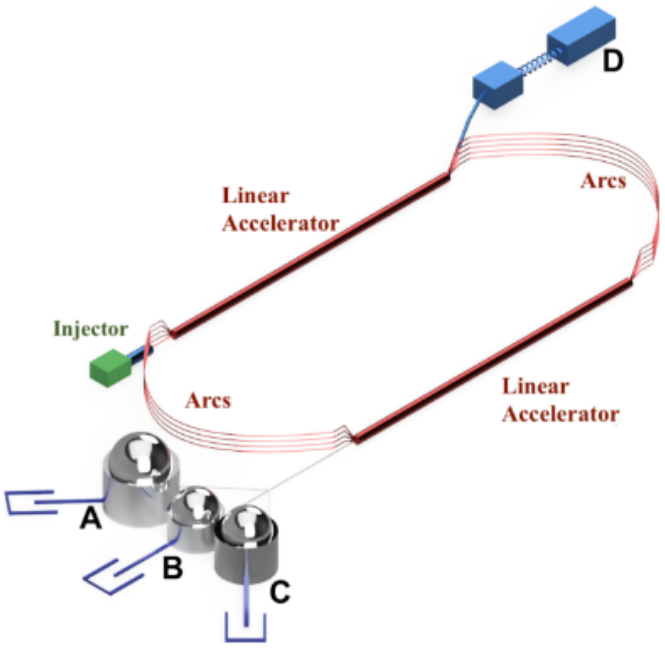

Figure 2.2: A schematic overview of CEBAF. The injector initiates the electron beam which gets accelerated by the two linear accelerators (LINACs). With the use of re-circulation arcs, the beam can circulate from one to five laps to gain energy and enter into the experimental halls A, B, and C. Hall-D can accept electrons from another additional half-lap of acceleration. Adapted from [3].

The electron beam is initiated at the injector, using the principle of spin-polarized photoelectron emission by shining a polarized laser light onto a gallium-arsenide (GaAs) semiconductor material. The photoemitted electrons are accelerated by a

high-voltage DC electron gun and are focused to create an initial beam of energy 100 keV. The laser is pulsed at one, two, or three interleaved but independent 499 MHz intervals, matched with the subsequent RF (radio-frequency) acceleration, which creates separate synchronous beam bunches accordingly. As will be described later, this allows the separation of beam bunches for the four experimental halls at any re-circulation pass. With recent technology developments, the CEBAF injector is currently capable of producing spin-polarized electrons of up to 85%. The E12-09-019 experiment's measurement technique is insensitive to the polarization of incoming electrons and final state particles. Therefore, no attempt was made to monitor the beam polarization of the electron beam either at the injector or inside Hall-A.

The initial beam from the injector first enters the north LINAC. LINACs consist of Superconducting Radiofrequency (SRF) cavities made with niobium and cooled with 2 K superfluid helium to well below the critical temperature for superconductivity for niobium ($\sim$ 9.3 K). The choice of SRF acceleration over warm-RF acceleration has made it possible for a relatively low-power operation of the accelerator, and also very importantly, much superior beam quality with a small relative energy spread of (Δp/p $< 2\times10^{-5}$). The original 6 GeV version of the LINACs consisted of 20 cryomodules made with 5-cell cavities in each LINAC. During the 12 GeV upgrade, 5 cryomodules made with 7-cell high-performing cavities were added to each LINAC. This gives rise to an energy increment of 1.1 GeV/LINAC and 2.2 GeV/pass in CEBAF. The electron speed after a single pass through a LINAC comes near the speed of light and due to the very slow relativistic rise of the electron speed as a function of energy, the relative difference between the speed increment between different pass beam energy is very small. This allows electron beam bunches with multiple beam energies (different passes) to be accelerated through the SRF cavities coincidentally. Beam re-circulation of up to five laps (5-pass) can be achieved with the original 9 arcs and the three experimental halls A, B, and C can receive it. With the addition of a tenth arc for the 12 GeV upgrade, Hall-D can receive 5.5 pass beam energy with maximum beam energy going up to 12 GeV. The re-circulation arcs consist of room temperature dipole magnets to deflect the high-energy electrons and quadrupole magnets to re-focus the beam. Just after the south LINAC exists the beam extraction switchyard. There are RF deflecting cavities in each re-circulation arc. They are phased accurately with the phase of the beam bunches and they can be used to extract any beam bunch in any re-circulation pass within 1-5. The extracted beam is further manipulated by additional magnets before being sent to the experimental halls' respective beamlines.

2.2 Target System

The standard Hall-A cryogenic target system was used during the GMn experiment. All cryogenic and solid targets were installed on a vertical ladder. This ladder was operated remotely via a graphical user interface from the Hall-A counting house, to position different targets along the path of the electron beam. The entire target ladder was placed inside an evacuated *scattering chamber* (see Figure 2.3), which connects directly to the incoming and exit beamline.

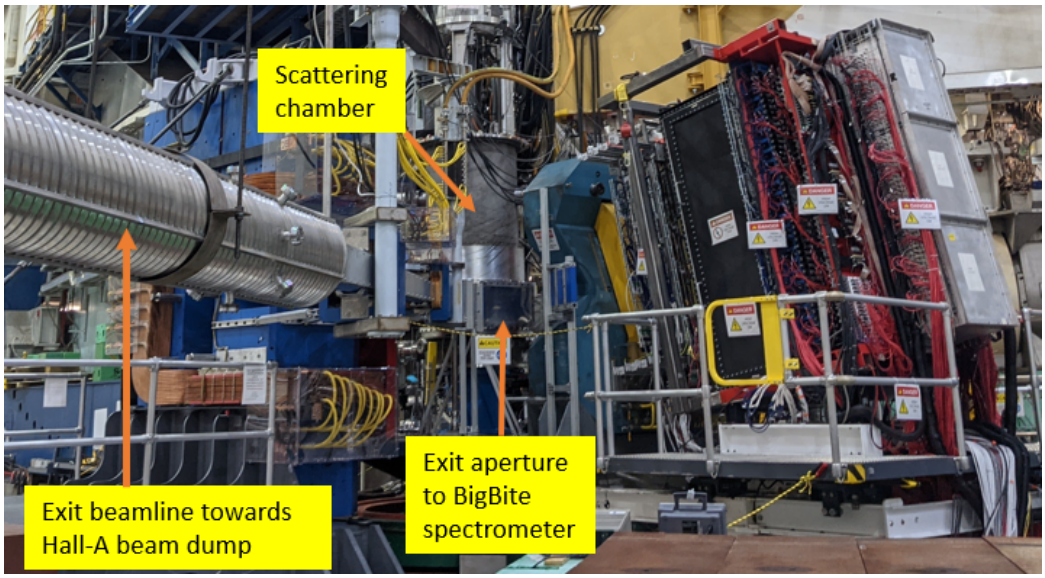

Figure 2.3: The view of the Hall-A cryogenic target scattering chamber. The exit beamline that goes to the beam dump is on the left and the BigBite spectrometer is towards the right from this view.

2.2.1 Cryotargets

The cryogenic target system consists of three recirculating loops of high purity liquid cryogenic target material. Primarily two loops were used during the GMn experiment, one with liquid deuterium (LD2) for production data taking and the other with liquid hydrogen (LH2) mainly used for detector calibration. Figure 2.4a shows the portion of the target ladder with the three cryogenic target loops with a total of six individual target cells. Under beam operation, the electron beam will interact with the target material and dissipate energy in the form of heat. This heat must be extracted to keep the liquid cryogenic target material from boiling off. The liquid deuterium must be maintained at a temperature of 22 $\pm$ 0.01 K and the liquid hydrogen at 19 $\pm$ 0.01 K. This is achieved by circulating the cryogenic target material through a heat

exchanger that is cooled by He coolant at 14 K, pressurized to 12 atm. This He coolant is provided by an End Station Refrigerator (ESR) that is shared by both halls A and C. A 60 Hz re-circulation fan/pump located inside the heat exchanger is used to force the liquid cryogenic target material through the entire loop. A Joule-Thomson (JT) valve is used to control the amount of He coolant sent into the heat exchanger unit. However, excessive cooling can lead to the freezing of the liquid cryogenic target material and this is especially a risk when the beam is down and no heating power is dumped by the beam into the target. To avoid this, there is a variable high power heater installed within the recirculating loop, before the heat exchanger unit. Temperatures are monitored right before and after the target cell, and also closer to the input of the heat exchanger unit. A PID (proportional integral derivative) feedback circuit is used to control the power of the heater and maintain the desired temperature of the cryogenic target material.

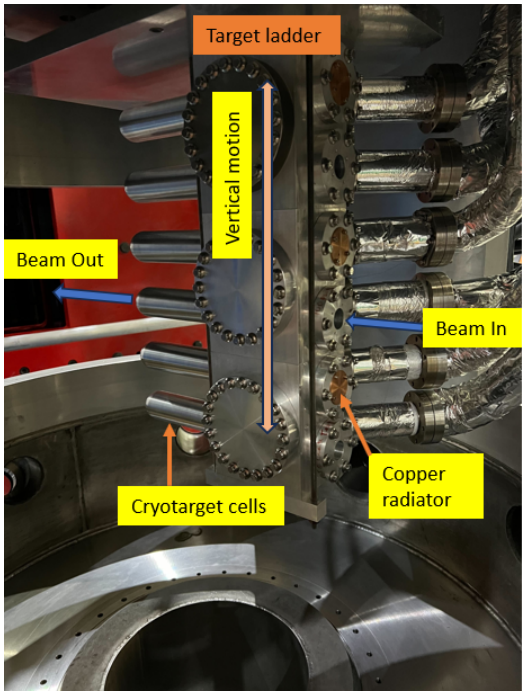

(a) Three cryogenic target loops. In each loop the top target cell is equipped with a copper radiator up-stream of the target cell for photon generation which is needed for some experiments.

(b) A front-on view of the target ladder with the solid targets in view in the bottom portion of the image.

Figure 2.4: The target ladder

The cryogenic target cells are made out of the alloy, AL 7075. The length of a target cell is 150 mm, and the entrance, wall, and tip thicknesses are 145 μm, 143

μm, 158 μm, respectively. Additional details about the cryotargets and solid targets during the GMn experiment is provided in [36]. The density of the liquid deuterium (at 22 $\pm$ 1 psia) and liquid hydrogen (at 25 $\pm$ 1 psia) used during the GMn experiment were 0.167 g/cm^3 and 0.0723 g/cm^3, respectively. Since the ratio method of GMn extraction does not rely on the absolute cross section values and rather depends on the cross section ratio of D(e,e′n)p and D(e,e′p)n processes, the density of the target material is mostly unimportant for the physics analysis. However, a parameter of importance that helps to gauge the success of the experiment's hardware and software apparatus would be the beam-on-target luminosity. The luminosity of a fixed target experiment can be calculated from the formula,

$$\mathcal{L}_{FT} = \Phi \rho_T l \tag{2.1}$$

Where, Φ is the beam flux, i.e. the number of particles per second, ρ_T is the nucleon number density of the target, and l is the target length. Accordingly, during the SBS GMn experiment, beam-on-target luminosities of up to $\approx 10^{38}$ cm^{-2}s^{-1} were reached.

2.2.2 Solid Targets

Several solid targets were used in the GMn target ladder for different calibration purposes. The so-called "dummy target" was used to study the background contribution from target entrance and exit windows. The dummy target was basically two aluminum foils located at Z positions (Z = 0 being the center of the target and +Z direction defined as the downstream direction along the beamline) that correspond to the cryotarget exit and entrance windows. Five and four carbon foil optics targets were used for momentum calibration of the BigBite spectrometer. The Z positions of the foils of the five foil optics target were $\pm$10 cm, $\pm$5 cm, and 0 cm, and for the four foil optics targets they were $\pm$2.5 cm and $\pm$7.5 cm. In addition, there was a single carbon foil target that was used during some initial detector checkouts. Finally, the other most notable solid target was the 2 mm carbon hole target. This target was frequently used to establish the desirable beam parameters including the beam X and Y positions on the target (beam centering) and the quality of the raster. See Figure 2.4b where the foil targets mentioned here are in view.

2.3 The BigBite Spectrometer

The BigBite spectrometer was originally used at the Internal Target Facility at Dutch National Institute for Subatomic Physics (NIKHEF) [4], for the detection of electrons. The original components of the BigBite spectrometer have been a room temperature non-focusing dipole magnet, along with multi-wire drift chambers, scintillators, and a Ĉerenkov detector. It has been specifically designed to have a large momentum and solid angle acceptance. The BigBite spectrometer was later acquired by Jefferson Lab, and it had already been used in several experiments in Hall-A, before being equipped with a new detector package and re-commissioned for the SBS experiments. Apart from the BigBite magnet, the entire detector package was replaced with a brand new set of detectors, which are more suited for high-luminosity and high-background experiment conditions. Figure 2.5a shows the magnet and detector configuration of the BigBite spectrometer prepared for the SBS experiments, and Figure 2.5b is a real-life image of the BigBite spectrometer during the GMn experiment in Hall-A. The BigBite magnet and the detector package are mounted on a common support frame that can be rotated around the target pivot to position the spectrometer at a desired polar scattering angle. As mentioned at the beginning of this chapter, in the SBS GMn experiment the Bigbite Spectrometer was used as the electron arm. In the next few subsections, an overview of each sub-system of BigBite spectrometer will be provided.

2.3.1 BigBite Magnet

As mentioned earlier, the BigBite magnet is the only legacy component used in the SBS BigBite spectrometer. BigBite is a room temperature single dipole magnet, weighing approximately 20 tonnes. The horizontal gap between the pole faces of the magnet measures 25 cm, and the height of the entrance aperture is 84 cm[4][37]. This gives BigBite spectrometer a large solid angle acceptance, an essential feature for the SBS experiments. In addition, the BigBite magnet is designed so that the entrance face of the magnet is perpendicular to the central particle trajectory and the exit face has a pole face rotation of 5°. This makes the particle dispersion more uniform throughout the spectrometer acceptance. A side and a top view of the BigBite magnet can be seen in Figure 2.5b and Figure 2.6, respectively.

The NIKHEF institute has measured a magnetic field strength of 0.92 T when a current of 518 A is passed through the coils[4]. The magnetic field is fairly uniform within the pole faces of the magnet and drops off rapidly outside of the pole faces.

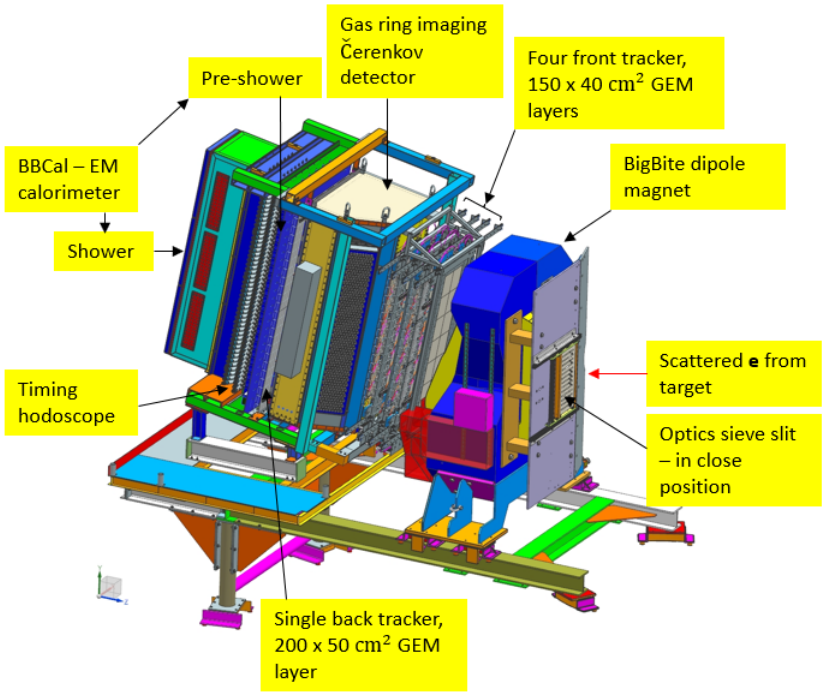

(a) A 3D CAD diagram of BigBite spectrometer for SBS experiments

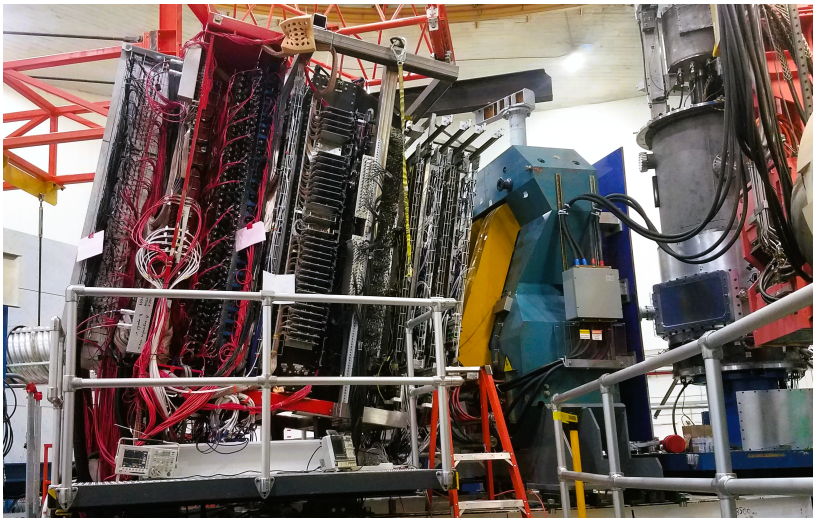

(b) A side view of BigBite spectrometer inside Hall-A

Figure 2.5: BigBite spectrometer during SBS GMn experiment

see Figure 2.7. In the SBS GMn experiment, the BigBite magnet was used with a current of 750 A to obtain maximum possible field strength.

2.3.2 Gas Electron Multiplier (GEM) tracker

GEM detectors were used in the BigBite spectrometer as the charged-particle tracking detectors. GEM detectors' high background rate tolerance (≈100 MHz/cm^2) and the

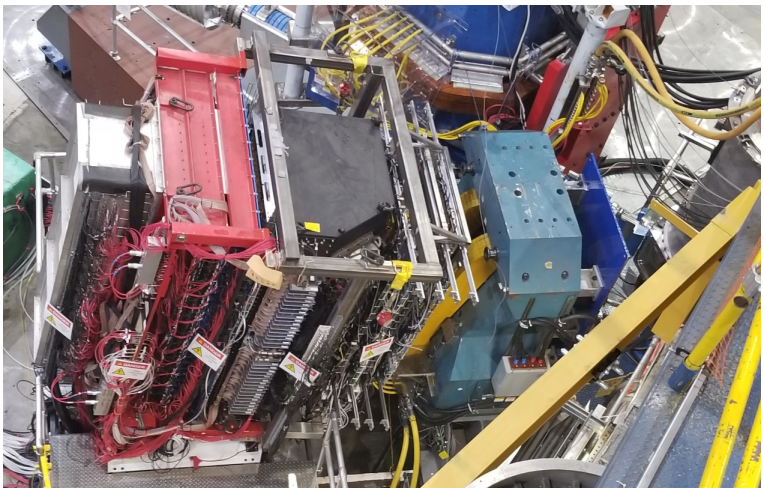

Figure 2.6: A top view of the BigBite spectrometer. The blue magnet yoke, the yellow coils around the pole faces, and the 25 cm horizontal gap are clearly visible. Also note the slanted exit face.

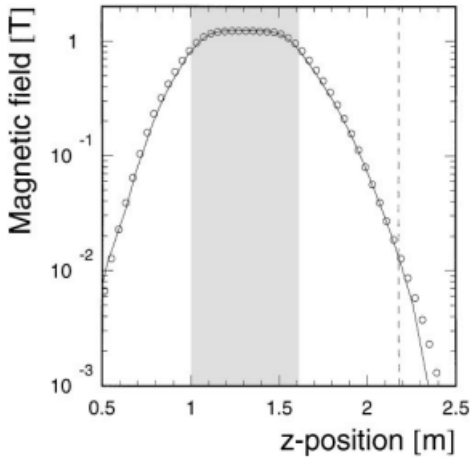

Figure 2.7: The magnetic field variation of the BigBite magnet across the mid-plane of the magnet along the horizontal line through the target. The circles denote the measured field, the solid lines are from a magnetic field calculation. The target is situated at the origin z = 0, the shaded area indicates the region between the pole faces. Adapted from [4]

.

ability to provide excellent spatial resolution (70-100 μm) make the open geometry spectrometer configurations along with the high beam-on-target luminosity concept of the SBS program possible. A detailed description of the GEM detectors in general, and the GEM detectors used in the Super BigBite Spectrometer program are given in Chapter 3.

Four front tracker GEM layers with active areas of 150×40 cm^2, located right

behind the BigBite magnet within a few centimeters, and a single 200×50 cm^2 GEM layer positioned behind the Ĉerenkov detector comprise the BigBite spectrometer's GEM tracker. The tracking algorithm always requires at least three out of five GEM layers to provide a 2D hit for a given event for track reconstruction to proceed. Due to the high occupancy in the GEM detectors as a result of the high background rates, the probability of false track reconstruction is high. The presence of five tracking planes helps in this regard by providing additional constraints to find real tracks.

2.3.3 Gas Ring Ĉerenkov (GRINCH)

The primary purpose of the GRINCH detector is pion rejection, based on the principle that pions with energies less than a medium-dependent upper-bound threshold will not emit Ĉerenkov optical photons while electrons with similar kinematics will. As shown in Figure 2.5a, GRINCH is positioned in between the four front tracker GEM layers and the single back tracker GEM layer within the BigBite spectrometer. The detector volume is filled with C_4F_8 heavy gas to promote Ĉerenkov radiation with a pion threshold of 2.7 GeV. Four highly reflective cylindrical mirrors are placed within the detector, at an angle, to reflect the optical photons into an array of 510 one-inch PMTs, organized into a honeycomb pattern. The small size of these PMTs, and the special readout electronics used, make it possible to use GRINCH in the high background experimental conditions of GMn and other SBS experiments. Figure 2.8 illustrates the process of Ĉerenkov optical photon generation within the GRINCH volume and reflection from the mirrors onto the PMT array. Except for the two nTPE kinematic points at $Q^2 = 4.5$ GeV^2/c^2, the GRINCH detector was not completely ready with a reasonable concentration of heavy gas for the other kinematic points of the GMn experiment which took data before the two nTPE kinematic points.

2.3.4 Timing Hodoscope (TH)

The BigBite TH detector's purpose is to provide high precision time information of minimum ionizing particles scattered into the BigBite spectrometer. This information can be used to calculate the *origin time* of the scattering event within the target, which in turn could be used to calculate the *time of flight* (TOF) of the nucleons in the hadron arm. In addition, data from the TH is extensively used for the calibration purposes of other detector sub-systems; especially the calorimeteric detectors.

The TH detector is a vertical stack of 90 plastic scintillator bars with two PMTs attached to each bar at either side of it (via light guides), contributing a total of 180

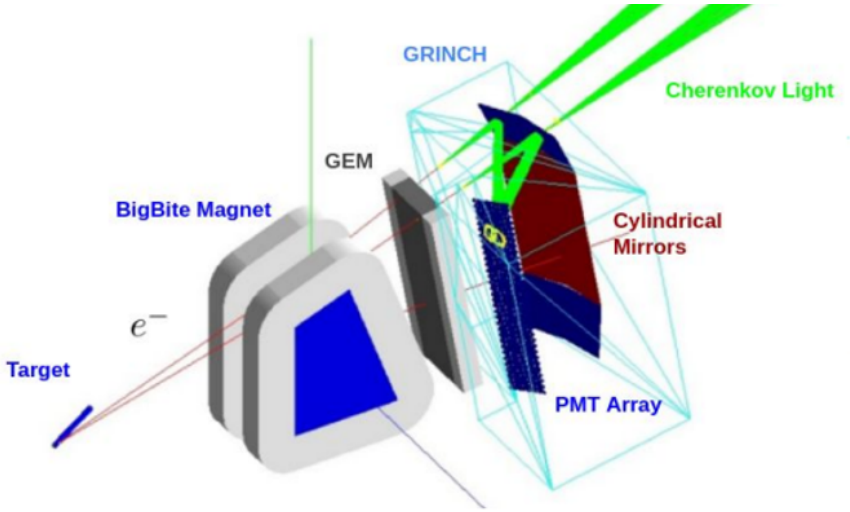

Figure 2.8: GRINCH detector operation in G4SBS simulation environment. Credit: M. Satnik

readout channels. The dimensions of a plastic scintillator bar are 2.5 cm × 2.5 cm × 60.0 cm, with the 60.0 cm side placed along the horizontal direction, perpendicular to the direction of particle motion within the BigBite spectrometer. As indicated in Figure 2.5a the TH detector is positioned in between the pre-shower and shower detector sub-systems within the BigBite spectrometer detector stack. See Figure 2.9 for a graphical representation of the geometry of the TH detector. Signals from the PMTs are sent to a NINO discriminator ASIC card, in which the signals are digitized with the use of TDCs. The mean time from the two PMTs attached to each scintillator bar could be used to accurately reconstruct the timing information of the ionizing particle that went through the paddle, removing the position dependence due to signal propagation time[38].

From the preliminary analysis of the TH detector performance during the GMn experiment, more than 98% detection efficiency based on tracks, a position resolution of 4-6 cm in the non-dispersive (horizontal) and 1.5-2 cm in the dispersive (vertical) directions, and time resolution of 500-750 ps have been observed.

2.3.5 BigBite Calorimeter (BBCal)

BBCal is an electromagnetic calorimeter, made of lead-glass blocks. Within these lead-glass blocks, high energy electrons and photons loose their energy in electromagnetic showers. The light created in these showers can be collected and quantified by the use of photo-multiplier (PMT) tubes. BBCal consists of two main sub-systems;

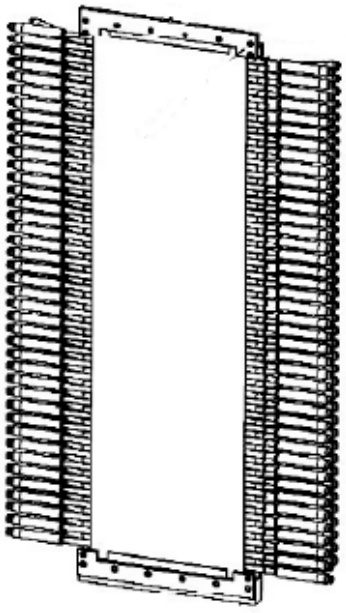

Figure 2.9: A 3D CAD diagram of the Timing Hodoscope detector. The central active area made with stacked scintillator bars can be seen with the PMTs attached via light-guides sticking out from either side. The support structure of the detector can also be seen at the top and bottom, which is also used to attach the detector to the BigBite spectrometer weldment.

pre-shower and *shower*.

The pre-shower detector consists of a total of 52 lead-glass blocks, each with the dimensions of 9 cm × 9 cm × 29.5 cm. The blocks are stacked in two 26-module columns, longer sides perpendicular to the direction of particle motion, with the blocks facing each other, and the PMTs attached to the two columns pointing in opposite directions. This configuration only covers 9 cm of path-length along the direction of particle motion. This provides an extra handle for pion identification and rejection, as heavier pions deposit less energy compared to the electrons within these "thin" lead-glass blocks.

The shower detector basically defines the end-of-flight for the scattered electrons within the BigBite spectrometer. It consists of 189 lead-glass blocks, each with dimensions of 8.5 cm × 8.5 × 34 cm. The blocks are stacked in a matrix of 27 rows and 7 columns, with the longer sides parallel to the direction of particle motion. With 34 centimeters of lead-glass along the direction of particle motion, particles such as electrons, positrons, and photons will deposit their entire energy within the shower detector. In principle, the sum of correlated cluster energy of the pre-shower and

shower detectors represents the total kinetic energy of the scattered electrons.

Figure 2.5a illustrates the positioning of the shower and pre-shower detectors within the BigBite spectrometer. The timing hodoscope is sandwiched between the pre-shower and the shower. Apart from the energy measurement of the scattered electrons and pion, the BBCal worked as the sole detector that provided the trigger for the entire data acquisition system during the GMn experiment. Furthermore, the cluster position information from BBCal provides a crucial constraint for the tracking algorithm which makes the track reconstruction feasible under the high background/occupancy conditions of the SBS experiments. Section 3.6.3 provides more information about this topic.

The most recent calibration results have shown, BBCal energy resolution ($\frac{\sigma_E}{E}$) to be in the range of 5.4-6.5 % across the entire set of kinematic settings of the GMn experiment.

2.4 Hadron Arm

The hadron arm of the GMn experiment primarily consisted of the 48D48 magnet, also known as the SBS magnet, and the hadron calorimeter detector (HCal). The HCal has no inherent ability to distinguish between neutrons and protons. Therefore, the primary source of particle ID between neutrons and protons comes from the magnetic deflection of protons by the SBS magnet. The magnetic deflection of protons with respect to the neutrons, and the cluster position, energy, and timing information from the HCal, form the basis of quasi-elastic D(e,e′n)p and D(e,e′p)n yield determination along with the contribution from the BigBite spectrometer for event selection and for the projection of $\vec{q}$ vector onto the face of the HCal.

2.4.1 48D48 Magnet (SBS magnet)

The 48D48 magnet was originally used at the kaon beamline of the AGS accelerator at the Brookhaven National Laboratory. It was acquired by the Jefferson Lab especially for the SuperBigbite Spectrometer program[39]. Figure 2.10 shows the 48D48 magnet inside JLab Hall-A. 48D48 is also a room temperature dipole magnet but much larger in size compared to the BigBite magnet. It weighs approximately 100 tons, is capable of producing a field integral of 2.0 - 2.5 Tm (depending on the magnet configurations) from a current of 2100 A which is the maximum current that was used and will be used during the SBS experiments. Documentation shows that the 48D48 magnet

could be operated at currents going up to 4000 A producing field integrals closer to 3 Tm. The horizontal gap of the entrance aperture is 46.9 cm, and the height is 121.9 cm. The magnetic field direction is horizontal, which induces a vertical bend for the charged particles that go through the magnet, a feature that is critical for the neutron-proton separation in the GMn experiment.

The 48D48 magnet is the central component of the very first SBS experiment that was approved by the JLab's program advisory committee, the GEp-V experiment (E12-07-109). The 48D48 is commonly referred to as the SuperBigbite or the SBS magnet. As indicated in Figure 2.10, part of the magnet yoke has been carved out to accommodate the exit beamline, so that the magnet can be moved to fairly forward scattering angles. Conducting coils on that side of the magnet have been redesigned because of this and it has been verified that the distortion of the homogeneity of the magnetic field is minimal due to this change.

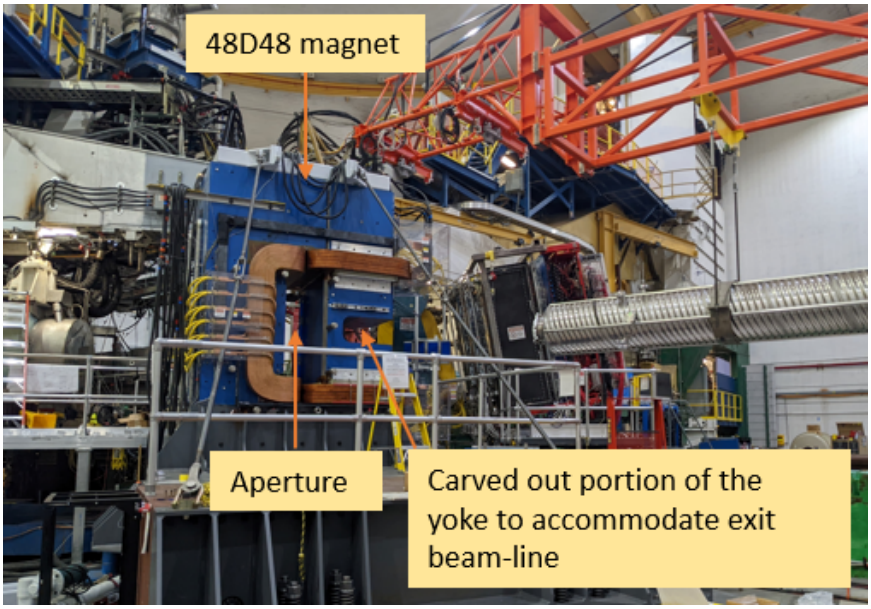

Figure 2.10: 48D48 magnet in Hall-A

During the five kinematic settings of the GMn experiment, the SBS magnet was operated at various field strengths to achieve the sufficient magnetic deflection of the protons, taking into account the nucleon momentum of the given kinematic setting. This was done by simply changing the current through the magnet coils and the field strength was recorded as a percentage of magnet current compared to the maximum current that could be applied, which is 2100 A. This percentage is referred to as the SBS magnet *field scale* and it will be frequently referred to in the discussion of the data analysis.

2.4.2 Hadron Calorimeter (HCal)

HCal is a sampling-calorimeter designed with a focus on detecting high-energy hadrons with high efficiency, regardless of their electric charge. This is achieved by the unique design of the HCal modules. Figure 2.11a depicts the cross-sectional view of a HCal module. The incoming high-energy hadrons can generate hadronic showers as a result of strong interactions with the nuclei of the iron absorbers. A portion of these hadronic showers contains electromagnetic components (electrons, positrons, and photons). The particles generated from the electromagnetic component are capable of exciting the scintillator material and generating photons with energy proportional to the EM component of the shower. This phenomenon is known as the "sampling" of energy of the original hadron. The wavelength shifter converts these photons to a more optimal wavelength which could be better detected by the PMTs. The interleaved iron absorbers and scintillator material design increases the probability of the occurrence of a hadron shower within the module and the EM components of that shower being sampled by the scintillator material. The dimensions of a HCal module are 15 cm $\times$ 15 cm $\times$ 100 cm, with the long dimension positioned along the direction of particle motion. HCal is made of a total of 288 of these modules, arranged in a matrix of 12 columns and 24 rows. This amounts to a large active area of 180 cm $\times$ 360 cm. Steel plates are placed in front of the HCal detector to further promote hadronic shower formation. Figure 2.11b is a real-life image of HCal inside Hall-A.

HCal serves as the single source of hadron detection for the GMn experiment and also for the other SBS experiments. The primary information used for analysis from HCal are the energy-weighted cluster positions, cluster energy, and the timing information. As mentioned earlier, no particle identification ability exists in HCal hardware and the GMn analysis completely relies on the magnetic deflection of the protons by the SBS magnet for this purpose. Being a sampling hadron calorimeter, HCal has only 40%-50% energy resolution ($\frac{\sigma_E}{E}$) while only approximately 10% of the kinetic energy of the hadrons are found to be sampled by the detector. The position resolution is found to be in the range of 5-7 cm and this is of critical importance as effectively this parameter along with the amount of magnetic deflection of protons by the SBS magnet determines the goodness of the neutron and proton separation.

The "ratio method" for the GMn extraction relies entirely on an accurate measurement of the quasi-elastic scattering cross section ratios of the two reactions, D(e,e′n)p and D(e,e′p)n. As it will be described in detail in Chapter 4, this cross-section ratio will be extracted by a comparison technique between experiment data and Monte Carlo simulated data. The systematic uncertainties introduced by this technique de-

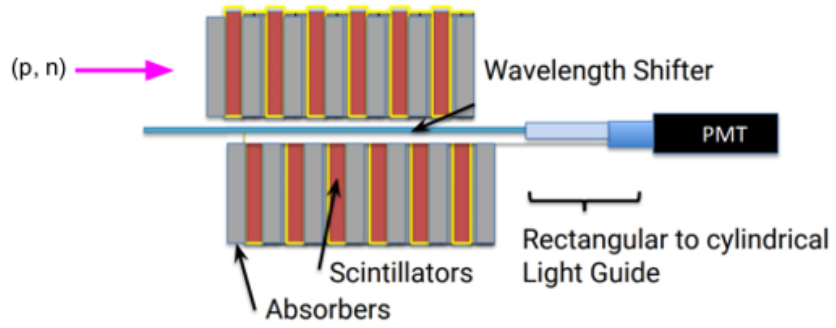

(a) HCal module cross-section. Image credit: S. Seeds.

(b) A side view of the HCal inside Hall-A

Figure 2.11: HCal detector

pend on how well the inelastic processes are simulated or accounted for, and how well the experiment setup is being simulated. While most of the parameters associated

with the electron arm, the target, and the beam are canceled when the cross-section ratio is considered, two of the very important parameters that do not cancel are the neutron and proton detection efficiencies of HCal. This must be accurately accounted for in the simulation in order to minimize systematic uncertainty of the final GMn extraction. A detailed simulation of the experiment setup, including the HCal detector, exists within the simulation framework. Figure 2.12 shows the neutron and proton detection efficiency of HCal from the MC simulations. Over 95% detection efficiencies with only about a 1% difference between neutrons and protons are predicted by the MC in the range of nucleon momenta of interest for the GMn experiment. Analysis to benchmark the simulated neutron and proton detection efficiencies using data from the calibration runs are presented in Chapter 4.

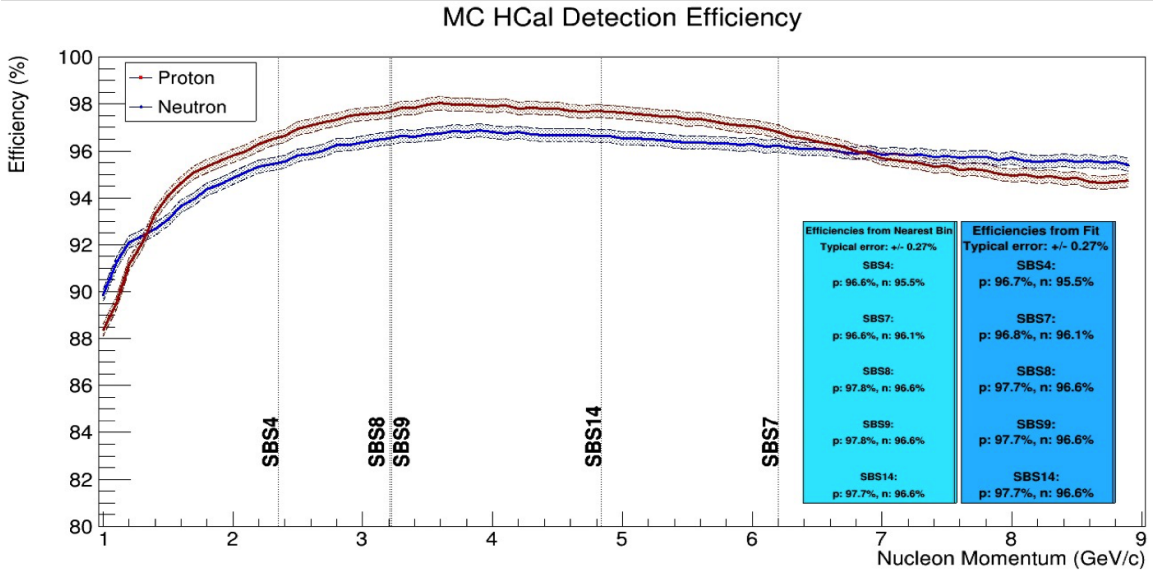

Figure 2.12: MC simulated HCal neutron and proton detection efficiencies as a function of nucleon momentum. The vertical dotted lines indicate the central nucleon momenta for the different kinematic settings of the GMn experiment. Plot credit: J. Body

2.5 Kinematic Settings of The Experiment

The Kinematic settings of the E12-09-019 experiment are shown in Table 2.1. Beam energy is decided on the accelerator settings. By changing the BigBite electron arm angle with respect to the incoming beamline, the desired Q^2 is obtained. The hadron arm (48D48 SBS magnet and the HCal) angle is then calculated based upon the elastic scattering kinematics. The other parameters like the BigBite spectrometer

distance from the target, SBS magnet distance from the target, and the HCal distance from the target are decided to optimize acceptance between the two spectrometer arms. The percentage current of the SBS dipole magnet is calculated with respect to the maximum current capability of the SBS magnet power supply. As mentioned in Section 2.4.1, this value is determined upon the nucleon momentum of elastic kinematics and it must generally be larger for higher Q^2 settings, to ensure adequate neutron and proton separation. The kinematic point labeled SBS-8 is dedicated for the neutron Two Photon Exchange (nTPE) experiment (E12-20-010), which is not discussed in this thesis.

Kin label	Q^2 $(GeV/c)^2$	E_{beam} (GeV)	ϵ	Scat. e mom. (GeV/c)	Scat. Nuc. mom. (GeV/c)	θ_e - BigBite angle (deg)	BigBite distance (m)	SBS angle (deg)	SBS distance (m)	SBS % current of 2100 A	HCal angle (deg)	HCal distance (m)
SBS-4	3	3.7393	0.486	2.11	2.35	36	1.8	31.9	2.25	30%, 50%	31.9	11
SBS-8	4.5	5.9826	0.668	3.59	3.22	26.5	2	29.9	2.25	50%, 70%, 100%	29.4	11
SBS-9	4.5	4.0268	0.274	1.63	3.21	49	1.55	22.5	2.25	70%	22	11
SBS-14	7.5	5.9828	0.31	2	4.84	46.5	1.85	17.3	2.25	70%	17.3	14
SBS-7	10	7.9308	0.415	2.67	6.2	40	1.85	16.1	2.25	85%	16.1	14
SBS-11	13.6	9.889	0.381	2.67	8.13	42	1.55	13.3	2.25	100%	13.3	14.5

Table 2.1: Kinematic settings of the E12-09-019 experiment

Chapter 3

Gas Electron Multiplier (GEM) Tracking Detectors

The Super BigBite Spectrometer (SBS) program's detector and spectrometer configurations are carefully designed to be optimized for nucleon form factor measurements at large four-momentum transfer (Q^2). The elastic electron-nucleon scattering cross section decreases rapidly as Q^{-12}. This makes it extremely challenging to collect enough statistics for a high-precision measurement. The only options are to increase beam-on-target luminosity and the solid angle acceptance of the spectrometers, in order to be able to collect enough statistics within a reasonable amount of time. This comes with many challenges such as high background rates in the detectors. The SBS spectrometer package is specifically designed to address these obstacles [39]. The SBS concept is based on large, open-geometry configuration spectrometers, which are capable of handling high rates, and have the ability to operate at relatively forward angles (approximately 10 degrees or more). One downside for the open configuration and small bend angles of the SBS spectrometers is that their detectors have a direct line-of-sight to the target, which contributes to increased background rates. SBS experiments are planned to be carried out at extremely high luminosities of up to 10^{39} electron/s-nucleon/cm^2. Because of these factors, background rates of about 500 kHz/cm^2 are expected at the foremost tracking detectors.

To meet this criterion, the GEM detector technology [40] was adopted for the SBS physics program for charged particle tracking. The GEM detectors have been demonstrated to provide stable gain of approximately 10,000 for rates up to several hundred MHz/cm^2 [5] and provide position resolution of the order of 70 μm [41]. The design of the SBS GEM detectors was motivated by the success of the COMPASS GEM detectors at CERN. COMPASS was the first time that GEM detectors were

used in a high-luminosity particle physics experiment [42].

3.1 GEM Detector Introduction

Gas Electron Multipliers, abbreviated as GEMs, belong to the family of Micro Pattern Gas Detectors (MPGD). MPGDs rely on micro-patterned structures of conductors and dielectric materials to *amplify* an ionization event created within a gaseous volume by ionizing radiation via a process known as Townsend Avalanche. In a Townsend Avalanche, a *free electron* generated by ionizing a gas molecule is accelerated to a high velocity, and thus high energy, by an intense electric field. This energetic electron can now collide with another gas molecule and create a secondary free electron, which in turn can be accelerated by the strong electric field and create even more electrons. Figure 3.1 illustrates this process. This gives rise to an exponential production of free electrons, starting from just a single free electron. The typical gains achieved in these processes are in the range of 10^2 - 10^4. This generates pulses in the millivolt range which are large enough to be detected by modern readout electronic devices. In MPGDs, this large electric field is produced by applying potential differences on the order of a few hundred volts between conducting parts, separated by dielectrics, all in the scale of tens of micrometers.

GEM technology was introduced by CERN scientist Fabio Sauli in 1997 [40]. A GEM is a thin ($\approx 50\mu m$) polymer foil, which is metal-coated on both sides and perforated with a high density of micrometer-sized holes. Figure 3.2a shows an electron microscope image of a GEM foil. In the given example, the diameter of these circular perforations is 70 μm, and the pitch between these perforations is approximately 140 μm. Figure 3.2b shows the cross-section of a single 'GEM hole'. The conical shape of the hole is an artifact of the manufacturing process. When a few hundred volts is applied across the two outer conducting surfaces of the GEM foil, a strong electric field is created within the GEM holes. See Figure 3.3a. *Free electrons* are generated through gaseous ionization caused by radiation at one side of the GEM foil. The applied electric field guides the electrons into the GEM holes. As they enter into the GEM holes, they will accelerate and will produce a "shower" of free electrons via ionizing collisions (Figure 3.3b), as described above. Due to the small mass of electrons, the diffusion and drift time of these electrons is minimal and they are tightly correlated with the original interaction point of the ionizing particle within the gas volume, allowing for high precision position determination of the ionizing particles that traverse through the detector.

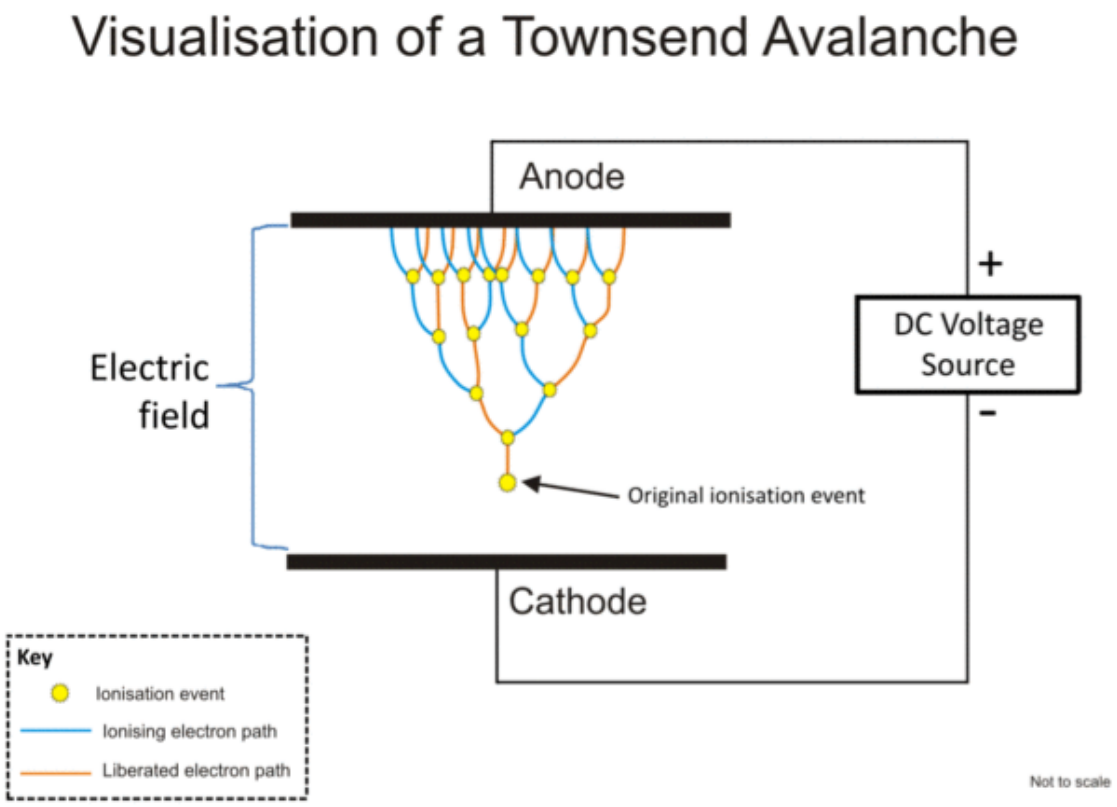

Figure 3.1: Townsend Avalanche process - Image by Dougsim via Wikimedia Commons

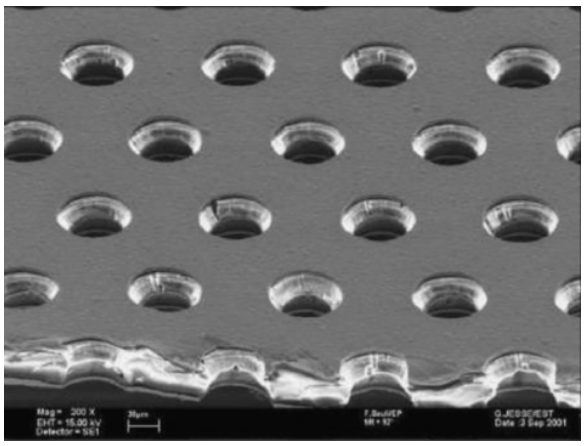

(a) A closer look at a GEM foil. GEM foil thickness is $50\mu m$, the hole diameter and pitch are $70\mu m$ and $140\mu m$, respectively [5].

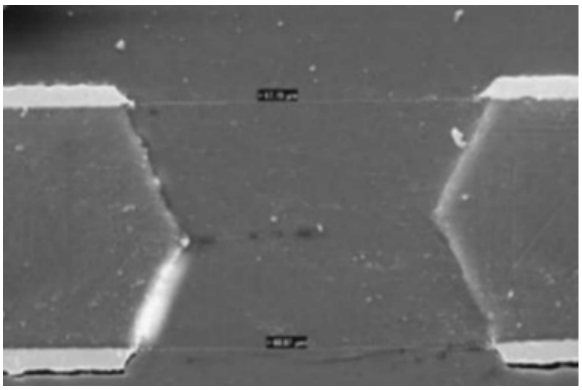

(b) GEM-hole cross-section.

Figure 3.2: Electron microscope images of a GEM foil [5].

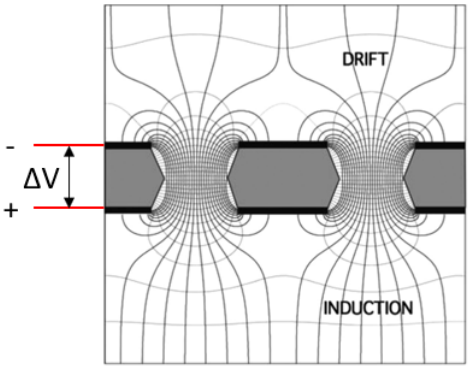

(a) Electric field and equipotential line distributions within the GEM holes and around the region of the GEM electrode.

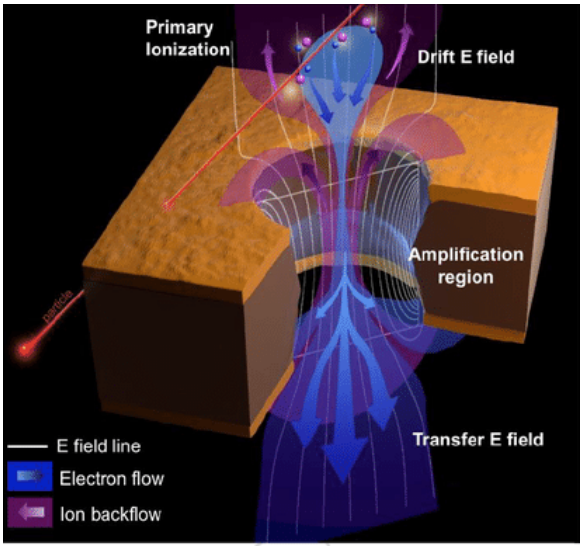

(b) A graphical representation of the avalanche process within a GEM hole.

Figure 3.3: Ionization avalanche process in the GEM holes due to the presence of a strong electric field.

3.1.1 Single Stage GEM Detector

The schematic in Figure 3.4 depicts the simplest form of a GEM detector. It is comprised of a GEM electrode inserted in between a drift cathode and a PCB readout board with 2D Cartesian conductive strips. The entire volume of the detector should be filled with a gas (or a gas mixture) capable of producing free electrons from ionizing radiation in a stable manner. When an ionizing particle creates ionizing events within the "drift gap" of the detector, the resulting electrons drift into the holes of the GEM detector and get multiplied. Then they are transferred into the "induction gap" where they can land onto the readout strips of the PCB electrode. The drift of the electrons towards readout strips induce voltage pulses on those strips; these pulses can be detected by readout electronics. The information of the hit strips from the two orthogonal sets of strips allows for the 2D position reconstruction of the ionizing particle that interacted with the gas volume in the drift gap. The inherent separation between the amplification and detection electrodes allows for flexibility in the choice of the readout electrode's strip/pixel patterns and also provides greater stability.

3.1.2 GEM Detector Gain

The GEM detector gain is the ratio of detected charge collected on the readout electrode to the charge generated by the ionization within the drift region. It is more

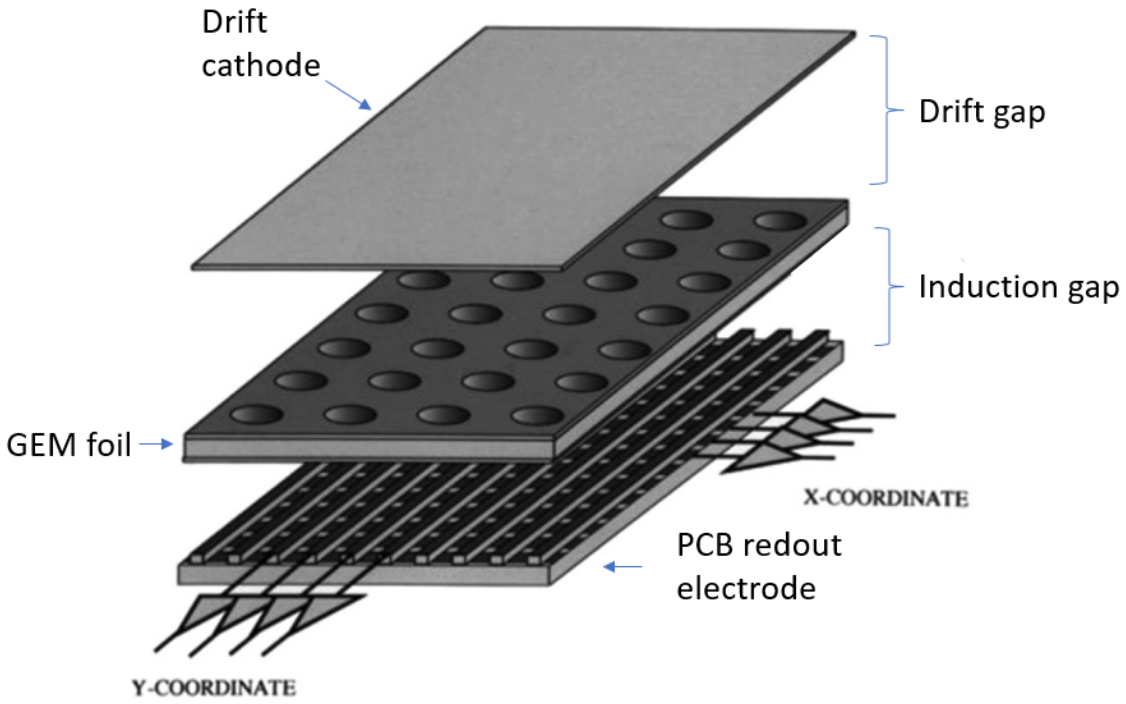

Figure 3.4: Schematic of a single stage GEM detector - Adapted from [5]

accurate to refer to this ratio as the "effective gain," since a fraction of electrons generated by avalanche amplification is absorbed by the GEM electrodes, decreasing the effective gain compared to the absolute gain. The gain of a GEM detector is a function of many variables: the properties of the gas in the detector, the GEM foil geometry, and the field strengths in the various regions of the GEM detector (drift, transfer, induction, etc.). The real field strengths are intricately correlated to the GEM foil geometry, but it is convenient to think of them as separate properties.

3.1.3 Choice of Gas

The choice of gas that "fuels" the ionization process is crucial for the performance of a GEM detector. An ideal candidate should have low ionization energy, be chemically inert, and have a low number of degrees of freedom. Lower degrees of freedom maximize the fraction of energy used for the ionization process rather than contributing energy to additional rotational and vibrational degrees of freedom. The most popular choice for GEM detectors is argon.

When argon on its own is used in a GEM detector, an undesirable phenomenon occurs: the argon ions produced by ionization can absorb additional energy in the ionization process and can elevate to excited states and release energy as they de-

excite. This released energy is in the form of photons in random directions. These can cause further ionization events within the gas medium. This will release free electrons that can initiate unwanted avalanches across random locations within the gas volume. To prevent this unwanted phenomenon, a so-called "quencher gas" is added alongside the argon in certain percentages. The quencher gases are usually complex molecules that have a rotational and vibrational degrees of freedom. They can absorb the photons released as a by-product of the ionization process. In the SBS program, carbon dioxide is used as a quencher gas and argon and carbon dioxide are used in the volume ratios of 75%/25%.

3.1.4 Ionization

When a high energy charged particle passes through any kind of matter, it ionizes the atoms of the medium, liberating electrons. The primary energy loss mechanism for many GeV charged particles, like the ones in SBS experiments, is Bremsstrahlung. However, ionization of the gas molecules is the primary process that gaseous radiation detectors rely on to measure the position and timing information of charged particles that traverse through the detector. GEM detectors are designed so that free electrons generated by gas ionization in the drift region are multiplied by a layered stack of one or more GEM foils.

For a singly charged relativistic particle, traveling at velocity $v = \beta c$, the average rate of ionization energy loss within a medium of atomic number Z, mass number A, and density ρ is given by the Bethe-Bloch formula.

$$\left\langle \frac{dE}{dx} \right\rangle = -\rho \frac{2K}{\beta^2} \frac{Z}{A} \left\{ \ln \left[\frac{2m_e c^2}{I_e} \beta^2 \gamma^2 \right] - \beta^2 - \frac{C}{Z} - \frac{\delta}{2} \right\} \tag{3.1}$$

Here, $K = \frac{4\pi N e^2}{m_e c^2}$, where N, e, m_e are Avogadro's number, the electron charge, and the electron mass respectively. I_e is the effective ionization potential of the material averaged over all atomic electrons. This is approximately given by $(10eV).Z$. The C/Z term represents an inner shell correction, which accounts for the reduced ionization efficiency for electrons in the inner shells of the atom, as a result of screening effects. $\delta/2$ is a density effect correction, which accounts for polarization effects due to the electric field of the relativistic charged particle; this effect is small for non-condensed media.

Because of the $1/\beta^2$ term, the ionization energy loss is largest for low-velocity particles. However, the particles we are interested in are on the order of several GeV and traverse close to the speed of light, $v \approx c$. Therefore, at relativistic particle

velocities, the ionization energy loss rate is a logarithmic function of $\beta\gamma$ ($\frac{p}{mc}$). This behavior can be seen in Figure 3.5, which causes the slow "relativistic rise" in high $\beta\gamma$.

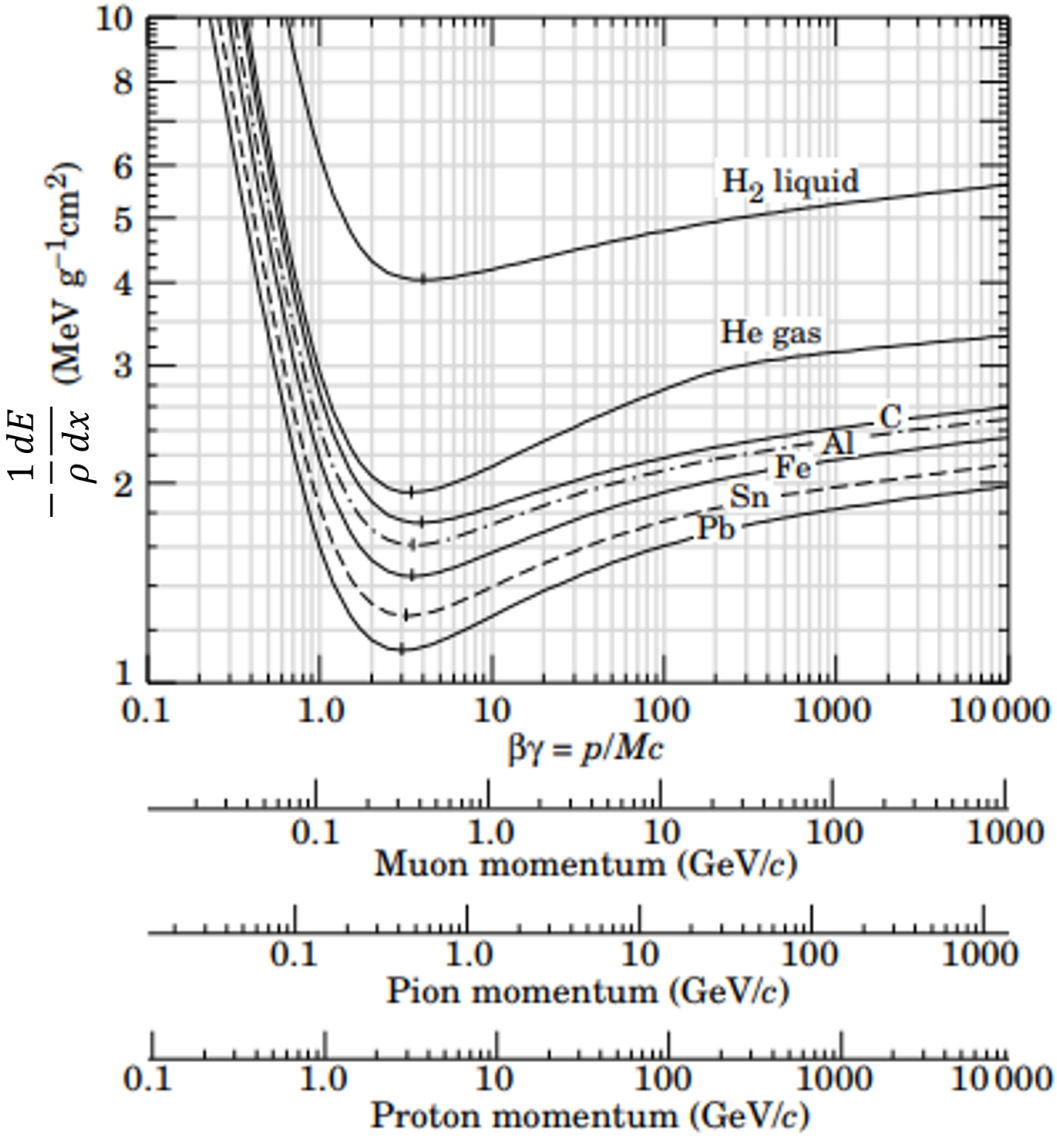

Figure 3.5: Ionization energy loss curves for a singly charged particle in several materials. Beringer *et al.* (2012).

It can be seen that the ionization energy loss does not depend strongly on the material, for a unit density. This can be explained by the Z/A term; for stable isotopes of nuclei, the Z/A ratio is roughly around 0.5. Near $\beta\gamma \approx 3$, all of the energy loss curves show a minimum. Charged particles near this kinematic region are referred to as minimum ionizing particles (MIPs). The several GeV electrons in the

GMn experiment loose only about a factor of 1.5 times the ionization energy loss of MIPs. This equates to about 2 MeV g^{-1} cm^2.

In Table 3.1, the information on ionization energy loss and the number of primary and total number of electron-ion pairs generated from a singly charged minimum ionizing particle is given for a set of different gases. In this context, the primary electron-ion pairs refer to the electron-ion pairs generated from the direct interaction of ionizing particles. However, more energy than the average ionization energy is usually released in the primary ionization process. Subsequently, the resulting electrons have enough kinetic energy to cause more ionization events, referred to as secondary ionization. For a 3 mm drift region of SBS GEM detectors, filled with Ar gas, it can be approximated that about 30 total electron-ion pairs are generated.

Gas	Density mg cm^{-3}	E_x eV	E_I eV	W_I eV	$dE/dx\|_{min}$ keV cm^{-1}	N_P cm^{-1}	N_T cm^{-1}
Ne	0.839	16.7	21.6	30	1.45	13	50
Ar	1.66	11.6	15.7	25	2.53	25	106
Xe	5.495	8.4	12.1	22	6.87	41	312
CH_4	0.667	8.8	12.6	30	1.61	37	54
C_2H_6	1.26	8.2	11.5	26	2.91	48	112
iC_4H_{10}	2.49	6.5	10.6	26	5.67	90	220
CO_2	1.84	7.0	13.8	34	3.35	35	100
CF_4	3.78	10.0	16.0	54	6.38	63	120

Table 3.1: Ionization properties of noble and molecular gases at nominal temperature and pressure (NTP: 20°C, one atm), for a singly charged minimum ionizing particle. E_x, E_I: first excitation and ionization energy; W_I: average energy per ion pair; $dE/dx|_{min}$, N_P , N_T: differential energy loss, primary and total number of electron-ion pairs per cm. Adapted from [7]

3.1.5 GEM Foil Geometry

Schematic views of a so-called standard GEM foil made by CERN are given in Figure 3.6. These holes are etched with a uniform separation between them (pitch, P), in parallel rows, with an offset equal to P/2 (Figure 3.6a). Typical GEM foils have a 50 μm polyimide layer, sandwiched by two 5 μm copper layers. Photolithographic techniques are used to engrave the GEM hole pattern on both conductor sides of the foil, and then a special solvent is used to dissolve the polyimide layer in the middle. This technique is known as the double-mask technique. Double-mask technique creates GEM holes with a double-conical shape since it involves etching of the GEM

holes and dissolving the polyimide insulation layer from both sides. This can be seen in the schematic in Figure 3.6b, and the microscope image in Figure 3.2b.

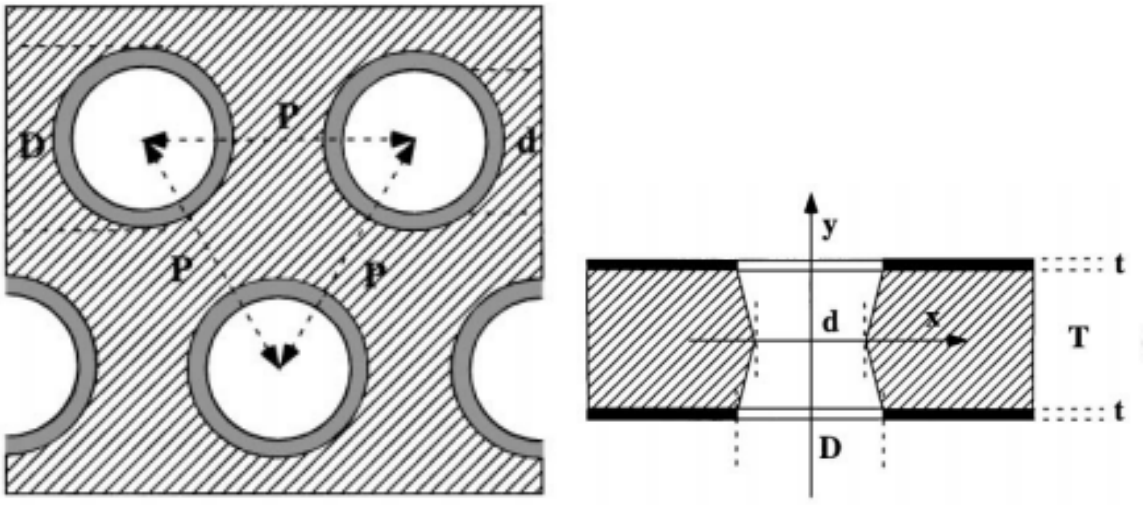

(a) GEM foil top view schematic.

(b) GEM foil side view schematic.

Figure 3.6: Schematics of a standard GEM foil - adapted from [6].

Intrinsic gain from a GEM foil can be defined as the ratio N/N_0 where N_0 is the initial number of electrons entering the GEM foil, and N is the total number of electrons leaving the GEM foil after the avalanche multiplication. In a uniform electric field, the relationship between N and N_0 can be modeled as [7]:

$$N = N_0 e^{\alpha x} \tag{3.2}$$

Here, α is the first Townsend coefficient, which is equal to $1/\lambda_i$, with λ_i being equal to the mean free path for ionization for the given gas under the applied field, and x is the distance over which the avalanche multiplication happens. With increasing field, λ_i decreases and after a gas-dependent threshold, it decreases exponentially, which marks the onset of the avalanche multiplication point.

For a given applied voltage in-between the conductive layers of the GEM foils, the electric field within the foils should increase with decreasing hole diameter. Even if this is true, it has been discovered that after reducing the hole diameter below approximately the GEM foil thickness, the effective gain starts to plateau [6]. The effective gain is calculated from the measured current in the readout electrode, and is ultimately the parameter of most importance. The effective GEM gain has been observed to increase exponentially with the applied voltage across the GEM electrode, as verified by Bachmann et. al [6].

The hole diameter (D) of the current standard CERN made GEM foils is 70 μm on the copper layers and the diameter at the middle of the hole (d) is about $\approx$ 50 μm due to the double-conical shape. In addition, a standard CERN GEM foil has a GEM hole pitch (P) of 140 μm. Figure 3.2a shows a microscopic image of a standard GEM foil.

A GEM foil is essentially a parallel plate capacitor, with the only difference being the presence of the GEM holes. When a potential difference is applied across the GEM foil, there will be electrostatic energy stored within the electric field between the top and the bottom conductive layers. The amount of this energy is proportional to the area of the GEM foils. In the event of a discharge/streamer created between the top and the bottom conductive planes, this energy will be dissipated in different forms such as heat, light, and sound. For small active area GEM modules (ex: 10 cm $\times$ 10 cm), the amount of energy released is not large enough to cause damage to the GEM foils. However, such an event can cause catastrophic and permanent damage when the active area is large, like in the SBS GEM chambers. Due to this reason, for some SBS GEM modules (active area 50 cm $\times$ 60 cm), one side of the GEM foil was divided into smaller high-voltage sectors and provided with HV via individual protective resistors. This sectorization, in general, prevents permanent damage to GEM foils in case of electrical discharges. However, in rare instances, a discharge coupled with any dust present in a GEM hole could lead to the permanent short in a GEM sector. While the sectorization prevented the whole GEM foil, and in turn the whole GEM module, from being unusable in such an event, it required a physical intervention of disconnecting the protective resistor from the damaged sector in order to restore the GEM module back to normal operation. In larger-sized GEM modules of the SBS (active area 150 cm $\times$ 40 cm), both sides of the GEM foil were sectorized. This design prevents the need for having to disconnect a damaged HV sector in order to bring the GEM module back to life. Figure 3.7 shows the rectangular sectors of a GEM foil.

3.1.6 GEM Readout Board

Due to the physical separation between the charge amplification and charge collection stages in a GEM detector, the readout board's strip/pixel pattern can be chosen without any constraints. Even though a pixel readout pattern would be an ideal candidate in high background environments (like those of the experiments in the SBS program), in order to eliminate the unavoidable multiple combinatorics issue

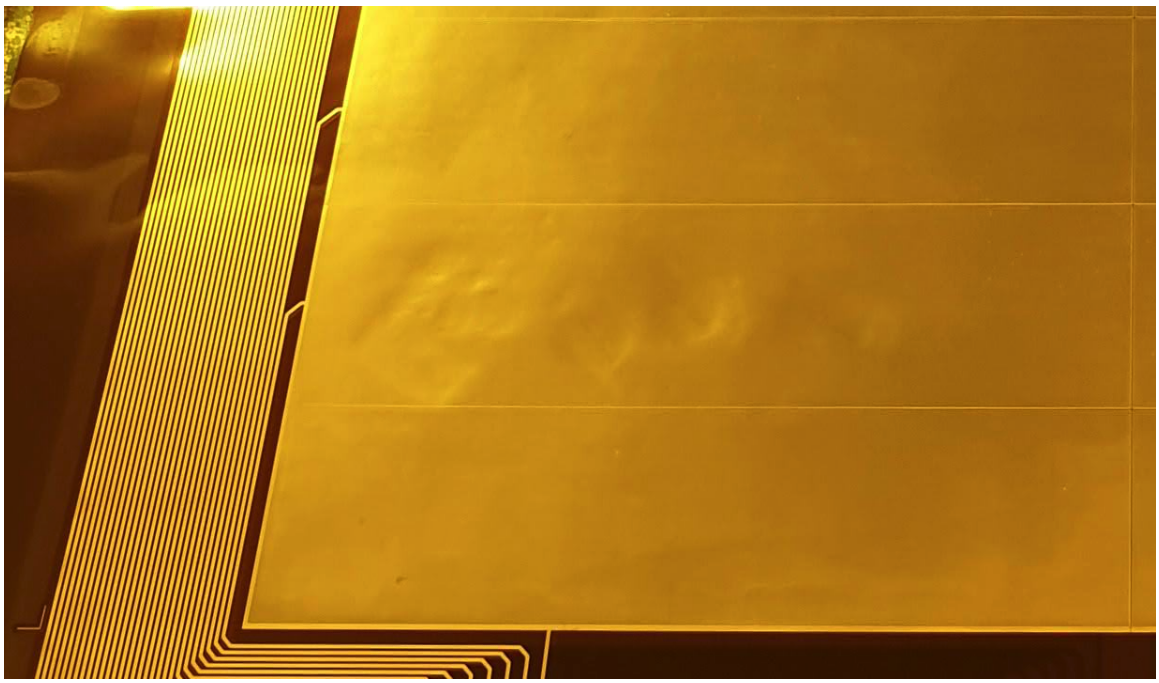

Figure 3.7: A GEM foil with visible HV sectors

that arises with strip-based readout patterns, the number of readout channels in a pixel readout board will be many orders of magnitude larger than in a strip readout scheme. This makes the pixel readout method cost prohibitive for large active area applications such as SBS. Therefore, strip-based readout boards with a 2D coordinate system are typically used in the large active area GEM detectors.

Similar manufacturing techniques used in the GEM foil fabrication process are used for the GEM readout board fabrication. Two sets of parallel metal strips, in a desired coordinate system, are engraved on two sides of a polymer foil. Then, after gluing the bottom side of the readout board to a support, the polymer spaces in between the top readout strips are etched away via a solvent. Figure 3.8a depicts the structure of a 2D X-Y Cartesian strip type readout board.

Since a considerable fraction of the bottom readout strips are covered by the top readout strips, the bottom readout strips are made to have larger thickness to ensure equal charge sharing between the two coordinate strips. This characteristic is important in the 2D hit reconstruction phase during the analysis, to disentangle multiple hit combinatorics from 1D clusters. One other thing that is important to consider when designing a readout board is the capacitance (pF/cm) of the readout channels, as it has been observed that there is a linear relationship between the strip capacitance and the noise in the front-end electronics. In all of the SBS GEM readout

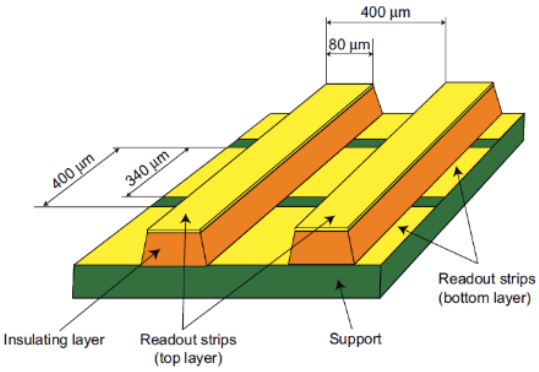

(a) GEM readout board schematic

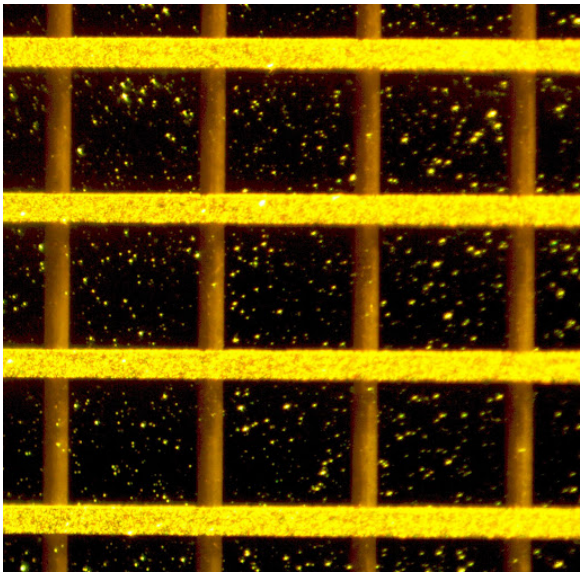

(b) SBS GEM readout board microscope image

Figure 3.8: SBS GEM X-Y readout board

boards, the top readout strips have a width of 80 μm where the bottom readout strips have a width of 340 μm. The pitch between the readout strips in both the top and bottom strips is 400 μm. The thickness of the Kapton layer that insulates the two sets of strips is 50 μm. The measurements are illustrated in Figure 3.8a. These parameters are chosen after numerous studies to optimize the number of readout channels, the double-track resolution, and capacitive load on the front-end electronics [43].

In the SBS GEM modules, three types of 2D readout strip patterns are used. One configuration was GEM modules that were manufactured in the early stages of preparation for the SBS program. These are the somewhat traditional X-Y readout type. These GEM modules have an active area of 50 cm $\times$ 60 cm. Figure 3.8b shows a microscope image of an X-Y type readout board used for SBS GEMs. Later on, the so-called U-V and X-W type readout GEM modules with an active area of 150 cm $\times$ 40 cm were manufactured. In total, four U-V and two X-W GEMs were developed. The U-V readout boards have a strip orientation of 60^0 with respect to the two sets of strips, and the X-W readout boards have a strip orientation of 45^0 with respect to the two sets of strips. The objective behind having these different types of strip orientations was to ease the strain on the track reconstruction process, by reducing the number of false tracks generated due to 2D hit ambiguity induced by the high background rate conditions.

3.1.7 Triple GEM detector

In Section 3.1.1, the simplest form of a GEM detector – the single stage GEM detector – with just a single GEM foil for avalanche amplification was introduced. However, it has been observed that the maximum attainable gain of a single stage GEM detector is limited due to the damages caused by discharges from heavily ionizing particles [44]. By stacking two or more GEM electrodes, in a cascading pattern, it has been demonstrated that much higher gain is attainable [6]. Per each addition of a GEM amplification stage, an increase of about one order of magnitude of effective gain is observed [45]. Furthermore, due to the sharing of amplification across multiple GEM electrodes, it is possible to operate the individual GEM electrodes at much lower voltages, which significantly reduces the probability of discharges. With the success of COMPASS triple GEM detectors, the triple GEM detector has been established as a standard for minimum ionizing particle tracking under high background rate conditions. Figure 3.9 is a schematic cross-sectional view of a triple GEM detector.

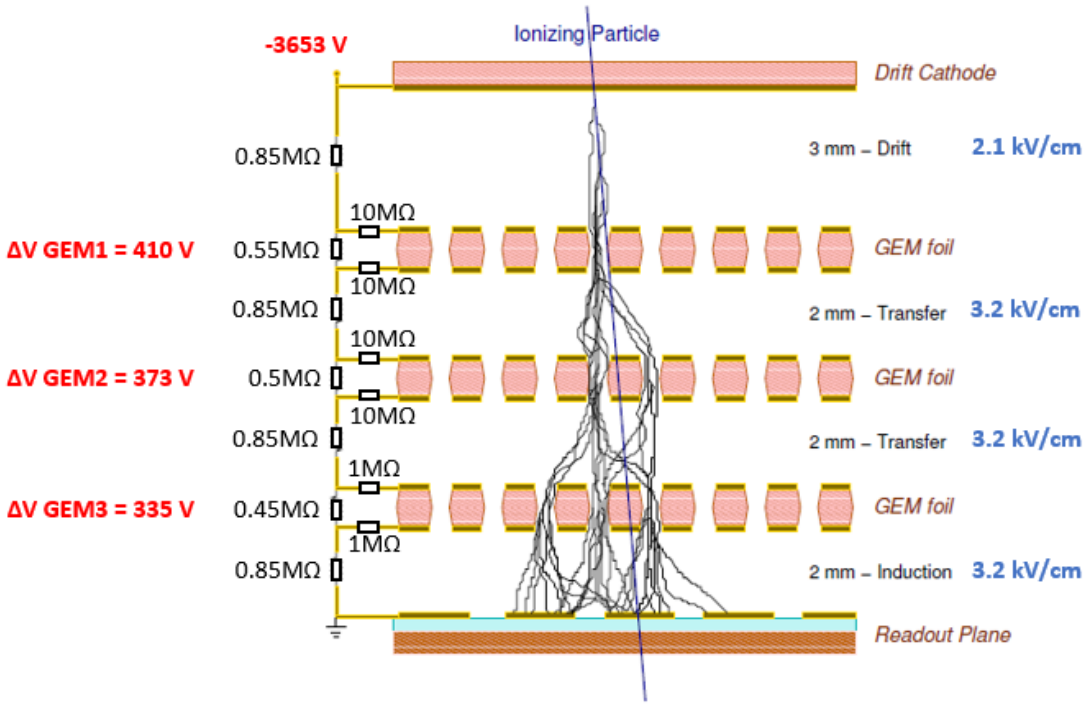

Figure 3.9: SBS triple GEM detector cross section schematic

A graphical representation of initial ionization within the drift region and the cascading avalanche multiplication across the three GEM foils is shown. A resistive divider chain with seven resistors in series is used for high-voltage distribution across the three GEM foils, the drift region, the two transfer regions, and the induction

region. 10 MΩ and 1 MΩ resistors are used as the protective resistors for the HV sectors, to prevent damages during discharges by limiting the current draw. The potential difference across the three GEM foils is intentionally made to be in a decreasing order, as can be seen from Figure 3.9. This is to reduce the probability of discharges; since the most number of electron-ion pairs are present within the third GEM foil, it has the largest probability for discharges. It has been demonstrated that for multi-stage GEM structures, an extremely important parameter for gain is the sum of voltage differences across the GEM foils rather than the individual values [6]. This allows slight modifications of individual voltages applied across different GEM foils, while keeping the sum of the voltage differences the same.

The average voltage difference across the three GEM foils is about 373 V, for the above configuration. For a standard CERN single GEM foil with comparable drift and induction field values (shown in blue on the right side of Figure 3.9), the approximate effective gain is in the range of 20-30 [6]. By increasing the gain by two orders of magnitude for the additional two stages of amplification, the minimum effective gain can very crudely be approximated to be about 2000 or more for this kind of triple GEM detector.

3.2 GEM Module Design and Assembly at UVA

The design of the UVA-built SBS GEM detectors is based on the R&D work for the COMPASS GEM detectors at CERN [46] [47], followed by additional R&D at the University of Virginia [48]. The design is optimized for high background rate conditions (as high as 0.5 MHz/cm^2) while sustaining spatial resolution of 70 μm.

In this context, a "GEM module" is defined as a single triple GEM detector, whereas a "GEM layer" is defined as a single tracking layer/plane that gets installed into the stack of trackers in a spectrometer. An individual tracker stack is made of one or more GEM modules. There are three different types of UVA-built GEM modules that have been used in the SBS experiments thus far. These are listed below in order of their production.

1. 50 × 60 cm^2 X-Y type readout: 50 produced
2. 150 × 40 cm^2 U-V type readout: 4 produced
3. 150 × 40 cm^2 X-W type readout: 2 produced

The fundamental difference between these different types of GEM modules can be mainly attributed to the 2D projective readout strip pattern of the readout electrode and the detector active areas. The U-V and X-W GEMs have the same active area while the X-Y GEMs have their own unique active area (50 x 60 cm^2). The motivation behind manufacturing GEM detectors with different readout strip patterns is explained in Section 3.1.6. Figure 3.10a depicts a cross-sectional view of the different regions of the triple GEM modules. The support structures of the detector are highlighted in Figure 3.10a. The Ar/CO_2 gas mixture will enter the detector from the Gas Window and flow down through the porous cathode foil into the Drift Region. Thereafter, the gas will go through the three porous GEM foils, across the two Transfer Regions and into the Induction Region. Finally, the gas can exit the detector via Gas Outlets at the readout board level. Figure 3.10b illustrates all of the structural components of a GEM detector along with the cathode, GEM, and readout electrodes.

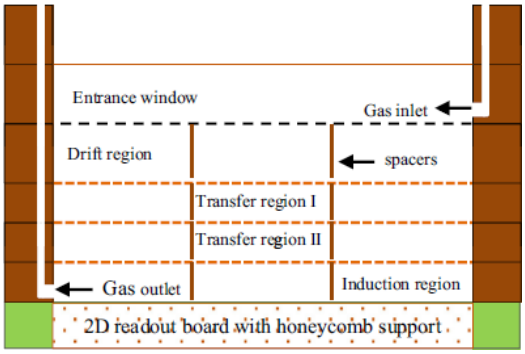

(a) Cross section schematic; adapted from [48]

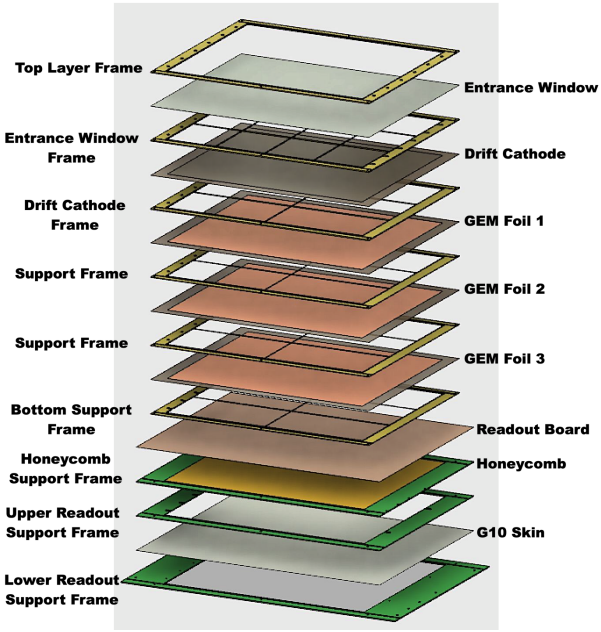

(b) Exploded CAD diagram; courtesy of J. Boyd

Figure 3.10: UVA made 50 cm × 60 cm X-Y readout GEM module structure

The assembly of GEM modules is a delicate and intricate process that must be done with excellent planning, precision, and cleanliness, along with the right tools and materials. Any particulates or humidity within the GEM detectors are extremely problematic. The top and bottom electrodes of a GEM foil are separated by only 50 micrometers. High voltage differences within these regions can give rise to sparks and

discharges which can cause permanent damage to the entire detector, especially the very sensitive GEM foils within. For this reason, all GEM detector assembly work up until the sealing of the chamber from the outside atmosphere is done inside a class-1000 clean room at the University of Virginia.

3.2.1 Support Frame Preparation

All of the support frames shown in Figure 3.10b were manufactured in an industrial factory in Belgium. They are made from a composite material, Permaglass, which is a material made with compressed fiberglass and epoxy. Support frames are first sanded to remove any sharp and protruding pieces. They are then cleaned in an ultrasonic bath filled with de-ionized water. The frames are then allowed to completely dry for a few days inside the clean room. Afterwards, the parts of the frames that come into contact with the electrodes will be varnished (polyurethane, Nuvovern LW + Hardener).

3.2.2 GEM Foil High-Voltage Sector Test

One of the more important tests at the beginning of the GEM module assembly process is the testing of the integrity of the individual high-voltage sectors of GEM foils. This is performed inside a special nitrogen-filled box. The nitrogen is pumped into the box in order to get rid of any humidity and other gases. On a 60 cm $\times$ 50 cm X-Y GEM foil, there are 30 HV sectors on one side of the GEM foil. Each individual sector is supplied with 550V and the current is measured. To confirm that a given HV sector is sufficiently insulated from the other side of the GEM electrode, the charging current should be below 5 nA.

3.2.3 GEM Foil Stretching and Gluing to the Support Frame

GEM foils must be adequately stretched so that they do not sag in the middle of the detector. However, the GEM foils must not be over-stretched either in order to prevent them from being deformed or potentially damaging the GEM hole matrix. To accomplish this, a special mechanical GEM foil stretching assembly is used; it includes plastic clamps along the edges of the GEM foil that apply tension. These clamps are coupled with digital tension sensors. The base of the GEM foil stretcher is an aluminum plate which includes alignment holes to match the holes made on the GEM foils and the support frames. Once the GEM foils are appropriately stretched,

the GEM support frame is then glued using a resin epoxy (Araldite AY103+HD991 Hardener) onto a GEM foil under tension. Figure 3.11 shows a stretched GEM foil with the support frame glued on top of it. The spacer grid of the support frame can be seen in the middle of the frame. The spacer grid helps maintain the distance between the neighboring GEM foils. An additional HV sector test is performed after this step inside the nitrogen box to ensure the integrity of the GEM HV sectors before the final assembly of the GEM module. The drift cathode and the gas entrance window are prepared in a similar manner.

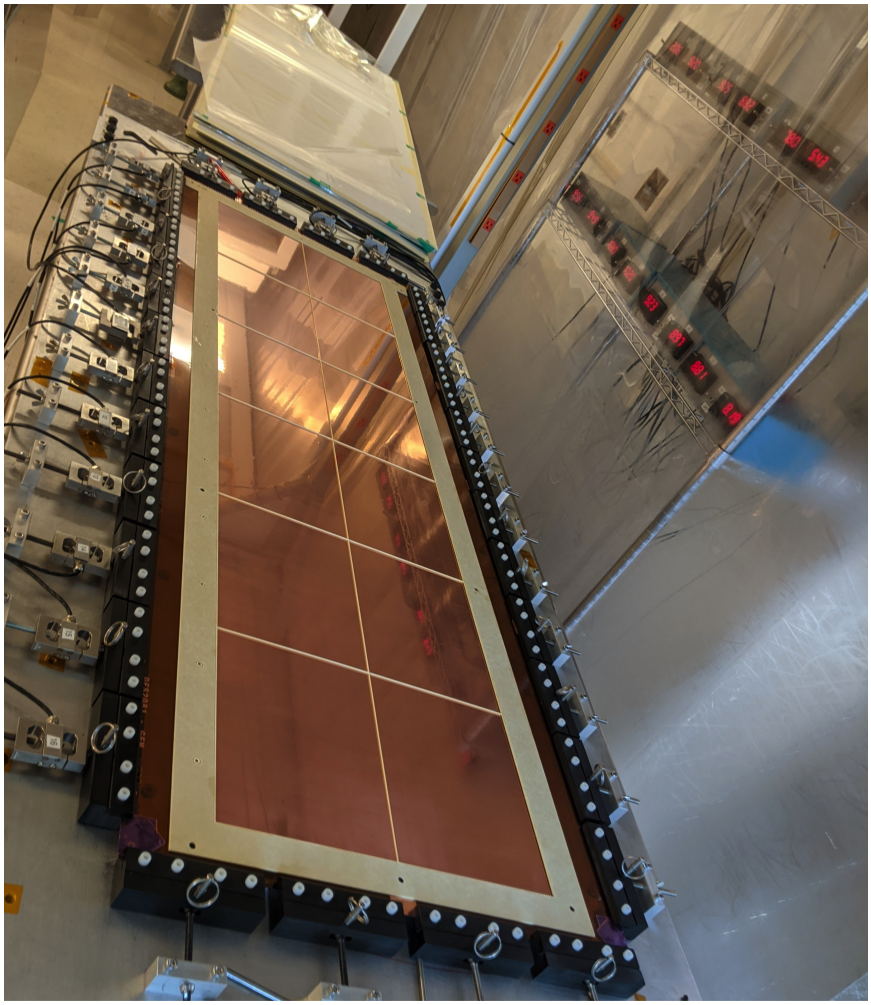

Figure 3.11: A 150 cm × 40 cm GEM foil on the mechanical stretcher with the support frame glued on top; courtesy of J. Boyd

3.2.4 Final Assembly

The final assembly of a GEM module is performed on an aluminum plate with dowel pins placed on the four corners to guide the frames during assembly. The assembly process starts with gluing the readout electrode to the honeycomb support board. Thereafter, the three GEM frames, the drift cathode frame, and the entrance gas window frame are glued one after the other. Figure 3.12 shows an exploded view of all of the components separated by dowel pins, in the order described above. Finally, gas connectors are glued onto the detector and the GEM module is then sealed. The GEM module can now be removed from the clean room and a layer of Dow Corning sealing material is applied along the four edges of the GEM module to prevent any possible gas leakage.

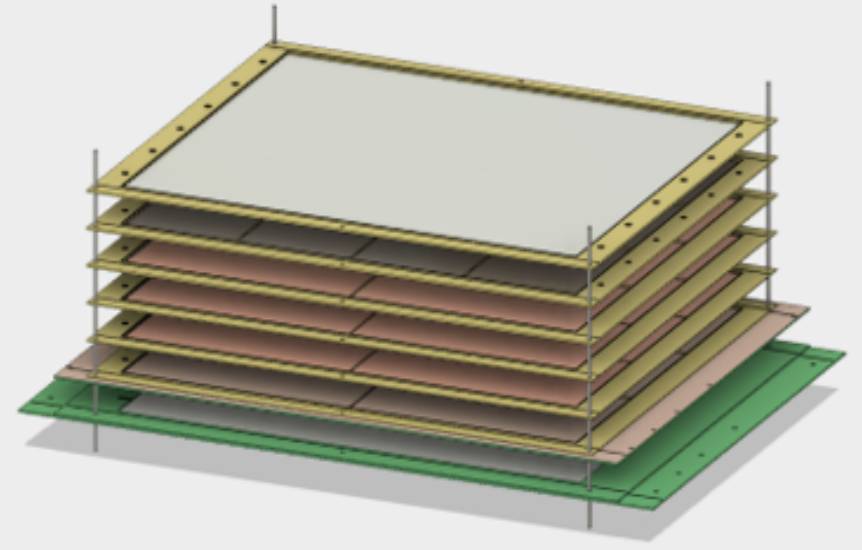

Figure 3.12: GEM module frames to be glued together.

3.2.5 HV Divider Board Installation and Final Testing

While the GEM module is being flushed with nitrogen gas, an additional HV sector test is performed on all of the GEM foils. After that, the HV divider chain along with the protective resistors is then soldered onto the detector. A final high voltage test with 4.2 kV applied across the entire resistive divider chain under nitrogen flowing through the detector is performed, lasting for about 24 hours. This step helps to establish the high voltage integrity of the detector while burning off any dust particulates within the GEM foils. Finally, Ar/CO_2 (75/25) is flushed through the detector and then cosmic characterization tests are performed.

3.3 GEM Tracking Layer Assembly, Testing, and Commissioning at JLab

Once the assembly and preliminary testing was completed at UVA, all of the GEM modules were brought to JLab. At JLab, they were mounted onto different support structures, cabled, tested extensively with cosmic-rays, and commissioned in different spectrometer detector packages. This section will provide a comprehensive description of this workflow from GEM module delivery to JLab through to their first in-beam operation.

A GEM layer consists of either a single GEM module or several of them. The GEM layers in the SBS program are designed in a highly modular manner. Any given GEM layer can be easily disconnected, unscrewed, and removed from one spectrometer, and installed onto another. The three types of GEM modules made for the SBS program (mentioned in Section 3.2) are utilized in a few different ways to make GEM tracking layers. These different configurations can be broadly categorized into two types, by their active area: 200×60 cm^2 and 150×40 cm^2. The larger 200×60 cm^2 GEM layers are made using the 50×60 cm^2 X-Y type readout GEM modules. The smaller 150×40 cm^2 GEM layers are made using the other 2 GEM module types.

3.3.1 Large 200×60 cm^2 GEM Layers

These GEM layers are the largest by active area and required the most demanding assembly. Four 50×60 cm^2, X-Y readout type, UVA-made GEM modules are used to assemble a single large 200×60 cm^2 layer. Figure 3.13 is an image of a 200×60 cm^2 layer, hoisted vertically via a crane. The 4 GEM modules and the 2 cable support trays are attached to a large Aluminum frame. This Aluminum frame can be installed into different spectrometer assemblies as needed. At the end of the cable trays, various components can be plugged into the respective sources/crates. These include HDMI, High-Voltage, Low-Voltage cables, and gas tubes, to name a few. The aluminum frame/structure is designed so that 4 GEM modules' outer support frames overlap in such a way that the GEM active area is effectively continuous throughout the layer. Figure 3.14 depicts this design.

The 200×60 cm^2 GEM layers were initially designed and assembled to be used in the proton polarimeter tracker of the GEp-V experiment. Eventually, they were also used in the GEn-RP experiment's polarimeter setup and as the back-tracker layer for the BigBite spectrometer. Figure 3.15 shows the use of 200×60 cm^2 GEM layers in

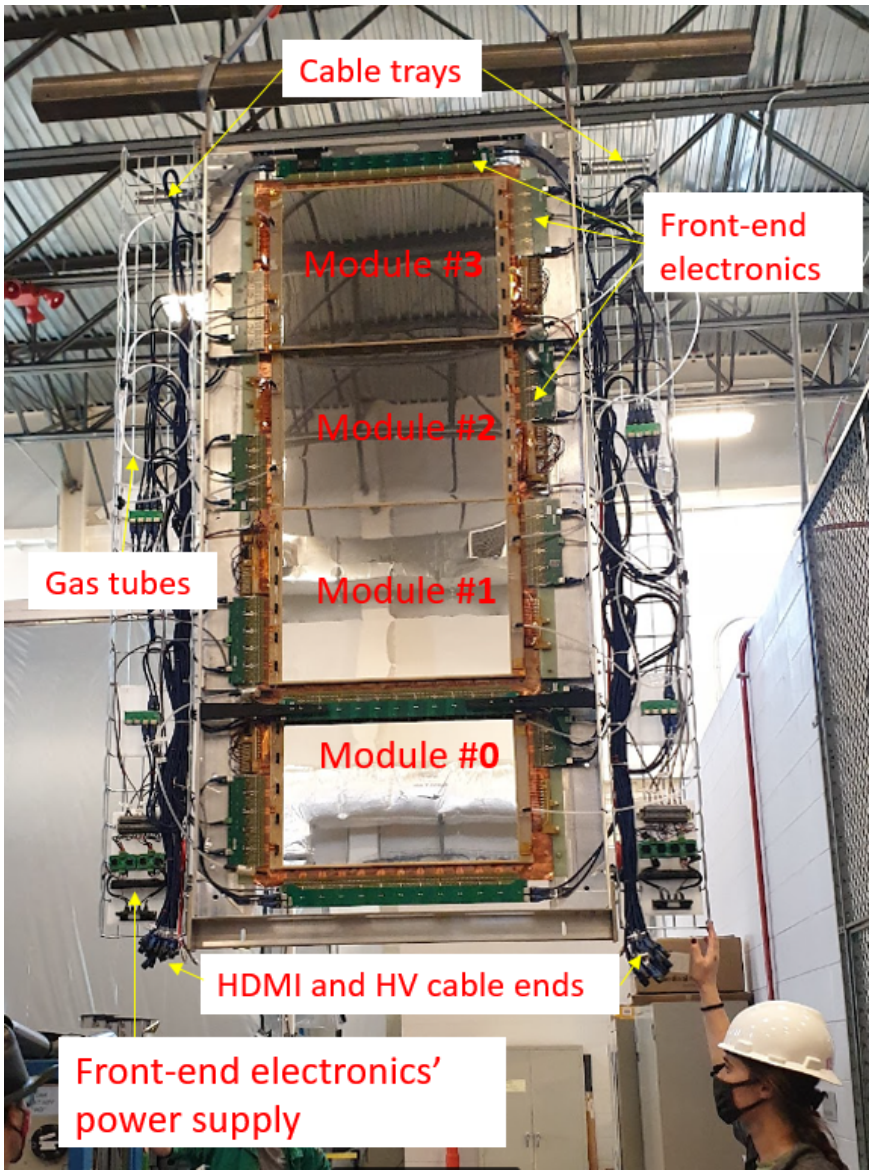

Figure 3.13: A large 200 × 60 cm^2 GEM layer

the GEp-V and GEn-RP experiments.

3.3.2 GEM Characterization Using Cosmic-Rays

Cosmic-ray testing is a reliable, cost-effective, and widely recognized technique to characterize certain properties of GEM detectors. The relative gain, detection efficiency, and position resolution are among a few of the most important properties of a GEM detector that can be studied using a cosmic-ray test. After the GEM layer assembly, extensive cosmic-ray testing was carried out at JLab. In addition to the study of the GEMs, the data from cosmic-ray testing was used to develop and enhance

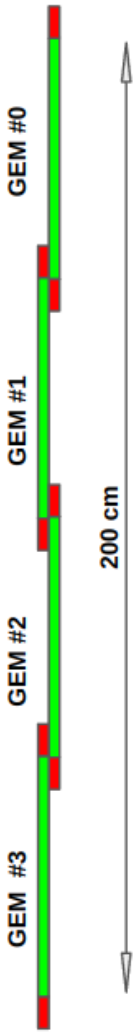

Figure 3.14: GEM module positioning in the 200 × 60 cm^2 layers. Green: GEM active area, Red: GEM support frame

the SBS GEM tracking algorithms.

A "cosmic-test-stand", which can be used to test up to 5 GEM layers at a time, was utilized; see Figure 3.16. The GEM layers were "stacked" horizontally and scintillator paddles were placed at the top and the bottom of the stack to generate *triggers* for the Data Acquisition (DAQ) system, for cosmic events that pass through the stack of GEMs. An average cosmic event rate of about 20 Hz was achieved in this setup. The details about the front-end electronics and the DAQ system used for both cosmic data taking and the experiments are outlined in Section 3.4.

In the analysis phase, the tracking software processes each event, generates straight line tracks that fit to all possible 2D cluster combinatorics over the 5 GEM layers, and

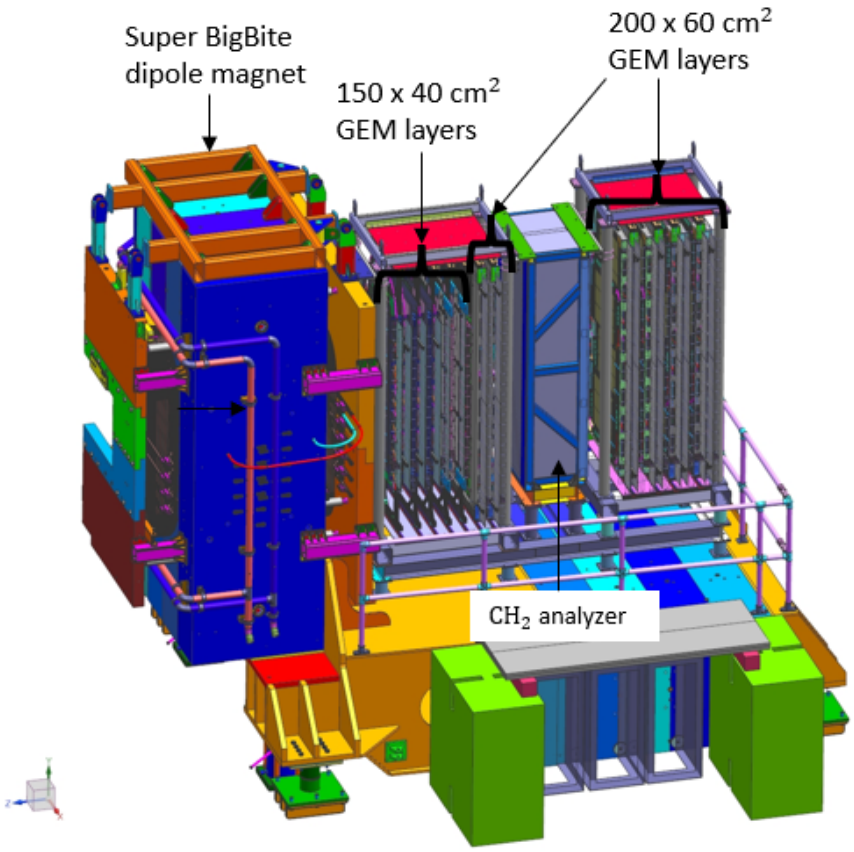

(a) GEM layers in the proton polarimeter of the GEp-V experiment

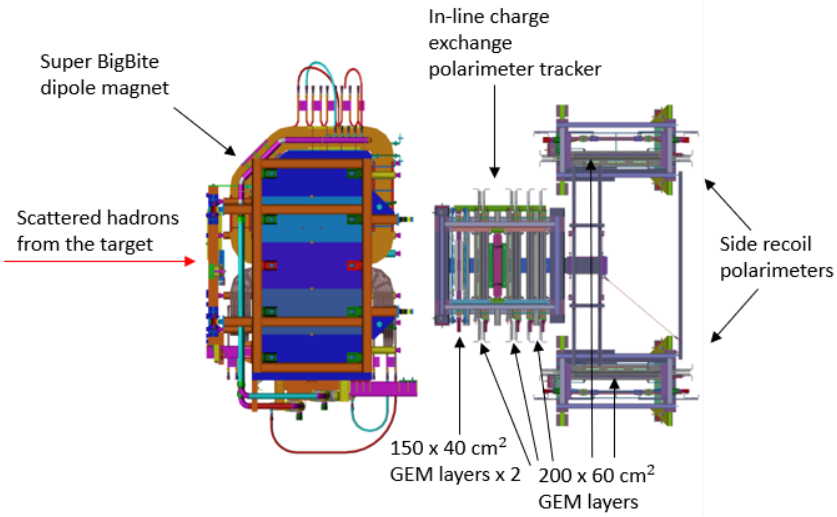

(b) GEM layers in the polarimeter setup of the GEn-RP experiment

Figure 3.15: 200 × 60 cm^2 GEM layers in use at different SBS experiment's spectrometer setups

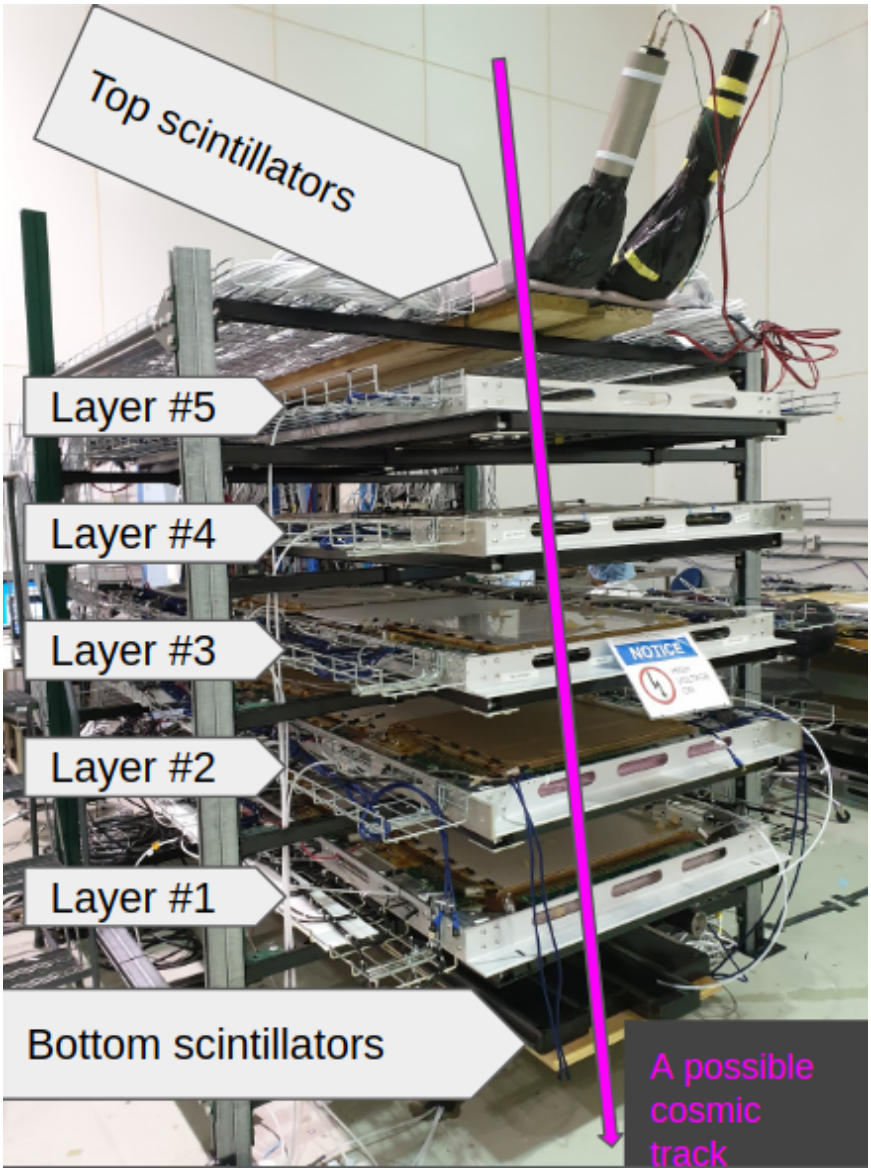

Figure 3.16: Cosmic-test-stand used for the cosmic data taking

identifies the best possible track as the track with the smallest χ^2. The Figure 3.17 shows a 2D histogram of the position of "clusters/hits" that participated in track-reconstruction of a cosmic run with 5 GEM layers with a large amount of statistics (over 1 million). The fine details within the GEM detectors such as spacer grids in the GEM active area and also GEM module boundaries within the GEM layer can be seen. The gaps in event distributions on certain places near the GEM module boundaries within the GEM layers is due to the imperfect overlapping of GEM active areas. In addition, towards the edges of the active areas, the event distributions show less statistics due to the limited trigger acceptance. Once good tracks are generated

from the cosmic data, properties such as tracking-efficiency and position resolution can be studied. The tracking-efficiency is studied by dividing the GEM module active area into small granulated bins, and making two sets of 2D histograms, namely a "did-hit" and a "should-hit" histogram. If a track passed through a given bin for a given event, then the number of entries of that bin in the should-hit histogram is incremented by one. Thereafter, if there is a hit in the corresponding GEM module that participated for the reconstruction of that particular track, the number of entries of the corresponding bin in the did-hit histogram is incremented by one as well. Then the tracking-efficiency for a given $(i,j)^{th}$ bin of GEM module active area is defined as:

$$\eta_{i,j} = \frac{f_{i,j}}{r_{i,j}} \tag{3.3}$$

where, $\eta_{i,j}$ is the efficiency of the $(i,j)^{th}$ bin and $f_{i,j}$ and $r_{i,j}$ are the number of entries of the did-hit and should-hit histograms respectively, for the $(i,j)^{th}$ bin. The figure 3.18 shows the bin tracking-efficiency values for a 5 GEM layer cosmic run. To obtain a *module average* tracking-efficiency, the calculation given in Equation 3.4 is performed using the above same did-hit and should-hit histograms. GEM module efficiencies of around 95% on average were observed in cosmic tests, when modules are operated with a 70/25 Ar/CO2 gas mixture and optimal HV settings.

$$\eta_{module} = \frac{\Sigma_{module} f_{i,j}}{\Sigma_{module} r_{i,j}} \tag{3.4}$$

GEM detector gain and therefore the tracking-efficiency, plateaus with the applied high voltage; see Figure 3.19. It is not beneficial to operate the GEM detectors above the high voltage range where the efficiency plateaus, as that would not make the efficiency increase and it will cause the attractive electrostatic forces between the neighboring GEM foils to go up, thus increasing the risk of GEM foils coming into contact with each other and potentially doing permanent damage to the detector. For the GEM module used for Figure 3.19, the chosen optimal operational High-Voltage point is shown by the red-dotted line.

The position resolution is another important parameter that is of interest to study for GEM detectors, especially as a tracking detector. The so-called "tracking residuals" are used to quantify the position resolution. Tracking residuals are the distances between the fitted track and the cluster positions in both the X and Y strip directions. The standard deviation of the tracking residuals distribution is interpreted as the position resolution of the GEM detectors.

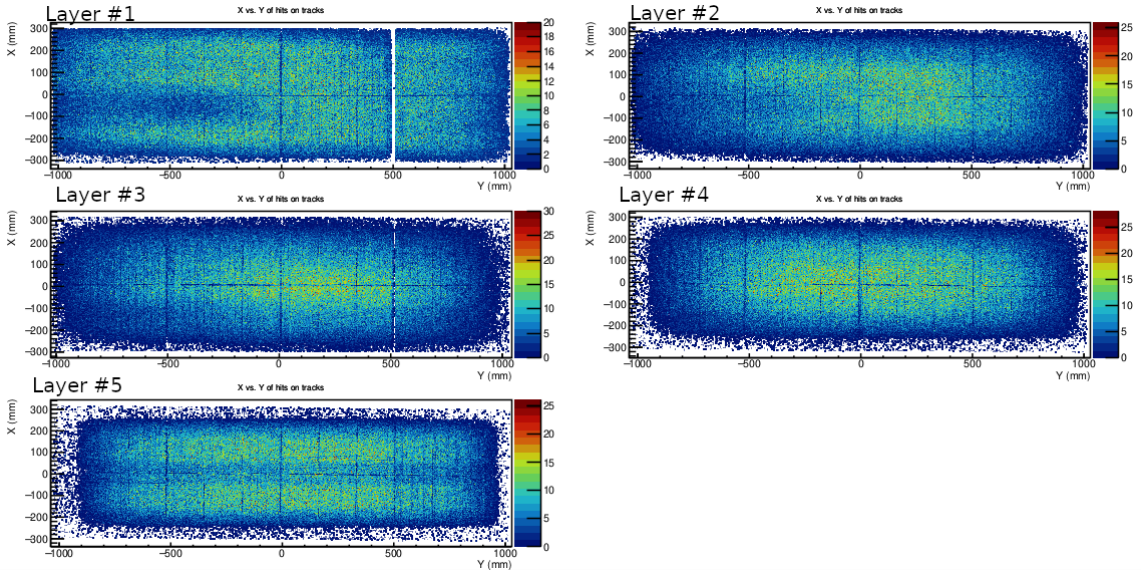

Figure 3.17: 2D histograms of the cosmic hits-on-tracks in the 5 GEM layers

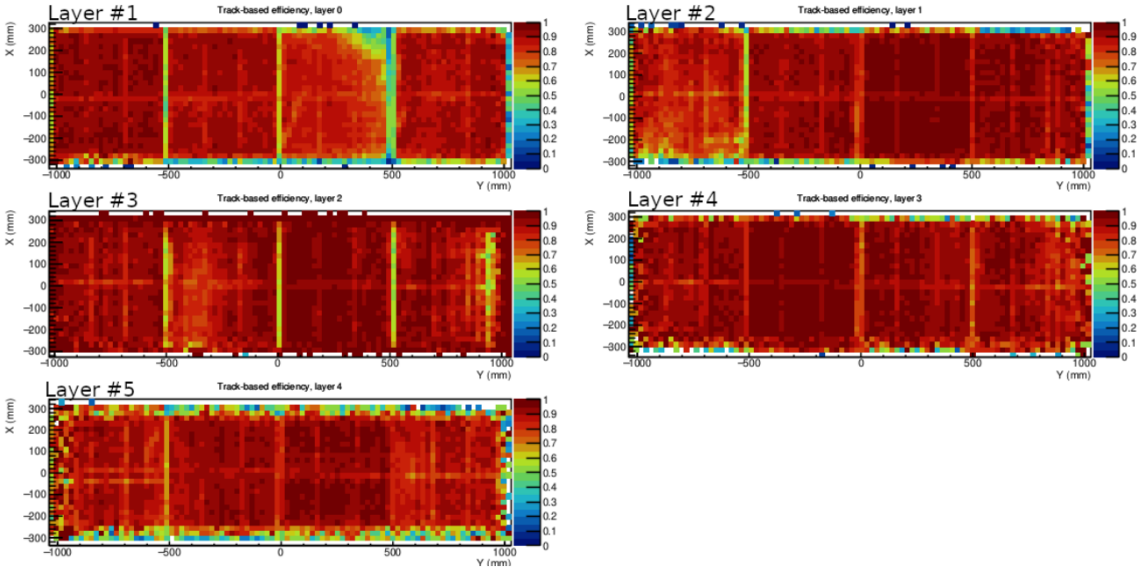

Figure 3.18: 2D histograms of the "track based efficiency" in the 5 GEM layer active areas

Tracks entering perpendicular to the plane of a GEM detector yield best tracking resolutions, while tracks with increasingly non-perpendicular angle cause worsening resolution. Due to the dimensions of the trigger scintillator paddles that were used, more non-perpendicular cosmic ray tracks with respect to the GEM plane were accepted along the long dimension of the GEM layers, making the position reconstruction along that direction to be slightly worse than the shorter dimension. A position resolution of 92 μm was observed along the shorter X dimension and 108 μm was ob-

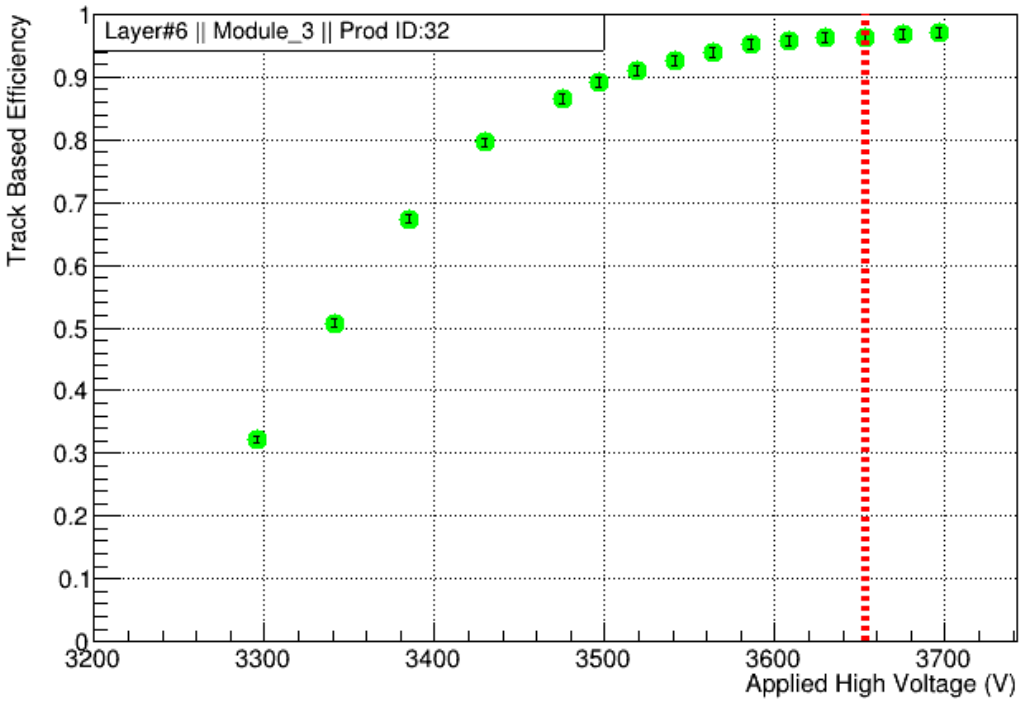

Figure 3.19: Tracking-efficiency Vs Applied High-Voltage for a single GEM module.

served along the longer Y dimension. These numbers are quite reasonable for position resolution determination from cosmic rays; for beam operation conditions where the particles incident on the GEM chambers are in a more or less perpendicular direction to the detector plane, the resolution is expected to be better. Figure 3.20 shows a picture of the cosmic stand indicating the X and Y dimensions and the distribution of the tracking residuals along both directions.

3.3.3 High Voltage Divider Modification to Improve Detector Stability

While during the cosmic data taking with high voltage applied under Ar/CO_2 (75:25) gas mixture, a few of 50 cm $\times$ 60 cm X-Y type GEM modules showed some unstable behavior accompanied by audible noise of fast vibration coming from inside the module. It was apparent that this noise was coming from either GEM foils and/or from the drift cathode foils vibrating, potentially coming into contact with each other. At the same time the noise is audible, the HV divider current draw will exceed the nominal range causing the power supply to trip the particular channel involved. This

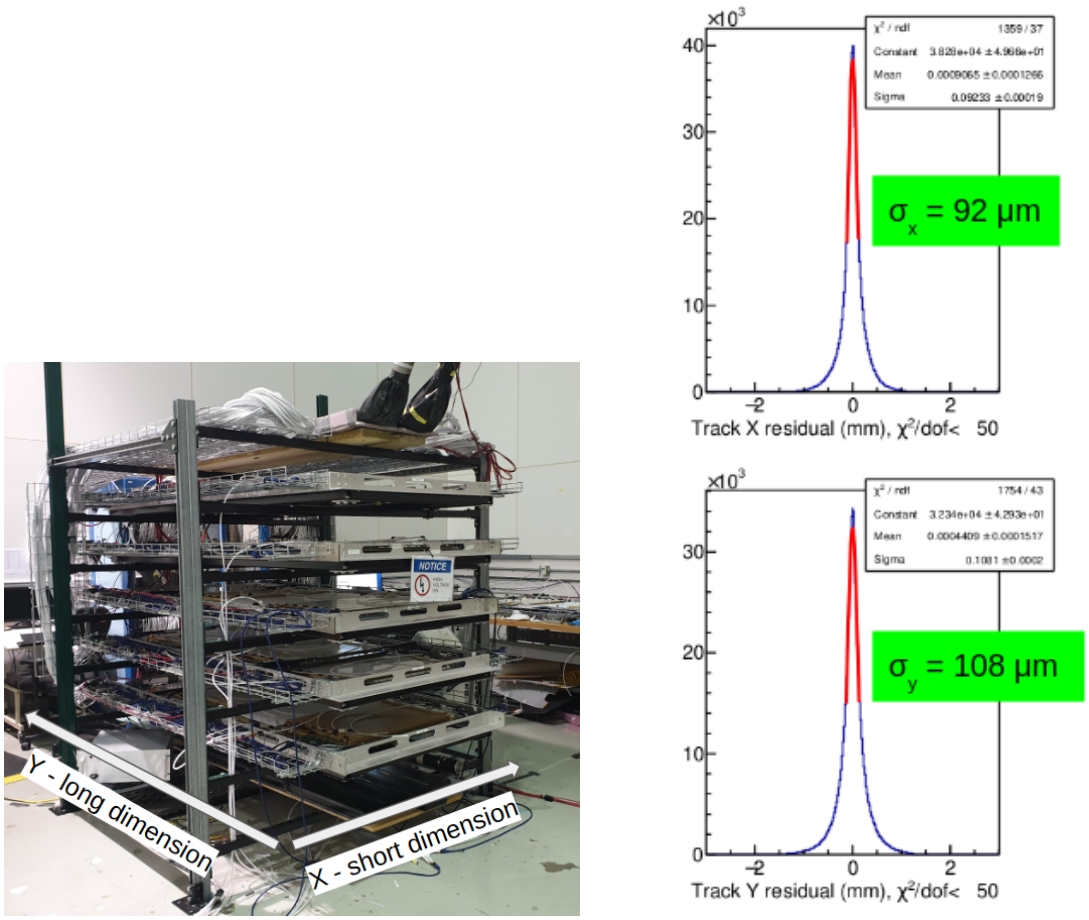

(a) X and Y dimensions of the GEM layers (b) Track residuals along X and Y directions

Figure 3.20: Position resolution from cosmic data

was not often observed right after turning the HV on, but rather a few minutes to a few hours into turning the HV on.

SBS GEM modules are all made by applying permanent glue between all the support frames; this means that it is not possible to disassemble the detector and investigate. It was hypothesized that a reduction in the drift, transfer, and induction region field strengths by a uniform fraction would help to remedy the situation as that would reduce the attractive forces between the neighboring electrode foils, without inducing a significant loss of gain. This could be easily achieved by altering the resistance values which correspond to the relevant regions in the resistive HV divider chain. Figure 3.21a shows a schematic representation of this modification and Figure 3.21b is an image of this modification applied onto the original ceramic HV divider from CERN.

Reducing the original resistance values of 1MΩ in these regions down to 85% of

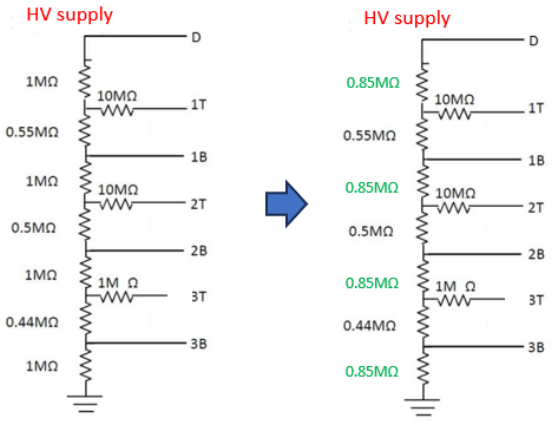

(a) Divider modification schematic

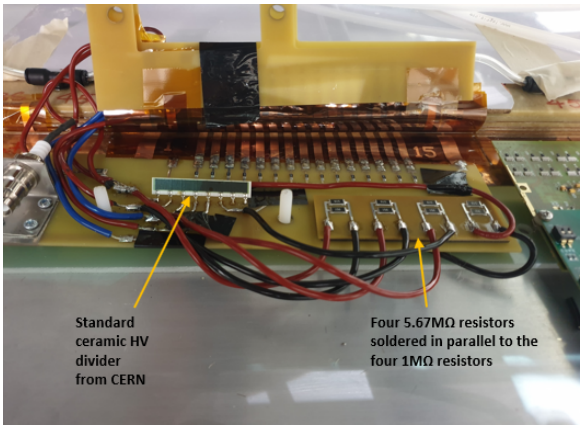

(b) Four 5.67MΩ resistors soldered in parallel to the 1MΩ resistors to bring the total resistance down to 0.85MΩ

Figure 3.21: Resistive HV divider modification

that (0.85MΩ), it was found that the detector instability issue was resolved and gain is comparable at nominal operating voltages. As this modification will reduce the total resistance across the HV divider chain, the HV value that needs to be applied across the divider chain to maintain a given voltage drop across the GEM foils as before will decrease. Figure 3.22 provides a comparison of a single GEM module's efficiency based on tracks, before and after the divider modification. The bottom X-axis corresponds to the red circles which are the original divider (100%), whereas the top X-axis corresponds to the blue circles, the track-based efficiency of the GEM module after the divider modification (85%). The two X-axes are matched in the sense that they represent the same voltage drop across the GEM foils, which should correspond to equivalent intrinsic gain by the GEMs. The nominal operating voltage with an old 100% divider scheme was about 4100 V, and for the 85% divider scheme, this corresponds to an equivalent voltage of about 3650 V. It can be seen that though the 85% divider scheme shows a drop in efficiency at lower voltages, it recovers and matches very well close to the operating point of the detector. Due to the success of this modification, it was applied across all the SBS 50 cm $\times$ 60 cm X-Y type GEM modules and later it was adapted for the U-V and X-W GEM modules as well.

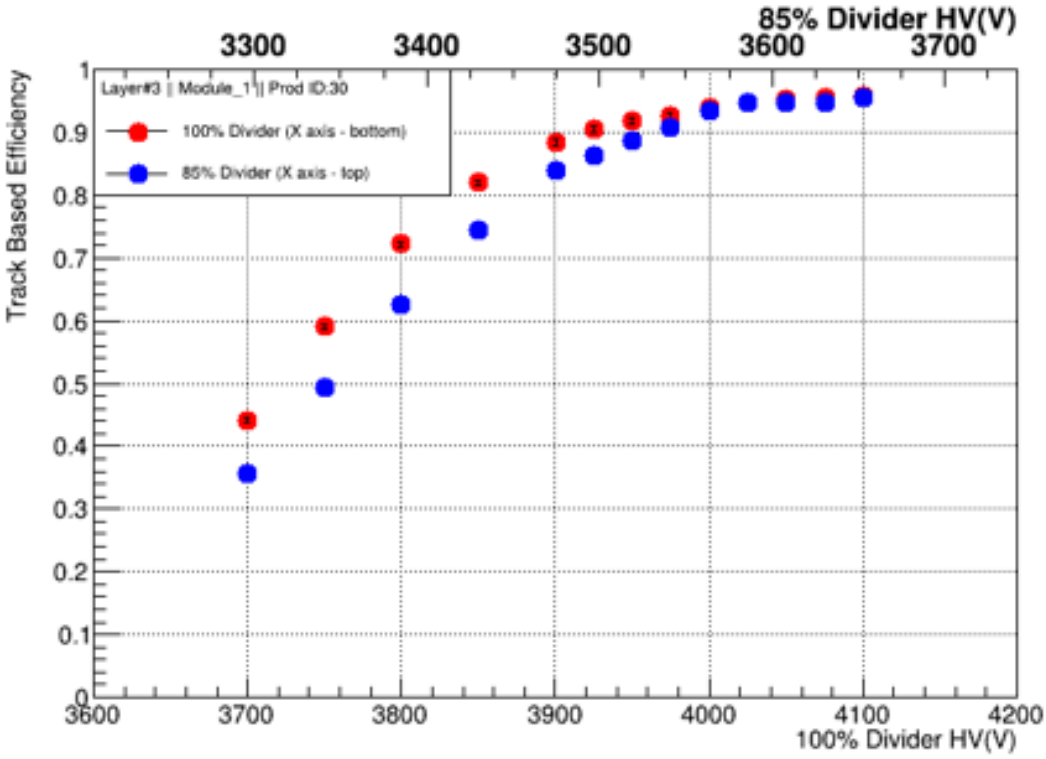

Figure 3.22: Efficiency comparison before and after divider modification

3.3.4 Electromagnetic Shielding to Alleviate Undesirable Common-Mode Fluctuations

During the cosmic-ray commissioning process, significant common-mode (see Section 3.6.1 for description of the common-mode) fluctuations of the raw signals read out by the APV25 cards attached to the GEM chambers were observed, by even over 100 ADC units, between the time samples of a given event and also in between the events as well. The typical pedestal RMS noise levels are around 10 ADC units and a minimum ionizing particle signal would not be larger than a few hundred ADC units. Therefore, this common-mode fluctuation is substantial. This phenomenon was deemed undesirable as it could cause the online common-mode subtraction algorithm to fail (see Section 3.6.2). Therefore, it was necessary to identify the source of this common-mode fluctuation and attempt to alleviate it.

Some of the major suspects were electrical noise introduced by the power supplies connected to the GEM readout electronics, instability in the electronic components due to ground loops, and the interference due to ambient electromagnetic waves. The first two hypotheses were relatively easy to test using oscilloscopes and ohm meters

respectively. No significant noise from the power supplies was observed. Some considerable resistance differences were observed throughout the ground points of the system, such as between the GEM module, power supply, and MPD readout crate grounds, which could cause ground loops. Heavy gauge conductors were used to enhance the conductivity and mitigate any possible ground loops. However, the undesirable common-mode fluctuation in the GEM signals did not improve. Therefore, the third hypothesis, the interference due to electromagnetic waves was investigated. One of the best-known methods to shield an object from electromagnetic waves is to put it inside a "Faraday cage." Even though it is possible to put a GEM module inside a conductive metallic enclosure or a box of some nature for testing purposes, that configuration is not feasible to be used in the experiment setup where many detectors need to be installed into a spectrometer frame within close proximity to each other. Thus, a special design was developed that will more or less fit the GEM module and occupy a minimum amount of additional space. Figure 3.23a shows the first GEM detector shield developed for the testing purposes on a single 50 cm $\times$ 60 cm GEM module. A copper foil has been essentially wrapped around the GEM module with the use of copper tapes.

From the very early tests of implementing the prototype electromagnetic shielding onto the GEM modules, it was clear that the large common-mode fluctuations were diminished greatly. Figure 3.24a illustrates the effect of shielding on a single APV25 card's common-mode fluctuation across the six time samples, for a single event. Figure 3.24b depicts the improvement due to shielding for the same APV25 card, across thousands of events. These plots are made by taking the common-mode difference between the first time sample and the next five time samples. By comparing the standard deviations of these spectra before and after shielding, an improvement by a factor between 3-4 is observed. It was decided that every GEM module should be equipped with electromagnetic shielding before being utilized in an experiment. Figure 3.23b shows a 200 cm $\times$ 60 cm X-Y GEM layer with all four GEM modules equipped with the final stage shielding. The final shielding design consists of aluminum L channels for the support structure around the GEM module with 50 micron aluminum foils replacing the copper foils in the original design. Even though copper has better conductive properties which makes it a better candidate for shielding, the larger radiation length of copper meant that aluminum was a better choice in order to reduce multiple scattering. No significant loss of effectiveness in the reduction of common-mode fluctuations was observed by the use of aluminum. Copper tape was used for attaching aluminum foils to the aluminum frames, and Kapton foils and

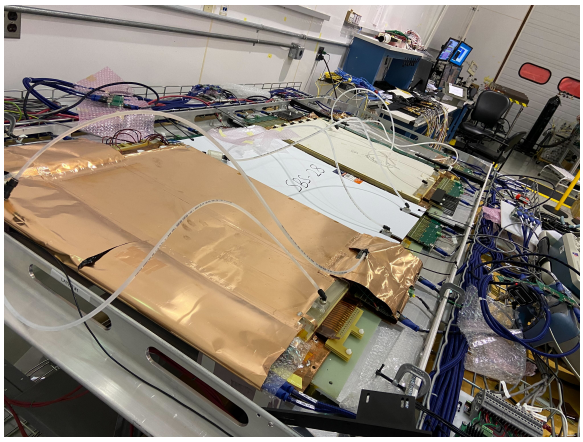

(a) The very first GEM shielding test with copper foils

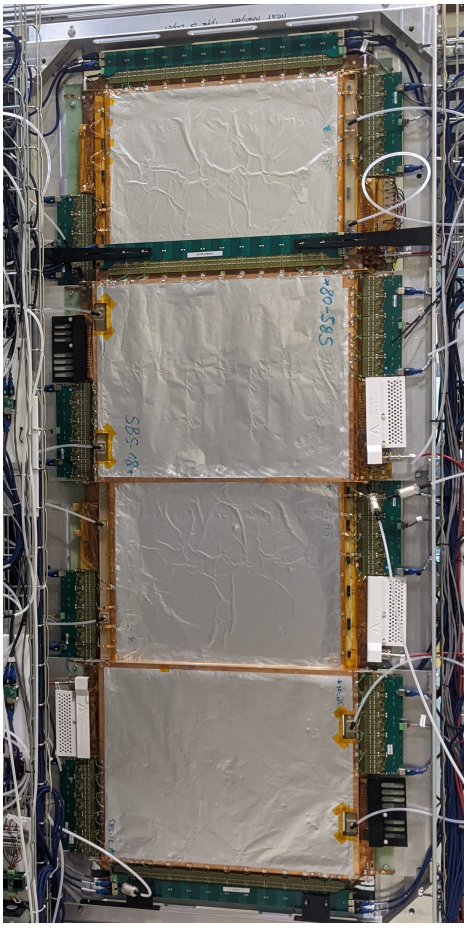

(b) A GEM layer with the final stage aluminum shielding

Figure 3.23: GEM electromagnetic shields

Kapton tape was used for electrical isolation when needed. The entire shield was connected to the ground potential of the system.

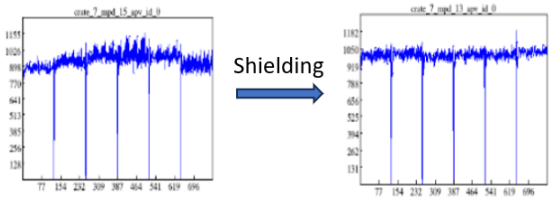

(a) Single event common-mode fluctuation

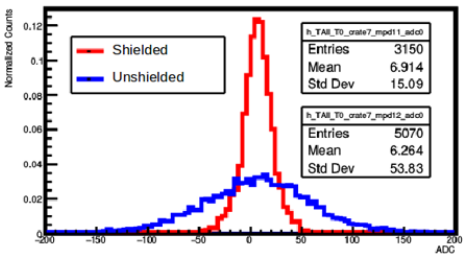

(b) Common-mode fluctuation spectra comparison. Plot Credit: X. Bai.

Figure 3.24: APV25 common-mode fluctuation comparison before and after shielding

3.4 GEM Data Acquisition System

In the GMn experiment, there were 41,984 readout channels from all the GEM detectors. For each trigger event, this many channels will generate a raw data volume of 0.5 MB. With a trigger rate of around 5 kHz, this gives rise to a raw data rate of 2.5 GB/s. These conditions demand a very capable high-speed, high-bandwidth data acquisition system. A brand-new GEM readout scheme was developed for SBS experiments, and it was during the GMn experiment that it was first used under real experimental conditions. Figure 3.25 outlines the scheme used in the GEM DAQ system.

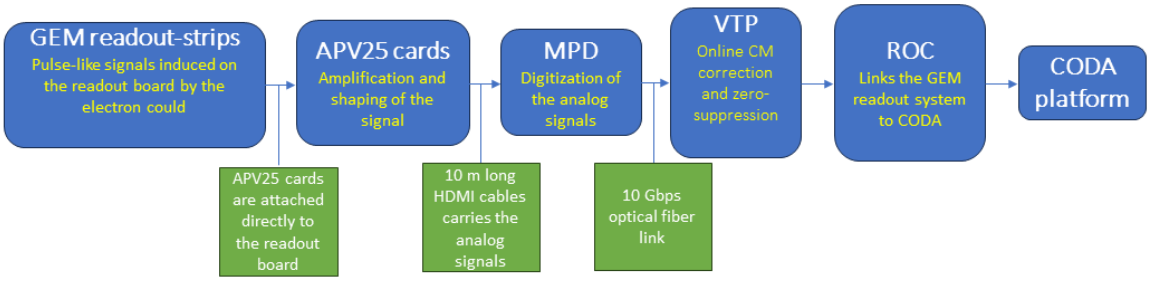

Figure 3.25: GEM DAQ system flow-chart

3.4.1 APV25

The front-end electronics of the SBS GEM readout system utilize APV25 chips [49] [50]. APV25 is a 128-channel analog pipeline chip, originally designed for the readout of silicon micro-strip detectors in the CMS tracker at the LHC. The SBS collaboration adopted this technology for GEM readout due to its radiation hardness and low cost per channel. Before SBS, the COMPASS experiment [41] used APV25 chips for GEM readout.

Signals induced at the GEM detector readout board strips by the charged electron clouds generated by GEM amplification are impulse-like and have only a few nanoseconds width. In the APV25 chip, this current impulse is integrated in a preamplifier and then shaped by a CR-RC circuit into a clean voltage pulse. This voltage pulse is then sampled every 25 nanoseconds and stored in an analog pipeline, which is read out if and when a trigger signal is received by the APV25 chip. Figure 3.26 shows the GEM front-end readout electronics, including the PCB cards with the APV25 chip (commonly referred to as an APV25 card).

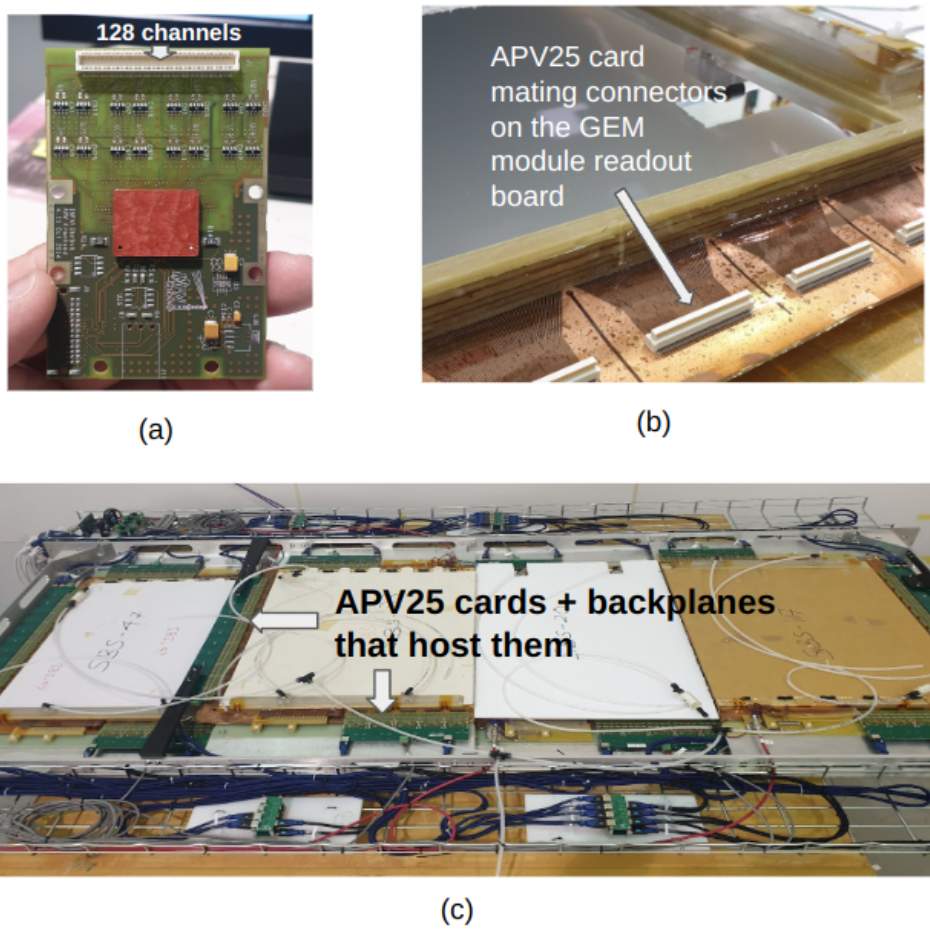

Figure 3.26: GEM front-end readout electronics. (a) APV25 card in close view. The APV25 chip is underneath the red RAD shielding. (b) "Panasonic" type APV mating connector on the GEM readout board. (c) Showcase of how the front-end electronics are connected to the GEMs in a layer and how the HDMI cables are connected to the backplanes.

3.4.2 MPD

MPD stands for Multi-Purpose Digitizer. The main objective of the MPD is to digitize analog signal pulses sent from the APV25 chips and output the digitized signals for further processing. In addition to digitization, MPD is responsible for transmitting control and configuration signals into the APV25 cards via separate digital channels. The MPD board, FPGA-based and designed by INFN for the SBS program, is capable of digitizing and organizing data from up to 16 APV25 front-end cards. However, in practice, a maximum of only 15 APV cards were handled by a single MPD board to accommodate the computational power needed to handle high trigger rates of approximately 2.5 kHz. In addition to digitizing the analog signals,

MPD can be used for further online signal processing such as common-mode correction and zero suppression. However, due to high trigger and occupancy conditions in the SBS experiments, these processes are entirely handled by the VXS Trigger Processor (VTP) unit upstream in the DAQ chain. The digitized signals are carried from optical fibers into the VTP for online data processing.

3.4.3 VTP

It is in the VTP (VXS Trigger Processor) that the online data reduction process is carried out, namely, common-mode subtraction and zero-suppression. The details on the online data reduction algorithms and process are elaborated in Section 3.6.2.

VTP is a powerful single-board "computer" with a much larger FPGA than MPD, memory, and fast Ethernet and optical fiber data transfer capabilities. A single VTP module is capable of processing data from up to 80 MPDs. However, only a maximum of about 40 MPDs were fed into a single VTP module due to other constraints in data transfer.

3.4.4 ROC and CODA Software Platform

ReadOut Controller (ROC) is usually a VME-based single-board computer that configures, controls, and receives data from one or more VTPs. It is through the ROCs of different detector subsystems that each subsystem interfaces with the CODA data acquisition software platform.

CODA, short for CEBAF Online Data Acquisition, is a data acquisition software toolkit developed and managed by Jefferson Lab's Data Acquisition Support group [51]. It is used by all four experimental halls in Jefferson Lab. Figure 3.27 is a high-level illustration of the components of the CODA software platform and how they operate. The final data files generated from CODA are in a special format called EVIO (Event I/O). These files are decoded for further analysis by the custom-made analysis software of Hall-A and the SBS collaboration.

3.5 Auxiliary Systems

3.5.1 Front-End Electronics Power Supply System

A dedicated low-voltage power supply system was designed and used to fulfill the power requirements of the APV25 readout cards and the backplanes that host them.

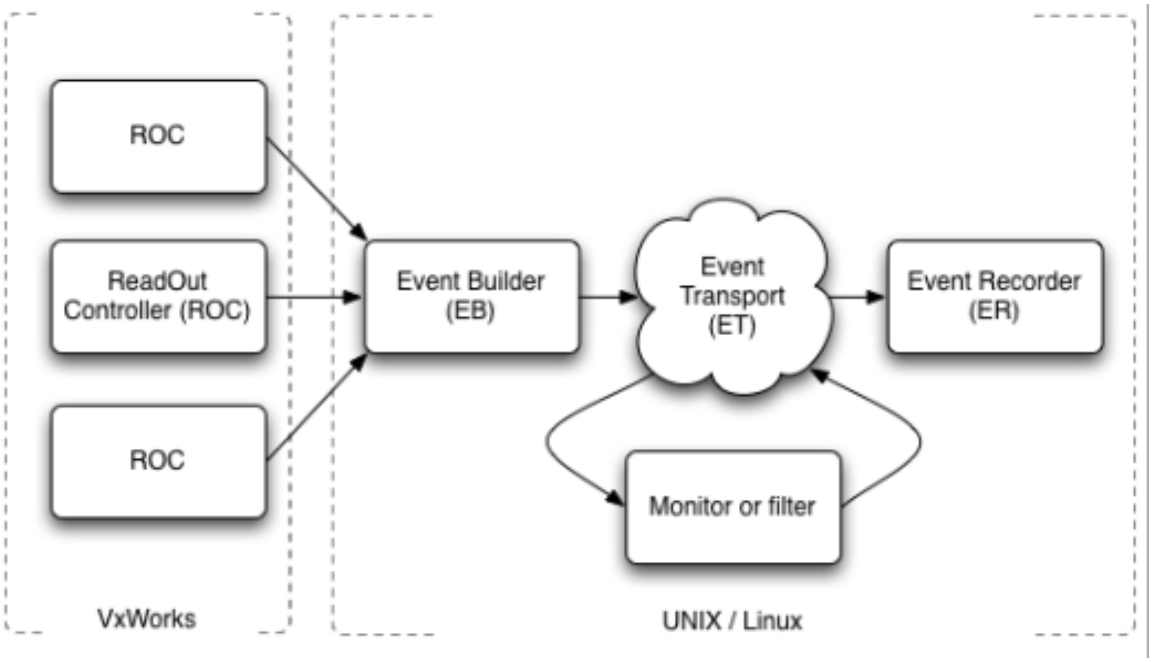

Figure 3.27: A simple CODA implementation - from the CODA website

According to the user manual of the APV25 chip, it uses 2.31 mW of power per readout channel [52]. This amounts to about 296 mW per APV25 chip when all the 128 channels are considered. If a large 200 $\times$ 60 cm^2 GEM layer is considered, as mentioned above in Section 3.3.1, it consists of 88 APV25 cards which means the APV25 chips alone in a 200 $\times$ 60 cm^2 GEM layer should draw of about 26 W of power. However, an estimate based on the maximum current draw by an APV25 card gives a value of about 72 W for a single 200 $\times$ 60 cm^2 GEM layer. A system capable of supplying about 30% more power than the maximum APV25 power consumption was used to power the entire GEM front-end readout system. This power supply unit was built by Jefferson lab electronics group. Also, the APV25 chip requires 3 voltage levels for operation, which are each 1.25 V apart from each other. Thus, 2.5 V, 1.25 V, and GND voltages were supplied from a special voltage regulator chip which was mounted on the GEM layer within close proximity to GEM front-end readout electronics, in order to minimize the resistive voltage drop along the wires. The block diagram in Figure 3.28 gives an overview of the entire power distribution system to the front-end readout electronics of the GEMs.

A radiation-hard special voltage regulator chip, LHC4913 [53], is used for step-down voltage regulation from 5 V DC to 2.5 V and 1.25 V DC voltages. This chip has been designed by CERN in conjunction with an electronics company to sustain rugged conditions in Nuclear and High Energy Physics experiment conditions and

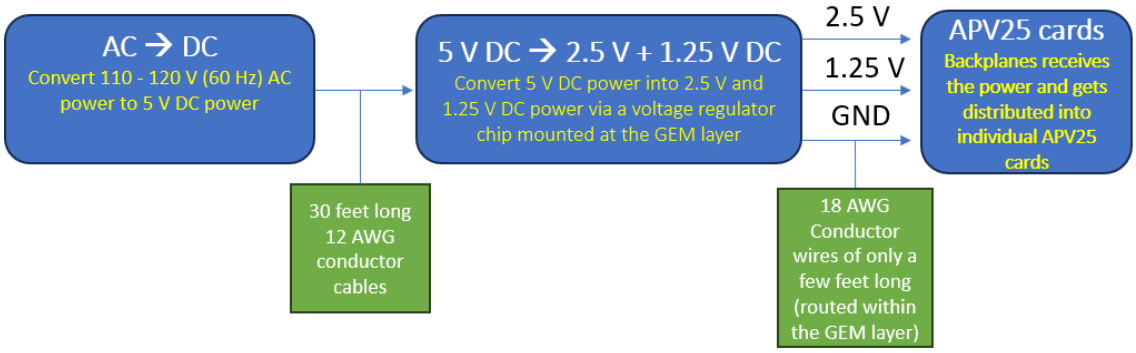

Figure 3.28: GEM front-end readout power supply system

space applications. Figure 3.29a shows a typical GEM layer mounted Low-Voltage power regulation assembly in the SBS experiments. For each GEM layer, 2 such assemblies are used, mounted at two cable trays at either side of a GEM layer. Figure 3.29b depicts how the regulated Low-Voltage power levels are input into the front-end readout electronics, i.e., backplanes and APV25 cards.

3.5.2 High-Voltage Power Supply System

In the first run-group of SBS experiments, HV for each GEM module was supplied by a single HV channel; a resistive divider chain installed on the GEM module was used to distribute different potential levels across the detector, as required. This method is very cost-effective and radiation tolerant. A WIENER MPOD computer controllable crate equipped with EHS 8060n HV modules was used. Each HV channel of the EHS 8060n module is capable of providing a negative voltage of up to 6 KV and supports a current draw of up to 1 mA. All of the UVA-made GEM modules' resistive divider chains needed to be provided an HV of approximately 3.65 KV to reach the optimal electric field strengths across the detector, and it would draw a current of about 745 μA at that voltage under negligible background rate conditions. A maximum current draw of 836 μA was recorded in one of the GEM modules at the highest background conditions during the GMn experiment, staying well below the 1 mA limit of the EHS 8060n HV modules.

However, under high background rate conditions of the GMn experiment, it was observed that this HV scheme compromises the GEM detector gain, leading to a lower detection efficiency. More details on this topic are provided in Section 3.7.3. The use of an individual floating channel HV power supply consisting of seven channels, which are capable of actively maintaining a pre-programmed potential difference across the

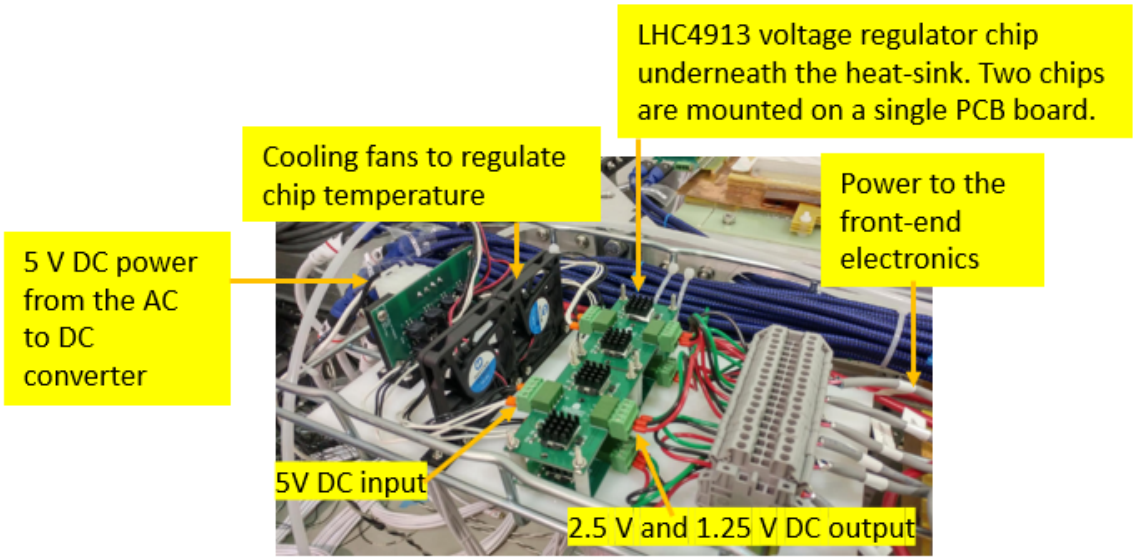

(a) Low-Voltage DC power regulation assembly mounted on a GEM layer

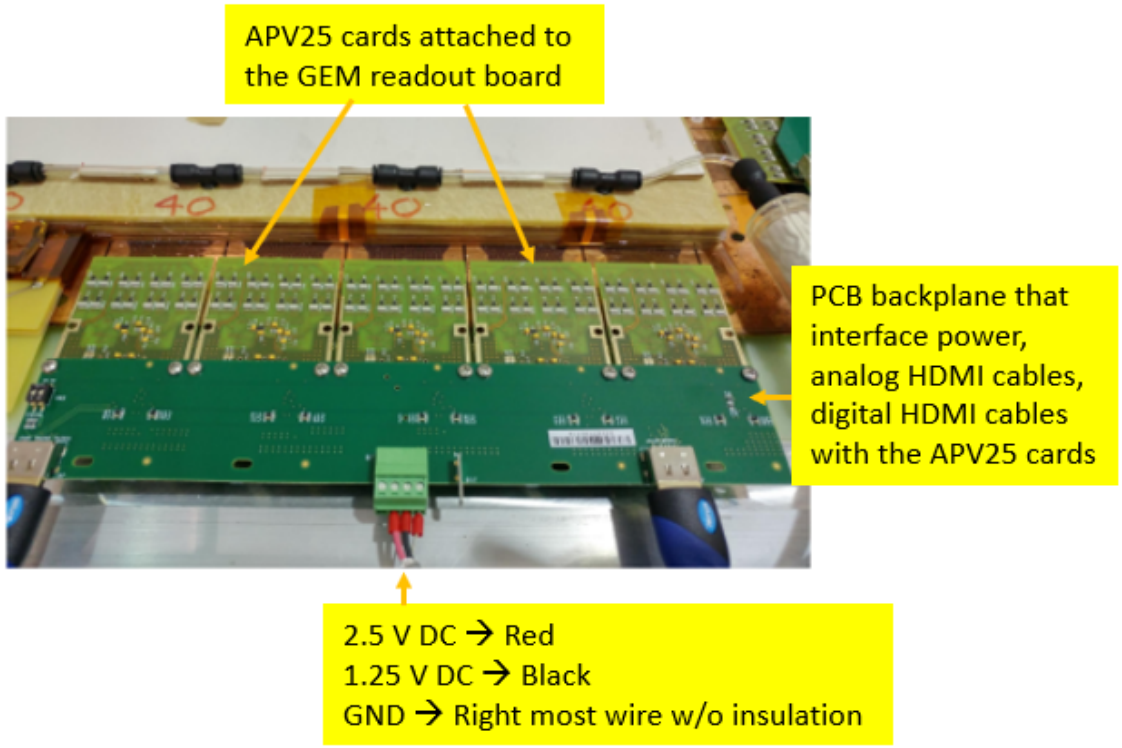

(b) PCB backplane that hosts 5 APV25 cards

Figure 3.29: Low-Voltage power setup on the GEM layer

neighboring channels, was found to be the best solution to mitigate this issue. This HV power supply scheme is implemented by removing the resistive HV divider and connecting the HV channels to the respective junction points. The CAEN A1515B

HV power supply modules[1] - specifically designed for GEM detectors, are currently being used to supply HV to all the GEM modules in the experimental Hall-A.

3.5.3 Gas Distribution System

For GEM detectors in the SBS program, a gas mixture of Ar/CO_2 with the volume ratio 75/25 is used in beam operation and cosmic data taking. A dedicated gas mixing and distribution system was designed and built to provide an accurate gas mixture for a large number of GEM detectors at a given time. The key components of the gas distribution system include the gas bottles, gas mixing system, gas flow-meter panel, and the online monitoring system. The block diagram in Figure 3.30 illustrates how these components work together to supply the Ar/CO_2 gas mixture into the individual GEM detectors.

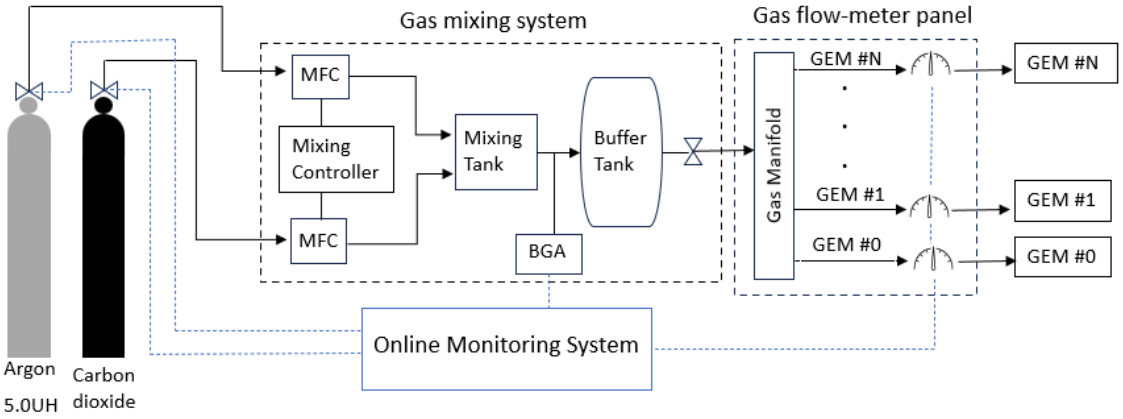

Figure 3.30: Gas distribution system

Gas lines from the Ar and CO_2 bottles enter into separate Mass Flow Controllers (MFC), which are controlled by a Mixing Controller unit. MFC controls the relative flow of Ar and CO_2 that enters into a Mixing Tank, where the gas mixture with the desired 75/25 volume ratio is produced. A Binary Gas Analyzer (BGA) is connected to measure the Ar/CO_2 gas mixture ratio, which is used to ensure the proper functioning of the mixing system and its calibration. Downstream of the Mixing Tank is the Buffer Tank, where a much larger gas volume is stored. The buffer tank supplies the Ar/CO_2 gas mixture into the gas flow meter panel inside Hall-A. This panel consists of individual flow-meters supplying gas to the GEM modules. Prior to the gas lines being connected to the GEM modules, 10-micron gas filters are used to filter

[1]Manufacturer web page: https://www.caen.it/products/a1515b/

out particles in the gas flow. As indicated by the diagram in Figure 3.30, an online monitoring system is used to monitor the gas bottle pressure, the ratio of the Ar/CO_2 mixture, and the flow rates to the individual GEM modules. One notable feature in the online monitoring system is that it is programmed to turn off the HV to the GEM modules if the gas mixture ratio is not within the desired range.

3.6 GEM Data Analysis

The GEM data processing is the most computationally intensive and time-consuming part of the entire data analysis process. There are several reasons for this:

- Large number of readout channels involved: 41984 in the GMn experiment
- High occupancy due to the number of background hits per event
- Ambiguity and complexity in cluster and track finding

As mentioned in Section 3.4, GEM data was already analyzed and processed up to a certain extent online while collecting data during the experiment. In this section, the details on both the online and offline GEM data analysis, up to track reconstruction, will be discussed.

3.6.1 Raw APV25 GEM Data Profile and Their Characteristics

In Figure 3.31, two examples of digitized data from an APV25 card are shown. These data frames are referred to as "raw-data-frames" as they represent the data coming out of MPDs, after the digitization of analog signals from the APV25 cards, prior to any online processing applied on them. As described in Section 3.4.1, once a trigger signal is received, the APV25 card outputs *snapshots* of all its 128 channels at intervals of 25 nanoseconds. In the SBS experiments, all the electronics' firmware is programmed to acquire 6 snapshots for each APV25 card, per trigger event. One such snapshot is referred to as a Time Sample (TS).

Figure 3.31a shows an APV25 raw-data-frame when there are no ionization signals present (e.g., GEM HV OFF). The vertical axis shows the signal strength in ADC units and the 5 long vertical lines spanning across the plot act as separators of six time-samples. When no GEM ionization amplification signals are present, such data is referred to as "noise signals" or more frequently as "pedestal data" in common

terminology. This data is important to characterize each and every channel of all APV25 cards, before real GEM signals can be extracted. Figure 3.31b represents a case where there are several good ionization signals in multiple channels of the APV25 card. The signal height variation across the six time-samples can be clearly seen which depicts the effect of the RC-CR shaper circuit in the APV25 chip.

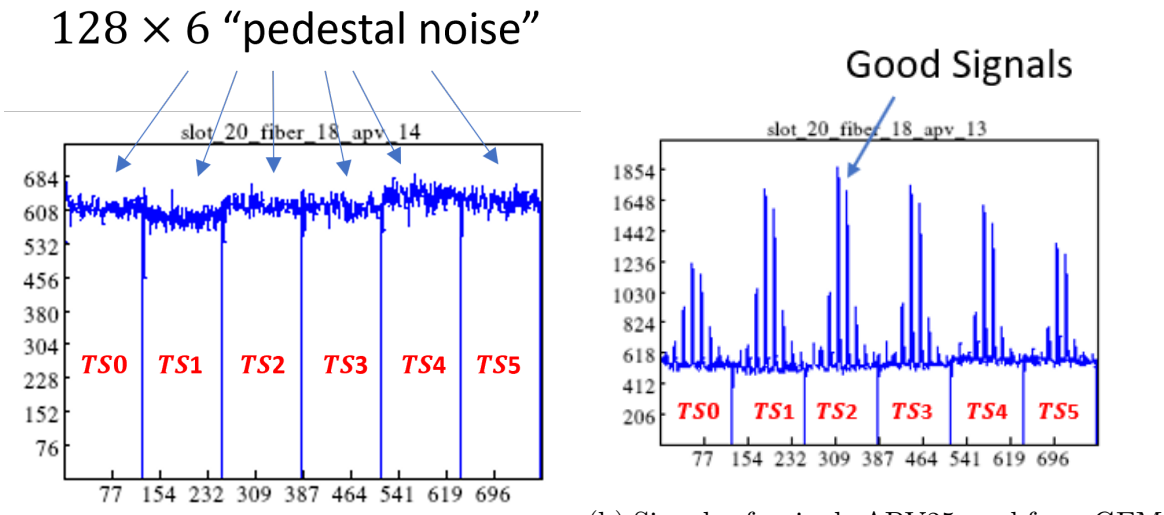

(a) Noise signals of a single APV25 card

(b) Signals of a single APV25 card from GEM ionization amplification

Figure 3.31: Digitized signals from an APV25 card across 6 time samples 25 nanoseconds apart

Common-Mode (CM)

All 128 channels within a given single APV25 card/chip fluctuates by a constant offset, time-sample by time-sample and event by event. This offset or the common group-shift is referred to as the common-mode (CM). This behavior is graphically represented in Figure 3.32; the common mode fluctuation is especially pronounced in this selected example. This common-mode shift is quite substantial, which is usually larger than the typical electronic noise of a channel, and therefore should be calculated and corrected event by event and time sample by time sample for each APV25 card, for an accurate extraction of the amplitude of GEM signals. This correction is referred to as the "common-mode subtraction." Figure 3.33 showcases an APV25 event with common-mode subtraction applied.

For the case where there are no fired channels due to no GEM amplification being present (e.g., Figure 3.32), the common-mode calculation is trivial and would be the arithmetic average of all 128 channels for a given time-sample. However, this becomes

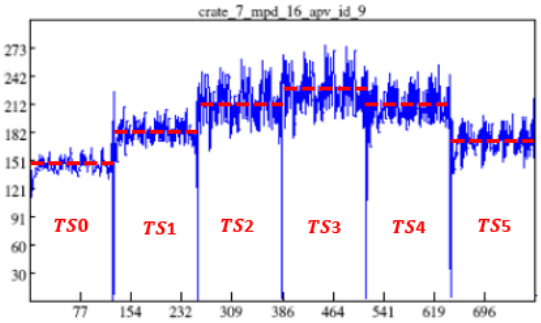

Figure 3.32: Common-mode variation across the 6 time-samples within a single APV25 card, for a single event. The red dashed lines show where the common-mode levels could be for each time-sample

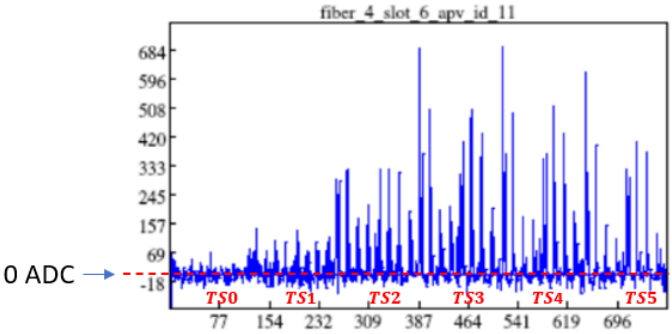

Figure 3.33: An APV25 data frame with common-mode subtraction applied. Note that the majority of non-fired channels have values fluctuating about 0 ADC units

more complicated when there are fired channels, as taking a simple average would bias the common-mode value.

The most traditional technique for common-mode calculation of digitized APV25 data is the so-called "sorting method." In this method, first, all the 128 channels are *sorted* according to the ascending order of ADC values. After that, a certain percentage of channels with the largest and smallest ADC values are taken out. This step aims to remove any bias that could be introduced by any channels that fired and any channels that have substantially lower than baseline level signals. The average taken after the above last step will be taken as the common-mode. However, this algorithm is expensive both in memory and computational time, which makes it unfeasible to be applied as an online common-mode calculation method (in the VTP), but it is widely used in offline analysis, especially in the analysis of pedestal data, due to its superior accuracy. The method used for online common-mode calculation will be discussed in Section 3.6.2.

Pedestal Offset and Pedestal Standard Deviation

Pedestal offset, μ_{ped}, and pedestal standard deviation, σ_{ped}, characterize the *electronic noise* level of each channel, which is unique to a given channel out of the 128 channels in the APV25 chip. In order to calculate these parameters, dedicated "pedestal runs" should be taken where there should not be any signals from GEM amplification/ionization. This can be achieved by turning the GEM HV off, or by using a random pulse trigger with the beam turned off, so that the cosmic signal rate inside the GEM chamber is negligible compared to the random pulse trigger window. Environmental factors, radiation damage, and aging could change the characteristics of pedestal noise. Thus, regular monitoring of the pedestal data is required, and new pedestal data should be acquired when the characteristics change.

For a given channel (1/128) of an APV25 card, it can be observed, on average, that the signals stay at a constant *offset* from the common-mode level, with some distribution around that offset value. Pedestal data distributions for all the channels are made by calculating the average of common-mode subtracted signals across all six time samples for each channel, for at least several thousand events (typically 5000). The average of this distribution is interpreted as the pedestal offset (μ_{ped}), and the distribution around this offset value is quantified by taking the standard deviation (σ_{ped}). Figure 3.34a and Figure 3.34b show the pedestal offset and pedestal standard deviation distributions respectively, for all the 128 channels of an APV25 card.

Once the raw signals from an APV25 card are corrected for pedestal offset and common-mode by subtracting those out, the remaining signal strength is compared with the pedestal standard deviation to distinguish whether the channel is "idle" or "fired." If the channel is determined to have fired from this comparison, this signal strength will be moved forward into the analysis as the "true" signal strength as opposed to the "reported" signal strength prior to common-mode and pedestal offset subtraction.

3.6.2 Online GEM Data Processing and Reduction

If all 41984 channels of GEMs were to be read out in full for every trigger event, regardless of whether a given channel has a true hit, the raw data rate would be 2.5 GB/s as mentioned in Section 3.4. It is neither feasible to be written to the disk at that rate, nor is useful, since the majority of the channels do not contain actual hits. In the GMn experiment, the GEM occupancy was calculated to be around 20% to 30% from simulation. Ideally, only these channels with true hits need to be retained

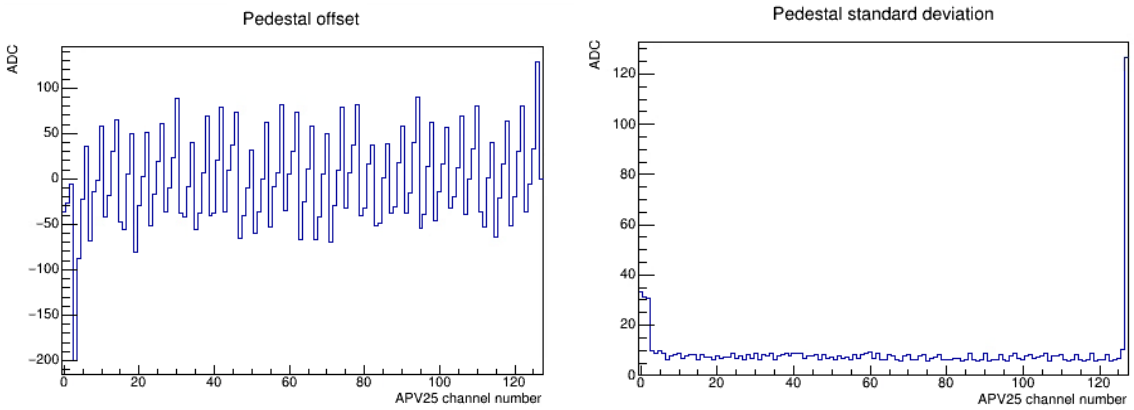

(a) Pedestal offset (b) Pedestal standard deviation

Figure 3.34: Pedestal characteristics for a single APV25 card

and the rest of the channels could be eliminated. It has been calculated that a factor of 10 to 15 data reduction can be achieved by this from simulation studies [54].

The high-level workflow in the online GEM data analysis is the following. First, the pedestal offset (μ_{ped}) of each channel is subtracted out. Next, the baseline fluctuations, the common-mode, of APV25 signals is calculated and subtracted from each channel, event by event and time-sample by time-sample. Then, the pedestal noise distribution around this baseline level (σ_{ped}), which is unique to each channel is used to determine whether a given channel has a "true hit." The signal values (ADC value) of the channels that pass this online analysis will be forwarded and written to the data files whereas the channels that did not pass will automatically be interpreted as having no signal, or zero, in the offline analysis. The finer details of this online analysis will be presented next.

Online Common-Mode Subtraction

As described in Section 3.6.1, the traditional "sorting method" cannot be used for online common-mode calculations, due to the hardware limitations in the VTP. As a solution, a much more lightweight yet effective algorithm was devised, referred to as the "Danning method" [54].

The Danning method takes advantage of a set of parameters calculated from a dedicated *pedestal run*, taken before the physics data acquisition and uploaded into the VTP. For each APV25 card, a common-mode mean, μ_{CM}, and a common-mode standard deviation, σ_{CM}, are also calculated by analyzing the pedestal data. For each APV25 card, the distribution of the averaged common-mode across the 6 time samples

can be obtained by analyzing a few thousand pedestal data events. From these distributions, the common-mode mean and common-mode standard deviation for each APV25 card can be calculated. In addition, for every channel of each APV25 card, the pedestal standard deviation (σ_{ped}), explained in Section 3.6.1, is also uploaded into the VTP. The first step in the Danning common-mode calculation method is to calculate an average, μ_{temp}, from channels with signals in the range between $\mu_{CM} \pm 5\sigma_{CM}$. Figure 3.35 illustrates this principle of using a common-mode *range*. To a certain extent, this ensures that channels without fired signals are used. Then, a second average, $\mu_{Danning}$, is calculated from channels with signals in the range $\mu_{temp} \pm n\sigma_{ped}$, where n is a multiplicative factor chosen empirically. This step further ensures that a large majority of fired channels are excluded. This second average, $\mu_{Danning}$, is used as the common-mode value. The second step could be performed multiple times to obtain a more accurate or true result for the common-mode. Three iterations were used in the GMn experiment. This algorithm was tested to be about a factor of 4 faster than the sorting algorithm [54] and uses only a smaller constant amount of memory.

For each APV25 card, and for each of the 6 time samples, a $\mu_{Danning}$ value is calculated, event-by-event, and is subtracted out from the respective signals of all the channels. This step is known as the common-mode subtraction.

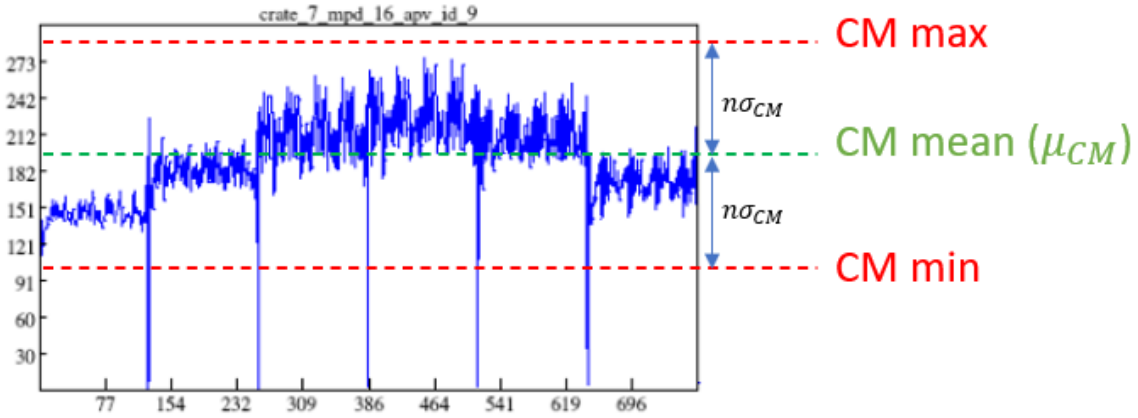

Figure 3.35: Common-mode range for a given APV25 card

Danning online CM subtraction was used both for the GMn experiment and later for the GEn-II experiment of the SBS program. However, a few shortcomings of the Danning method were identified during the running of these experiments. For example, the APV CM could shift with time during their operation and making the CM range go out of the initial $\mu_{CM} \pm 5\sigma_{CM}$ range, causing the online CM calculation

to fail. A new method, referred to as the Histogramming Method has been proposed and developed to address the shortcomings of the Danning method. See reference [55] for more details about the Histogramming Method.

Online Zero-Suppression

After the common-mode subtraction, the online zero-suppression is the next step in the online data processing. As the first step, the average ADC value of the six time samples, from the common-mode subtracted signals for all the channels, will be calculated. If the resulting value is larger than the empirical factor of 3, times the pedestal standard deviation (σ_{ped}), those channels will be considered as fired channels and the VTP will forward them into the data stream, while the rest of the channels will be ignored or zero-suppressed. Figure 3.36 shows a data frame of an APV25 card, for a single event, after common-mode subtraction and zero-suppression is applied. The considerable amount of data reduction is apparent from this graphical representation.

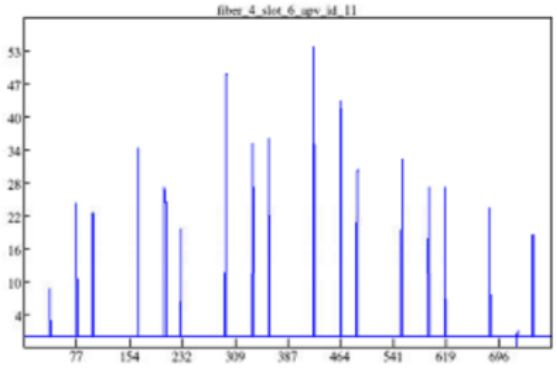

Figure 3.36: An APV25 data frame after common-mode subtraction and zero-suppression applied

3.6.3 Offline GEM Data analysis

The entire offline GEM data analysis, along with the analysis of other detector subsystems is performed using the SBS-offline software package[2]. SBS-offline software package inherits several core libraries from the Hall-A's standard analysis software package, Hall-A analyzer, which is also referred to as "Podd"[3]. A brief overview of

[2]https://github.com/JeffersonLab/SBS-offline
[3]https://github.com/JeffersonLab/analyzer

GEM data analysis starting after the GEM data decoding, up to the track reconstruction process is given below.

Defining a Calorimeter Search Region

Given the large number of channels and high occupancy environment in the SBS experiments, considering the whole active areas across all the GEM tracking planes is computationally unattainable. Figure 3.37 is a snapshot of a GEM event-display for a single event in the BigBite spectrometer. All the fired strips are shown color-coded according to their respective ADC values. It is obvious how many U and V combinations would be needed to be considered if all the active areas across all 5 GEM tracking planes were to be considered.

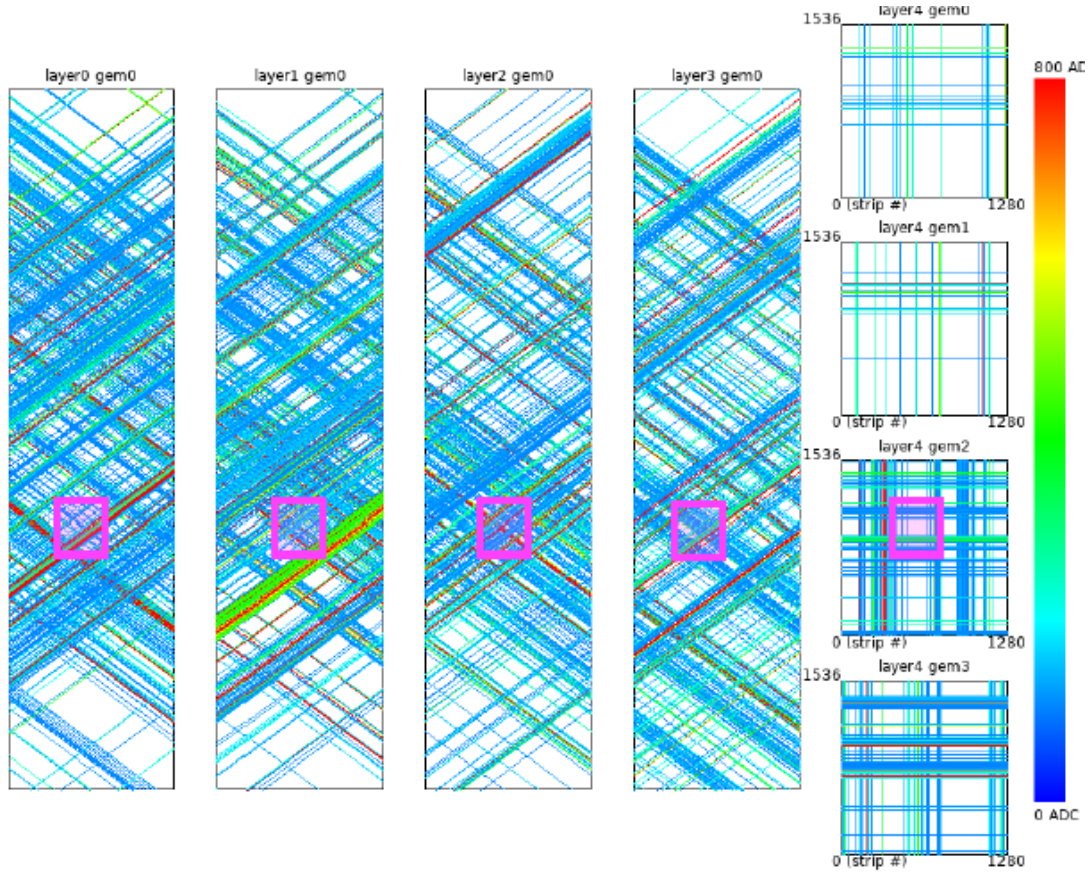

Figure 3.37: BigBite GEM event display with all fired strips color-coded by ADC values. The magenta square represents the calorimeter search region defined by the highest energy cluster in the BigBite calorimeter. Plot credit: X. Bai.

In order to overcome this obstacle, a "search-region" defined by the highest energy calorimeter cluster and the target is defined. This search-region essentially outlines a

very conservative area for each tracking plane through which the scattered electron from the target must have traveled. The magenta squares in Figure 3.37 represent this search region for the particular event. Computationally expensive processes of 2D hit association and track reconstruction are only considered within this region.

1D Cluster Formation and 2D Hit Association

The 1D cluster formation along the two separate sets of strips will be the first step after GEM data decoding in the GEM data analysis. A typical minimum ionizing particle will create clusters with the number of strips fired along a particular strip direction in the range from two (minimum enforced) to even up to five or slightly above. First, the strips with local maxima of ADC values are found along the given strip direction. Then the contiguous fired strips that agree with some timing criteria (to ensure they correlate to the same event) are added to the respective local maxima to form 1D clusters. The hit location along the considered 1D direction is calculated using an ADC weighted center of gravity algorithm which uses the ADC values of the strips in the 1D cluster and the strip pitch.

Once the 1D clustering is completed for both sets of readout strips of a given GEM tracking plane/module, 2D hit association is performed within the calorimeter search region to form 2D hits. All possible 2D hit associations are formed with the optional requirements of cluster ADC and timing correlations between the two strip coordinates.

Track Finding

A comprehensive description of the track finding algorithm would be a broad and lengthy discussion, and only a simplified explanation is provided here. At the start of the track finding process, each tracking plane's active area is divided into small *grid bins* ($\approx$5mm$\times$5mm). All the bins with 2D hits in the front tracking layer are considered and a straight line is drawn between each grid bin center with 2D hit/hits to the center of the calorimeter constraint's center. Then grid bins within the region of interest of the back tracking layer, defined by the front grid bin and the back constraint point, are looped over. Then for each single hit combination between the front and back tracking layers, within the chosen combinations of front and back tracker grid bins, a straight line is projected which goes through all the tracking planes in the middle. Now the grid bins in the middle layers that the straight line goes through, plus some other grid bins within some tolerance region, are all considered. A

quite sizable set of allowed combinations of grid bins are now generated across all the tracking layers. Thereafter, 3D straight line fits are performed across all the 2D hit combinations within the grid bin combinations, and the 2D hit combination with the best chi-squared per degree of freedom is found. Priority will be given for tracks with the maximum number of 2D GEM hits along the tracks, with the minimum allowed number of 2D hits per track being three.

3.7 In-Beam Results

At the time of this writing, SBS GEM detectors have been used in three different experiments across the SBS physics program, namely GMn, nTPE, and GEn-II. They will also be used in two upcoming experiments, GEn-RP and GEp-V, which are the two experiments that will use the most number of GEM modules/layers. Overall, the UVA-made detectors exhibited stable and reliable behavior. All the GEM modules that were introduced to the beam are still functioning without a noticeable loss of gain/efficiency. Only a handful of GEM foil HV sectors (2-3) were shorted out of the 28 GEM modules that were exposed to experiment conditions.

However, this is the first time large-area GEM detectors were used in such high rates at Jefferson Lab and in the world. A significant number of challenges had to be faced and many solutions were tested for those challenges and successfully implemented to mitigate almost all the issues that arose. A brief overview of these challenges and solutions implemented will be described towards the end of this section.

3.7.1 Bigbite Electron Arm GEM Performance

Except for the GEp-V experiment, all the other SBS experiments utilize the Bigbite spectrometer. The name "Bigbite" is used because this spectrometer consists of the Bigbite dipole magnet, which has been used in several other experiments in Hall-A before the SBS program. However, apart from the magnet, the detector package in the Bigbite spectrometer has undergone many modifications including the addition of several brand-new detectors such as GEMs, GRINCH, and the Timing Hodoscope.

The Bigbite electron spectrometer consists of five GEM tracking layers, out of which four are positioned towards the front of the spectrometer (front tracker GEM layers) whereas one is positioned behind the GRINCH detector (back tracker GEM layer). A diagram of the Bigbite spectrometer is shown in Figure 2.5a. At the very beginning of the GMn experiment, which was the very first time this newly modified

version of the Bigbite spectrometer was used in beam conditions, two out of the four front tracker GEM layers were 150 cm×40 cm UVA-made U-V GEM layers, and the other two were GEM layers with the same active area made by National Institute of Nuclear Physics in Italy (INFN). The INFN GEM layers were made by vertically stacking three 50 cm×40 cm X-Y readout GEM modules. However, these INFN GEM layers were replaced with another two UVA-made 150 cm×40 cm U-V GEM layers in the middle of the GMn run. Only the results when all four front tracker GEM layers are U-V GEM layers are shown here.

Figure 3.38 shows a 2D hit map of all five GEM layers in the Bigbite spectrometer under beam operation. Layers 0-3 represent the four front tracker 150 cm×40 cm U-V type GEM layers, while Layer 4 represents the 200 cm×60 cm X-Y type back tracker GEM layer. A total of five dead HV sectors can be seen across the 4 front tracker U-V layers as marked by the red arrows. Some of these dead sectors were identified immediately after the production of the fabrication and some developed during the operation in the experiments. In addition, a few bad readout channels are also visible as indicated by the magenta arrows. These are most likely due to poor connections between the Panasonic connector on the readout board and the readout strips. The angular direction of these dead channels is expected because of the orientation of the U-V readout strips by design. The X-Y back tracker GEM modules do not have any dead readout channels or dead HV sectors. However, there is a single malfunctioning APV25 card as indicated by the blue arrow. This APV25 card was located in an area in the spectrometer that was not accessible and therefore it could not be replaced for this experiment run. Figure 3.39 shows a plot of tracking residuals along a single strip coordinate (U/X) for the Bigbite spectrometer. A Gaussian plot of the central peak region gives a standard deviation of 91 μm. It should be noted that this residual contains contributions from multiple scattering of the track between the GEM chambers, in addition to the intrinsic resolution of the GEM modules.

3.7.2 SuperBigbite Hadron Arm GEM Performance

GEM tracking layers named as the "inline charge exchange polarimeter" in Figure 3.15b were installed in the SuperBigbite hadron arm and commissioned during the GEn-II experiment. This particular configuration is intended to be used in the upcoming GEn-RP experiment. These GEM layers were not necessary for the GEn-II experiment and therefore they were not used during most of the experiment run except for their commissioning purposes. There are a total of eight GEM tracking

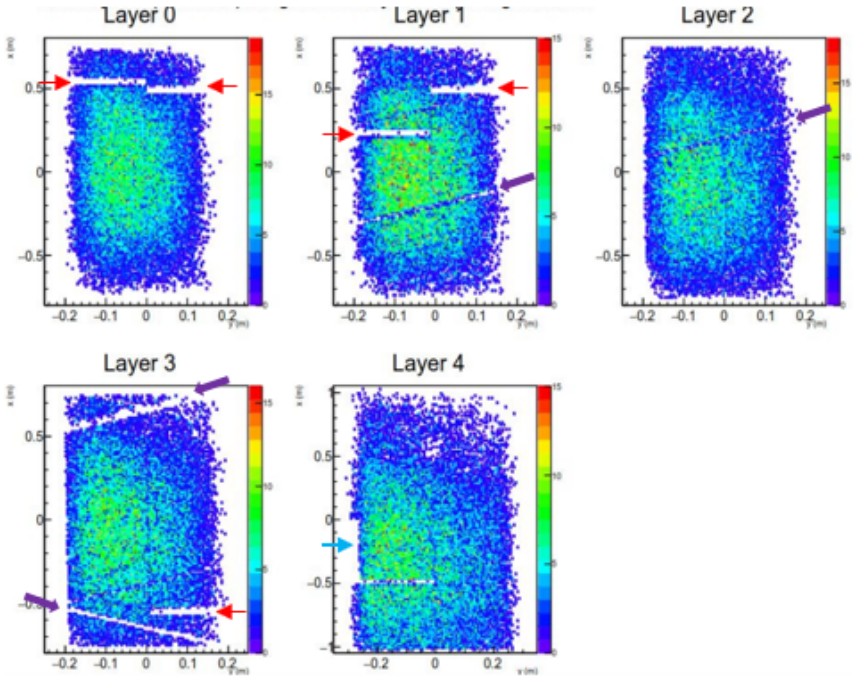

Figure 3.38: 2D plots of hits-on-tracks for the five GEM layers in the Bigbite spectrometer under beam operation

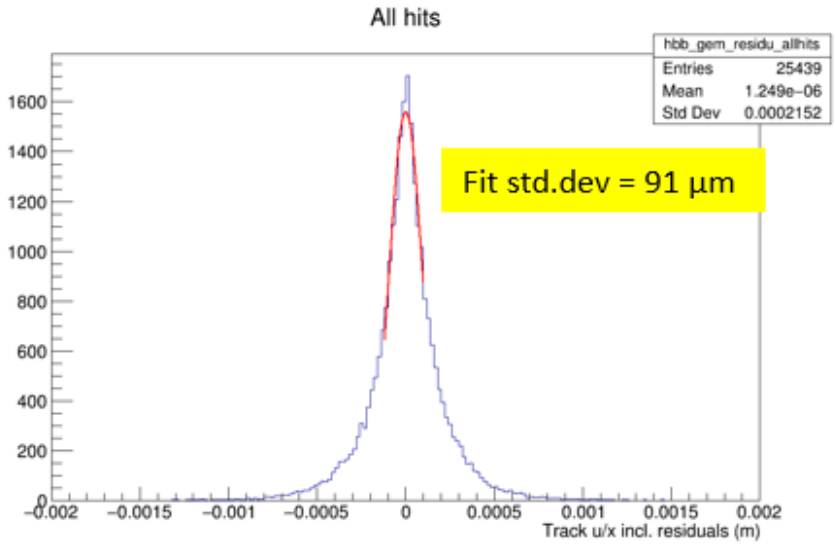

Figure 3.39: Tracking residuals along the X coordinate direction for all the GEM module hits of the Bigbite spectrometers

layers in this setup and only six were operated. Figure 3.40 shows a 2D hit map of all six 200 cm×60 cm X-Y type GEM layers that were commissioned and tested during the GEn-II experiment run. After the completion of the GEn-RP experiment, these

six GEM layers and an additional ten GEM layers will form the proton polarimeter tracker of the GEp-V experiment, as shown in Figure 3.15a.

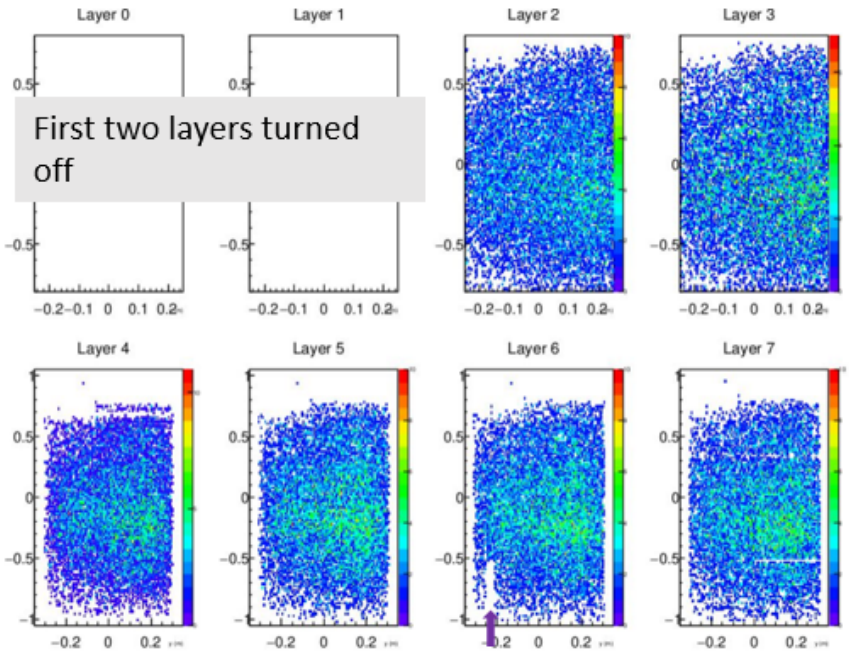

Figure 3.40: 2D plots of hits-on-tracks for six 200 cm×60 cm X-Y type GEM layers in the SuperBigbite spectrometer

3.7.3 GEM Gain Drop Under High-Rate and Solutions

An appropriate observable to study the GEM detector gain as a function of the background rate is the current flow through the HV divider chain. Under no significant background conditions (e.g., when there is no beam present in the experimental hall), the divider current is stable and agrees with Ohm's law expectation for given the divider total resistance. Under significant background rates, the divider current rises above the nominal value because a significant fraction of ions and electrons created from the GEM avalanche process lands on the GEM foil electrodes and then travel into the divider chain. If the GEM detector gain remains constant, this *excess divider current* should increase linearly with the total rate experienced by the GEM detector. Figure 3.41 shows a plot of Excess Divider Current vs Beam Current of a GEM module in the front tracker of the BigBite spectrometer during the GMn experiment. All run conditions through all the data points in this plot remained the same, while the beam current increased. As can be seen, with increasing beam current, the Ex-

cess Divider Current departs from the linear behavior and begins to plateau. This is symptomatic of the GEM detector gain being reduced.

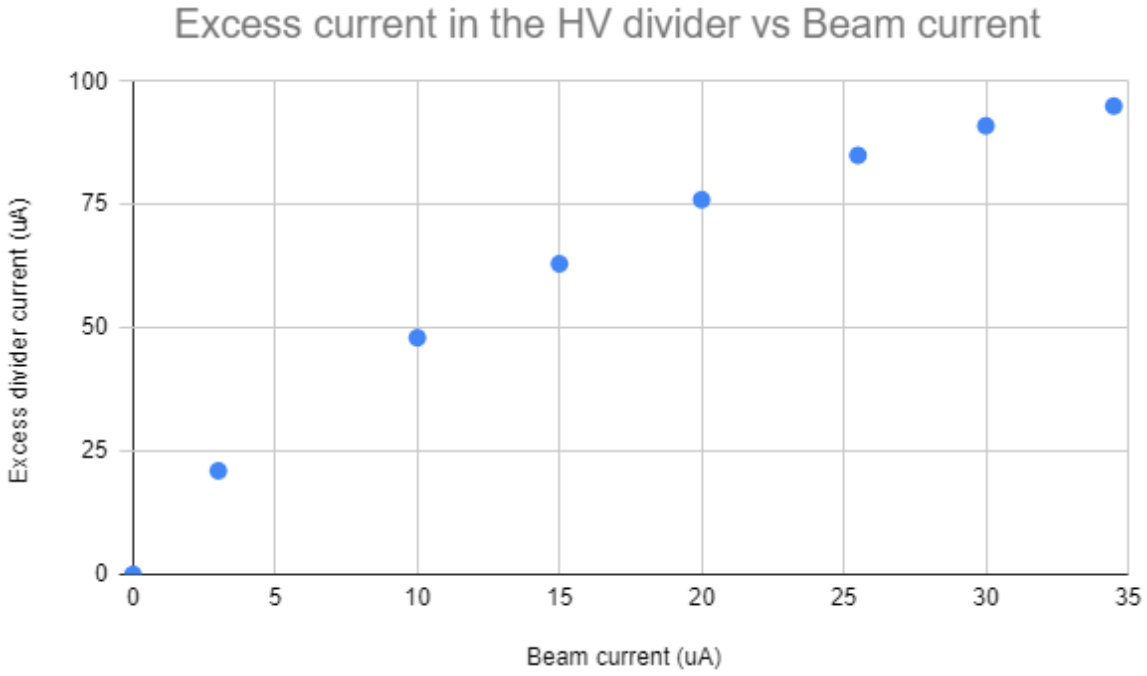

Figure 3.41: A plot of Excess Divider Current (current through the HV divider under beam conditions minus the current through the HV divider with no beam) vs the beam current (linearly proportional to the background rate)

The drop in the gain was due to the current flowing through the GEM foils at high rate exposure lowering of the effective potential difference across the GEM electrodes. Two different solutions for this problem were tested by the University of Virginia GEM detector group. One method was to implement a so-called "two-path" resistive divider, which essentially reduces the resistance of the resistive divider chain by one half. Now when the same HV is applied as before, the current through the divider chain will be doubled, thus making the fractional effect due to additional current induced by the background rates smaller, helping to keep the potential differences across the resistive divider chain more uniform. This method was tested at the University of Virginia GEM detector lab and was implemented in some GEM modules in the BigBite spectrometer during the second run-group (GEn-II) experiment, and moderate improvement compared to the original HV divider was observed. The second and more promising solution was to use the so-called "individual floating channel HV supply" method. In this method, each GEM module will be provided with seven HV channels that directly provides the required high voltage to each GEM

electrode, anode and the cathode. This method was implemented after the conclusion of the GMn experiment; more details of this power-supply scheme could be found in reference [55]. Significant improvement compared to using a resistive divider chain HV supply scheme was observed with this method.

Chapter 4

Data Analysis

As discussed in Chapter 1, the physics observable required for the calculation of the magnetic form factor of the neutron, G_M^n, is the e-neutron and e-proton elastic scattering differential cross-section ratio

$$R = \frac{\left(\frac{d\sigma}{d\Omega}\right)_{n(e,e')}}{\left(\frac{d\sigma}{d\Omega}\right)_{p(e,e')}}$$

The details of this ratio extraction and an overview of the associated systematic uncertainty estimations will be provided in this chapter.

Since a deuterium (^{2}H/D) target is used, the scattering reactions experimentally observed will be quasi-elastic scattering, D(e,e′n)p and D(e,e′p). This means various nuclear effects, such as nuclear binding energy, nucleon Fermi momentum within the deuteron nucleus, and final state interactions, will be folded into the observed reaction cross-sections. In addition, multiple effects will be induced by the finite momentum resolution of BigBite—the electron arm spectrometer—and the ratio extraction is directly affected by the neutron and proton detection efficiencies of the HCal detector. Furthermore, the extremely large amount of inelastic contamination at the large Q^2 values being considered will further complicate an accurate extraction of elastic-event cross-sections.

To account for these effects, a comprehensive simulation machinery is used to generate simulated data mimicking the experiment data. Beginning with quasi-elastic event generation, radiative effects, and all the relevant detector effects are carefully included in the simulation. The simulated data is also subjected to an analysis procedure identical to the one used for experiment data. Finally, by comparing the experiment data and simulated data, the ratio R is extracted. A broad overview of the E12-09-019 experiment's data analysis procedure followed in this dissertation

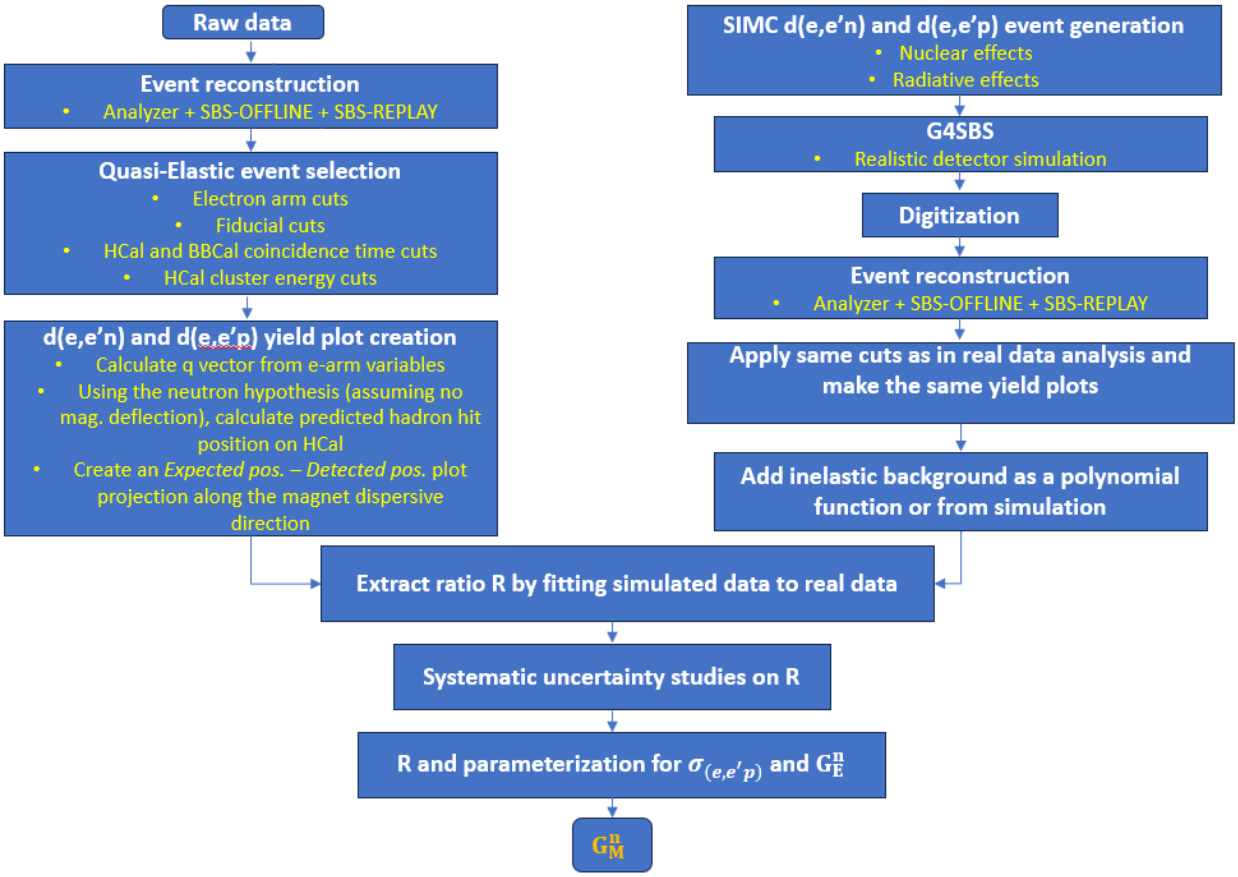

Figure 4.1: High-level analysis workflow

analysis is provided in Figure 4.1.

4.1 Analysis Machinery

4.1.1 Hall-A Analyzer

The Hall-A analyzer[1] is an analysis framework developed by the JLab Hall-A/C software group for the analysis of Hall-A experiment data. Written in C++ and built on top of CERN's ROOT data analysis framework, it has the important properties of modularity and extensibility. It is primarily used for raw data decoding, event reconstruction, and primary physics variable formation. In addition, it can also be used to analyze digitized simulated data. The analysis workflow of the Hall-A analyzer is shown in Figure 4.2. The final output is ROOT files with all the necessary variables

[1]Hall-A analyzer Wiki: https://redmine.jlab.org/projects/podd/wiki, and Git repository: https://github.com/JeffersonLab/analyzer

for physics analysis and calibration work.

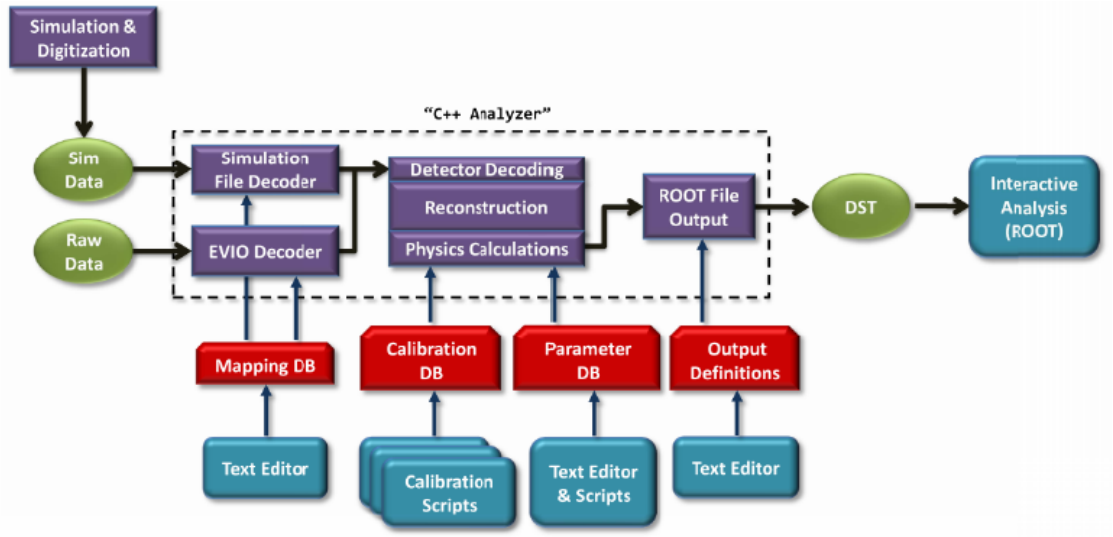

Figure 4.2: Hall-A analyzer workflow. Credit: Hall-A software group.

However, the SuperBigbite experiment program has introduced a brand-new set of detectors and spectrometers, which require a large amount of additional software for event reconstruction, with the GEM analysis machinery arguably being the most bulky addition. Given the extensible nature of the Hall-A analyzer, this additional software is written by creating new classes derived from existing base classes of the analyzer, and therefore some of the core processes can be used without needing to be rewritten.

4.1.2 SBS-OFFLINE and SBS-REPLAY

SBS-OFFLINE[2] is the primary reconstruction and analysis software for SuperBigbite experiments in Hall-A, written by the SBS software group. Built using the parent classes from the Hall-A analyzer, it contains all the software needed for the event reconstruction of the SBS experiments that have finished running.

SBS-REPLAY[3] consists of all the database files, replay scripts, analysis scripts, and calibration scripts for SBS experiments. Broadly speaking, the database files and the replay scripts contain the specific information needed to configure and run the analyzer and SBS-OFFLINE. The analysis scripts and calibration scripts are used

[2]SBS-OFFLINE Git repository: https://github.com/JeffersonLab/SBS-offline
[3]SBS-REPLAY Git repository: https://github.com/JeffersonLab/SBS-replay

for the physics analysis and calibration work, which is carried out using the output ROOT files from the analyzer and SBS-OFFLINE. SBS-REPLAY only consists of scripts and text files that do not require a build/install procedure to use them.

4.1.3 G4SBS

G4SBS[4] is the Monte Carlo simulation framework used to simulate SBS experiments. It is written by the SBS software group and is based on the Geant4 simulation toolkit[56] by CERN. All detector packages and spectrometers in SBS are defined within G4SBS, and the simulation can be run for any given SBS experiment by configuring the simulation using configuration files. Once the experiment is first specified, e.g., GMn, the other variable parameters like the beam energy, beam current, spectrometer angles, and the target (e.g., LD2 or LH2) can be configured, and the simulation can be run to produce a desired number of events. The output is in the form of ROOT files that basically contain charge and energy depositions within each detector channel, along with some basic physics variables. The output ROOT files from G4SBS must be digitized before they can be fed into the data analysis machinery described above. A separate software package called LIBSBSDIG is used to digitize the G4SBS-generated results. Figure 4.3 depicts the E12-09-019 experiment setup as viewed from the Geant4 graphical interface.

Several built-in physics event generators exist within G4SBS. These include elastic/quasi-elastic event generation based on some nucleon form factor parameterizations (Kelly fit for G_E^p, G_M^p, G_M^n, and Hall-A G_E^n collaboration fit from G_E^n data), nuclear spectral functions, inelastic event generation for the inclusive inelastic electron-proton and electron-deuteron scattering using Christy-Bosted parameterizations[57][58], and wide-angle pion photoproduction, to name a few. However, radiative effects are not accounted for within these generators in G4SBS. As a result, the SIMC event generator described below, which is external to G4SBS, is used to generate events for comparison with real data and cross-section extractions. These SIMC-generated events are passed through the very detailed detector simulators in G4SBS to generate simulated data that mimic the real experiment data.

[4]G4SBS Git repository: https://github.com/JeffersonLab/g4sbs

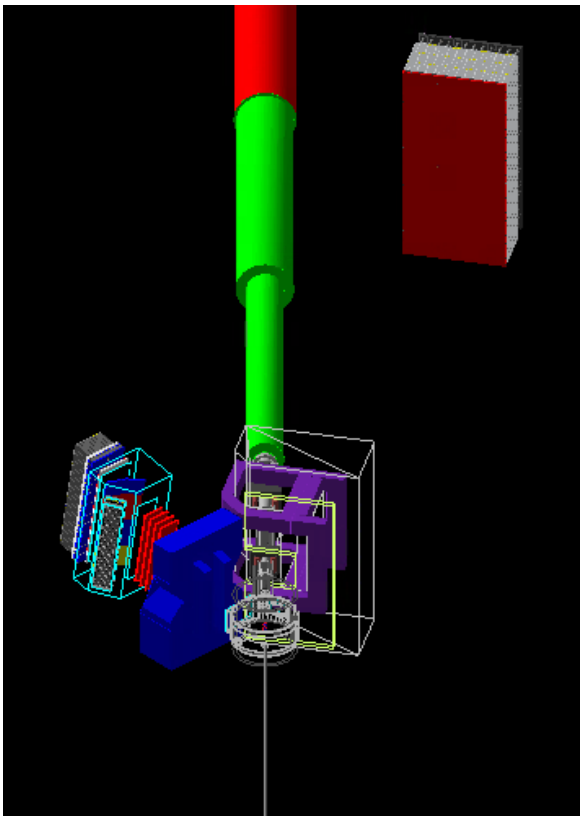

Figure 4.3: GMn (E12-09-019) experiment setup from Geant4 graphical interface, looking from a beam upstream and vertically up point of view.

4.1.4 SIMC

SIMC (simc_gfotran) is a Monte Carlo simulation toolkit written by JLab Hall-C, for simulating coincidence reactions[5]. It was adapted for SBS to work in conjunction with the existing detector simulation package, G4SBS [59]. The main purpose of interfacing SIMC with G4SBS is to use SIMC's capabilities of including radiative effects in the quasi-elastic scattering process. SIMC simulates both internal and external Bremsstrahlung at the target vertex. In addition, with the help of a built-in deuteron model, it also simulates nuclear effects such as Fermi smearing and nuclear binding. Final state interactions (FSI) of the outgoing nucleons are not modeled by SIMC.

[5]simc_gfotran Git repository: https://github.com/JeffersonLab/simc_gfortran

4.1.5 Final Physics Analysis Machinery - GMn-adr-ana

The analysis machinery written by the author to extract the physics results and generate the plots shown in this dissertation is named GMn-adr-ana[6]. This is a standalone repository that relies on the ROOT files generated by the aforementioned software packages created by the Hall-A and SBS software groups.

This repository contains programs to perform various analysis tasks such as detector calibrations, physics variable calculations, elastic event selection, experiment data and MC data comparison, ratio R extraction, and systematic uncertainty studies.

4.2 Event Selections

4.2.1 Good Electron Cuts

The first step in the event selection process is the application of the so-called "good electron cuts." The purpose of these cuts is to narrow down the data sample to select only the quasi-elastic scattering events in the desired kinematic regime, with an electron scattered and detected within the BigBite electron spectrometer. Inelastic scattering, scattering that happens outside of the target length, pion production events, and poorly reconstructed events (high probability of false tracks, etc.) are examples of the events that we want to remove at this stage. For the example plots shown in the subsequent sections, mostly the kinematic point labeled SBS-4 ($Q^2 = 3.0$ GeV$^2/c^2$) is used.

Track-Quality Cuts

The quality of the reconstructed tracks from the GEM tracking planes plays a pivotal role in this analysis. The accuracy of the results from the momentum reconstruction and the interaction vertex reconstruction depends directly on the quality of the reconstructed GEM track. The BigBite electron spectrometer consists of five tracking planes. The SBS-OFFLINE track-finding algorithm requires a minimum of three 2D GEM hits on a track for successful track reconstruction. However, due to the high background conditions experienced by the GEM detectors, the probability of false track generation is high. One parameter that helps significantly to control the amount of fake track events in the data sample is the number of GEM hits present in

[6]GMn-adr-ana Git repository: https://github.com/anuruddhadilshan/GMn-adr-ana

the reconstructed track. All the analysis presented in this dissertation uses a three-hit minimum on the reconstructed GEM track.

Another track-quality cut that is useful to apply is the track χ^2/ndf cut. Since this parameter is directly used in the track-finding algorithm, and a good GEM alignment gives a good χ^2/ndf value, this cut cannot be used to remove a very large number of poorly reconstructed tracks. A cut that accepts events with tracks with χ^2/ndf 15 or lower is generally used in this analysis.

Vertex Z Position Cut

The length of the deuterium and hydrogen cryogenic targets during the E12-09-019 experiment was 15 cm. In the Hall coordinate system, the target is centered at the origin and the +Z direction is pointing toward the beam downstream direction. Hence, the reconstructed vertex Z position gives us the point of interaction of the scattering event as determined by the GEM track along the target length. Any scattering events that are coming from outside of the target length must be removed, and this can be achieved by applying a simple cut that requires the reconstructed vertex Z position to be within the target length. The vertex Z resolution of the BigBite spectrometer is in the range of 4 mm to 7 mm, depending on the kinematic settings.

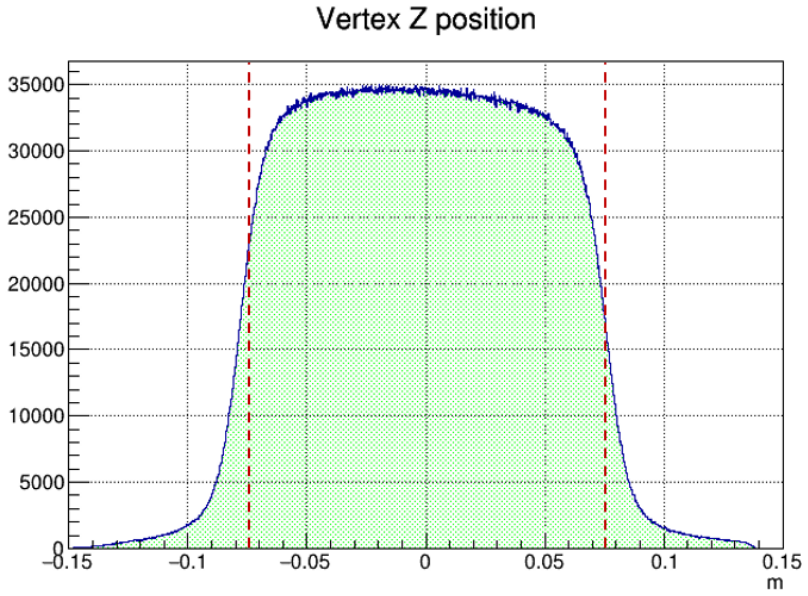

Figure 4.4: The reconstructed vertex Z position of all the deuterium data of SBS-4, 30% SBS magnetic field setting kinematic point. The two red vertical dashed lines indicate the end-cap position of the target with -0.075 m being the upstream end-cap position and 0.075 m being the downstream end-cap position.

Figure 4.4 shows a plot of the reconstructed vertex Z position for the entire SBS-4, 30% SBS field scale setting's deuterium data. A typical vertex Z cut used in this analysis accepts events within a 5-10 mm safety margin from the upstream and downstream end-cap positions to account for vertex resolution and to ensure that only events originating within the target length are accepted.

Pre-Shower Energy Cut

As mentioned in Section 2.3.5, the primary purpose of the pre-shower detector is pion rejection. The GRINCH detector was not fully commissioned during the majority of kinematic points of the E12-09-019 experiment, and hence the pre-shower detector served as the only handle to control the amount of pion contamination within the data samples. The heavier pions deposit systematically lower energy in the short length of the pre-shower blocks as opposed to electrons.

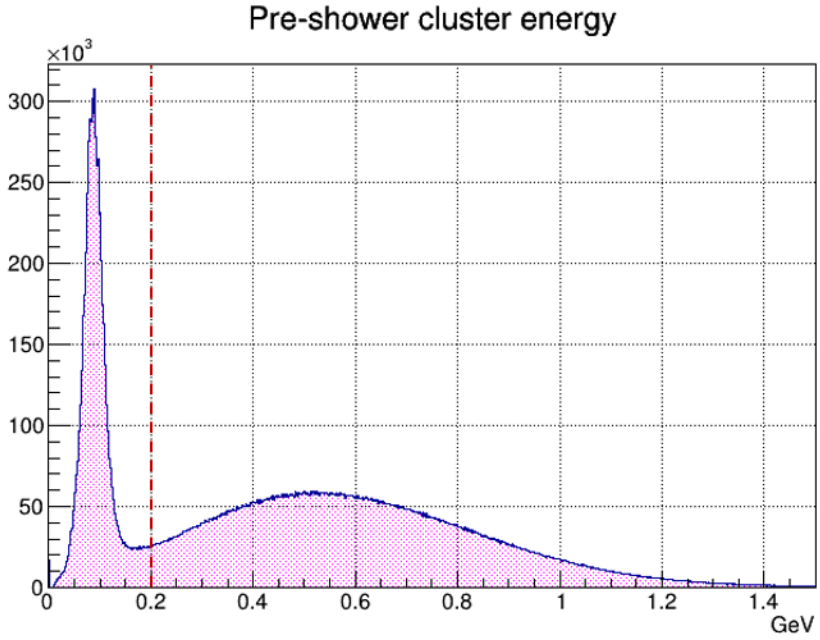

Figure 4.5: Pre-shower cluster energy. The sharper peak at the beginning arises due to pions, and the broader peak towards the right is due to electron events. The red dashed line at 0.2 GeV indicates the cut-off point used during the preliminary analysis to select electron events.

E/P Cut

In the GeV energy scale, the electron rest mass is negligible, and to a very good approximation, $E \approx P$, where E represents the electron kinetic energy sampled by the

BigBite calorimeter, and P represents the magnitude of the electron track momentum. With proper momentum calibrations in BigBite magnet optics and energy calibrations in BBCal, the ratio E/P must be a sharply peaked function around unity. For the pass-2 mass replayed data used for this analysis, this is indeed the case, as seen in Figure 4.6. As can be seen, this plot shows that the momentum and energy calibration is in good status for all events. Therefore, in this analysis, an event selection based on the E/P ratio is not applied. However, a sharp cut around the E/P peak was used for the analysis prior to calibration to remove events from poorly calibrated channels.

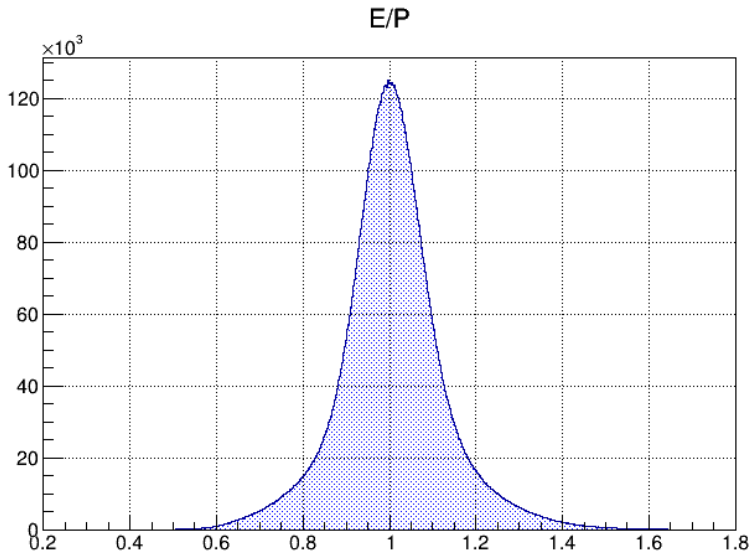

Figure 4.6: E/P distribution for the entire SBS-4, 30% SBS field scale, deuterium data set.

4.2.2 Invariant-Mass-Squared (W^2)

The invariant-mass-squared is the single most important elastic event selection cut that could be applied to obtain as clean as possible a sample of quasi-elastic scattering events. By using the scattered electron's four-momentum as measured by the BigBite spectrometer and by reasonable assumptions about the kinematics of the incoming beam electrons and the target, we can calculate the invariant mass of the virtual photon-nucleon system. Section A.1 provides a description of the definition of W^2 and how it is calculated.

For quasi-elastic D(e,e'n)p or D(e,e'p)n scattering, a spectrum of W^2 should be peaked around 0.88 GeV^2. This is due to the fact that the neutron and proton rest mass difference is negligible at these scales, and the square of the average of neutron

and proton rest masses is ≈ 0.88 GeV^2. However, the inelastic contamination could skew the absolute peak position of the W^2 distribution, and at higher Q^2 kinematic points the inelastic contamination is so overwhelming that it is impossible to spot a clear elastic peak in the W^2 distribution.

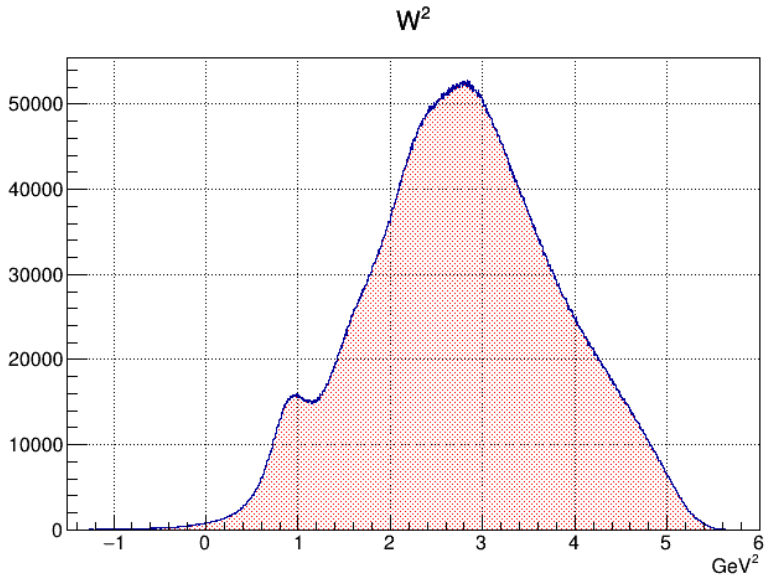

Figure 4.7: W^2 distribution for SBS-4, 30% SBS field scale deuterium data. The "elastic peak" could be clearly seen around 0.88 GeV, and a much larger amount of inelastics could be seen as well.

See Figure 4.7 for an example of a W^2 distribution from the kinematic setting of SBS-4. At this relatively lower Q^2 setting, the elastic peak is visible. But as will be seen in some of the later examples from higher Q^2, the elastic peak will not be visible. In further physics analysis, a cut centered around 0.88 GeV will be applied to remove the large inelastic contamination as much as possible while retaining as many elastic events as possible. The exact values of these cut boundaries will be determined from the systematic studies and will be presented later.

4.2.3 HCal Δx vs Δy, Δx, and Δy Plots

Figure 4.8 shows a diagrammatic view of HCal when looking at its face in the downstream direction, standing near the target. The internal coordinate system of HCal is defined following the standard spectrometer transport convention. The positive X axis points towards the bottom of HCal, and the positive Y axis points towards the left of HCal as defined by this point of view. The SBS magnet deflects protons

vertically upwards, i.e., in the -X direction. Hence, the X-axis is also referred to as the dispersive direction and the Y-axis as the non-dispersive.

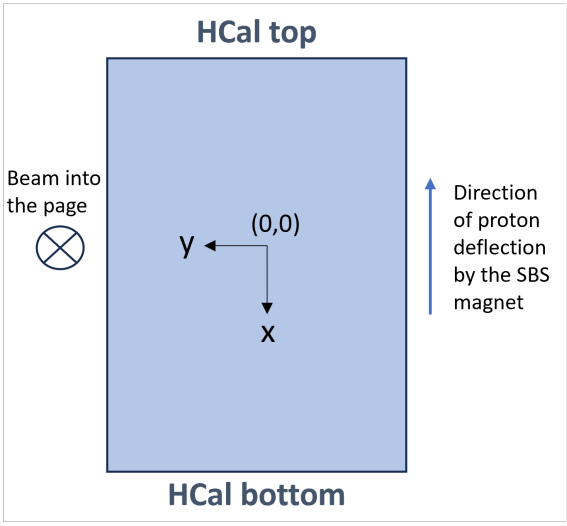

Figure 4.8: HCal detector face with the detector coordinate system.

In order to extract D(e,e′n)p and D(e,e′p)n quasi-elastic yields, correlations should be made between the detected hit positions in HCal and the predicted hit positions as calculated from the scattered electron kinematics from the BigBite spectrometer. See Section A.2 for the details of this calculation. We define,

$$\Delta \mathrm{x} = \mathrm{x}_{detected} - \mathrm{x}_{predicted} \tag{4.1}$$

and,

$$\Delta \mathrm{y} = \mathrm{y}_{detected} - \mathrm{y}_{predicted} \tag{4.2}$$

As described in Section A.2, the predicted positions are calculated using the so-called "neutron hypothesis," where all the hadrons are treated as neutrons and the deflection due to the SBS magnet field is neglected. Figure 4.9 shows a 2D correlation plot of Δx vs Δy for the kinematic setting of SBS-4, with data taken with 30% SBS magnetic field. A set of event selection cuts as mentioned above is used in making this plot, including a W^2 cut of 0.2 GeV^2 $< W^2 <$ 1.2 GeV^2. The clear separation of the neutron and proton scattering events could be seen in this plot. However, it would be unnecessarily complicated to extract the D(e,e′n)p and D(e,e′p)n quasi-elastic yields from such a 2D plot, compared to a 1D plot of Δx, which is essentially the projection of the 2D Δx vs Δy plot onto the dispersive direction. Such a 1D plot contains all features necessary for a D(e,e′n)p and D(e,e′p)n quasi-elastic yield extraction.

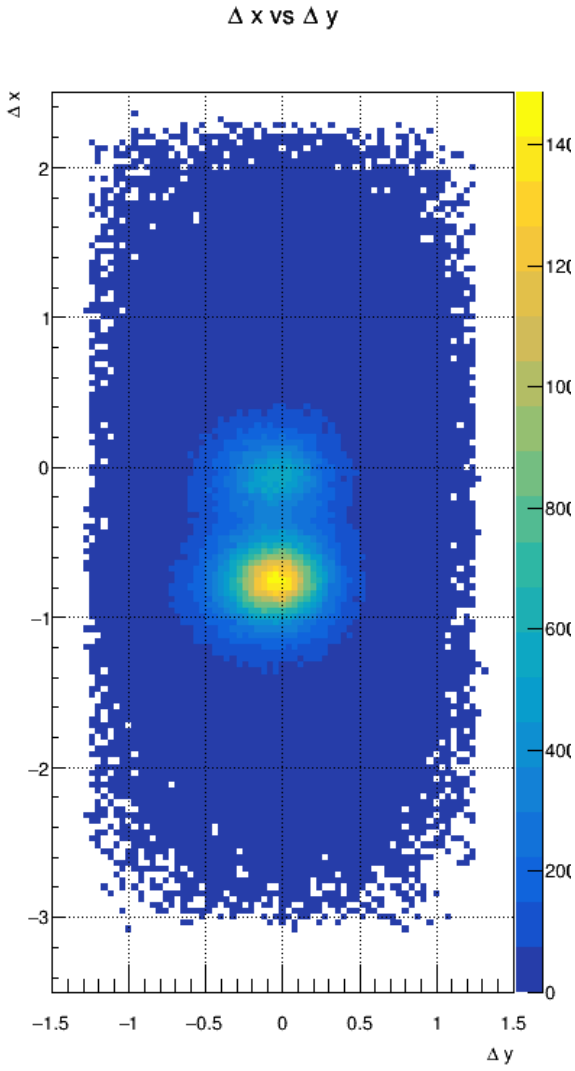

Figure 4.9: A plot of Δx vs Δy. The "neutron spot" could be seen centered around (0,0) and the "proton spot" is below it centered roughly around (0, -0.8 m).

Figure 4.10 is a 1D Δx plot for the same data set as in Figure 4.9. In the E12-09-019 experiment analysis, the 1D Δx plots are used to extract D(e,e′n)p and D(e,e′p)n yields, and more importantly, yield ratios. Methods ranging from crude techniques like fitting Gaussian functions for the neutron and proton peaks and polynomials for the background, to making Δx plots closely matching to real data distributions from the simulation machinery described earlier in the chapter were used over the course of this data analysis.

Figure 4.11 shows a 1D Δy plot for the same data set as above. The Δy plot is a useful tool to study and apply elastic event selection cuts not affecting the ratio

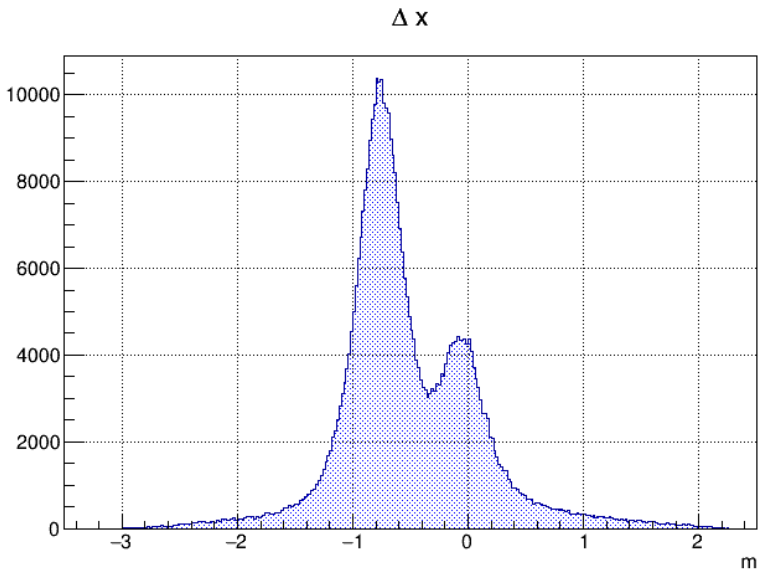

Figure 4.10: A plot of Δx. The "neutron peak" is centered around 0 and the proton around -0.8 m.

measurement similar to the W^2 cuts.

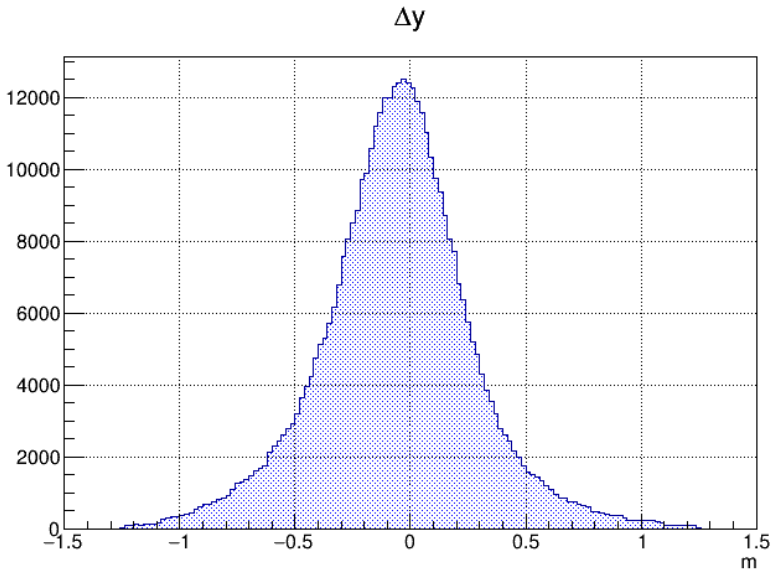

Figure 4.11: A plot of Δy.

4.2.4 Fiducial Cut

Due to the magnetic deflection of protons compared to neutrons, the point of impact on HCal for a proton, relative to a neutron that corresponds to the same scattered

electron kinematics, is different. For the D(e,e′n)p and D(e,e′p)n scattering differential cross-section ratio extraction to be accurate, the acceptance for neutrons and protons must be matched and be equivalent for the scattered electron phase space considered. One edge case that illustrates the importance of applying a fiducial cut can be described as follows: Imagine that for a given electron kinematics, the scattered neutron strikes at a certain vertical height on HCal. For a proton that corresponds to the same electron kinematics as the aforementioned neutron, the SBS magnet deflection will cause it to hit at the very top edge of HCal. For any neutrons that strike HCal above the previous neutron hit position, the corresponding proton will fly over HCal and would not be detected. Therefore, if the second neutron mentioned above is considered in our analysis, we will erroneously measure the ratio R to be larger than what it actually is.

Only the *predicted* neutron and proton hit positions based on the reconstructed $\vec{q}$, vertex Z position, and HCal position and geometry information should be used in this selection (calculation described in Section A.2). While it is straightforward to determine the point of interaction for the neutron under the neutron hypothesis, for the proton, the magnetic deflection by the SBS magnet must be considered. In addition to the predicted hit positions, the spread of the neutron and proton distributions along both the dispersive and non-dispersive directions must be considered as well. An empirical method is used in this analysis to calculate these quantities. By fitting two Gaussians for the neutron and proton peaks to the Δx plot and a Gaussian to the Δy plot mentioned in Section 4.2.3, these quantities can be extracted. See Figures 4.12a and 4.12b for an example of these fits applied to a Δx and Δy plot, respectively.

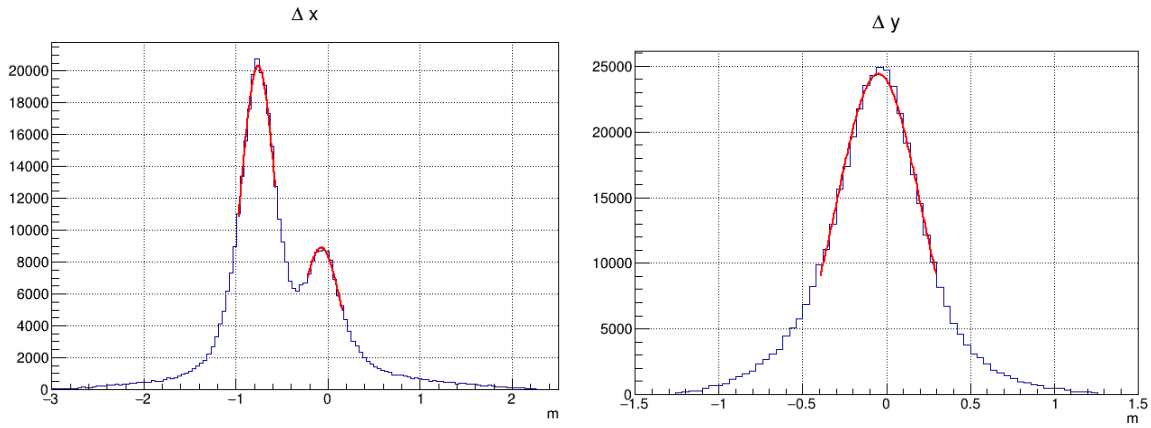

(a) Δx plot with two Gaussian fits.

(b) Δy plot with a Gaussian fit.

Figure 4.12: Fits to the Δx and Δy plots to extract empirical parameters for the fiducial cut.

In this analysis, the mean value from the proton peak's Gaussian fit in the Δx is interpreted as the *average deflection* of the protons for that given kinematic setting. The standard deviations of the neutron and proton peaks' Gaussian fits in the Δx plot could be used to quantify the spread of the respective peaks along the dispersive direction. Since the relative difference between the two standard deviation values is not significant, an average between the two is used. The spread of both the neutron and proton peaks along the non-dispersive direction is quantified by the standard deviation of the Gaussian fit to the Δy plot. These parameters are subject to change based on the nucleon momentum and the SBS magnetic field applied and hence must be evaluated separately for each kinematic setting. Figure 4.13 illustrates the principle behind the fiducial cuts. The left-hand side plot contains predicted hadron hit positions on HCal calculated via the neutron hypothesis. The right-hand side plot contains the same set of events, shifted by the average proton deflection along the dispersive direction. Hence, it is referred to as the proton hypothesis predicted hit positions.

For a given event to pass the fiducial cut, it must be within the innermost rectangle defined by the dashed magenta lines in both cases. Figure 4.14 shows the events that passed this criterion. The dashed magenta lines represent the so-called safety margins that account for the spread of neutron and proton peaks along both the dispersive and non-dispersive directions as mentioned. The offsets of the dashed magenta lines to their respective parallel red lines are defined as a product between the standard deviation along the considered direction and a chosen multiplicative factor. In this particular case, a factor of 2.0 along the dispersive (x) direction and a factor of 1.0 along the non-dispersive (y) direction is used. These multiplicative factors could introduce a bias to the ratio extraction and therefore must be carefully chosen after a systematic study.

4.2.5 HCal Best Cluster Selection Algorithm

SBS-OFFLINE's HCal cluster formation algorithm creates clusters, crudely, as follows. First, the HCal blocks that pass an energy threshold are organized in descending order with respect to the energy of the blocks. Starting with the highest energy block, the neighboring blocks with energy over a threshold are added to the primary block, and clusters are formed. The total energy deposited by the hadron will be interpreted as the energy sum of all blocks in the cluster. The cluster positions are calculated via an energy-weighted centroid algorithm. In addition, timing information for the clus-

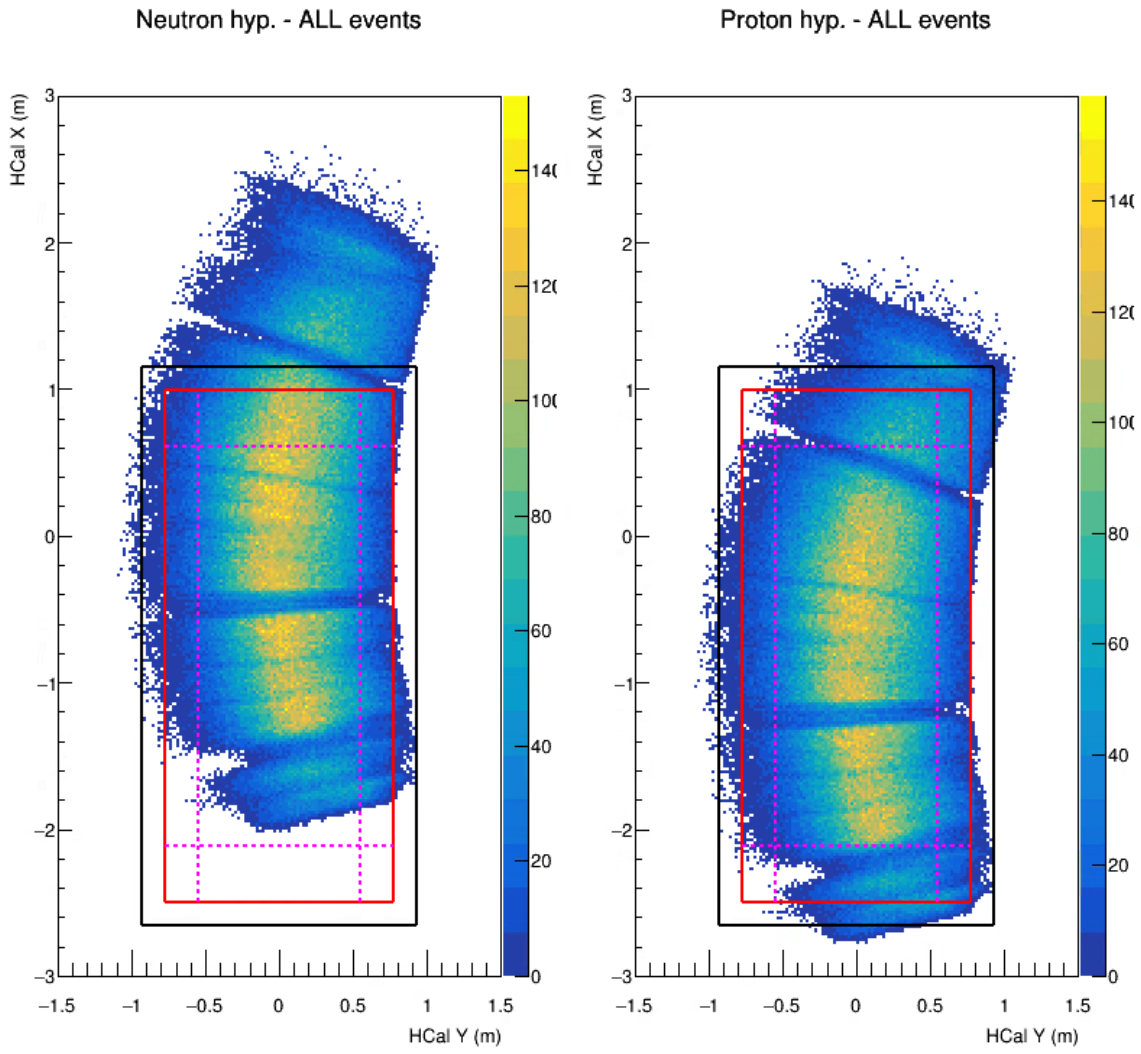

Figure 4.13: Graphical representation of fiducial regions on HCal. In both the left and the right plots, the black rectangle represents the physical outer perimeter of HCal. The inner red rectangle represents a reduced active area with one layer of calorimeter blocks removed from all four edges. This is intended to discard any events that could potentially lose a portion of the shower from the outer edges of the detector. The rectangular region defined by the magenta dotted lines represents the final fiducial regions.

ter is also created using the ADC and TDC data of the primary block in the cluster. In the analysis of the E12-09-019 experiment, timing information from FADC data, i.e., ADC-time, is primarily used.

In the default selection by SBS-OFFLINE for the *primary cluster*, the cluster that is most likely to correlate to the elastic/quasi-elastic scattering is taken as the cluster that initially had the highest energy primary block. This would be the first

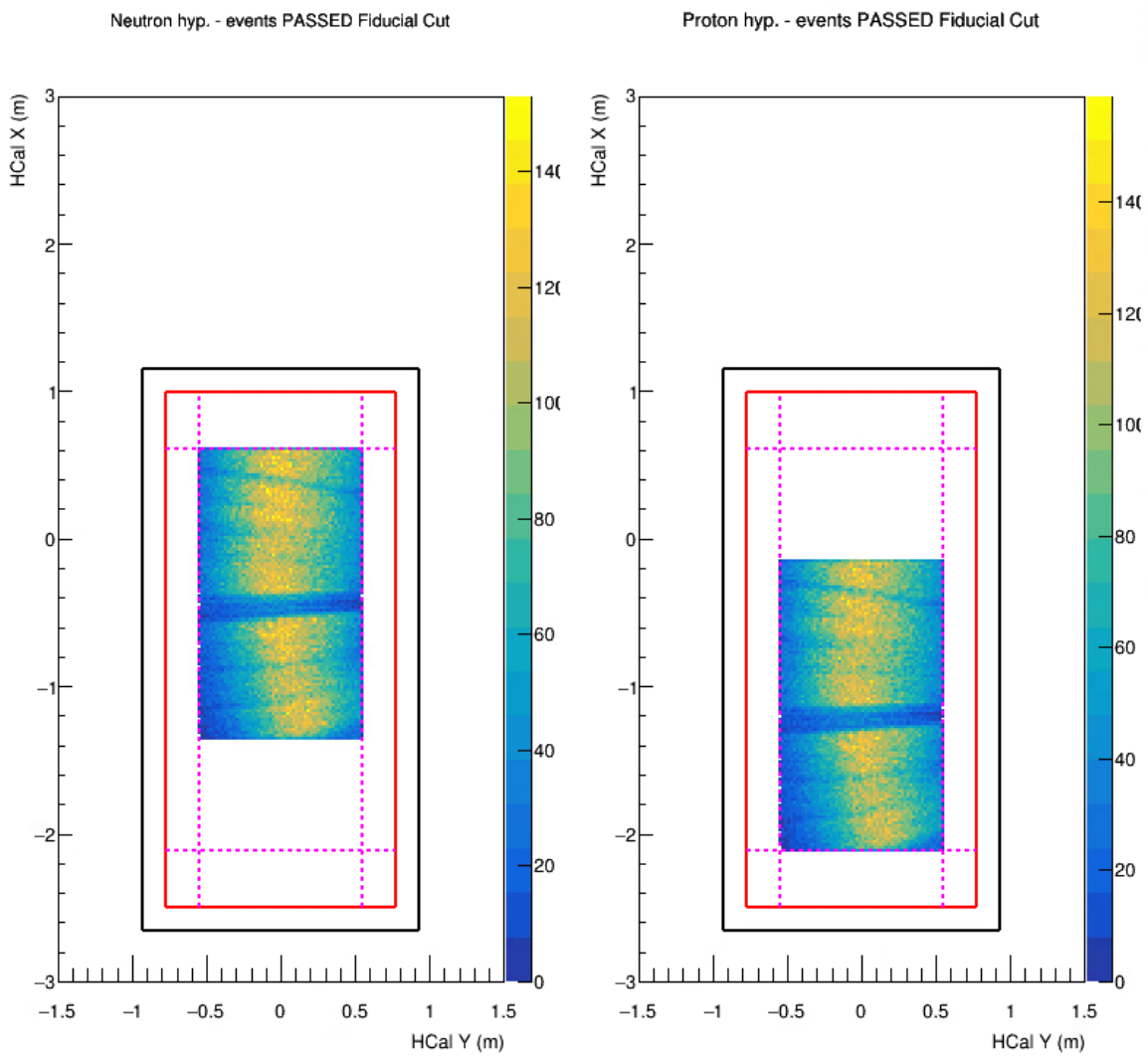

Figure 4.14: Graphical representation of all the events that passed the fiducial cut.

cluster created according to the above ordering. However, it has been found that this is necessarily not the most efficient primary cluster selection algorithm, and a non-negligible amount of elastic yield is lost by this method. An alternate cluster selection algorithm that prioritizes the clusters with *total cluster energy* (instead of the cluster with the highest energy primary block) and agrees with the coincidence ADC time distribution with BigBite shower detector is observed to outperform the default selection of SBS-OFFLINE. It should be noted that for the majority of the events, the primary cluster selected by this algorithm will be the highest energy block cluster selected by SBS-OFFLINE. This algorithm is motivated by the argument that considering the total energy of the cluster is more physically meaningful rather than considering the energy of the primary block. Unlike electromagnetic showers, hadron

showers are not tightly contained and have a wider spatial spread. In addition, the highly energetic elastic/quasi-elastic scattered nucleons and electrons should have a very tight time-of-flight correlation. This is reflected by the following HCal and BigBite shower ADC time difference plot in Figure 4.15. The sharp peak around 0 ns is due to real coincidence events, including quasi-elastic events, and the rest of the events in the shoulders could be attributed to accidental coincidence background. The red curve indicates a Gaussian fit applied to a tight region around the peak to obtain the mean and the standard deviation of the real coincidence event distribution.

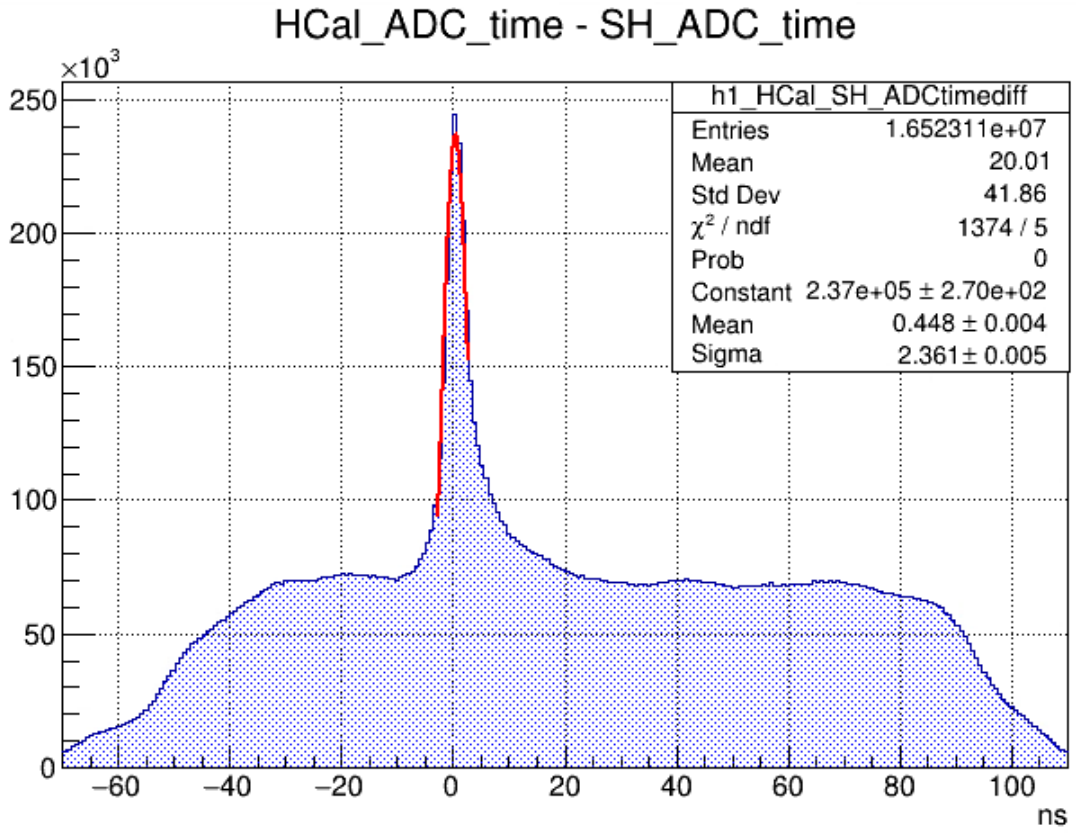

Figure 4.15: A histogram of ADC time difference between the highest energy block of the primary HCal cluster and the primary BigBite shower cluster.

As a first step, this algorithm re-orders the HCal clusters generated from SBS-OFFLINE in descending order of total cluster energy. Then, starting from the highest energy cluster, the ADC time difference between the cluster and the BigBite shower cluster is checked to be within several sigma values (4.0 used in this analysis) from the mean of the above distribution in Figure 4.15. If that is the case, that cluster will be chosen as the primary cluster. If that is not the case, the next highest energy cluster will be checked for the above timing requirement. This procedure is followed

until the highest energy cluster that satisfies the above-mentioned timing requirement is found. In this dissertation, the HCal cluster selected from this algorithm will be referred to as the "highest energy in-time cluster". See Figure 4.16 for a comparison of elastic yields obtained from the standard SBS-OFFLINE highest energy block cluster and the highest energy in-time cluster algorithms. Here, zero-field (SBS-magnetic field set to zero) LD2 data of the SBS-4 kinematic setting is used. The use of zero-field data makes a direct comparison much more straightforward due to no separation of neutron and proton events. In this particular case, an elastic yield improvement of approximately 5% is observed when using the highest energy in-time cluster algorithm.

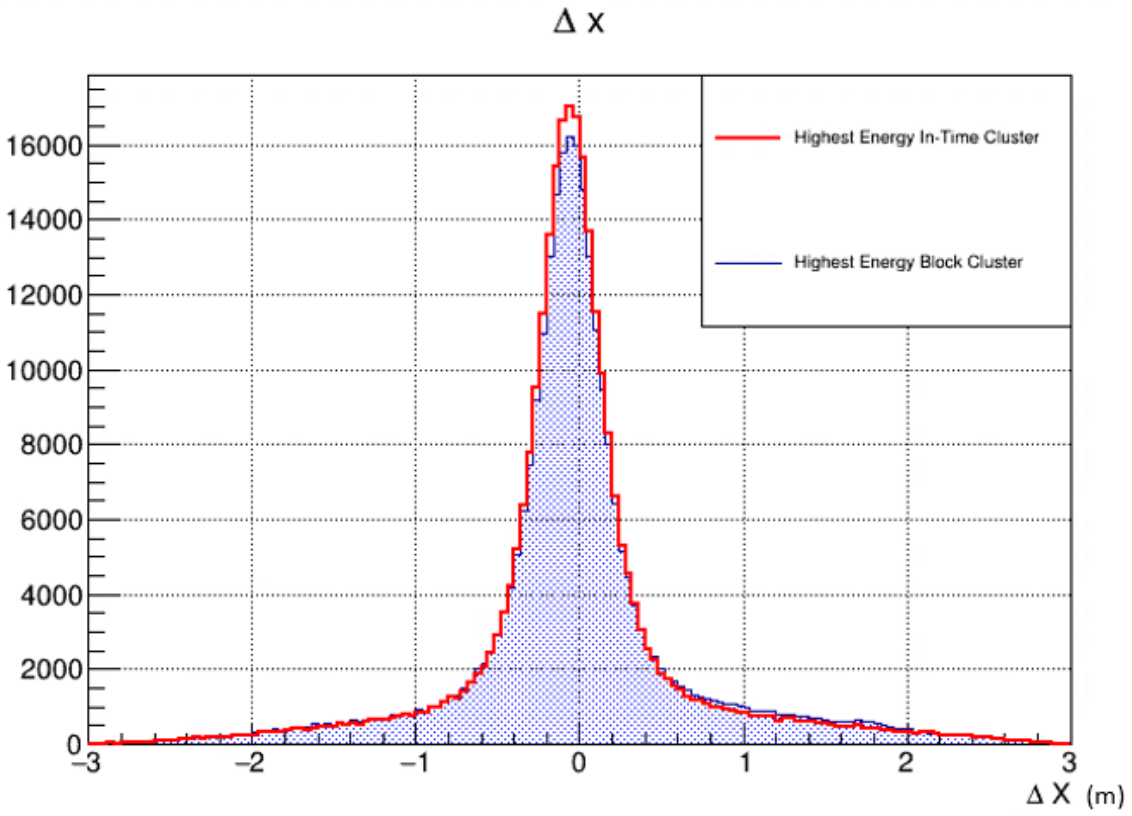

Figure 4.16: Δx plots for the SBS-4, 0% SBS field-scale, LD2 data. Compares elastic yields from the HCal primary cluster selection algorithms. The blue histogram represents the results from the default algorithm in SBS-OFFLINE and the red histogram refers to the algorithm being described.

The highest energy in-time algorithm will be used for all the experiment data analysis presented in this dissertation. For the analysis of the simulated data, due to the fact that ADC times are not properly simulated and statistics is not a concern, this algorithm is not used and the default highest energy block cluster provided by

SBS-OFFLINE is used.

4.2.6 HCal and SH Coincidence Time Cut

In addition to the good-electron cuts and the elastic cuts such as the invariant mass cut mentioned above, the HCal and BBCal shower coincidence time could also be used as a valuable tool for elastic event selection and to get rid of accidentals. As introduced in Figure 4.15, this cut will essentially reject events that lie outside of a chosen number of standard deviations from the mean. The exact value for the number of standard deviations to use should come from careful systematic studies of the variation of the ratio R and will be presented later on.

4.3 Benchmarking HCal Simulated Neutron and Proton Detection Efficiency

As described at the beginning of this chapter, the ratio R extraction of this analysis is performed by a simulated data fitting technique to the experimental data. The relative difference between the neutron and proton detection efficiencies of HCal detector directly affects the accuracy of the ratio extraction, and the simulation should reflect these differences at sub-percent level accuracy to meet the desired systematic uncertainty goals. Analysis efforts to benchmark the simulated neutron and proton detection efficiencies using experimental data are described in this section.

Both experimental detection efficiency analysis techniques described use "tagged" nucleons with the nucleon momentum vector calculated using the electron kinematics measured from the BigBite spectrometer. For the proton detection efficiency, the elastic electron scattering off from a hydrogen target, p(e,e′)p reaction is used. For the neutron detection efficiency, the single pion photoproduction, p(γ,π^+)n reaction is used.

4.3.1 Proton Detection Efficiency (PDE) Analysis

The data taken with a liquid hydrogen target across the entire set of kinematic points is used to evaluate the proton detection efficiency. The elastic p(e,e′)p reaction is used with the BigBite spectrometer to measure the scattered electron.

At relatively low Q^2 kinematic points (e.g., SBS-4, SBS-8, and SBS-9), the inelastic contamination is quite small and can be largely eliminated by stringent track

quality and elastic cuts. The study presented in this section focuses on SBS-4, SBS-8, and SBS-9 proton detection efficiency analysis. The SBS-8 kinematic point's liquid hydrogen data taken with the SBS magnet field set to zero is used in the plots presented in this section. The following steps are followed for this analysis:

- Electron arm analysis:
  - Tight electron arm track quality, optics, and W^2 cuts are applied for good electron event selection and inelastic background removal.
  - The predicted hit positions on the face of the HCal are calculated.
  - A HCal acceptance cut is applied to accept only events where the electron kinematics predict the corresponding proton to hit HCal.
  - Two histograms are created: one with projections of predicted proton hit positions on HCal along the X direction and another along the Y direction.
- A Δx vs. Δy histogram is created, and a tight cut around the *proton spot* is applied to select elastic scattering protons detected by HCal. Figure 4.17 shows two Δx vs. Δy plots with and without the proton spot cut applied. Figure 4.18 shows that by choosing a tight enough cut in W^2, the inelastic contamination can be significantly reduced. The W^2 region indicated is used for the "denominator histograms" along the X and Y directions mentioned in the previous step.
- Now, "numerator histograms" along the X and Y directions are created by plotting the predicted X and Y hit positions on HCal for events **within** the proton spot defined in the previous step.
- "Ratio histograms" are then created by taking the bin content ratio between the numerator and denominator histograms, which yields position-dependent proton detection efficiencies along the X and Y directions of HCal. See Figure 4.19.
- The average detection efficiency along the X and Y directions is obtained by performing straight-line fits to the respective ratio histograms.
- The total HCal proton detection efficiency is obtained by calculating the error-weighted average of the efficiency along the X and Y directions; from this analysis, it is calculated to be 94.22 $\pm$ 0.05% for SBS-8 hydrogen data taken with zero SBS magnet field.

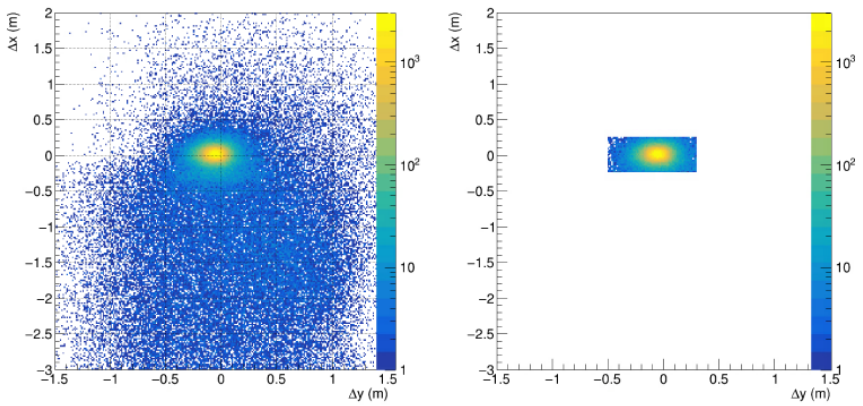

Figure 4.17: Δx vs. Δy plots with all the event selection cuts (i.e., denominator events) on the left, and the same plot with a graphical 2D cut applied around the proton spot (i.e., numerator events). Plot credit: A. Puckett.

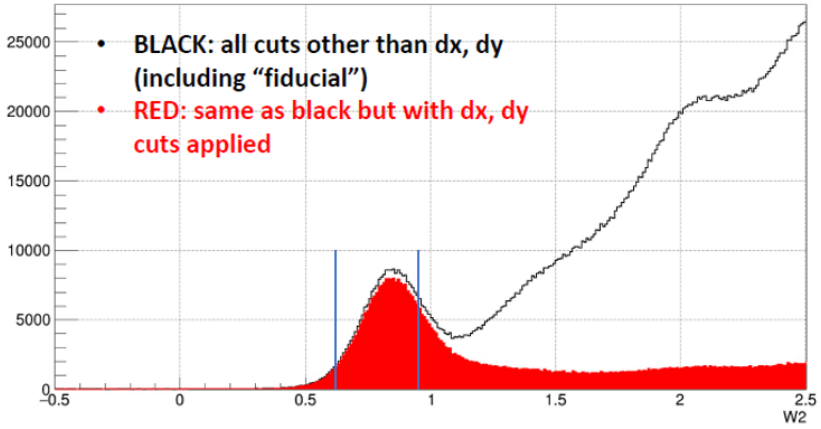

Figure 4.18: The W^2 plot for all the events passing the event selection cuts other than the proton spot cut - black. W^2 plot for the same events inside the proton spot - red. Plot credit: A. Puckett.

This technique also allows for a study of the variation of the detection efficiency across the active area of the HCal detector. Such a study is important to establish the validity of the HCal simulations as currently the HCal detector is defined within the simulation to have uniform detection efficiency across its entire active area. By inspecting the leftmost plot of Figure 4.19, it can be seen that there are some non-uniformities in the HCal detection efficiency. It has been identified that this is due to several under-performing channels along the corresponding calorimeter rows. This effect has been identified to be even more pronounced in the SBS-9 kinematic point where several of these bad channels are located near the center of the elastic event envelope on HCal for that kinematic point. Several solutions to incorporate these

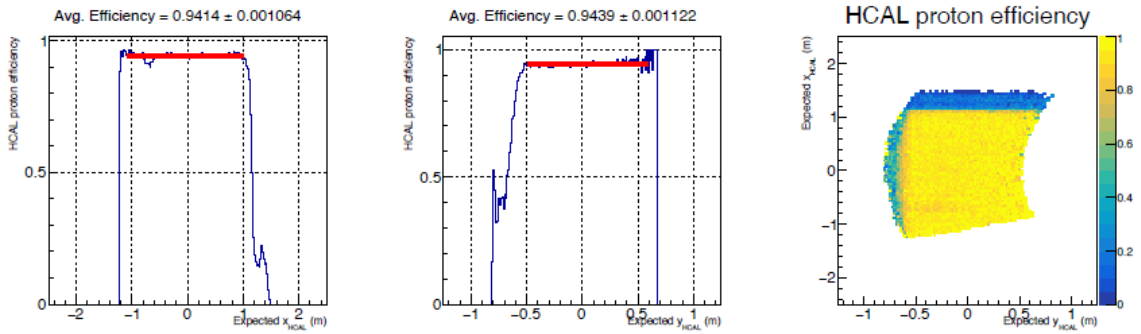

Figure 4.19: HCal averaged proton detection efficiency along X (left), Y (middle), and a 2D detection efficiency map (right), from SBS-8 zero SBS field hydrogen data. Plot credit: A. Puckett.

effects into the simulation have been proposed and they are currently under investigation (see reference [60]). In this dissertation, details about those methodologies will not be discussed. Since the other kinematic points are less affected, these effects will not be taken into consideration for the preliminary extractions presented later on.

For the high Q^2 points, this method of PDE extraction is not possible due to the significant amount of inelastic contamination. However, a variation of "relative detection efficiency" across the HCal active area could be studied as part of future analysis. A method that involves careful inelastic background unfolding of both the numerator and denominator events will have to be adapted for a PDE measurement at the high Q^2 point using the hydrogen data. One such method is the estimation of total elastic yield by only using a W^2 plot with background subtracted. The total elastic protons that were actually detected by HCal could be obtained by the use of a Δx plot, with a similar technique used for the background subtraction. The ratio of the latter elastic yield to the former can be interpreted as the proton detection efficiency of HCal. An example of such an analysis is presented in reference [60]. Only an active-area-averaged PDE could be obtained from this method.

4.3.2 Neutron Detection Efficiency (NDE) Analysis

This section provides an exploratory NDE analysis. Due to the statistical, acceptance, and event-selection limitations, the current status of this analysis cannot provide an accurate measurement of the HCal neutron detection efficiency across the full active area of the HCal detector. However, it could serve as a proof of principle for this technique, and a similar analysis could be extended to other kinematic points

beyond the single kinematic point (SBS-9) of the E12-09-019 experiment for which this analysis is performed. The principles outlined in the experiment proposal [34] are followed in this analysis. Most of the focus of this analysis is on the π^+ event selection in the BigBite spectrometer, from the reaction channel p(γ,π^+)n. This provides us with a *tagged* neutron source that could be used for NDE calibration.

No dedicated runs were taken for this analysis during the actual production running of the experiment. Data taken with a hydrogen target is used, but without the use of a copper radiator, and hence this analysis relies on the Bremsstrahlung photons produced within the target itself. In addition, the BigBite magnet polarity is set for upward bending for the electrons (e^-), which causes the π^+ from the p(γ,π^+)n channel to bend downwards in the magnetic field. This results in the loss of a large number of events of interest, and only a small corner of the HCal ($\approx 15\%$) is within the acceptance that coincides with BigBite.

"End-Point" Method for Event Selection

As mentioned, the most important aspect of this analysis is the careful selection of the exclusive single pion photoproduction p(γ,π^+)n reaction channel while excluding multi-body pion final state channels, using only the BigBite spectrometer. This can be achieved by calculating the maximum possible π^+ momentum for the two-pion production, three-body p(γ,π^+)π^0n reaction (for a given beam energy and polar scattering angle) and selecting events with the BigBite track's momentum larger than that. This technique is referred to as the end-point method within this context.

The formalism of end-point threshold calculations is explained in detail in Appendix B. Once the maximum possible π^+ momentum/energy for two-pion production for a given beam energy and polar scattering angle is known, only if the BigBite track has a momentum 1.5% larger will that event be used for the analysis. In addition, other stringent track-quality cuts are also applied, which are discussed below. The 1.5% margin between the lowest π^+ momentum of the selected events and the highest momentum from the two-pion channel allows sufficient safety bounds to account for the momentum resolution of the BigBite spectrometer. The limit on minimum allowed π^+ momentum, in turn, sets a limit for the minimum allowed photon energy that could be used and the part of the bremsstrahlung end-point region that could be used for this analysis. Table 4.1 summarizes all the relevant threshold calculations carried out using the central spectrometer angles for the kinematic settings of the E12-09-019 experiment.

For example, if the SBS-9 kinematic point highlighted in blue is considered, given

Kin num	Q^2 (GeV/c)^2	E_{beam} (GeV)	θ_e (deg)	HCal angle (deg)	neutron angle $p(\gamma,\pi^+)n$ (deg)	E_π^{max} (γ,π) (GeV)	E_π^{max} $(\gamma,2\pi)$ (GeV)	E_π^{limit} (γ,π) (GeV)	% diff.	E_γ^{min} (GeV)
SBS 4	3.0	3.7393	36.0	31.9	31.5	2.120	2.037	2.068	2.5	3.581
SBS 8	4.5	5.9826	26.5	29.4	30.1	3.579	3.492	3.544	0.9	5.887
SBS 9	4.5	4.0268	49.0	22.0	22.6	1.623	1.564	1.588	2.2	3.816
SBS 14	7.5	5.9828	46.5	17.0	17.7	1.999	1.950	1.979	1.0	5.812
SBS 7	10	7.9308	40.0	16.1	16.5	2.659	2.610	2.649	0.5	7.846
SBS 11	13.6	9.889	42	13.3	12.8	2.662	2.623	2.662	0	9.891

Table 4.1: End-point threshold calculations for the E12-09-019 experiment's kinematic points. $E_\pi^{max}(\gamma,\pi)$, the end-point pion energy for single-pion production; $E_\pi^{max}(\gamma,2\pi)$, the end-point pion energy for two-pion production; $E_\pi^{limit}(\gamma,\pi)$, the minimum π energy to be used for this analysis (to exclude $E_\pi^{max}(\gamma,2\pi)$ by 1.5%); % diff., the percentage difference between $E_\pi^{limit}(\gamma,\pi)$ and $E_\pi^{max}(\gamma,\pi)$. This is the width of the π^+ energy range used for selecting single-pion production events cleanly. E_γ^{min}, minimum photon energy needed for producing a single pion with energy $E_\pi(\gamma,\pi)$ above $E_\pi^{limit}(\gamma,\pi)$.

the end-point photon energy, the maximum π^+ energy corresponding to single-pion production is 1.623 GeV. And, the two-pion reaction cannot produce pions above 1.564 GeV. With the discussed safety margin included, only pions within the energy range of 1.588 GeV and 1.623 GeV are considered to be coming from the single-pion reaction channel. However, due to the large acceptance of the spectrometers, these thresholds are calculated event-by-event to accommodate the variations in the polar scattering angle within the BigBite spectrometer acceptance. For the analysis presented in this dissertation, the SBS-9 kinematic point is used. The fact that the percentage difference between $E_\pi^{limit}(\gamma,\pi)$ and $E_\pi^{max}(\gamma,\pi)$ is reasonable at 2.2%, and the availability of a large amount of hydrogen data, were the main reasons for using this kinematic setting for the analysis presented. A separate optics model was used for the reconstruction of down-bending π^+ tracks in the BigBite magnet.

Event Selection Cuts Using BigBite

The pions from the single-pion photoproduction channel with kinematics that predict the corresponding neutron to strike within the acceptance of HCal form the "denominator" of the NDE calculation. No information from the HCal detector is used, and only the knowledge of its geometry and positioning within the experimental hall is applied. The BigBite cuts used for the event selection for the denominator events are listed below for this analysis.

- Number of GEM hits on a track > 3.

- The vertex z position: -0.045 < z < 0.065, intentionally made tighter compared to the standard z-vertex cut to control background.
- Pre-shower energy cut: 0 < pre-shower energy < 0.20 GeV, note how this cut is opposite to how it is used in the regular analysis and the range is set to select pions instead of rejecting them.
- Track χ^2/ndf < 15.
- Optics validity cut: only accept BigBite tracks coming through the fiducial region of the BigBite magnet with reliable optics reconstruction.
- Using the momentum counterparts of the above energy threshold definitions: $P_{\pi}^{limit}(\gamma,\pi) - 0.1$ < BigBite track momentum < $P_{\pi}^{max}(\gamma,\pi)$ - 1.5%, 1.5% subtracted from the maximum limit to account for the BigBite momentum resolution. A constant value of 0.1 GeV/c is subtracted from the calculated $P_{\pi}^{limit}(\gamma,\pi)$ value to provide some leeway and to gain some useful statistics in this exploratory analysis.
- HCal acceptance cut: accept only the events with the predicted neutron hit position to be within HCal.

See Figure 4.20 for the distribution of reconstructed vertex z positions of the events passing all the above cuts. As opposed to Figure 4.4 of electron scattering vertex reconstruction, notice how the number of scattering events increases towards the downstream direction (+Z) of the target. This can be attributed to the pions scattered off from photons generated upstream after interacting with the target material. Figure 4.21 depicts the effects of polar scattering angle-dependent end-point momentum threshold cuts. Both the upper and lower momentum threshold cuts described above are applied to the data presented here. With the increasing polar scattering angle, the acceptable momentum values decrease, but the range broadens.

The reconstructed photon energy calculated using Eq. B.22 is shown in Figure 4.22. Notice how the maximum photon energy is sharply cut off near the bremsstrahlung end-point close to the beam energy of 4.0268 GeV. The minimum photon energy is restricted by the end-point momentum cuts.

The predicted hit position of the neutron on the face of HCal can be calculated by following a similar technique outlined in Section A.2. With the knowledge of the π^+, the direction vector of the neutron can be calculated using the p(γ,π^+)n reaction kinematics. Figure 4.23 shows a plot of predicted neutron 2D hit positions on the

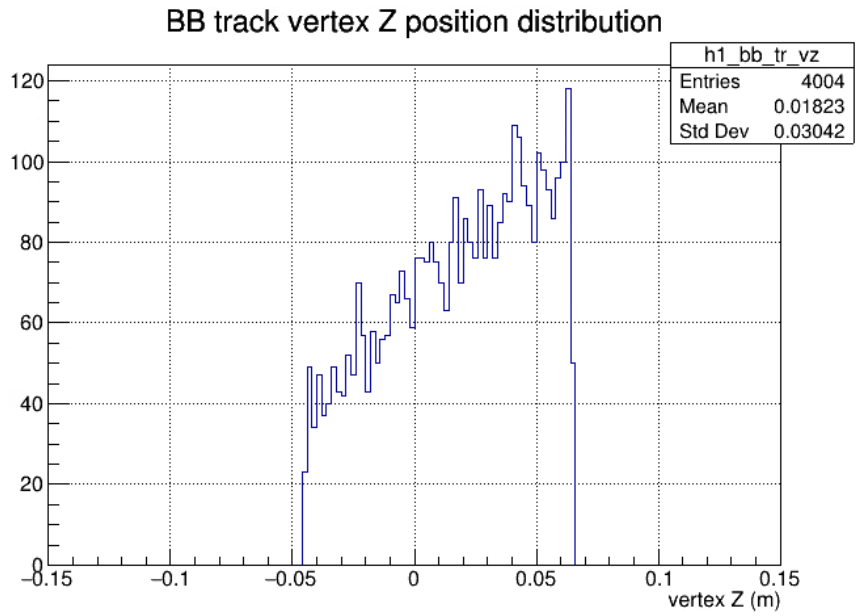

Figure 4.20: Vertex Z position with a cut at -4.5 cm and 6.5 cm.

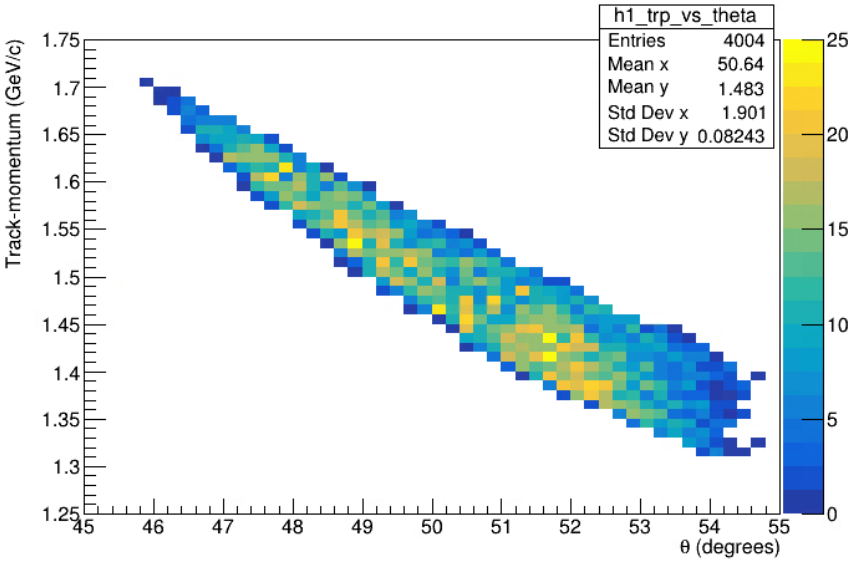

Figure 4.21: BigBite track momentum vs. the polar scattering angle θ.

face of the HCal for the data being considered. As mentioned earlier, the sub-optimal acceptance of this reaction channel is clearly seen, and only a corner of the detector is predicted to be illuminated by the neutrons that correspond to the pions detected by the BigBite spectrometer. Safety margins of 2.0 standard deviations along the X and Y directions, by considering the Δx and Δy plots along those directions similar to the regular physics analysis, are implemented for event selection.

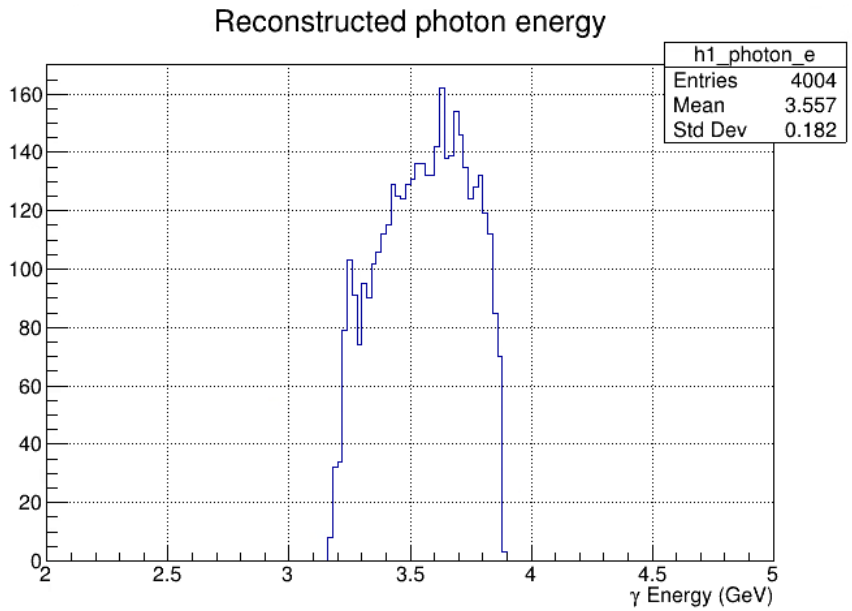

Figure 4.22: Reconstructed photon energy.

Δx vs. Δy Plot

Once the event selection stage is completed, a Δx vs. Δy plot can be generated to investigate the correlation of predicted and detected positions on HCal. The highest energy in-time algorithm (described in Section 4.2.5) was used for the HCal primary cluster selection in this analysis. See Figure 4.24 for a Δx vs. Δy plot of all the events that passed the above event selection criteria.

A very clear "neutron spot" centered near (0,0) can be seen, providing evidence for detection of neutrons in HCal from the p(γ,π^+)n channel. However, the denominator event selection criteria are still not robust enough for selecting a clean enough event sample for an NDE extraction. The momentum distributions of multi-pion photoproduction channels should be studied with the help of a simulation toolkit to decide upon better momentum cut thresholds to separate the single-pion channel from multi-pion background. It should be noted that the limited momentum resolution of the BigBite spectrometer could be a potential problem when applying any tight momentum cuts with relative differences less than 1.5%. In addition, the useful acceptance of the HCal that is being used in production running does not have much overlap with the HCal acceptance covered in this technique. This makes it difficult to obtain a proper acceptance-averaged NDE value for HCal. Nevertheless, a crude attempt is made as follows to obtain an exploratory NDE value from this method:

- Take the number of events passing through all the event selection criteria de-

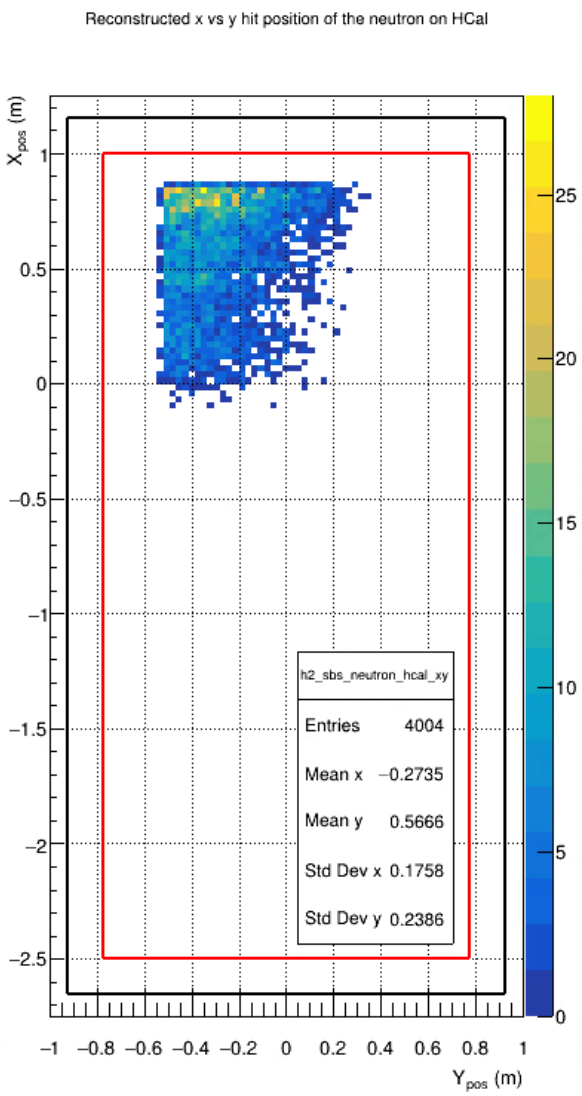

Figure 4.23: The X versus Y predicted hit positions of the neutrons on HCal. The outer black rectangle represents the physical perimeter of HCal. The inner red rectangle represents a reduced active area with one layer of calorimeter blocks removed from all four edges. This is intended to discard any events that could potentially lose a portion of the shower from the outer edges of the detector. The gap between the red rectangle and the events is due to safety margins included.

scribed above as the denominator.

- Apply Gaussian fits to the Δx and Δy distributions of the neutron peak around their peaks to obtain the mean and standard deviation in the respective distributions.

- Count the number of events within four standard deviations from the mean on

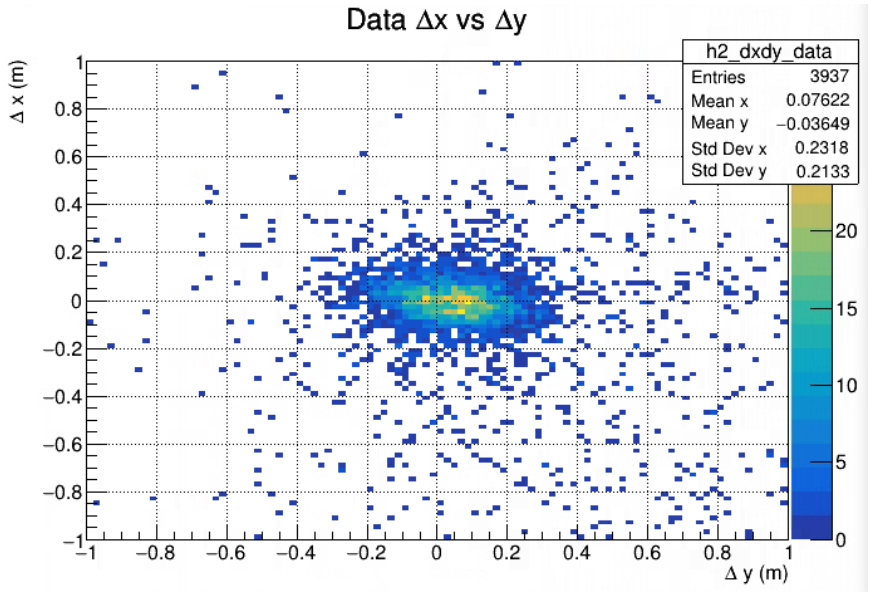

Figure 4.24: A plot of Δx vs. Δy. Detected X and Y positions come from the highest energy in-time algorithm.

either side of the mean in **both** Δx and Δy distributions.

- The ratio between the previous step and the first step is taken as the NDE.

An NDE value of 73.5% is obtained from the method described above. The central nucleon momentum for the SBS-9 kinematic point that this analysis was performed is 3.21 GeV/c. Indeed, this efficiency value depends on the choice of the number of standard deviations used in the above step three. The four standard deviations were chosen to allow for any possible non-Gaussian tails. Still, the value obtained is less than about twenty percentile points from what we get from the simulation for the NDE at this kinematic setting. We will attribute this difference mainly to imperfect denominator event selection in BigBite, as already mentioned, rather than an actual NDE difference between the real HCal and simulation.

4.3.3 Simulated HCal Neutron and Proton Detection Efficiency

The HCal neutron and proton detection efficiency within the G4SBS simulation package is extracted using the following method. Neutrons and protons within the momentum range of 1-9 GeV/c are thrown flat on the active area of HCal so that at least 1000 events per calorimeter block are reached. A spectrum is created that shows the energy deposited within HCal with respect to the nucleon momentum. Figure 4.25

shows the spectrum of HCal energy deposited as a function of nucleon momentum. For each momentum bin, a fit is performed to extract the mean of the energy distribution for each momentum bin. For each momentum bin, the ratio of the number of events with energy larger than a chosen fraction of the mean energy to the total number of events within the momentum bin is interpreted as the detection efficiency for the corresponding nucleon within that momentum bin.

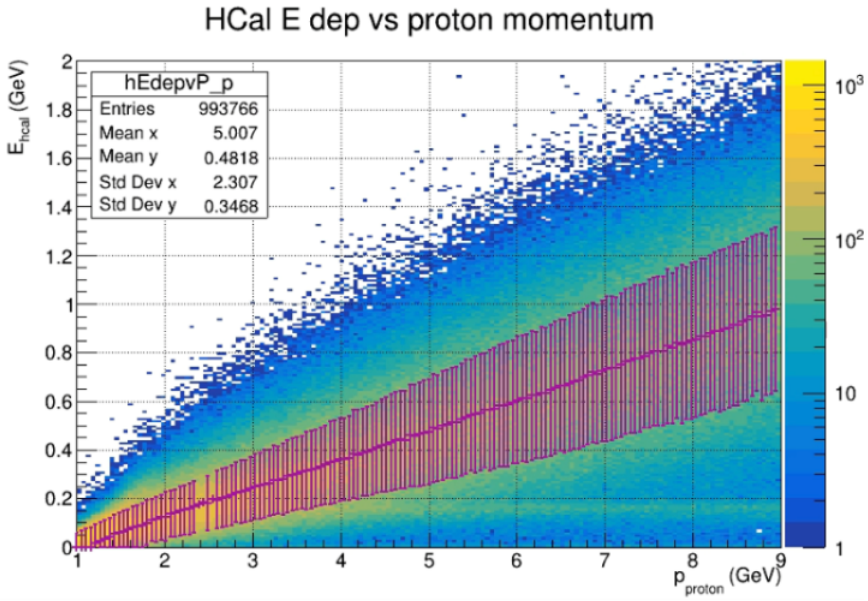

Figure 4.25: HCal energy deposition versus the proton momentum in G4SBS simulation. Courtesy of S. Seeds.

Figure 4.26 shows the HCal neutron and proton detection efficiency in G4SBS simulation as a function of nucleon momentum within the range of 1-8 GeV/c. The proton detection efficiency is indicated by red dots and the neutrons by blue dots. Polynomial fits are performed for both data sets in their respective colors. The fraction/energy threshold used for the estimation of simulated HCal detection efficiency is rather arbitrary. The energy threshold used in this analysis to calculate the detection efficiency is $0.38E_{mean}$ (labeled E_{peak} in the plot). This factor has been chosen to make the proton detection efficiency from the simulation match the proton detection efficiency value coming from the real data analysis from the SBS-4 kinematic point, shown by a black circle around 2.4 GeV/c nucleon momentum. By comparing the relative positioning of the experimental proton detection efficiency results of the other kinematic points (Ex: see SBS-8 proton detection efficiency indicated by the black square), the performance of the G4SBS simulation's proton detection can be evaluated. Due to the reasons mentioned in Section 4.3.1, the experimental

proton detection efficiency is markedly lower than the simulation's proton detection efficiency for the SBS-9 kinematic point. Modifications to the simulation package to reflect these effects in the actual HCal detector during the experiment run period are under development. All three experimental PDE values were evaluated using the first technique ("proton spot cut" on Δx vs. Δy plot method) described in Section 4.3.1.

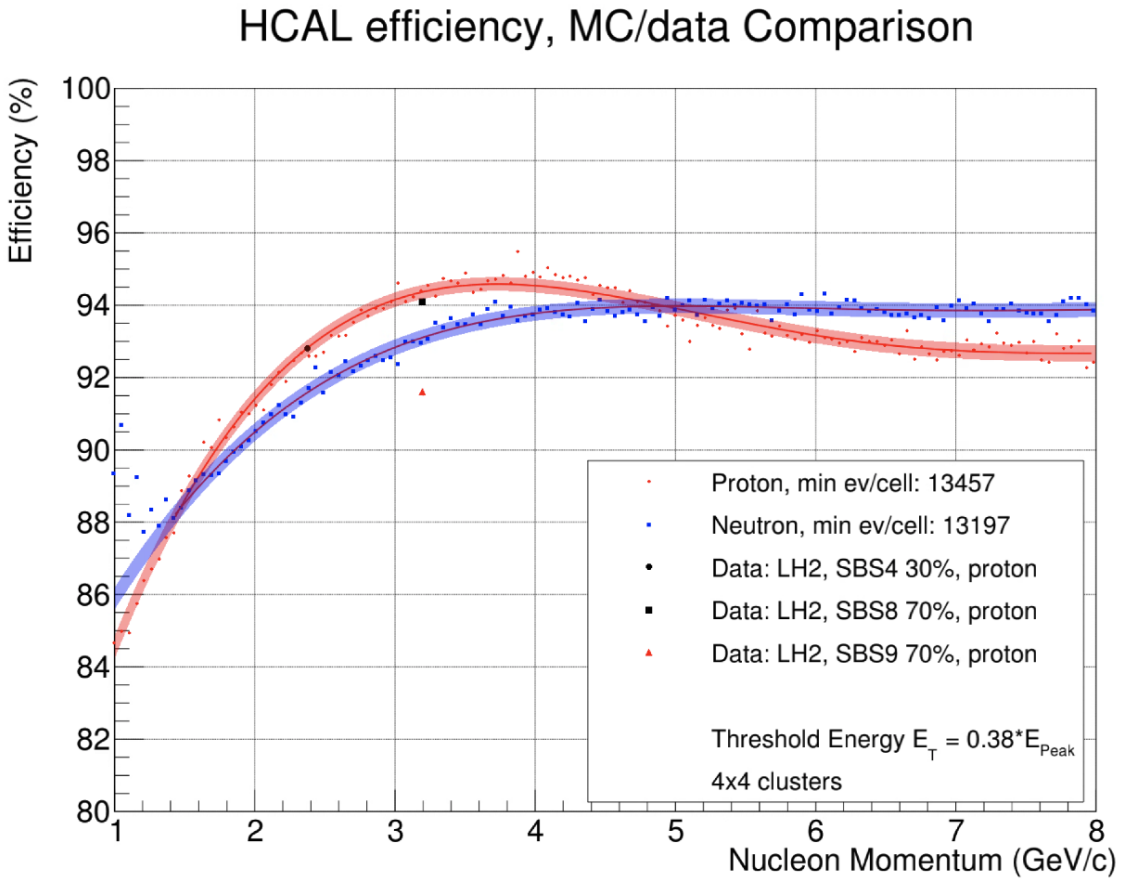

Figure 4.26: HCal nucleon detection efficiency of G4SBS as a function of nucleon momentum. Proton detection efficiency from liquid hydrogen data analysis for SBS-4, SBS-8, and SBS-9 kinematic points are overlaid. Courtesy of S. Seeds.

4.4 Ratio R Extraction

Once the Δx histogram from the experimental data is generated (e.g., see Fig. 4.10), the first step for extracting G_M^n is to generate a similar plot from the simulated data. As mentioned earlier, the quasi-elastic D(e,e′n)p and D(e,e′p)n events generated from SIMC and processed through the G4SBS detector simulation are used for this purpose.

The nuclear and radiative effects are included when generating these simulated data. The inelastic background is added to the simulation data Δx histogram by means of a polynomial function or using the inelastic generator of the G4SBS package. The built-in proton and neutron form factor parameterizations in the SIMC event generator provide an initial n(e,e$'$) and p(e,e$'$) inclusive elastic scattering differential cross section ratio R_{sim},

$$R_{sim} = \frac{\left(\frac{d\sigma}{d\Omega}\right)_{n(e,e'),sim}}{\left(\frac{d\sigma}{d\Omega}\right)_{p(e,e'),sim}} \tag{4.3}$$

If $N_{D(e,e'n)p}$ and $N_{D(e,e'p)n}$ are the quasi-elastic neutron and proton yields *detected* by HCal within the simulation, ε_n^{sim} and ε_p^{sim} are the neutron and proton detection efficiencies of the HCal detector within the G4SBS simulation machinery, PF_n^{sim} and PF_p^{sim} are the phase-space factors for the neutron and proton acceptance, respectively, f_{nuclr}^{sim} is the simulation nuclear correction factor, and f_{rad}^{sim} is the simulation radiative correction factor, we can write R_{sim} as follows:

$$R_{sim} = \frac{N_{D(e,e'n)p,sim} \times \frac{1}{\varepsilon_n^{sim}} \times PF_n^{sim}}{N_{D(e,e'p)n,sim} \times \frac{1}{\varepsilon_p^{sim}} \times PF_p^{sim}} \times f_{nuclr}^{sim} \times f_{rad}^{sim} \tag{4.4}$$

By implementing fiducial cuts, we ensure that neutrons and protons have the same phase-space acceptance, thus we have $PF_n^{sim} = PF_p^{sim}$.

We calculate R_{sim} using the OPE approximation for both neutron and proton differential cross sections and using the nucleon form factor parameterizations within the simulation machinery for cross section modeling. For the proton form factors G_E^p, G_M^p, and the neutron magnetic form factor G_M^n, the Kelly 2004 parameterization [61] is used. For the neutron electric form factor G_E^n, a parameterization derived from a previous JLab Hall-A G_E^n experiment is used [59].

Next, we *scale* these individually simulated D(e,e$'$n)p, D(e,e$'$p)n, and inelastic background peaks to match the real data via a χ^2 minimization technique between the data Δx histogram and the simulation composite Δx histogram of D(e,e$'$n)p, D(e,e$'$p)n, and the inelastic background (polynomial function or background signal obtained using the inelastic generator of G4SBS). We can then write the *detected* neutron and proton elastic yields from the experiment as follows:

$$N_{D(e,e'n)p,real} = f_n N_{D(e,e'n)p,sim} \tag{4.5}$$

$$N_{D(e,e'p)n,real} = f_p N_{D(e,e'p)n,sim} \tag{4.6}$$

Here, f_n and f_p are the χ^2-minimizing scale factors of the D(e,e′n)p and D(e,e′p)n peaks that best match the data and the simulation composite Δx histograms. Now, the n(e,e′) and p(e,e′) differential cross section ratio R_{real} needed for the G_M^n extraction can be written as:

$$R_{real} = \frac{N_{D(e,e'n)p,real} \times \frac{1}{\varepsilon_n^{real}} \times PF_n^{real}}{N_{D(e,e'p)n,real} \times \frac{1}{\varepsilon_p^{real}} \times PF_p^{real}} \times f_{nuclr}^{real} \times f_{rad}^{real} \tag{4.7}$$

All the terms follow the same naming convention as in Eq. 4.4. Similar to the simulation data, the fiducial cuts implemented in the real data analysis yield $PF_n^{real} = PF_p^{real}$. Additionally, we assume that the SIMC event generator accurately recreates the nuclear and radiative effects present within the experiment data, leading to the further simplifications $f_{nuclr}^{sim} = f_{nuclr}^{real}$ and $f_{rad}^{sim} = f_{rad}^{real}$.

Using equations 4.4, 4.5, 4.6, 4.7, and the aforementioned approximations, we can write R_{real} as:

$$R_{real} = \left(\frac{f_n}{f_p}\right) \times R_{sim} \times \left(\frac{\varepsilon_n^{sim}}{\varepsilon_n^{real}}\right) \times \left(\frac{\varepsilon_p^{real}}{\varepsilon_p^{sim}}\right) \tag{4.8}$$

Hence, the scale factor ratio $\left(\frac{f_n}{f_p}\right)$ will be the effective observable extracted from the experimental data and carried forward for the G_M^n extraction. Furthermore, if the assumption is made that the simulated detection efficiencies perfectly agree with the real HCal detection efficiencies, the following simplification can be made:

$$R_{real} = \left(\frac{f_n}{f_p}\right) \times R_{sim} \times \cancelto{1}{\left(\frac{\varepsilon_n^{sim}}{\varepsilon_n^{real}}\right)} \times \cancelto{1}{\left(\frac{\varepsilon_p^{real}}{\varepsilon_p^{sim}}\right)} = \left(\frac{f_n}{f_p}\right) R_{sim} \tag{4.9}$$

For the purpose of extracting the pre-preliminary results presented in this thesis, we will use Eq. 4.9.

Figure 4.27 shows a comparison between a data Δx histogram and a simulation Δx histogram with an inelastic background signal added by using a third-order polynomial function. The black circles represent the experimental data (error bars are small in comparison and hence not visible). The magenta histogram is the simulated D(e,e′p)n data, and the cyan histogram is the simulated D(e,e′n)p data. The green histogram at the bottom is the inelastic background signal produced using a third-

order polynomial. The red triangles represent the sum of the simulated D(e,e′p)n, D(e,e′n)p, and polynomial background histograms. The simulated histograms shown are post-scaling/fitting, and reasonable agreement with the experimental data can be visually observed.

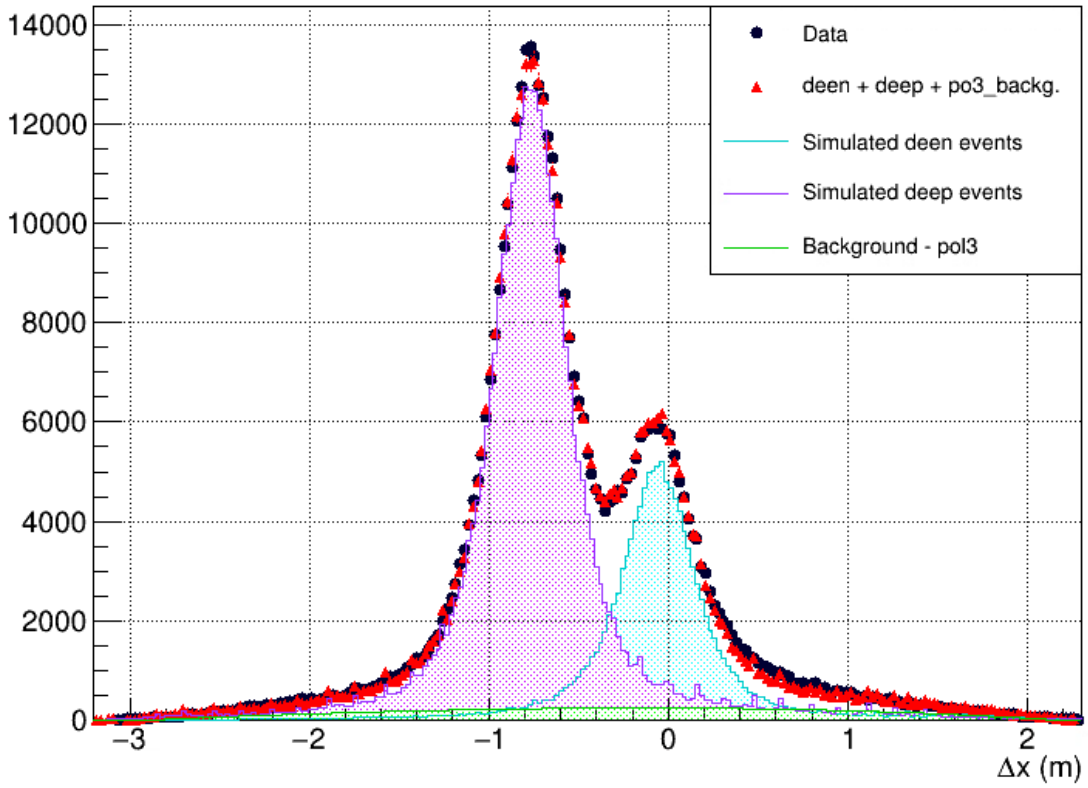

Figure 4.27: Comparison between experimental data and simulated data Δx histograms for SBS-4 ($Q^2 = 3.0$ GeV^2).

The χ^2 between the data Δx and composite simulation Δx histograms is defined as:

$$\chi^2 = \sum \frac{(D_i - S_i)^2}{S_i} \tag{4.10}$$

where D_i and S_i are the bin contents of the data and simulation histograms, respectively. A local minimizer, the MIGRAD algorithm, is used via the TMinuit[7] class of CERN ROOT for the χ^2 minimization process, with variable parameters being f_n, f_p, and the parameters of the polynomial function if a polynomial is used for the description of the shape of the inelastic data. If not, a single scale factor f_b is used if simulated inelastic data from the G4SBS inelastic generator is used.

[7]TMinuit class reference: https://root.cern.ch/doc/master/classTMinuit.html

Chapter 5

Results and Conclusions

The analysis and preliminary G_M^n extractions of the three kinematic points, SBS-4 ($Q^2 = 3.0$ GeV$^2/c^2$, 30% SBS field scale), SBS-7 ($Q^2 = 9.8$ GeV$^2/c^2$), and SBS-11 ($Q^2 = 13.5$ GeV$^2/c^2$), are presented in this chapter. For the SBS-4 kinematic point, only the data from the 30% SBS field scale setting is presented, and when the label SBS-4 is used in the following text, it always means data from the 30% SBS field scale setting.

5.1 G_M^n Extraction from Ratio R and Uncertainty Calculation

From the ratio R, the magnetic form factor G_M^n can be calculated as given by Eq. 1.26,

$$G_M^n = \sqrt{\left[R\left(\frac{1+\tau_n}{1+\tau_p}\right)\frac{\sigma_{R,p}}{\epsilon_p} - (G_E^n)^2\right]\frac{\epsilon_n}{\tau_n}}$$

We will use the Ye parameterization [2] for the proton cross section and G_E^n for the G_M^n extractions presented in this thesis. The Ye parameterization is the most modern electromagnetic form factor parameterization available at the time of this writing. For example, it incorporates the most up-to-date two-photon exchange corrections to the existing cross section world data.

For the purpose of uncertainty evaluation, we can simplify the above formula by making the assumption

$$\frac{1+\tau_n}{1+\tau_p} \approx 1 \tag{5.1}$$

yielding

$$G_M^n \approx \sqrt{\left[R\frac{\sigma_{R,p}}{\epsilon_p} - (G_E^n)^2\right]\frac{\epsilon_n}{\tau_n}} \tag{5.2}$$

The three variable parameters in this formula are R, $\sigma_{R,p}$, and G_E^n. For a function $f(x_1, x_2, x_3, ..., x_n)$ with independent variables $x_1, x_2, x_3, ..., x_n$, we can write down the uncertainty in f, δf, in terms of individual errors of $x_1, x_2, x_3, ..., x_n$ as,

$$(\delta f)^2 = \sum_{i=1}^{n}\left(\frac{\partial f}{\partial x_i}\delta x_i\right)^2 \tag{5.3}$$

Following that we can write,

$$(\delta G_M^n)^2 = \left(\frac{\partial G_M^n}{\partial \sigma_{R,p}}\delta\sigma_{R,p}\right)^2 + \left(\frac{\partial G_M^n}{\partial G_E^n}\delta G_E^n\right)^2 + \left(\frac{\partial G_M^n}{\partial R}\delta R\right)^2 \tag{5.4}$$

The proton reduced cross section term could be written as,

$$\frac{\partial G_M^n}{\partial \sigma_{R,p}}\delta\sigma_{R,p} = \frac{1}{2G_M^n}\frac{R}{\tau_n}\frac{\epsilon_n}{\epsilon_p}\delta\sigma_{R,p} \approx \frac{1}{2G_M^n}\frac{R}{\tau_n}\delta\sigma_{R,p} \tag{5.5}$$

The proton reduced cross section error $\delta\sigma_{R,p}$ is calculated by error propagation of G_E^p and G_M^p in Eq. 1.20. The individual errors of the two form factors given by the Ye error parameterization [2] are used, assuming that they are uncorrelated. However, this is not entirely accurate as described in Ye et al. [2], and smaller errors on the proton reduced cross section could potentially be obtained.

The neutron electric form factor term could be written as

$$\frac{\partial G_M^n}{\partial G_E^n}\delta G_E^n = \frac{-G_E^n}{G_M^n}\frac{\epsilon_n}{\tau_n}\delta G_E^n \tag{5.6}$$

The uncertainty due to the neutron electric form factor δG_E^n is directly taken as given by the G_E^n fit uncertainty parameterization in Ye et al. [2].

And the uncertainty term due to the ratio R could be written as

$$\frac{\partial G_M^n}{\partial R}\delta R = \frac{1}{2G_M^n}\frac{\sigma_{R,p}}{\tau_n}\frac{\epsilon_n}{\epsilon_p}\delta R \approx \frac{1}{2G_M^n}\frac{\sigma_{R,p}}{\tau_n}\delta R \tag{5.7}$$

Statistical uncertainty from the fitting technique used to extract R, along with various systematic effects, contribute to the total uncertainty in R. By propagating the uncertainties through Eq. 4.9, we obtain the statistical uncertainty of R. The er-

rors of the scale factors f_n and f_p are provided by ROOT's TMinuit minimization algorithm. ROOT provides these errors by calculating the covariance matrix at the minimum of the χ^2 minimization process. To estimate the systematic contribution to the uncertainty in R, we are focusing on a selected set of possible sources in this preliminary analysis, as described in the next section.

5.2 Systematic Uncertainty Estimation of Ratio R

5.2.1 Systematic Uncertainty Due to Inelastic Background Modeling

In high-Q^2 form factor extractions, we expect the inelastic background contamination to be a major source of systematic uncertainty. In order to estimate it, we employ three different background modeling techniques and study the variation of ratio R. The three background modeling techniques are as follows:

1. Polynomial background scaling technique: First, we fit the experimental Δx distribution using a sum of a polynomial and two Gaussians. The polynomial part will fit the background, and the two Gaussians fit the neutron and proton peaks. Then, while preserving the shape of the polynomial, a single scale factor (f_b) is used along with f_n and f_p during the χ^2 minimization process between the data and simulation histograms.

2. Polynomial background technique: In this technique, all parameters of the polynomial function are allowed to vary along with the neutron and proton peak scale factors. Hence, this technique provides a better fit when compared with the first one, though it still lacks a physics motivation for inelastic background modeling.

3. G4SBS inelastic generator: A Δx histogram is generated using the data from the inelastic generator of the G4SBS simulation package described in Section 4.1.3. Similar to the first method, a single scale factor f_b is used along with the neutron and proton scale factors to make the fit to the real data.

The ratio R is extracted using all three techniques, and the standard deviation of the three values is used as the systematic uncertainty of R due to the inelastic background modeling, $\delta R_{inel.backg}$. Figures 5.1, 5.2, and 5.3 show the results of these studies carried out at the kinematic points SBS-4, SBS-7, and SBS-11, respectively.

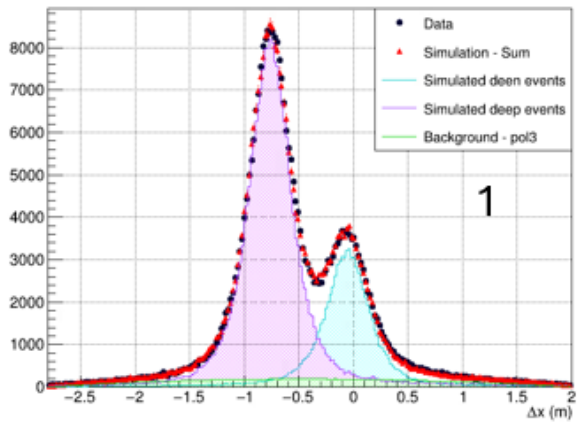

(a) Polynomial background scaling

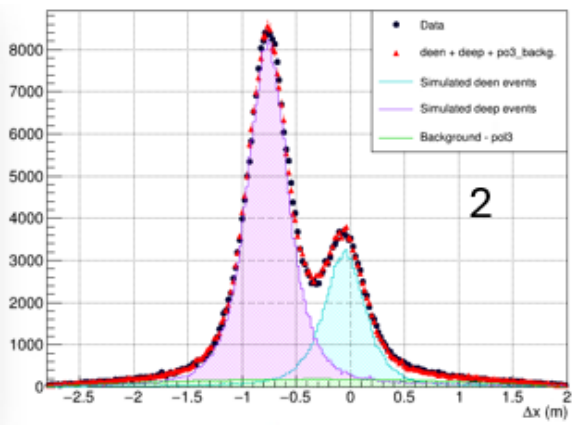

(b) Polynomial background

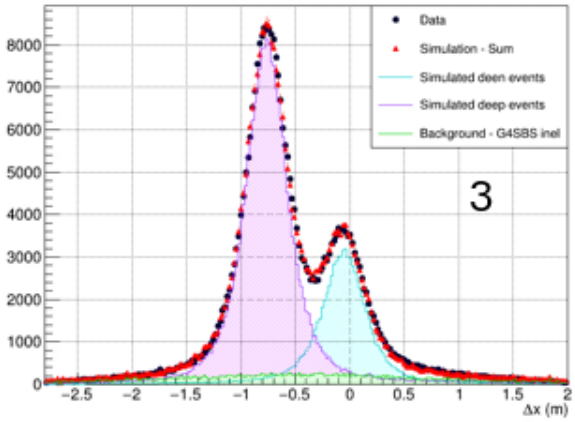

(c) G4SBS inelastic generator background

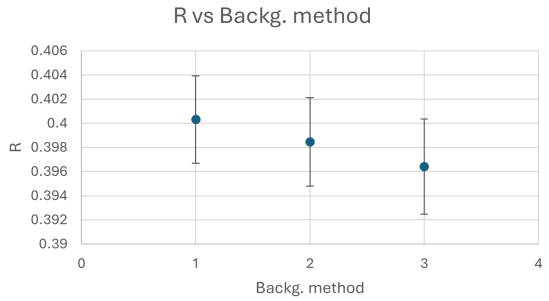

(d) SBS-4 R extraction with different background models. The X-axis numbers directly relate to the background model numbering defined in the text.

Figure 5.1: SBS-4 kinematic point inelastic background model studies

Sub-figures (a), (b), and (c) give the Δx plots for each kinematic point with the above three background modeling techniques employed in the order 1, 2, and 3, respectively. Sub-figure (d) provides a plot of R vs. background technique number for each kinematic point. Except for SBS-11, the ratio R extraction agrees within statistical error for all the background modeling techniques, whereas for SBS-11, the polynomial background scaling technique (1) is a clear outlier.

The $\delta R_{inel.backg}$ values for each of the three kinematic points and their percentages with respect to the ratio R are given below.

- SBS-4: $\delta R_{inel.backg} = 0.002$, $\delta R_{inel.backg}/R = 0.53\%$
- SBS-7: $\delta R_{inel.backg} = 0.005$, $\delta R_{inel.backg}/R = 1.31\%$
- SBS-11: $\delta R_{inel.backg} = 0.04$, $\delta R_{inel.backg}/R = 1.12\%$

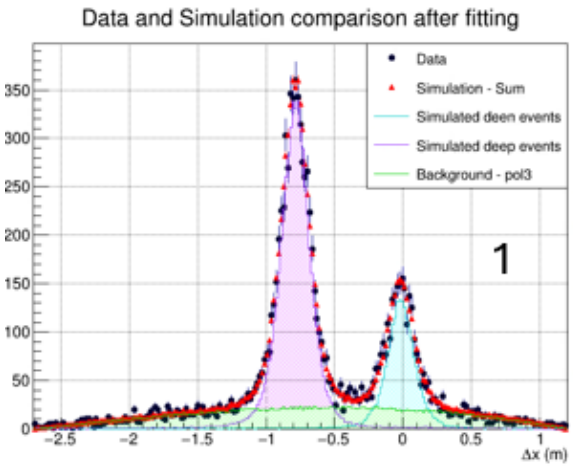

(a) Polynomial background scaling

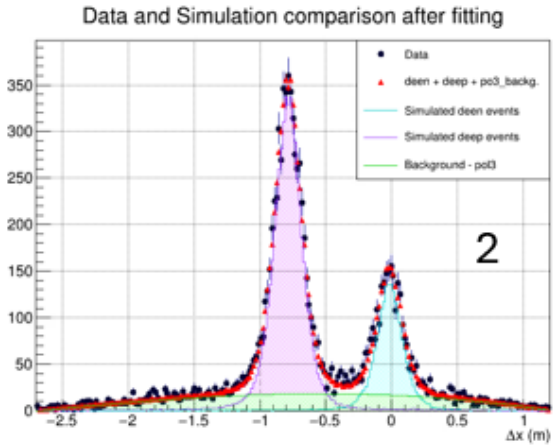

(b) Polynomial background

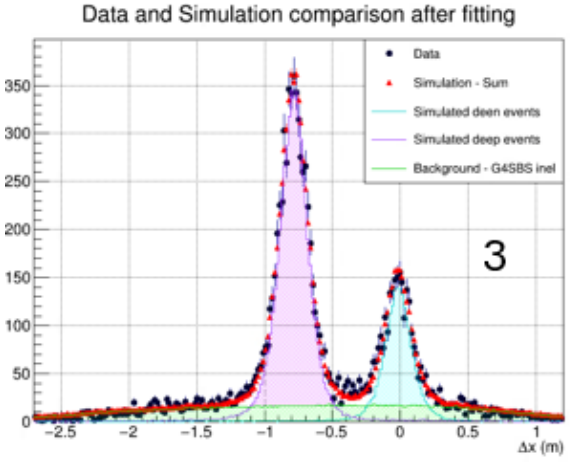

(c) G4SBS inelastic generator background

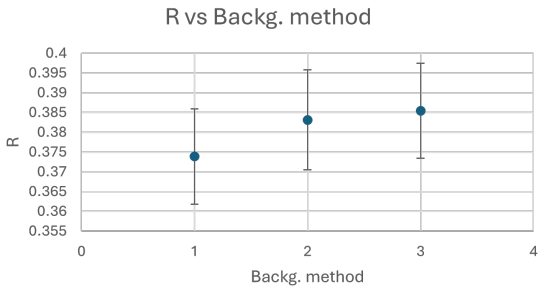

(d) SBS-7 R extraction with different background models. The X-axis numbers directly relate to the background model numbering defined in the text.

Figure 5.2: SBS-7 kinematic point inelastic background model studies

5.2.2 HCal NDE and PDE Agreement Between Reality and Simulation

Section 4.3 has provided a detailed description of the ongoing efforts to benchmark simulated HCal NDE and PDE against real data. The NDE analysis is not mature enough to perform a direct comparison with the simulated NDE. The PDE analysis, on the other hand, has shown reasonable agreement with the simulated PDE values as discussed. However, without a convincing and complete NDE analysis, the systematic uncertainty contribution on R due to the differences in HCal NDE and PDE between real life and the simulation cannot be estimated. The ratio R extractions and G_M^n extractions presented in this thesis assume perfect agreement in detection efficiencies between the real HCal and the HCal within the G4SBS simulation framework. It

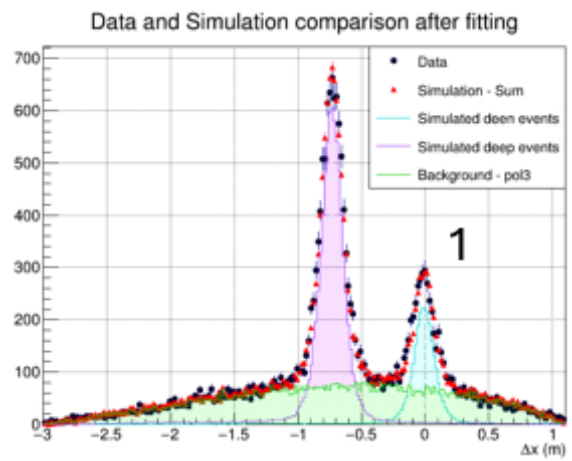

(a) Polynomial background scaling

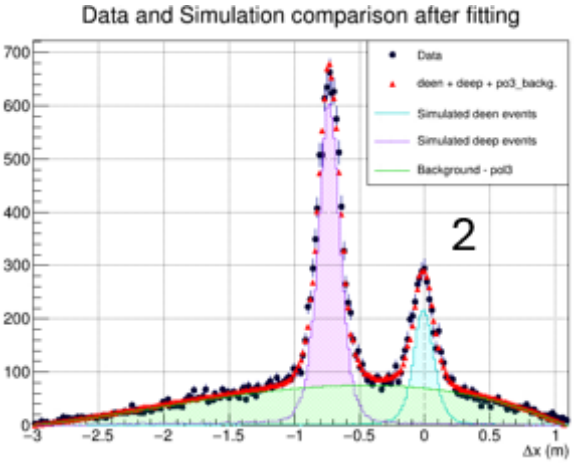

(b) Polynomial background

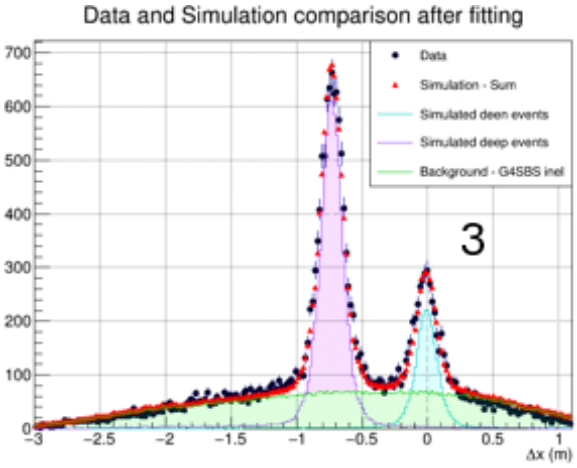

(c) G4SBS inelastic generator background

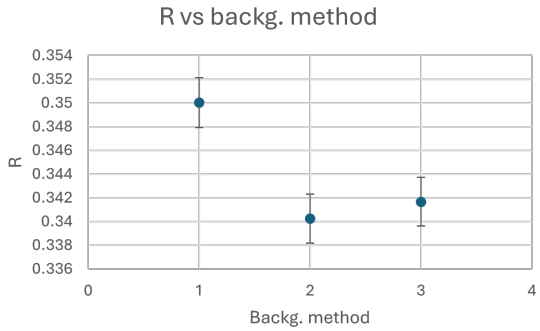

(d) SBS-11 R extraction with different background models. The X-axis numbers directly relate to the background model numbering defined in the text.

Figure 5.3: SBS-11 kinematic point inelastic background model studies

needs to be emphasized that this remains one of the important pieces of work that need to be completed for the successful completion of the E12-09-019 experiment's data analysis.

5.2.3 Systematic Uncertainty Due to Cut Thresholds/Regions

The ratio R could change based on the choice of event selection cuts' thresholds or regions used to accept/reject events. To evaluate the effect of these cuts, a set of studies was performed where only a given cut type is changed in both the experiment and simulated data while keeping all the other cut thresholds/regions the same, and the ratio R was extracted. This will allow us to study the variation of R as a function of the given cut type's threshold/regions and to identify stability regions to make

decisions about the exact cut values to use. The following set of cuts was subjected to this analysis:

1. The W^2 cut
2. The Δy cut
3. The fiducial cut safety margins in both x and y directions
4. HCal and BigBite shower ADC time coincidence cut

The other cuts/analysis constraints, or parameters that could introduce additional systematic uncertainties to the ratio R include, but not limited to:

- BigBite pre-shower energy cut
- Reconstructed vertex-z position cut
- HCal cluster energy threshold - this cut not used in this analysis presented in this thesis
- The stability of the ratio R as a function of BigBite electron arm active area - also helps to study the detection efficiency uniformity of HCal

In principle, the systematic uncertainty due to all the electron arm variables and quantities calculated thereof should cancel out in the ratio. However, this should be verified and stability regions for the ratio extraction should be identified for a robust extraction.

Collectively, the W^2 and Δy cuts represent what we refer to as *elastic cuts*. The W^2 cut ensures that the scattered electron kinematics correlate to elastic scattering, and the Δy cut ensures the correlation between the detected nucleon's scattering angle and the angle of the reconstructed $\vec{q}$ vector. As expected, these two variables are correlated, and this correlation should be taken into account when systematic studies are carried out. Figure 5.4 shows 2D Δy vs W^2 plots for all the three kinematic points being considered. The intersection point of the red-dashed lines that go through the 0.88 GeV^2 point on the X-axis and 0.0 m on the Y-axis represents the center of elastic event concentration.

For SBS-4 ($Q^2 = 3.0\ GeV^2$), a very clear concentration of elastic events with minimal inelastic contamination can be seen. However, for SBS-7 ($Q^2 = 9.8\ GeV^2$) and SBS-11 ($Q^2 = 13.5\ GeV^2$), which are the two highest Q^2 points of the experiment, the inelastic contamination is overwhelming and only a small peak around the

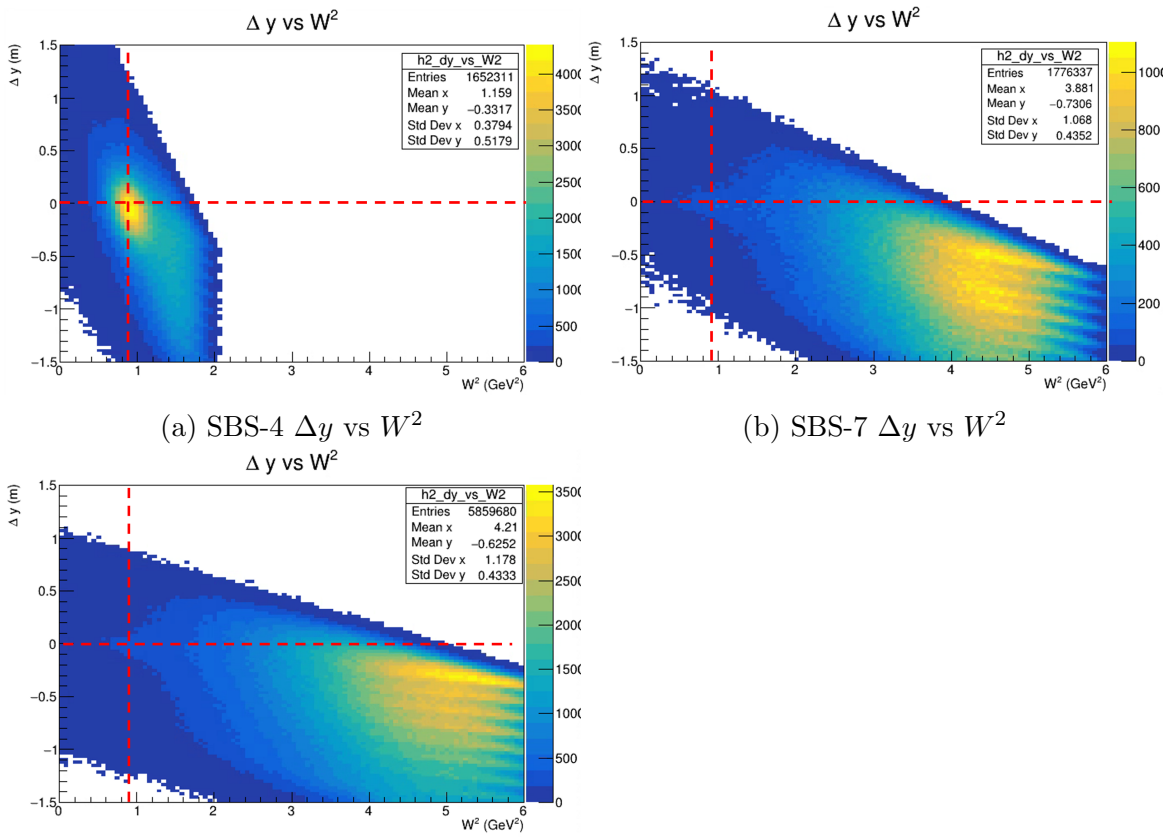

(a) SBS-4 Δy vs W^2

(b) SBS-7 Δy vs W^2

(c) SBS-11 Δy vs W^2

Figure 5.4: Δy vs W^2 distributions

intersection point of the two red-dashed lines is visible. As a result, for final ratio R extractions, very tight cuts around W^2 and Δy distributions are used. But for studies of systematic variation of R with the cut thresholds, when one variable is considered, the constraints on the other are kept sufficiently loose. Apart from the W^2 and Δy cuts, any possible correlations between the other variables are not taken into account in this study, and they are assumed to be inherently uncorrelated.

W^2 Cut Systematic Study

Two types of W^2 cut variation studies were performed in this analysis. The first method includes a scan across the elastic peak with slices of W^2 regions chosen at each step for both experimental data and simulated data, and performing the fitting technique described in Section 4.4 to extract the ratio R. This study is used to identify the *stability region* to set the W^2 cut region for final extractions. In the second method, the W^2 cut is defined as equidistant upper and lower bounds from the nucleon mass squared at 0.88 GeV^2. The change in statistics between consecutive regions that

largely overlap with each other is small in this technique, and the standard deviation of the ratio extractions from this method is used to calculate the systematic uncertainty in R extraction due to the choice of W^2 cut region. Δy cuts of -1.0 $< \Delta y <$ 1.0 for SBS-4, and -0.5 $< \Delta y <$ 0.5 for for SBS-7 and SBS-11 were used in this systematic study.

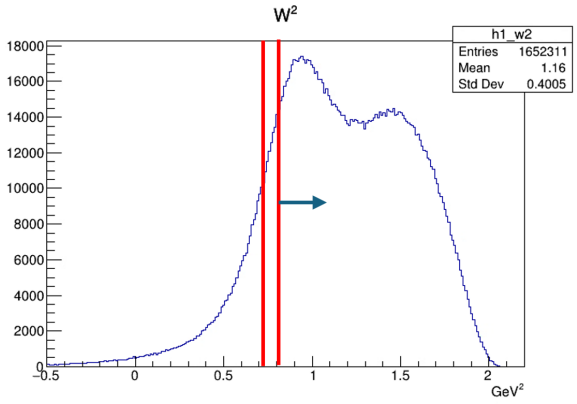

(a) W^2 plot sliced scan

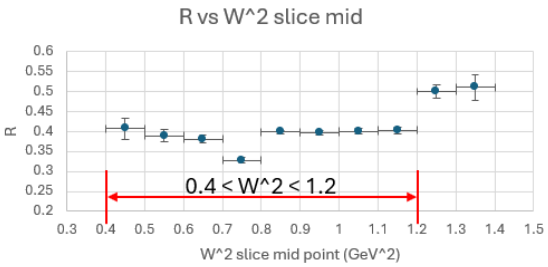

(b) R vs W^2 slice midpoint value

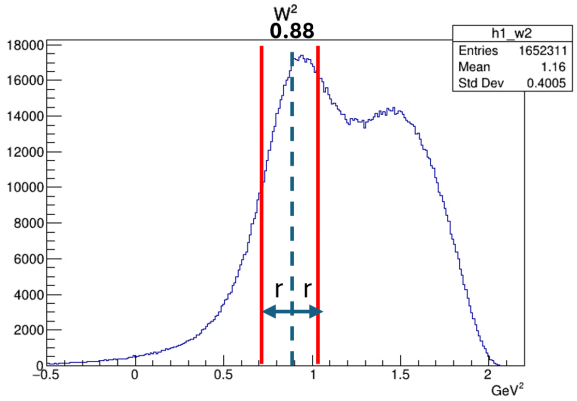

(c) W^2 cut centered around 0.88 GeV^2

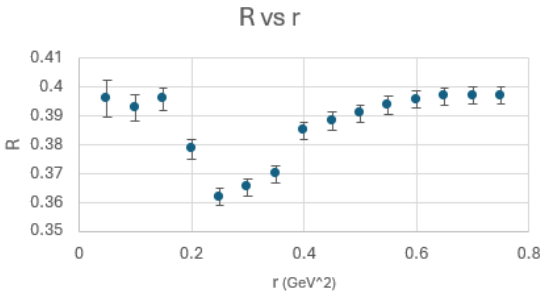

(d) R vs W^2 cut r

Figure 5.5: SBS-4 W^2 cut systematic studies

Figures 5.5, 5.6, and 5.7 show the results of the W^2 cut systematic studies performed for the SBS-4, SBS-7, and SBS-11 kinematic points, respectively. The subfigures (a) and (b) relate to the W^2 sliced range scan method. The graphics in Figure (a) show how the W^2 slices are selected for each separate ratio R extraction, and Figure (b) provides the results of the R extraction as a function of the midpoint of the W^2 slice being analyzed. The horizontal error bars represent the width of the W^2 slice, and the vertical error bars represent purely the statistical error. The range of W^2 chosen for the final ratio R extractions is indicated by the red horizontal double-sided arrow in Figure (b) of each kinematic point. Figures (c) and (d) relate to the

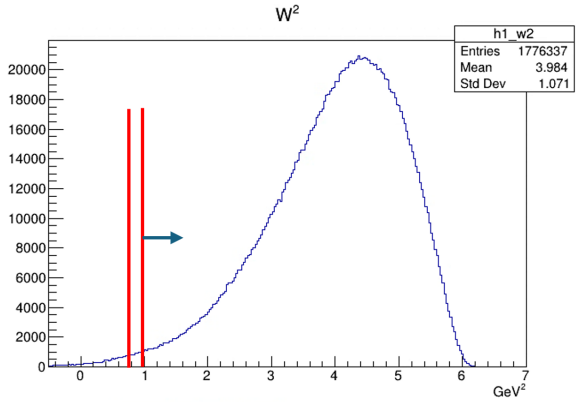

(a) W^2 plot sliced scan

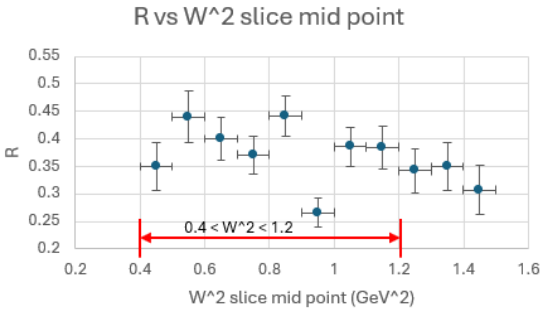

(b) R vs W^2 slice midpoint value

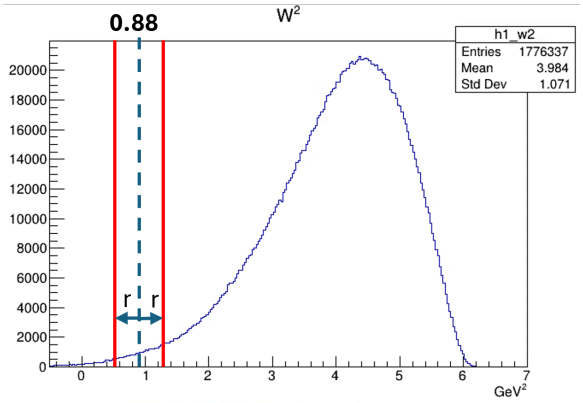

(c) W^2 cut centered around 0.88 GeV^2

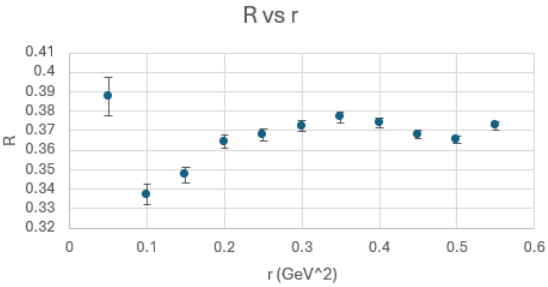

(d) R vs W^2 cut r

Figure 5.6: SBS-7 W^2 cut systematic studies

method of increasing the W^2 range on either side of the nucleon mass squared at 0.88 GeV^2 by an amount r. Figure (c) illustrates how the W^2 region is chosen in this method, and Figure (d) provides the results of the R extraction as a function of r. Again, the vertical error bars are purely the statistical error.

The systematic error of ratio R due to the choice of W^2 cut $\delta R_{W^2 cut}$ for each kinematic point, obtained by taking the standard deviation of the data points in sub-figure (d) of Figures 5.5, 5.6, and 5.7, is:

- SBS-4: $\delta R_{W^2 cut} = 0.012$, $\delta R_{W^2 cut}/R = 3.13\%$
- SBS-7: $\delta R_{W^2 cut} = 0.013$, $\delta R_{W^2 cut}/R = 3.45\%$
- SBS-11: $\delta R_{W^2 cut} = 0.013$, $\delta R_{W^2 cut}/R = 3.72\%$

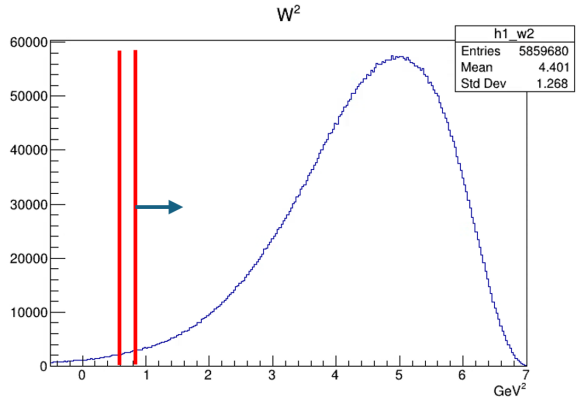

(a) W^2 plot sliced scan

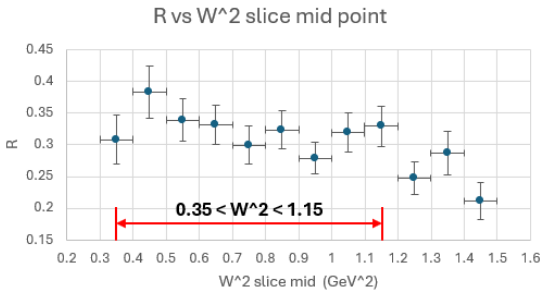

(b) R vs W^2 slice midpoint value

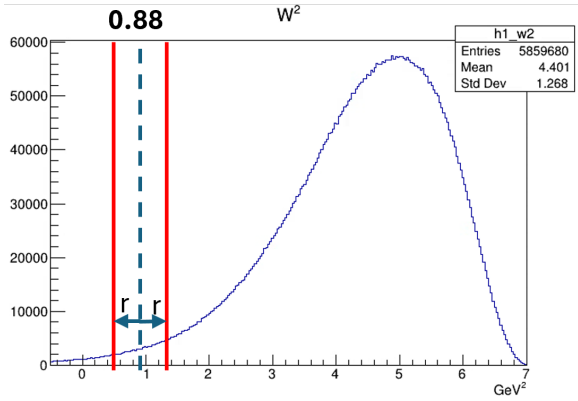

(c) W^2 cut centered around 0.88 GeV^2

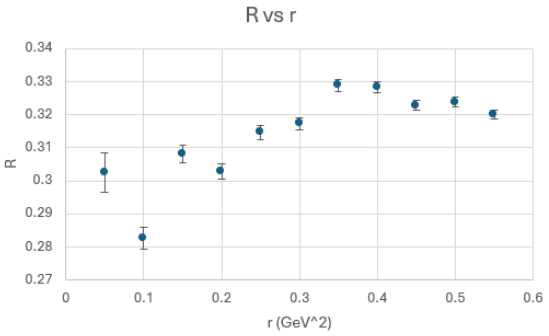

(d) R vs W^2 cut r

Figure 5.7: SBS-11 W^2 cut systematic studies

Δy Cut Systematic Study

The systematic studies of the Δy cut follow the same procedure used for the W^2 cut described above. A W^2 cuts of $0.4 < W^2 < 1.5$ was used for these systematic studies, for all three kinematic points.

Figures 5.8, 5.9, and 5.10 show the results of the Δy cut systematic studies performed for the SBS-4, SBS-7, and SBS-11 kinematic points, respectively. The subfigures (a) and (b) relate to the Δy sliced range scan method. The graphics in Figure (a) show how the Δy slices are selected for each separate ratio R extraction, and Figure (b) provides the results of the R extraction as a function of the midpoint of the Δy slice being analyzed. The horizontal error bars represent the width of the Δy slice, and the vertical error bars represent purely the statistical error. The range of Δy chosen for the final ratio R extractions is indicated by the red horizontal double-sided arrow in Figure (b) of each kinematic point. Figures (c) and (d) relate to the method of increasing the Δy range on either side of zero by an amount r. Figure (c)

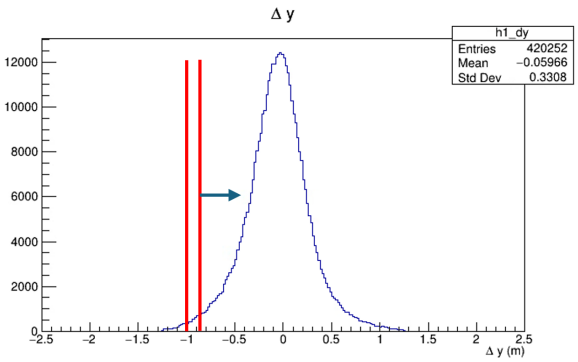

(a) Δy plot sliced scan

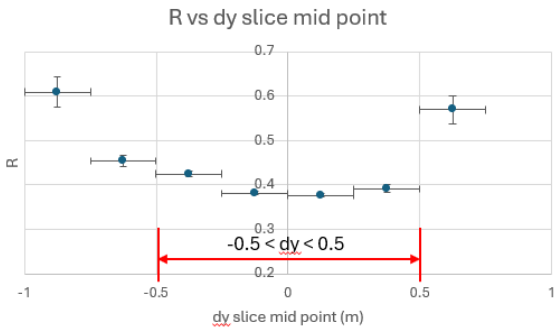

(b) R vs Δy slice midpoint value

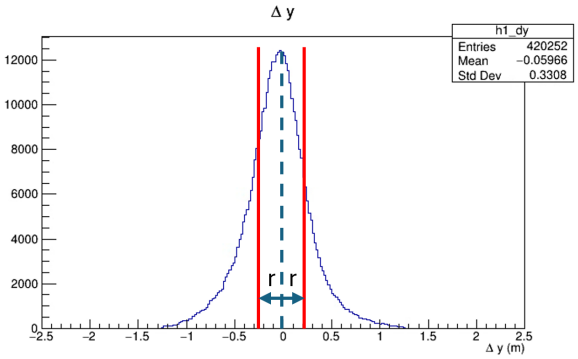

(c) Δy cut centered around zero

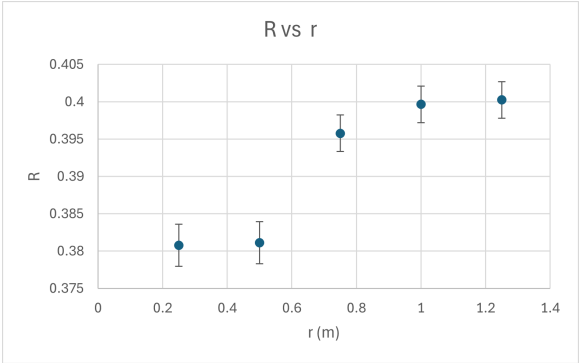

(d) R vs Δy cut r

Figure 5.8: SBS-4 Δy cut systematic studies

illustrates how the Δy region is chosen in this method, and Figure (d) provides the results of the R extraction as a function of r. Again, the vertical error bars are purely the statistical error.

The systematic error of ratio R due to the choice of Δy cut $\delta R_{\Delta ycut}$ for each kinematic point, obtained by taking the standard deviation of the data points in sub-figure (d) of Figures 5.8, 5.9, and 5.10, is:

- SBS-4: $\delta R_{\Delta ycut} = 0.009$, $\delta R_{\Delta ycut}/R = 2.29\%$
- SBS-7: $\delta R_{\Delta ycut} = 0.006$, $\delta R_{\Delta ycut}/R = 1.50\%$
- SBS-11: $\delta R_{\Delta ycut} = 0.004$, $\delta R_{\Delta ycut}/R = 1.06\%$

Fiducial Cut Systematic Study

Section 4.2.4 discusses the fiducial cut used in this analysis and how the choice of safety margins along the dispersive (x) and non-dispersive (y) directions could affect the ratio extraction.

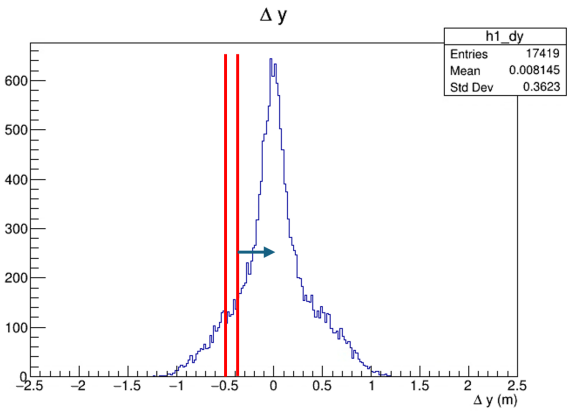

(a) Δy plot sliced scan

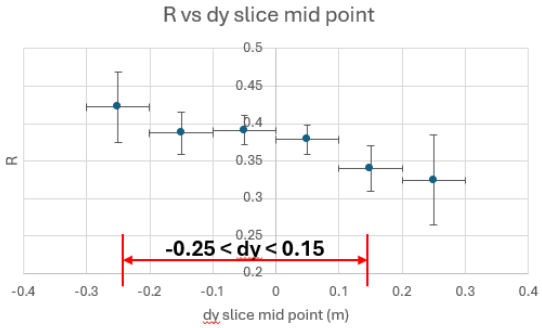

(b) R vs Δy slice midpoint value

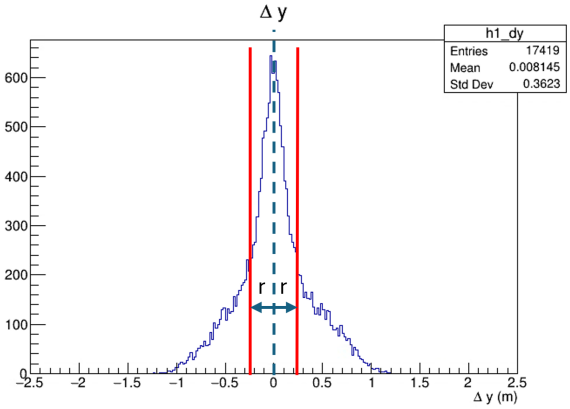

(c) Δy cut centered around zero

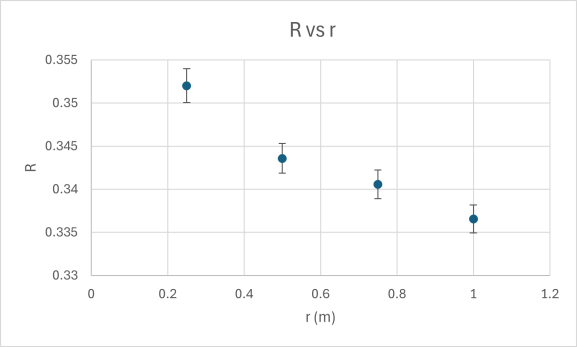

(d) R vs Δy cut r

Figure 5.9: SBS-7 Δy cut systematic studies

Figures 5.11, 5.12, and 5.13 show the results of the systematic studies performed to study the variation of ratio R when the fiducial cut safety margins are changed. Sub-figures (a) give the distributions of R vs. the standard deviation factor used for the x direction, whereas sub-figures (b) give the distributions for the y direction. When the standard deviation multiplication factors increase, this represents increased safety margins. This could also be visualized as bringing the magenta dashed lines in Figure 4.13 towards the center, hence reducing the fiducial region. As it can be seen, all the data points are highly correlated in all the plots. One main reason is the reduced HCal active area considered by removing the outer calorimeter blocks, as describes in the Figure 4.13. This effectively adds a constant safety margin on top of what's added in this study. A sigma multiplication factor of 1.5 is chosen for both x and y directions in the analysis of all three kinematic points under discussion. The error due to the fiducial cut along the x ($\delta R_{fid.x}$) and y ($\delta R_{fid.y}$) directions are as follows:

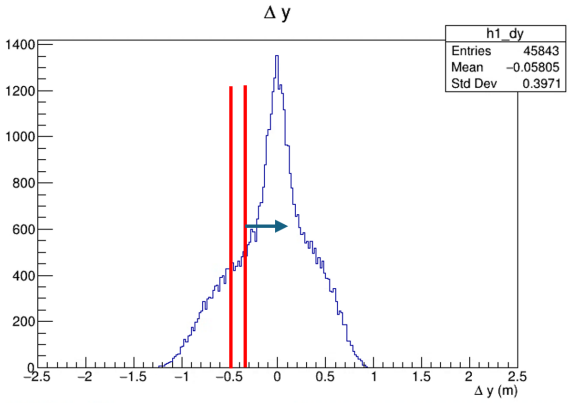

(a) Δy plot sliced scan

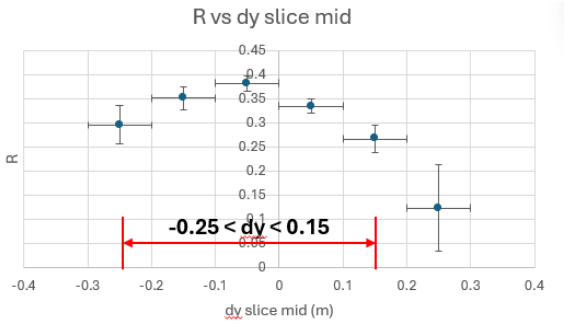

(b) R vs Δy slice midpoint value

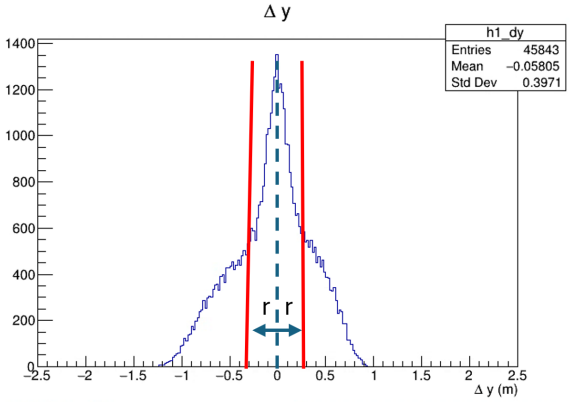

(c) Δy cut centered around zero

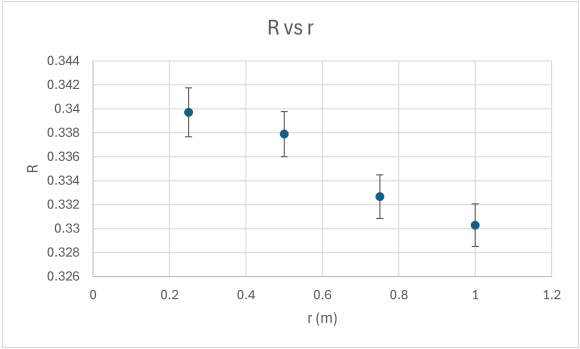

(d) R vs Δy cut r

Figure 5.10: SBS-11 Δy cut systematic studies

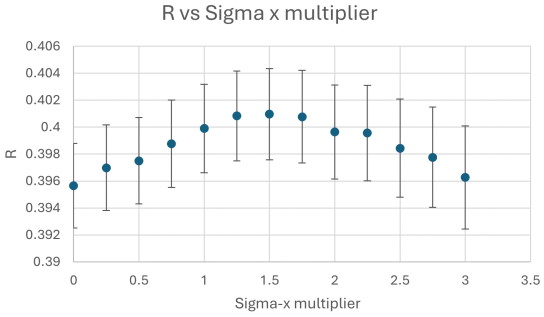

(a) R vs sigma-x multiplier

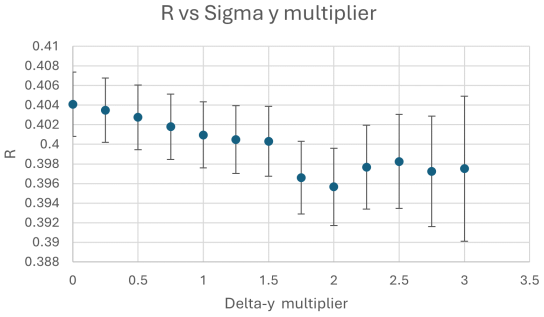

(b) R vs sigma-y multiplier

Figure 5.11: SBS-4 fiducial cut systematic studies

- SBS-4:
  - $\delta R_{fid.x} = 0.002$, $\delta R_{fid.x}/R = 0.45\%$
  - $\delta R_{fid.y} = 0.003$, $\delta R_{fid.y}/R = 0.71\%$

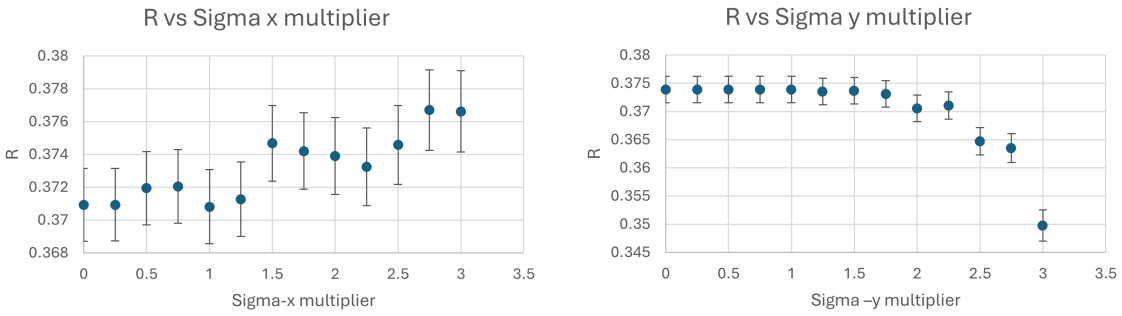

(a) R vs sigma-x multiplier (b) R vs sigma-y multiplier

Figure 5.12: SBS-7 fiducial cut systematic studies

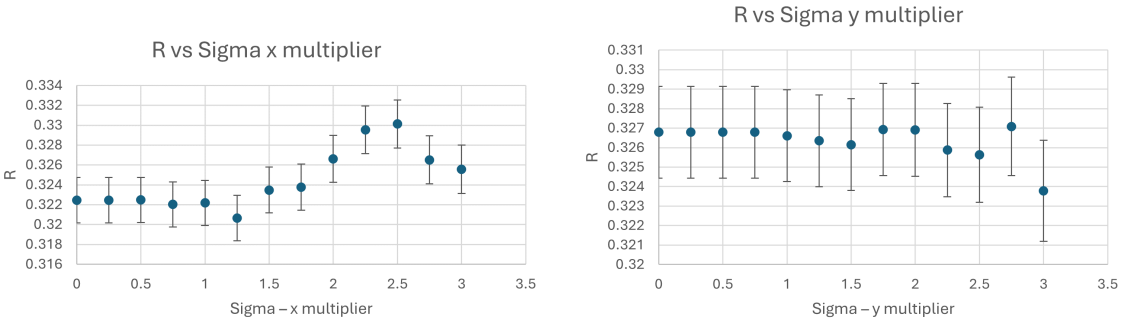

(a) R vs sigma-x multiplier (b) R vs sigma-y multiplier

Figure 5.13: SBS-11 fiducial cut systematic studies

- SBS-7:
  - $\delta R_{fid.x} = 0.002$, $\delta R_{fid.x}/R = 0.52\%$
  - $\delta R_{fid.y} = 0.007$, $\delta R_{fid.y}/R = 1.77\%$
- SBS-11:
  - $\delta R_{fid.x} = 0.003$, $\delta R_{fid.x}/R = 0.81\%$
  - $\delta R_{fid.y} = 0.001$, $\delta R_{fid.y}/R = 0.23\%$

HCal and BigBite Shower ADC Coincidence Time Cut Systematic Study

As indicated in Section 4.2.6, a careful analysis of the variation of ratio R as a function of the number of standard deviations from the mean, used to define the lower and upper bounds of HCal and BigBite shower ADC coincidence time, was performed for all three kinematic points under discussion. It must be noted that this particular

coincidence cut was not implemented for the simulated data, as pure quasi-elastic events were used for simulation where no accidental events are present.

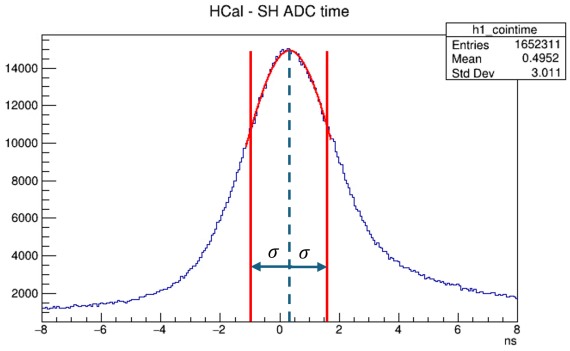

(a) HCal and BBCal Shower coin time. σ = 2.4 ns. The σ shown in the plot is for illustration only.

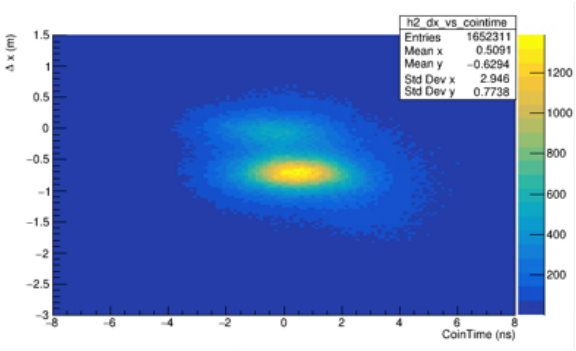

(b) Δx vs coin time

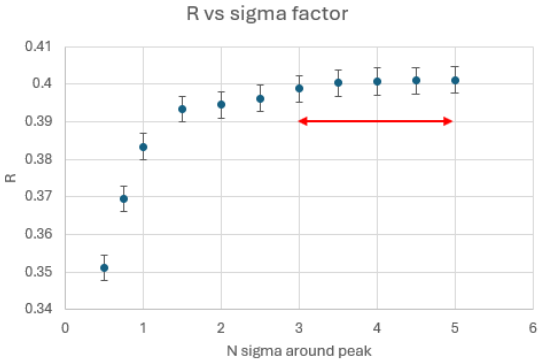

(c) R vs coin time sigma

Figure 5.14: SBS-4 HCal and BigBite Shower ADC coincidence time systematic study

Figures 5.14, 5.15, and 5.16 show the coincidence time systematic studies performed for kinematic points SBS-4, SBS-7, and SBS-11, respectively. Sub-figures (a) give a plot of HCal and BigBite Shower ADC time difference for each kinematic point, with a Gaussian fit performed around the peak of the distribution. The vertical red lines indicate an upper and lower bound cut with one sigma from either side of the mean from the fit. Sub-figures (b) give a plot for the 2D distribution of Δx vs coincidence time. For all the kinematic points, a clear positive offset of the proton spot (bottom) with respect to the neutron spot (top) can be seen. The exact reason for the cause of this effect is still under investigation. Sub-figures (c) provide plots of ratio R extracted as a function of the number of standard deviations used to define the cut region for coincidence time around either side of the mean. The effect on R by the skewed distributions of proton and neutron events in sub-figures (b) can

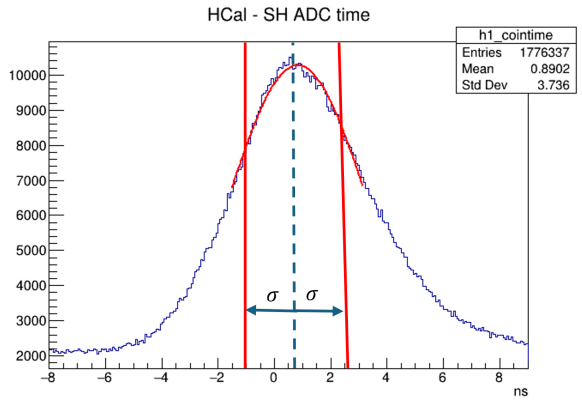

(a) HCal and BBCal Shower coin time. σ = 2.3 ns. The σ shown in the plot is for illustration only.

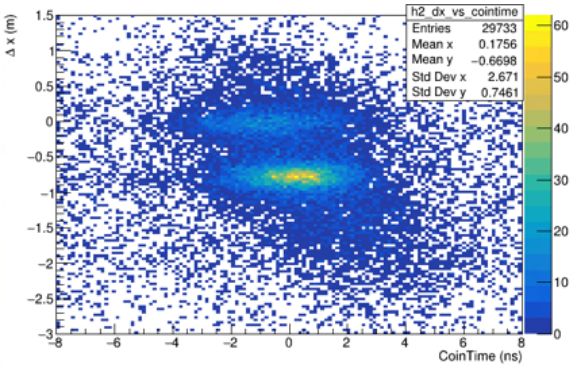

(b) Δx vs coin time

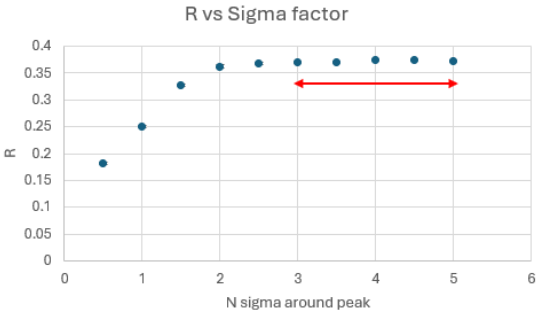

(c) R vs coin time sigma

Figure 5.15: SBS-7 HCal and BigBite Shower ADC coincidence time systematic study

clearly be seen by systematically lower and increasing values of R with the number of standard deviations. This suggests that using a too narrow coincidence cut region unevenly removes neutron and proton events, leading to an inaccurate ratio extraction. We used a four sigma coincidence cut for the final ratio extractions for all three kinematic points presented in this thesis, where the ratio shows to be very stable. The systematic error due to the coincidence time cut $\delta R_{coin.cut}$ for each kinematic point is obtained by taking the standard deviation of data points indicated by red double-sided arrows in respective R vs coincidence time plots (sub-figures (c)), and as follows:

- SBS-4: $\delta R_{coin.cut} = 0.001$, $\delta R_{coin.cut}/R = 0.22\%$
- SBS-7: $\delta R_{coin.cut} = 0.001$, $\delta R_{coin.cut}/R = 0.27\%$
- SBS-11: $\delta R_{coin.cut} = 0.002$, $\delta R_{coin.cut}/R = 0.65\%$

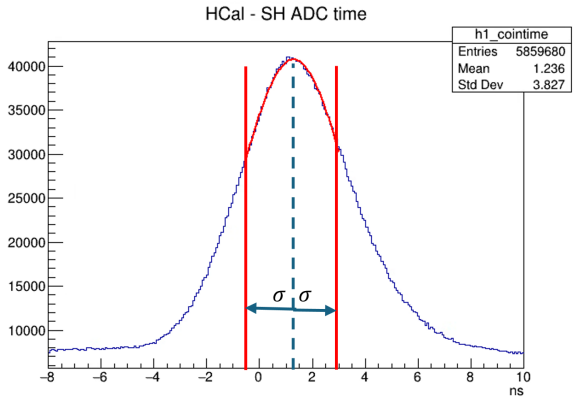

(a) HCal and BBCal Shower coin time. $\sigma = 2.3$ ns. The σ shown in the plot is for illustration only.

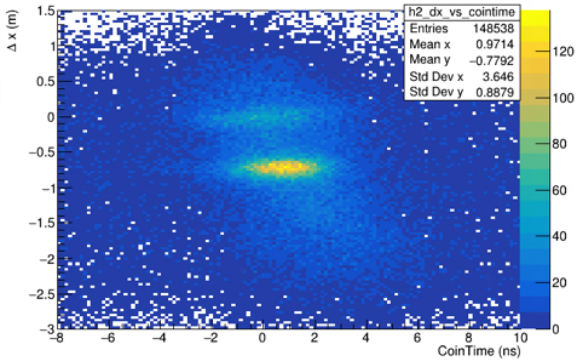

(b) Δx vs coin time

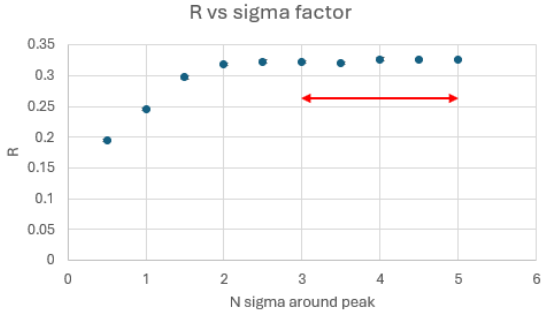

(c) R vs coin time sigma

Figure 5.16: SBS-11 HCal and BigBite Shower ADC coincidence time systematic study

5.3 Preliminary G_M^n Extractions

Following the analysis process described in Chapter 4 for ratio R extraction and the prescription for G_M^n calculation detailed in Section 5.1, very preliminary results for ratio R and G_M^n are presented for the kinematic points SBS-4, SBS-7, and SBS-11. However, these values should not be considered the final results of the E12-09-019 experiment. As previously mentioned, and as will be summarized at the end of this chapter, understanding certain aspects of the core analysis machinery and completing a more comprehensive error analysis are still in progress.

Figures 5.17, 5.18, and 5.19 show the Δx plots used for the ratio R extraction for SBS-4, SBS-7, and SBS-11 kinematic points, respectively. Sub-figures (a) show the experimental data histograms (black dots), individual post-scaling simulation quasi-elastic peaks (magenta filled - D(e,e′p)n, cyan filled - D(e,e′n)p), post-scaling simulated background (green filled) from the G4SBS inelastic generator, and the

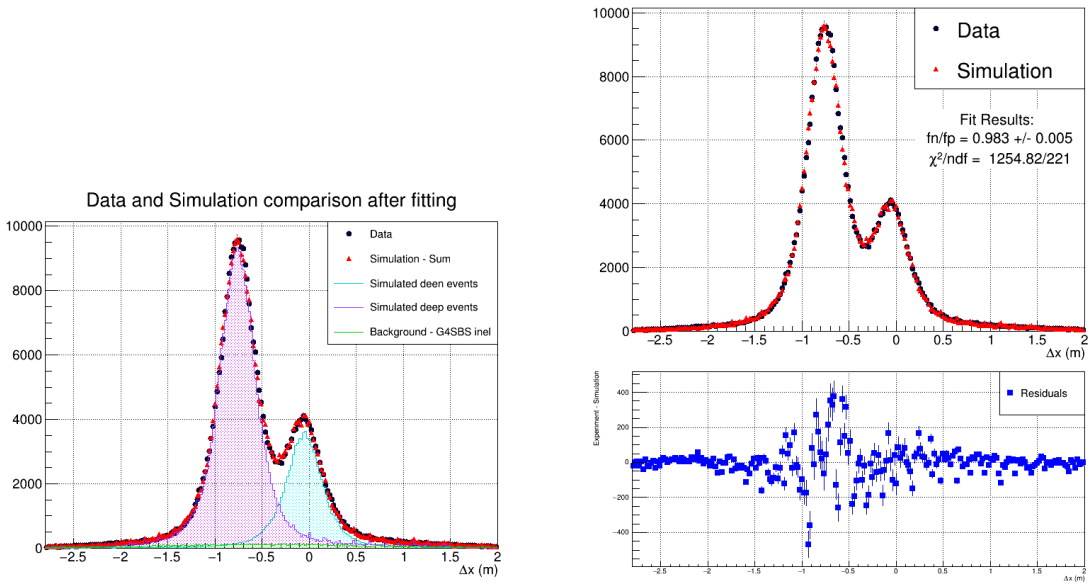

(a) Δx plot with individual D(e,e′n)p, D(e,e′p)n simulated quasi-elastic and G4SBS inelastic generator background histograms.

(b) Δx plot with only experimental data and final scaled simulation composite histograms, along with a residual plot at the bottom.

Figure 5.17: SBS-4 data and post-scaling simulation Δx plots used for extracting ratio R.

composite post-scaling simulation histogram (red triangles). In sub-figures (b), only the data and composite simulation histogram are shown, as in sub-figures (a), with the scale factor ratio f_n/f_p obtained from the χ^2 minimization process between the simulation composite histogram and the experimental data histogram. The χ^2 per degree of freedom in the final simulation Δx plot fit to the experimental Δx plot is also provided. At the bottom of the sub-figures (b), residual plots show the difference between the experimental data and simulation Δx histograms for each bin. Ideally, a random distribution of residuals around zero across the entire Δx distribution is desired, suggesting complete agreement between the systematic effects in the experimental and simulated data. Relatively small systematic shifts of the residual distributions near the peak of the larger proton distributions can be observed. Other than that, the residual distributions are fairly randomly distributed around zero.

A drastic increase in the relative background contribution is observed from the lowest Q^2 point SBS-4 (2.97 GeV$^2/c^2$) to the highest Q^2 point SBS-11 (13.52 GeV$^2/c^2$). However, for the two higher Q^2 points of SBS-7 and SBS-11, much tighter elastic event selection criteria have been used. The increase in background level is expected as the elastic scattering cross section decreases as Q^{-12}, and the vast majority of events col-

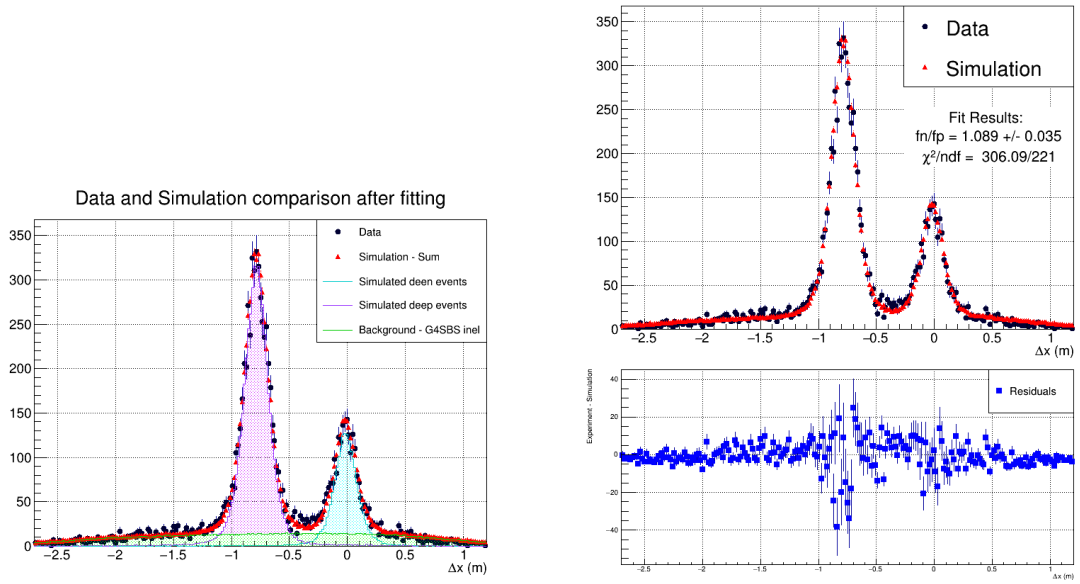

(a) Δx plot with individual D(e,e′n)p, D(e,e′p)n simulated quasi-elastic and G4SBS inelastic generator background histograms.

(b) Δx plot with only experimental data and final scaled simulation composite histograms, along with a residual plot at the bottom.

Figure 5.18: SBS-7 data and post-scaling simulation Δx plots used for extracting ratio R.

lected are inelastic. Looking at the residual distributions in Figures 5.17b, 5.18b, and 5.19b, outside of the quasi-elastic peaks, it can be seen that the background modeling does a reasonable job of estimating the shape of the inelastic distribution. All the event-selection cut thresholds/regions used for experimental and simulated data are provided in Table C.1. The HCal and BigBite shower coincidence time cut was not applied to the simulated data, as stated earlier.

Kinematic point	Q^2 (GeV$^2/c^2$)	R	Statistical error	Systematic error
SBS-4	2.97	0.390	0.002	0.016
SBS-7	9.81	0.399	0.013	0.017
SBS-11	13.52	0.360	0.010	0.015

Table 5.1: Kinematic points and corresponding values for R.

The ratio R extractions and the corresponding G_M^n extractions are provided in Tables 5.1 and 5.2, respectively. Figure 5.20 shows a plot of the pre-preliminary G_M^n extraction results from this work.

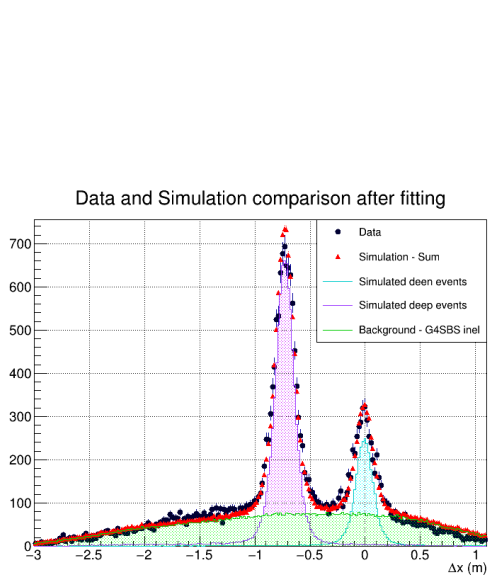

(a) Δx plot with individual D(e,e′n)p, D(e,e′p)n simulated quasi-elastic and G4SBS inelastic generator background histograms.

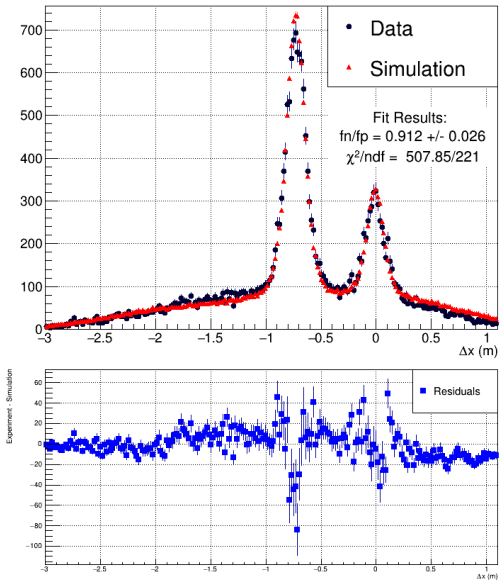

(b) Δx plot with only experimental data and final scaled simulation composite histograms, along with a residual plot at the bottom.

Figure 5.19: SBS-11 data and post-scaling simulation Δx plots used for extracting ratio R.

Kinematic point	Q^2 (GeV$^2/c^2$)	$G_M^n/(\mu_n G_D)$	Statistical error	Systematic error
SBS-4	2.97	0.991	0.003	0.024
SBS-7	9.81	0.862	0.014	0.024
SBS-11	13.52	0.756	0.011	0.023

Table 5.2: Kinematic points and corresponding values for $G_M^n/(\mu_n G_D)$.

5.4 Discussion

It must be noted that the analysis results presented in this thesis are preliminary or exploratory in nature. The ratio R and G_M^n extractions presented in this chapter represent mostly the individual work of the author, and they are not by any means the final results of the E12-09-019 experiment, i.e., the SBS GMn experiment.

Several major analysis tasks remain for the successful completion of the SBS GMn experiment analysis. Implementing data-based HCal neutron and proton detection efficiency corrections to the ratio R and accounting for position-dependent non-uniformities of HCal detection efficiencies stand out as among the most important work remaining. These systematic effects affect the neutron and proton yields differently and do not cancel out in the ratio R. Ongoing work for these HCal detec-

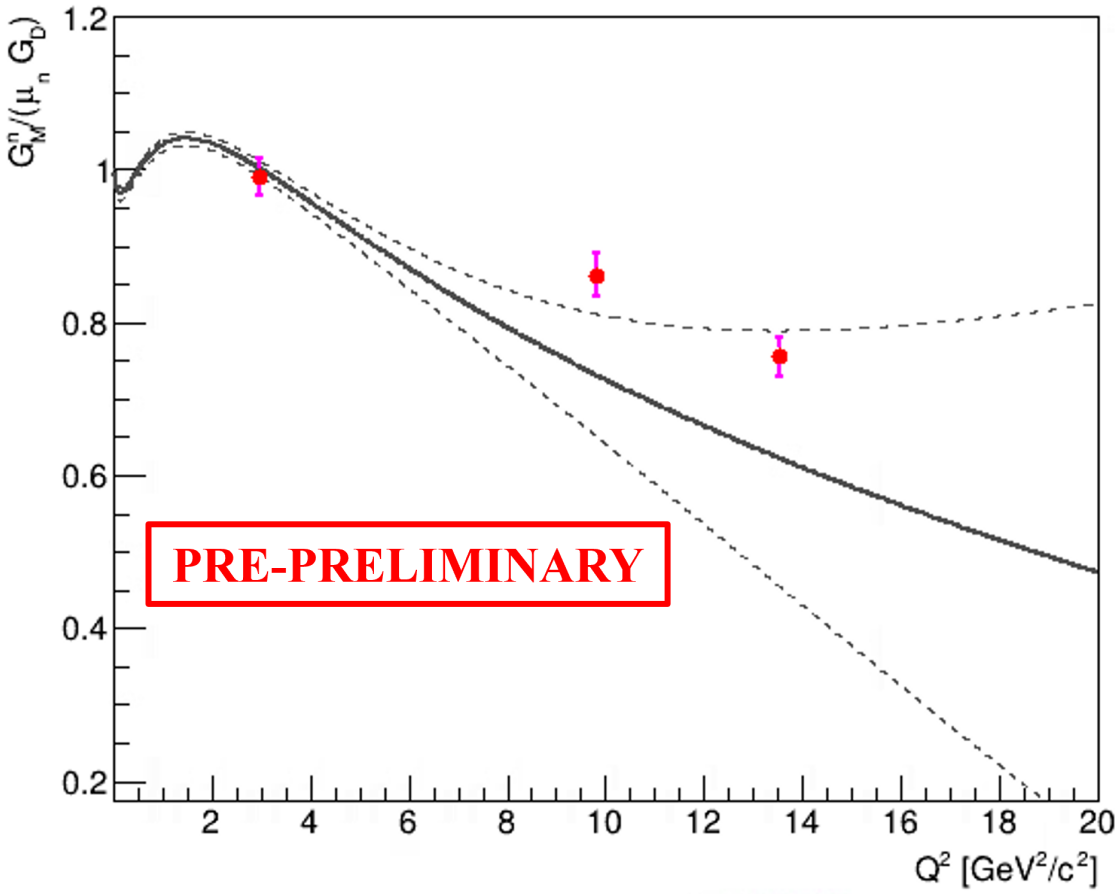

Figure 5.20: Pre-preliminary G_M^n results for SBS-4, SBS-7, and SBS-11 kinematic points. The preliminary G_M^n extractions from this work are shown by red filled circles. The magenta error bars represent the total error obtained by the quadrature sum of the systematic and statistical errors of each data point. The gray line shows the Ye parameterization [2] for $G_M^n/\mu_n G_D$, with the gray dashed lines indicating the error bounds of the parameterization.

tion efficiency analyses is described in detail under Section 4.3. Any data-based HCal detection efficiency corrections or corrections for position-dependent HCal detection efficiency non-uniformities are not implemented in the analysis results presented in this thesis. In addition, the cut stability studies must be extended to other variables beyond the four variables considered in this analysis, as mentioned under Section 5.2.3.

SIMC event generator does not model Final State Interactions (FSI) between the outgoing nucleons during the quasi-elastic scattering process. Though the effects due to FSI are largely expected to cancel in the ratio, a proper theoretical correction must be applied.

The prescription used for the G_M^n calculation via the ratio R in this thesis, outlined in Section 5.1, inherently neglects the Two Photon Exchange (TPE) contribution for D(e,e′n)p and D(e,e′p)n quasi-elastic yields. The G_M^p, G_E^p, and G_E^n form factor parameterizations used for G_M^n calculation give the *true form factors* that were derived from TPE-corrected cross-section measurements. As a result, for accurate *true* G_M^n extractions, the ratio R must be corrected for TPE effects prior to the G_M^n calculation using the true proton form factors and neutron electric form factor.

In summary, pre-preliminary extractions of ratios of cross sections R are obtained with total error bounds between 4.0% and 5.5% for all the kinematic points, including the two highest Q^2 points. These error bounds are well within the projected uncertainties [34]. However, these ratio extractions and error bounds are subject to change during the final and more comprehensive analyses.

Bibliography

[1] Franz Gross, Eberhard Klempt, Stanley J. Brodsky, Andrzej J. Buras, Volker D. Burkert, Gudrun Heinrich, Karl Jakobs, Curtis A. Meyer, Kostas Orginos, Michael Strickland, Johanna Stachel, Giulia Zanderighi, Nora Brambilla, Peter Braun-Munzinger, Daniel Britzger, Simon Capstick, Tom Cohen, Volker Crede, Martha Constantinou, Christine Davies, Luigi Del Debbio, Achim Denig, Carleton DeTar, Alexandre Deur, Yuri Dokshitzer, Hans Günter Dosch, Jozef Dudek, Monica Dunford, Evgeny Epelbaum, Miguel A. Escobedo, Harald Fritzsch, Kenji Fukushima, Paolo Gambino, Dag Gillberg, Steven Gottlieb, Per Grafstrom, Massimiliano Grazzini, Boris Grube, Alexey Guskov, Toru Iijima, Xiangdong Ji, Frithjof Karsch, Stefan Kluth, John B. Kogut, Frank Krauss, Shunzo Kumano, Derek Leinweber, Heinrich Leutwyler, Hai-Bo Li, Yang Li, Bogdan Malaescu, Chiara Mariotti, Pieter Maris, Simone Marzani, Wally Melnitchouk, Johan Messchendorp, Harvey Meyer, Ryan Edward Mitchell, Chandan Mondal, Frank Nerling, Sebastian Neubert, Marco Pappagallo, Saori Pastore, José R. Peláez, Andrew Puckett, Jianwei Qiu, Klaus Rabbertz, Alberto Ramos, Patrizia Rossi, Anar Rustamov, Andreas Schäfer, Stefan Scherer, Matthias Schindler, Steven Schramm, Mikhail Shifman, Edward Shuryak, Torbjörn Sjöstrand, George Sterman, Iain W. Stewart, Joachim Stroth, Eric Swanson, Guy F. de Téramond, Ulrike Thoma, Antonio Vairo, Danny van Dyk, James Vary, Javier Virto, Marcel Vos, Christian Weiss, Markus Wobisch, Sau Lan Wu, Christopher Young, Feng Yuan, Xingbo Zhao, and Xiaorong Zhou. 50 years of quantum chromodynamics: Introduction and review. *The European Physical Journal C*, 83(12):334–345, December 2023.

[2] Zhihong Ye, John Arrington, Richard J. Hill, and Gabriel Lee. Proton and neutron electromagnetic form factors and uncertainties. *Physics Letters B*, 777:8–15, 2018.

[3] Sandra Santiesteban, L. Tracy, D. Flay, Douglas Higinbotham, D. Marchand,

Pascal Vernin, and A Saha. Precise beam energy determination for hall a after the cebaf 12 gev upgrade. 10 2021.

[4] D.J.J de Lange, J.J.M Steijger, H de Vries, M Anghinolfi, M Taiuti, D.W Higinbotham, B.E Norum, and E Konstantinov. A large acceptance spectrometer for the internal target facility at nikhef. *Nuclear Instruments and Methods in Physics Research Section A: Accelerators, Spectrometers, Detectors and Associated Equipment*, 406(2):182–194, 1998.

[5] Fabio Sauli. The gas electron multiplier (gem): Operating principles and applications. *Nuclear Instruments and Methods in Physics Research Section A: Accelerators, Spectrometers, Detectors and Associated Equipment*, 805:2–24, 2016. Special Issue in memory of Glenn F. Knoll.

[6] S. Bachmann, A. Bressan, L. Ropelewski, F. Sauli, A. Sharma, and D. Mörmann. Charge amplification and transfer processes in the gas electron multiplier. *Nuclear Instruments and Methods in Physics Research Section A: Accelerators, Spectrometers, Detectors and Associated Equipment*, 438(2):376–408, 1999.

[7] C. Amsler, M. Doser, M. Antonelli, D.M. Asner, K.S. Babu, H. Baer, H.R. Band, R.M. Barnett, E. Bergren, J. Beringer, G. Bernardi, W. Bertl, H. Bichsel, O. Biebel, P. Bloch, E. Blucher, S. Blusk, R.N. Cahn, M. Carena, C. Caso, A. Ceccucci, D. Chakraborty, M.-C. Chen, R.S. Chivukula, G. Cowan, O. Dahl, G. D'Ambrosio, T. Damour, A. de Gouvêa, T. DeGrand, B. Dobrescu, M. Drees, D.A. Edwards, S. Eidelman, V.D. Elvira, J. Erler, V.V. Ezhela, J.L. Feng, W. Fetscher, B.D. Fields, B. Foster, T.K. Gaisser, L. Garren, H.-J. Gerber, G. Gerbier, T. Gherghetta, G.F. Giudice, M. Goodman, C. Grab, A.V. Gritsan, J.-F. Grivaz, D.E. Groom, M. Grünewald, A. Gurtu, T. Gutsche, H.E. Haber, K. Hagiwara, C. Hagmann, K.G. Hayes, J.J. Hernández-Rey, K. Hikasa, I. Hinchliffe, A. Höcker, J. Huston, P. Igo-Kemenes, J.D. Jackson, K.F. Johnson, T. Junk, D. Karlen, B. Kayser, D. Kirkby, S.R. Klein, I.G. Knowles, C. Kolda, R.V. Kowalewski, P. Kreitz, B. Krusche, Yu.V. Kuyanov, Y. Kwon, O. Lahav, P. Langacker, A. Liddle, Z. Ligeti, C.-J. Lin, T.M. Liss, L. Littenberg, J.C. Liu, K.S. Lugovsky, S.B. Lugovsky, H. Mahlke, M.L. Mangano, T. Mannel, A.V. Manohar, W.J. Marciano, A.D. Martin, A. Masoni, D. Milstead, R. Miquel, K. Mönig, H. Murayama, K. Nakamura, M. Narain, P. Nason, S. Navas, P. Nevski, Y. Nir, K.A. Olive, L. Pape, C. Patrignani, J.A. Peacock, A. Piepke, G. Punzi, A. Quadt, S. Raby, G. Raffelt, B.N. Ratcliff, B. Renk, P. Richardson, S. Roesler, S. Rolli,

A. Romaniouk, L.J. Rosenberg, J.L. Rosner, C.T. Sachrajda, Y. Sakai, S. Sarkar, F. Sauli, O. Schneider, D. Scott, W.G. Seligman, M.H. Shaevitz, T. Sjöstrand, J.G. Smith, G.F. Smoot, S. Spanier, H. Spieler, A. Stahl, T. Stanev, S.L. Stone, T. Sumiyoshi, M. Tanabashi, J. Terning, M. Titov, N.P. Tkachenko, N.A. Törnqvist, D. Tovey, G.H. Trilling, T.G. Trippe, G. Valencia, K. van Bibber, M.G. Vincter, P. Vogel, D.R. Ward, T. Watari, B.R. Webber, G. Weiglein, J.D. Wells, M. Whalley, A. Wheeler, C.G. Wohl, L. Wolfenstein, J. Womersley, C.L. Woody, R.L. Workman, A. Yamamoto, W.-M. Yao, O.V. Zenin, J. Zhang, R.-Y. Zhu, P.A. Zyla, G. Harper, V.S. Lugovsky, and P. Schaffner. Review of particle physics. *Physics Letters B*, 667(1):292, 2008. Review of Particle Physics.

[8] R. Frisch and O. Stern. Über die magnetische ablenkung von wasserstoff-molekülen und das magnetische moment des protons. *I. Z. Physik*, pages 4–16, 1933.

[9] Robert Hofstadter. Electron scattering and nuclear structure. *Rev. Mod. Phys.*, 28:214–254, Jul 1956.

[10] R. G. Sachs. High-energy behavior of nucleon electromagnetic form factors. *Phys. Rev.*, 126:2256–2260, Jun 1962.

[11] P. A. M. Guichon and M. Vanderhaeghen. How to reconcile the rosenbluth and the polarization transfer methods in the measurement of the proton form factors. *Phys. Rev. Lett.*, 91:142303, Oct 2003.

[12] E.B.Hughes et al. *Phys. Rev.*, 141:973, 1965.

[13] B. Grossetête, S. Jullian, and P. Lehmann. Electrodisintegration of the deuteron around $q^2 = 3.5$ f^{-2}. *Phys. Rev.*, 141:1435–1440, Jan 1966.

[14] A.S.Esaulov et al. *Sov. J. Nucl. Phys.*, 45:258, 1987.

[15] A. Lung, L. M. Stuart, P. E. Bosted, L. Andivahis, J. Alster, R. G. Arnold, C. C. Chang, F. S. Dietrich, W. R. Dodge, R. Gearhart, J. Gomez, K. A. Griffioen, R. S. Hicks, C. E. Hyde-Wright, C. Keppel, S. E. Kuhn, J. Lichtenstadt, R. A. Miskimen, G. A. Peterson, G. G. Petratos, S. E. Rock, S. H. Rokni, W. K. Sakumoto, M. Spengos, K. Swartz, Z. Szalata, and L. H. Tao. Measurements of the electric and magnetic form factors of the neutron from q^2=1.75 to 4.00 (gev/c)^2. *Phys. Rev. Lett.*, 70:718–721, Feb 1993.

[16] R. G. Arnold, D. Benton, P. Bosted, L. Clogher, G. DeChambrier, A. T. Katramatou, J. Lambert, A. Lung, G. G. Petratos, A. Rahbar, S. E. Rock, Z. M. Szalata, B. Debebe, M. Frodyma, R. S. Hicks, A. Hotta, G. A. Peterson, R. A. Gearhart, J. Alster, J. Lichtenstadt, F. Dietrich, and K. van Bibber. Measurements of transverse quasielastic electron scattering from the deuteron at high momentum transfers. *Phys. Rev. Lett.*, 61:806–809, Aug 1988.

[17] P. Stein, M. Binkley, R. McAllister, A. Suri, and W. Woodward. Measurements of neutron form factors. *Phys. Rev. Lett.*, 16:592–594, Mar 1966.

[18] W. Bartel et. al. *Phys. Rev. Lett.*, 13B:285, 1969.

[19] P. Markowitz, J. M. Finn, B. D. Anderson, H. Arenhövel, A. R. Baldwin, D. Barkhuff, K. B. Beard, W. Bertozzi, J. M. Cameron, C. C. Chang, G. W. Dodson, K. Dow, T. Eden, M. Farkhondeh, B. Flanders, C. Hyde-Wright, W.-D. Jiang, D. Keane, J. J. Kelly, W. Korsch, S. Kowalski, R. Lourie, R. Madey, D. M. Manley, J. Mougey, B. Ni, T. Payerle, P. Pella, T. Reichelt, P. M. Rutt, M. Spraker, D. Tieger, W. Turchinetz, P. E. Ulmer, S. Van Verst, J. W. Watson, L. B. Weinstein, R. R. Whitney, and W. M. Zhang. Measurement of the magnetic form factor of the neutron. *Phys. Rev. C*, 48:R5–R9, Jul 1993.

[20] R. J. Budnitz, J. Appel, L. Carroll, J. Chen, J. R. Dunning, M. Goitein, K. Hanson, D. Imrie, C. Mistretta, J. K. Walker, and Richard Wilson. Neutron form factors from quasi-elastic electron-deuteron scattering. *Phys. Rev.*, 173:1357–1390, Sep 1968.

[21] K. M. Hanson, J. R. Dunning, M. Goitein, T. Kirk, L. E. Price, and Richard Wilson. Large-angle quasielastic electron-deuteron scattering. *Phys. Rev. D*, 8:753–778, Aug 1973.

[22] E. B. Hughes, M. R. Yearian, and R. Hofstadter. Neutron form factors from inelastic electron scattering in tritium and helium-3. *Phys. Rev.*, 151:841–845, Nov 1966.

[23] S. N. Santiesteban, S. Li, D. Abrams, S. Alsalmi, D. Androic, K. Aniol, J. Arrington, T. Averett, C. Ayerbe Gayoso, J. Bane, S. Barcus, J. Barrow, A. Beck, V. Bellini, H. Bhatt, D. Bhetuwal, D. Biswas, A. Camsonne, J. Castellanos, J. Chen, J-P. Chen, D. Chrisman, M. E. Christy, C. Clarke, S. Covrig, R. Cruz-Torres, D. Day, D. Dutta, E. Fuchey, C. Gal, F. Garibaldi, T. N. Gautam,

T. Gogami, J. Gomez, P. Guèye, T. J. Hague, J. O. Hansen, F. Hauenstein, W. Henry, D. W. Higinbotham, R. J. Holt, C. Hyde, K. Itabashi, M. Kaneta, A. Karki, A. T. Katramatou, C. E. Keppel, P. M. King, L. Kurbany, T. Kutz, N. Lashley-Colthirst, W. B. Li, H. Liu, N. Liyanage, E. Long, A. Lovato, J. Mammei, P. Markowitz, R. E. McClellan, F. Meddi, D. Meekins, R. Michaels, M. Mihovilovič, A. Moyer, S. Nagao, D. Nguyen, M. Nycz, M. Olson, L. Ou, V. Owen, C. Palatchi, B. Pandey, A. Papadopoulou, S. Park, T. Petkovic, S. Prematilake, V. Punjabi, R. D. Ransome, P. E. Reimer, J. Reinhold, S. Riordan, N. Rocco, V. M. Rodriguez, A. Schmidt, B. Schmookler, E. P. Segarra, A. Shahinyan, S. Širca, K. Slifer, P. Solvignon, T. Su, R. Suleiman, L. Tang, Y. Tian, W. Tireman, F. Tortorici, Y. Toyama, K. Uehara, G. M. Urciuoli, D. Votaw, J. Williamson, B. Wojtsekhowski, S. Wood, Z. H. Ye, J. Zhang, and X. Zheng. Novel measurement of the neutron magnetic form factor from A = 3 mirror nuclei. *Phys. Rev. Lett.*, 132:162501, Apr 2024.

[24] Brendan Anderson, L Auberbach, Todd Averett, W. Bertozzi, Taishon Black, Jr Calarco, L. Cardman, Gordon Cates, Z.W Chai, Jian-ping Chen, Seonho Choi, E. Chudakov, S Churchwell, G.s Corrado, Christopher Crawford, Dan Dale, Allen Deur, P. Djawotho, Dipangkar Dutta, and Piotr Zolnierczuk. Extraction of the neutron magnetic form factor from quasielastic 3he(e,e') at q2=0.1-0.6 (gev/c)2. *Physical Review C*, 75, 03 2007.

[25] W. Xu, B. Anderson, L. Auberbach, T. Averett, W. Bertozzi, T. Black, J. Calarco, L. Cardman, G. D. Cates, Z. W. Chai, J. P. Chen, S. Choi, E. Chudakov, S. Churchwell, G. S. Corrado, C. Crawford, D. Dale, A. Deur, P. Djawotho, T. W. Donnelly, D. Dutta, J. M. Finn, H. Gao, R. Gilman, A. V. Glamazdin, C. Glashausser, W. Glöckle, J. Golak, J. Gomez, V. G. Gorbenko, J.-O. Hansen, F. W. Hersman, D. W. Higinbotham, R. Holmes, C. R. Howell, E. Hughes, B. Humensky, S. Incerti, C. W. de Jager, J. S. Jensen, X. Jiang, C. E. Jones, M. Jones, R. Kahl, H. Kamada, A. Kievsky, I. Kominis, W. Korsch, K. Kramer, G. Kumbartzki, M. Kuss, E. Lakuriqi, M. Liang, N. Liyanage, J. LeRose, S. Malov, D. J. Margaziotis, J. W. Martin, K. McCormick, R. D. McKeown, K. McIlhany, Z.-E. Meziani, R. Michaels, G. W. Miller, J. Mitchell, S. Nanda, E. Pace, T. Pavlin, G. G. Petratos, R. I. Pomatsalyuk, D. Pripstein, D. Prout, R. D. Ransome, Y. Roblin, M. Rvachev, A. Saha, G. Salmè, M. Schnee, T. Shin, K. Slifer, P. A. Souder, S. Strauch, R. Suleiman, M. Sutter, B. Tipton, L. Todor, M. Viviani, B. Vlahovic, J. Watson, C. F. Williamson, H. Witała,

B. Wojtsekhowski, F. Xiong, J. Yeh, and P. Żołnierczuk. Plane-wave impulse approximation extraction of the neutron magnetic form factor from quasielastic $^3\mathrm{He} \rightarrow (\vec{e}\,, e')$ at $Q^2 = 0.3$ to $0.6(\mathrm{GeV}/c)^2$. *Phys. Rev. C*, 67:012201, Jan 2003.

[26] W. Xu, D. Dutta, F. Xiong, B. Anderson, L. Auberbach, T. Averett, W. Bertozzi, T. Black, J. Calarco, L. Cardman, G. D. Cates, Z. W. Chai, J. P. Chen, S. Choi, E. Chudakov, S. Churchwell, G. S. Corrado, C. Crawford, D. Dale, A. Deur, P. Djawotho, B. W. Filippone, J. M. Finn, H. Gao, R. Gilman, A. V. Glamazdin, C. Glashausser, W. Glöckle, J. Golak, J. Gomez, V. G. Gorbenko, J.-O. Hansen, F. W. Hersman, D. W. Higinbotham, R. Holmes, C. R. Howell, E. Hughes, B. Humensky, S. Incerti, C. W. de Jager, J. S. Jensen, X. Jiang, C. E. Jones, M. Jones, R. Kahl, H. Kamada, A. Kievsky, I. Kominis, W. Korsch, K. Kramer, G. Kumbartzki, M. Kuss, E. Lakuriqi, M. Liang, N. Liyanage, J. LeRose, S. Malov, D. J. Margaziotis, J. W. Martin, K. McCormick, R. D. McKeown, K. McIlhany, Z.-E. Meziani, R. Michaels, G. W. Miller, E. Pace, T. Pavlin, G. G. Petratos, R. I. Pomatsalyuk, D. Pripstein, D. Prout, R. D. Ransome, Y. Roblin, M. Rvachev, A. Saha, G. Salmè, M. Schnee, T. Shin, K. Slifer, P. A. Souder, S. Strauch, R. Suleiman, M. Sutter, B. Tipton, L. Todor, M. Viviani, B. Vlahovic, J. Watson, C. F. Williamson, H. Witała, B. Wojtsekhowski, J. Yeh, and P. Żołnierczuk. Transverse asymmetry $A_{T'}$ from the quasielastic $^3\vec{\mathrm{he}}\,(\vec{e}, e')$ process and the neutron magnetic form factor. *Phys. Rev. Lett.*, 85:2900–2904, Oct 2000.

[27] H. Gao, J. Arrington, E. J. Beise, B. Bray, R. W. Carr, B. W. Filippone, A. Lung, R. D. McKeown, B. Mueller, M. L. Pitt, C. E. Jones, D. DeSchepper, G. Dodson, K. Dow, R. Ent, M. Farkhondeh, J.-O. Hansen, W. Korsch, L. H. Kramer, K. Lee, N. Makins, R. G. Milner, D. R. Tieger, T. P. Welch, E. Candell, J. Napolitano, B. B. Wojtsekhowski, C. Tripp, and W. Lorenzon. Measurement of the neutron magnetic form factor from inclusive quasielastic scattering of polarized electrons from polarized ^{3}He. *Phys. Rev. C*, 50:R546–R549, Aug 1994.

[28] Loyal Durand. Inelastic electron-deuteron scattering cross sections at high energies. *Phys. Rev.*, 115:1020–1038, Aug 1959.

[29] J. Lachniet, A. Afanasev, H. Arenhövel, W. K. Brooks, G. P. Gilfoyle, D. Higinbotham, S. Jeschonnek, B. Quinn, M. F. Vineyard, G. Adams, K. P. Adhikari, M. J. Amaryan, M. Anghinolfi, B. Asavapibhop, G. Asryan, H. Avakian, H. Bagdasaryan, N. Baillie, J. P. Ball, N. A. Baltzell, S. Barrow, V. Batourine, M. Battaglieri, K. Beard, I. Bedlinskiy, M. Bektasoglu, M. Bellis, N. Benmouna,

B. L. Berman, A. S. Biselli, B. E. Bonner, C. Bookwalter, S. Bouchigny, S. Boiarinov, R. Bradford, D. Branford, W. J. Briscoe, S. Bültmann, V. D. Burkert, J. R. Calarco, S. L. Careccia, D. S. Carman, L. Casey, L. Cheng, P. L. Cole, A. Coleman, P. Collins, D. Cords, P. Corvisiero, D. Crabb, V. Crede, J. P. Cummings, D. Dale, A. Daniel, N. Dashyan, R. De Masi, R. De Vita, E. De Sanctis, P. V. Degtyarenko, H. Denizli, L. Dennis, A. Deur, S. Dhamija, K. V. Dharmawardane, K. S. Dhuga, R. Dickson, C. Djalali, G. E. Dodge, D. Doughty, P. Dragovitsch, M. Dugger, S. Dytman, O. P. Dzyubak, H. Egiyan, K. S. Egiyan, L. El Fassi, L. Elouadrhiri, A. Empl, P. Eugenio, R. Fatemi, G. Fedotov, R. Fersch, R. J. Feuerbach, T. A. Forest, A. Fradi, M. Y. Gabrielyan, M. Garçon, G. Gavalian, N. Gevorgyan, K. L. Giovanetti, F. X. Girod, J. T. Goetz, W. Gohn, E. Golovatch, R. W. Gothe, L. Graham, K. A. Griffioen, M. Guidal, M. Guillo, N. Guler, L. Guo, V. Gyurjyan, C. Hadjidakis, K. Hafidi, H. Hakobyan, C. Hanretty, J. Hardie, N. Hassall, D. Heddle, F. W. Hersman, K. Hicks, I. Hleiqawi, M. Holtrop, J. Hu, M. Huertas, C. E. Hyde-Wright, Y. Ilieva, D. G. Ireland, B. S. Ishkhanov, E. L. Isupov, M. M. Ito, D. Jenkins, H. S. Jo, J. R. Johnstone, K. Joo, H. G. Juengst, T. Kageya, N. Kalantarians, D. Keller, J. D. Kellie, M. Khandaker, P. Khetarpal, K. Y. Kim, K. Kim, W. Kim, A. Klein, F. J. Klein, M. Klusman, P. Konczykowski, M. Kossov, L. H. Kramer, V. Kubarovsky, J. Kuhn, S. E. Kuhn, S. V. Kuleshov, V. Kuznetsov, J. M. Laget, J. Langheinrich, D. Lawrence, A. C. S. Lima, K. Livingston, M. Lowry, H. Y. Lu, K. Lukashin, M. MacCormick, S. Malace, J. J. Manak, N. Markov, P. Mattione, S. McAleer, M. E. McCracken, B. McKinnon, J. W. C. McNabb, B. A. Mecking, M. D. Mestayer, C. A. Meyer, T. Mibe, K. Mikhailov, T. Mineeva, R. Minehart, M. Mirazita, R. Miskimen, V. Mokeev, B. Moreno, K. Moriya, S. A. Morrow, M. Moteabbed, J. Mueller, E. Munevar, G. S. Mutchler, P. Nadel-Turonski, R. Nasseripour, S. Niccolai, G. Niculescu, I. Niculescu, B. B. Niczyporuk, M. R. Niroula, R. A. Niyazov, M. Nozar, G. V. O'Rielly, M. Osipenko, A. I. Ostrovidov, K. Park, S. Park, E. Pasyuk, C. Paterson, S. Anefalos Pereira, S. A. Philips, J. Pierce, N. Pivnyuk, D. Pocanic, O. Pogorelko, E. Polli, I. Popa, S. Pozdniakov, B. M. Preedom, J. W. Price, Y. Prok, D. Protopopescu, L. M. Qin, B. A. Raue, G. Riccardi, G. Ricco, M. Ripani, B. G. Ritchie, G. Rosner, P. Rossi, D. Rowntree, P. D. Rubin, F. Sabatié, M. S. Saini, J. Salamanca, C. Salgado, A. Sandorfi, J. P. Santoro, V. Sapunenko, D. Schott, R. A. Schumacher, V. S. Serov, Y. G. Sharabian, D. Sharov, J. Shaw, N. V. Shvedunov, A. V. Skabelin, E. S. Smith, L. C. Smith, D. I. Sober, D. Sokhan, A. Starostin, A. Stavinsky, S. Stepanyan, S. S.

Stepanyan, B. E. Stokes, P. Stoler, K. A. Stopani, I. I. Strakovsky, S. Strauch, R. Suleiman, M. Taiuti, S. Taylor, D. J. Tedeschi, R. Thompson, A. Tkabladze, S. Tkachenko, M. Ungaro, A. V. Vlassov, D. P. Watts, X. Wei, L. B. Weinstein, D. P. Weygand, M. Williams, E. Wolin, M. H. Wood, A. Yegneswaran, J. Yun, M. Yurov, L. Zana, J. Zhang, B. Zhao, and Z. W. Zhao. Precise measurement of the neutron magnetic form factor G_M^n in the few-gev^2 region. *Phys. Rev. Lett.*, 102:192001, May 2009.

[30] H. Anklin, E.E.W. Bruins, D. Day, D. Fritschi, B. Groft, F.C.P. Joosse, J. Jourdan, J. Lichtenstadt, M. Loppacher, G. Masson, J. Mitchell, I. Sick, and H.J.J. van Veen. Precision measurement of the neutron magnetic form factor. *Physics Letters B*, 336(3):313–318, 1994.

[31] E. E. W. Bruins, Th. S. Bauer, H. W. den Bok, C. P. Duif, W. C. van Hoek, D. J. J. de Lange, A. Misiejuk, Z. Papandreou, E. P. Sichtermann, J. A. Tjon, H. W. Willering, D. M. Yeomans, H. Reike, D. Durek, F. Frommberger, R. Gothe, D. Jakob, G. Kranefeld, C. Kunz, N. Leiendecker, G. Pfeiffer, H. Putsch, T. Reichelt, B. Schoch, D. Wacker, D. Wehrmeister, M. Wilhelm, E. Jans, J. Konijn, R. de Vries, C. Furget, E. Voutier, and H. Arenhövel. Measurement of the neutron magnetic form factor. *Phys. Rev. Lett.*, 75:21–24, Jul 1995.

[32] H. Anklin, L.J. deBever, K.I. Blomqvist, W.U. Boeglin, R. Böhm, M. Distler, R. Edelhoff, J. Friedrich, D. Fritschi, R. Geiges, J. Götz, A. Honegger, P. Jennewein, J. Jourdan, M. Kahrau, M. Korn, H. Kramer, K.W. Krygier, G. Kubon, V. Kunde, A. Liesenfeld, G. Masson, K. Merle, R. Neuhausen, E.A.J.M. Offermann, Th. Petitjean, Th. Pospischil, M. Potokar, L.M. Qin, A.W Richter, A. Rokavec, G. Rosner, P. Sauer, S. Schardt, I. Sick, S. Sirca, Ph. Trueb, M. Tuccillo, B. Vodenik, A. Wagner, Th. Walcher, G. Warren, S. Wolf, J. Zhao, M. Zeier, and B. Zihlmann. Precise measurements of the neutron magnetic form factor1work supported by the schweizerische nationalfonds and deutsche forschungsgemeinschaft, sfb 201.1. *Physics Letters B*, 428(3):248–253, 1998.

[33] G Kubon, H Anklin, P Bartsch, D Baumann, W.U Boeglin, K Bohinc, R Böhm, M.O Distler, I Ewald, J Friedrich, J.M Friedrich, M Hauger, A Honegger, P Jennewein, J Jourdan, M Kahrau, K.W Krygier, A Liesenfeld, H Merkel, U Müller, R Neuhausen, Ch Normand, Th Petitjean, Th Pospischil, M Potokar, D Rohe, G Rosner, H Schmieden, I Sick, S Širca, Ph Trueb, A Wagner, Th Walcher,

G Warren, M Weis, H Wöhrle, M Zeier, J Zhao, and B Zihlmann. Precise neutron magnetic form factors. *Physics Letters B*, 524(1):26–32, 2002.

[34] J. Annand, R. Gilman, B. Quinn, and B. Wojtsekhowski (spokespersons). PR12-09-019: Precision Measurement of the Neutron Magnetic Form Factor up to Q^2 = 18.0 $(GeV/c)^2$ by the Ratio Method. https://www.jlab.org/exp$_p$*rog*/*proposals*/09/$PR12-09-019.pdf$.

[35] Christoph W. Leemann, David R. Douglas, and Geoffrey A. Krafft. The continuous electron beam accelerator facility: Cebaf at the jefferson laboratory. *Annual Review of Nuclear and Particle Science*, 51(Volume 51, 2001):413–450, 2001.

[36] Dave Meekins. Hall A target configuration from October 2021 to February 2022. https://logbooks.jlab.org/entry/3987411, 2022. Log entry in Jefferson Lab Hall-A electronic logbook.

[37] Miha Mihoviloviĉ. *Measurement of double polarized asymmetries in quasi-elastic processes 3He(e,e'd) and 3He(e,e'p)*. PhD thesis, University of Ljubljana, 2012.

[38] R.M. Marinaro. *Performance and Commissioning of the BigBite Timing Hodoscope for Nucleon Form Factor Measurements at Jefferson Lab*. PhD thesis, University of Glasgow, 2023.

[39] Donato Castelluccio. The super-bigbyte spectrometer for jefferson lab hall a. https://userweb.jlab.org/~mahbub/HallA/SBS/SBS-CDR_New.pdf, 01 2010.

[40] F. Sauli. Gem: A new concept for electron amplification in gas detectors. *Nuclear Instruments and Methods in Physics Research Section A: Accelerators, Spectrometers, Detectors and Associated Equipment*, 386(2):531–534, 1997.

[41] B. Ketzer, Q. Weitzel, S. Paul, F. Sauli, and L. Ropelewski. Performance of triple gem tracking detectors in the compass experiment. *Nuclear Instruments and Methods in Physics Research Section A: Accelerators, Spectrometers, Detectors and Associated Equipment*, 535(1):314–318, 2004. Proceedings of the 10th International Vienna Conference on Instrumentation.

[42] C. Altunbas, M. Capéans, K. Dehmelt, J. Ehlers, J. Friedrich, I. Konorov, A. Gandi, S. Kappler, B. Ketzer, R. De Oliveira, S. Paul, A. Placci, L. Ropelewski, F. Sauli, F. Simon, and M. van Stenis. Construction, test and commissioning of the triple-gem

tracking detector for compass. *Nuclear Instruments and Methods in Physics Research Section A: Accelerators, Spectrometers, Detectors and Associated Equipment*, 490(1):177–203, 2002.

[43] S Bachmann, A Bressan, B Ketzer, M Deutel, L Ropelewski, F Sauli, A Bondar, A Buzulutskov, L Shekhtman, A Sokolov, A Tatarinov, A Vasil'ev, S Kappler, and E Schulte. Performance of gem detectors in high intensity particle beams. *Nuclear Instruments and Methods in Physics Research Section A: Accelerators, Spectrometers, Detectors and Associated Equipment*, 470(3):548–561, 2001.

[44] A Bressan, J.C Labbé, P Pagano, L Ropelewski, and F Sauli. Beam tests of the gas electron multiplier. *Nuclear Instruments and Methods in Physics Research Section A: Accelerators, Spectrometers, Detectors and Associated Equipment*, 425(1):262–276, 1999.

[45] S. Bachmann, A. Bressan, M. Capeáns, M. Deutel, S. Kappler, B. Ketzer, A. Polouektov, L. Ropelewski, F. Sauli, E. Schulte, L. Shekhtman, and A. Sokolov. Discharge studies and prevention in the gas electron multiplier (gem). *Nuclear Instruments and Methods in Physics Research Section A: Accelerators, Spectrometers, Detectors and Associated Equipment*, 479(2):294–308, 2002.

[46] C. Altunbas, M. Capéans, K. Dehmelt, J. Ehlers, J. Friedrich, I. Konorov, A. Gandi, S. Kappler, B. Ketzer, R. De Oliveira, S. Paul, A. Placci, L. Ropelewski, F. Sauli, F. Simon, and M. van Stenis. Construction, test and commissioning of the triple-gem tracking detector for compass. *Nuclear Instruments and Methods in Physics Research Section A: Accelerators, Spectrometers, Detectors and Associated Equipment*, 490(1):177–203, 2002.

[47] B. Ketzer, Q. Weitzel, S. Paul, F. Sauli, and L. Ropelewski. Performance of triple gem tracking detectors in the compass experiment. *Nuclear Instruments and Methods in Physics Research Section A: Accelerators, Spectrometers, Detectors and Associated Equipment*, 535(1):314–318, 2004. Proceedings of the 10th International Vienna Conference on Instrumentation.

[48] K. Gnanvo, N. Liyanage, V. Nelyubin, K. Saenboonruang, S. Sacher, and B. Wojtsekhowski. Large size GEM for Super Bigbite Spectrometer (SBS) polarimeter for Hall A 12 GeV program at JLab. *Nuclear Instruments and Methods in Physics Research Section A: Accelerators, Spectrometers, Detectors and Associated Equipment*, 782:77–86, 2015.

[49] Leila Jones, Marcus French, Quentin Morrissey, Andrea Neviani, Marthin Raymond, Paulo Moreira, and G. Cervelli. The apv25 deep submicron readout chip for cms detectors. 01 1999.

[50] R. Turchetta, M.J. French, L.L. Jones, Q. Morrisse, A. Neviani, J. Fulcher, G. Hall, E. Noah, M. Raymond, G. Cervelli, P. Moreria, and G. Marseguerra. Design and results from the apv25, a deep sub-micron cmos front-end chip for the cms tracker. *Nuclear Instruments and Methods in Physics Research Section A: Accelerators, Spectrometers, Detectors and Associated Equipment*, 466:359–365, July 2001.

[51] Data Acquision Support - Thomas Jefferson National Accelerator Facility. https://coda.jlab.org/drupal/content/welcome. Accessed: 2024-02-21.

[52] Lawrence Jones. *APV25-S1 User Guide Version 2.2.*

[53] N. Boetti, F. Faccio, and P. Jarron. A radiation hardened voltage regulator for lhc and space applications. Technical report, CERN, 2000.

[54] Danning Di. *High Momentum Transfer Nucleon Elastic Electromagnetic Form Factor Measurements Using Super BigBite Spectrometer at Jefferson Lab.* PhD thesis, University of Virginia, 2019.

[55] Sean Patrick Jeffas. *Measurement of the Neutron Electromagnetic Form Factor Ratio at High Momentum Transfer.* PhD thesis, University of Virginia, 2024.

[56] S. Agostinelli, J. Allison, K. Amako, J. Apostolakis, H. Araujo, P. Arce, M. Asai, D. Axen, S. Banerjee, G. Barrand, F. Behner, L. Bellagamba, J. Boudreau, L. Broglia, A. Brunengo, H. Burkhardt, S. Chauvie, J. Chuma, R. Chytracek, G. Cooperman, G. Cosmo, P. Degtyarenko, A. Dell'Acqua, G. Depaola, D. Dietrich, R. Enami, A. Feliciello, C. Ferguson, H. Fesefeldt, G. Folger, F. Foppiano, A. Forti, S. Garelli, S. Giani, R. Giannitrapani, D. Gibin, J.J. Gómez Cadenas, I. González, G. Gracia Abril, G. Greeniaus, W. Greiner, V. Grichine, A. Grossheim, S. Guatelli, P. Gumplinger, R. Hamatsu, K. Hashimoto, H. Hasui, A. Heikkinen, A. Howard, V. Ivanchenko, A. Johnson, F.W. Jones, J. Kallenbach, N. Kanaya, M. Kawabata, Y. Kawabata, M. Kawaguti, S. Kelner, P. Kent, A. Kimura, T. Kodama, R. Kokoulin, M. Kossov, H. Kurashige, E. Lamanna, T. Lampén, V. Lara, V. Lefebure, F. Lei, M. Liendl, W. Lockman, F. Longo, S. Magni, M. Maire, E. Medernach, K. Minamimoto, P. Mora de Freitas, Y. Morita, K. Murakami, M. Nagamatu, R. Nartallo, P. Nieminen, T. Nishimura, K. Ohtsubo, M. Okamura, S. O'Neale, Y. Oohata, K. Paech,

J. Perl, A. Pfeiffer, M.G. Pia, F. Ranjard, A. Rybin, S. Sadilov, E. Di Salvo, G. Santin, T. Sasaki, N. Savvas, Y. Sawada, S. Scherer, S. Sei, V. Sirotenko, D. Smith, N. Starkov, H. Stoecker, J. Sulkimo, M. Takahata, S. Tanaka, E. Tcherniaev, E. Safai Tehrani, M. Tropeano, P. Truscott, H. Uno, L. Urban, P. Urban, M. Verderi, A. Walkden, W. Wander, H. Weber, J.P. Wellisch, T. Wenaus, D.C. Williams, D. Wright, T. Yamada, H. Yoshida, and D. Zschiesche. Geant4—a simulation toolkit. *Nuclear Instruments and Methods in Physics Research Section A: Accelerators, Spectrometers, Detectors and Associated Equipment*, 506(3):250–303, 2003.

[57] M. E. Christy and P. E. Bosted. Empirical fit to precision inclusive electron-proton cross sections in the resonance region. *Phys. Rev. C*, 81:055213, May 2010.

[58] P. E. Bosted and M. E. Christy. Empirical fit to inelastic electron-deuteron and electron-neutron resonance region transverse cross sections. *Phys. Rev. C*, 77:065206, Jun 2008.

[59] Provakar Datta. Implementation of D(e,e'n) process in simcgfortran. https://redmine.jlab.org/issues/758#change-2110, 2023. Log entry in SBS GMn experiment analysis Redmine page.

[60] John Alan Boyd III. *Measurement of the Neutron Magnetic Form Factor and the Two-Photon Exchange Contribution to the Electron-Neutron Elastic Scattering Cross Section*. PhD thesis, University of Virginia, 2024.

[61] J. J. Kelly. Simple parametrization of nucleon form factors. *Phys. Rev. C*, 70:068202, Dec 2004.

Appendix A

Elastic Scattering Kinematics

A.1 Elastic Kinematics Formalism and Basic Definitions

A brief overview of the kinematic calculations pertaining to elastic electron-nucleon scattering is given. The natural unit system is used. The spacial coordinate system used is +Z axis pointing along the direction of particle motion of the incoming electron beam, the +X towards the beam left, and +Y pointing vertically up towards the ceiling of the experiment Hall, forming a right-handed coordinate system. The incoming electron's momentum four-vector can be defined as:

$$p_e^\mu = (E_b, 0, 0, p_{z,e}) \tag{A.1}$$

Where, E_b is the beam energy and p_z the electron momentum along the +Z direction. However, the rest mass of the electron is negligible in the energy scales considered (ultra-relativistic) and thus to good approximation $p_z \approx E_b$. The target nucleon is assumed to be at rest. The nucleon's initial four momentum vector can therefore be defined as:

$$p_N^\mu = (M, 0, 0, 0) \tag{A.2}$$

Where, M is the nucleon mass. The BigBite spectrometer detects the scattered electron and measures all the parameters needed to form its four momentum:

$$p_{e'}^\mu = (E', p_{x,e'}, p_{y,e'}, p_{z,e'}) \tag{A.3}$$

The scattered electrons are also in many GeV regime and the above same ultra-

relativistic approximation still holds:

$$E' = p_{e'} = \sqrt{p_{x,e'}^2 + p_{y,e'}^2 + p_{z,e'}^2} \tag{A.4}$$

The four momentum transferred to the nucleon or alternatively the four-momentum of the virtual photon can be defined as:

$$q = p_e^\mu - p_{e'}^\mu \tag{A.5}$$

The energy-momentum conservation requires:

$$p_e^\mu + p_N^\mu = p_{e'}^\mu + p_{N'}^\mu \tag{A.6}$$

With $p_{N'}^\mu$ being the four momentum of the scattered nucleon or the virtual photon - nucleon system. By solving for $p_{N'}^\mu$ and taking the invariant dot product gives us the so called invariant mass squared:

$$W^2 = (p_e^\mu - p_{e'}^\mu + p_N^\mu)^2 = (q + p_N^\mu)^2 \tag{A.7}$$

Further simplification gives,

$$W^2 = q^2 + M^2 + 2q.p_N^\mu \tag{A.8}$$

q is spacelike and hence q^2 is negative. We define $-q^2 = Q^2$,

$$Q^2 = -(\cancelto{0}{p_e^\mu.p_e^\mu} + \cancelto{0}{p_{e'}^\mu.p_{e'}^\mu} - 2p_e^\mu.p_{e'}^\mu) = 2(E_b E' - E_b p_{z,e'}) \tag{A.9}$$

But from Eq. A.4,

$$p_{z,e'} = p_{e'}\cos\theta = E'\cos\theta \tag{A.10}$$

With θ being the polar scattering angle of the electron. This simplifies Eq. A.9:

$$Q^2 = 2E_b E'(1 - \cos\theta) \tag{A.11}$$

This gives us a final simplified version of the invariant mass square:

$$W^2 = -Q^2 + M^2 + 2M(E_b - E') \tag{A.12}$$

By the knowledge of the scattered electron momentum and the polar scattering angle from the BigBite spectrometer, and the beam energy, the W^2 could be calculated. Alternatively, it can be calculated numerically directly using the Eq. A.7 as

well. The latter approach was used during this analysis. Theoretically, for elastic or quasi-elastic electron-nucleon scattering in which the final products are strictly the scattered electron and the ground-state nucleon, the W^2 should give a value equivalent to M^2.

A.2 Calculation of HCal Predicted Hit Position Under the *Neutron Hypothesis*

This section will provide the formalism used to calculate the predicted 2D hit position of the scattered nucleon on the face of HCal. The vertical deflection of the protons due to the SBS magnetic field is neglected in this calculation and therefore, this method of calculating the predicted hadron position on HCal is referred to as the *neutron hypothesis*. As a result, when a coordinate difference between the detected and predicted locations on the face of HCal is taken, the true neutron events must be centered around (0,0). The true proton events on the other hand must be shifted from the neutron events, in the dispersive direction (-X direction in the HCal coordinate system) by the average magnetic deflection of protons for that kinematic setting.

See Figure: A.1 for a vector diagram that this calculation will be based on. All the five vectors (1-5) that originate from the target, and vector 6, is defined in the so called Hall coordinate system. In this coordinate system, the origin is located at the center of the Hall, which is also the center of the target. The +X direction is towards the beam left, +Y direction is vertically up pointing towards the ceiling of the experimental hall, and the +Z direction is towards the down-stream beam direction, forming a right-handed coordinate system. In bottom left of the Figure: A.1, the Hall coordinate system is defined and the Y axis is pointing out of the frame from the point of view considered which is looking down at the target from the ceiling of the experimental Hall. The face of the HCal is rotated 90°to coincide with the plane of the page in order to provide a better view. The vectors marked with a cross lie on the face of the HCal. The other vectors are all three dimensional and should not be imagined to be necessarily on the plane of the page. The HCal internal coordinate system is defined on the face of the HCal. SBS-OFFLINE will provide HCal cluster position in this coordinate system. The final goal of this calculation is to find the predicted nucleon position (under neutron hypothesis) in this internal HCal coordinate system.

In terms of the Hall coordinate system, the unit vectors of the HCal coordinate

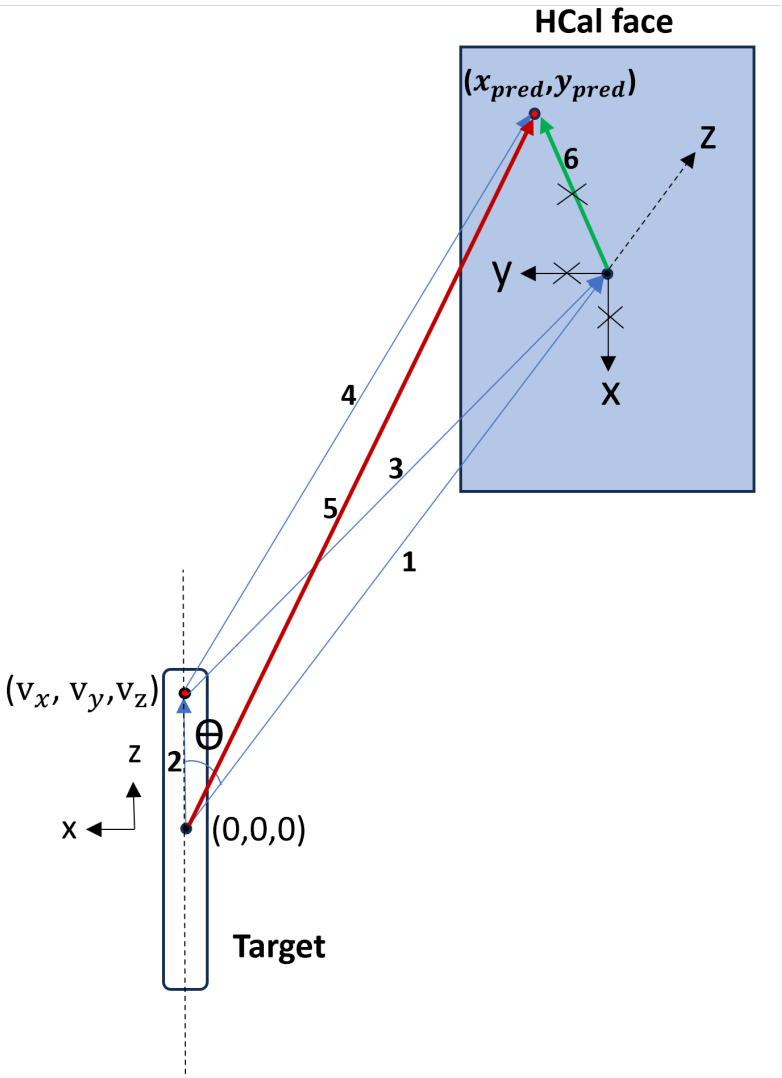

Figure A.1: Diagram to illustrate the vector calculation used to calculate the predicted hadron position from the neutron hypothesis.

system can be defined as follows,

$$\hat{x} = (0, -1, 0) \tag{A.13}$$

$$\hat{z} = (-\sin\theta, 0, \cos\theta) \tag{A.14}$$

$$\hat{y} = \hat{z} \times \hat{x} \tag{A.15}$$

θ is the polar angle of HCal's Z axis with respect to the Hall's Z axis. The vector-1

defines the origin of the HCal detector which can be written as,

$$\vec{v_1} = (-d\sin\theta, 0, d\cos\theta) \tag{A.16}$$

With d being the distance of HCal from the Hall origin. The vector-2 defines the vertex position of the scattering event, as measure by the BigBite spectrometer and the definition of this vector is given within the diagram itself. The variation of the components v_x and v_y is minimal and is in the few millimeter range, mainly due to the beam rastering. Vector-3, which points to the origin of HCal starting from the scattering vertex can be written as,

$$\vec{v_3} = \vec{v_1} - \vec{v_2} \tag{A.17}$$

Vector-4 connects the scattering vertex to the face of HCal, along the direction of the $\vec{q}$ vector.

$$\vec{v_4} = l\hat{q} \tag{A.18}$$

Where l is the length of the vector. The unit vector of $\vec{q}$ can be extracted from the above Eq. A.5, and could be defined simply as,

$$\hat{q} = \frac{\vec{q}}{|q|} \tag{A.19}$$

Both vector-3 and vector-4 starts from the scattering vertex and ends at the face of HCal. The value l can be extracted from the fact that the dot products between either of these vectors and the unit vector of HCal's Z axis should yield the same horizontal distance between the scattering vertex and the face of the HCal. Therefore, l can be written as,

$$l = \frac{\vec{v_3} \cdot \hat{z}}{\hat{q} \cdot \hat{z}} \tag{A.20}$$

Now vector-5 that start from the Hall origin and ends at the predicted hit position of the hadron on the HCal surface could be written as,

$$\vec{v_5} = \vec{v_2} + \vec{v_4} \tag{A.21}$$

And vector-6 follows as,

$$\vec{v_6} = \vec{v_5} - \vec{v_1} \tag{A.22}$$

Now what is left is to extract the x_{pred} and y_{pred} positions in the HCal coordinate

system which can be achieved by taking dot products with the respective unit vectors.

$$x_{pred} = \vec{v_6} \cdot \hat{x} \tag{A.23}$$

$$y_{pred} = \vec{v_6} \cdot \hat{y} \tag{A.24}$$

Appendix B

End-Point Method Threshold Calculation Formalism

We want to calculate the maximum possible momentum/energy of π^+ in the lab frame for the reaction $p(\gamma, \pi^+)\pi^0 n$ for a given photon energy. We will assume the photon energy to be equal to the beam energy (E_{beam}). For the sake of simplicity, first this calculation can be done for the reaction $p(\gamma, \pi^+)n$ and the polar scattering angles will be assumed to be zero with respect to the lab frame. Then these calculations will be extended to the two-pion channel and non-zero polar scattering angles.

B.1 Considering Reaction $p(\gamma, \pi^+)n$

Define four-momenta of the particles involved in the reaction as p^μ_γ, p^μ_p, $p^\mu_{\pi^+}$, and p^μ_n. Where we can write values before the reaction as,
$p^\mu_\gamma = (E_\gamma, 0, 0, E_\gamma)$ and $p^\mu_p = (m_p, 0, 0, 0)$
the four momenta of the photon and the proton before the scattering reaction. In order for the momentum of resulting π^+ to be maximum, we can argue that the π^+ must be ejected in the +Z/beam direction and the neutron in the -Z/opposite to the beam direction. This situation is easier to evaluate in the CM frame and find the momentum of π^+ there and then Lorentz transform that momentum into the lab frame. In the CM frame, let's assume that the π^+'s 3-momentum is $\vec{P}'_{\pi^+}$ and neutron 3-momentum is $\vec{P}'_n$. But because we are at CM frame $\vec{P}'_{\pi^+} + \vec{P}'_n = 0$. Here the direction of the $\vec{P}'_{\pi^+}$ vector should be in the +Z/+Z′. We will identify S as our lab frame and S′ as our CM frame. Therefore, we will use prime notation for all the quantities measured in the CM frame.
Then we can use the Mandelstam 's' variable, which is a Lorentz invariant to simplify

our calculation. For a two-body scattering reaction of the type A(B,C)D,

$$s = (p_A^\mu + p_B^\mu)^2 \tag{B.1}$$

Therefore, from the lab frame, we can write s as,

$$s = (p_\gamma^\mu + p_p^\mu)^2 = (p_\gamma^\mu)^2 + (p_p^\mu)^2 + 2p_\gamma^\mu p_p^\mu = m_p^2 + 2E_\gamma m_p \tag{B.2}$$

Then in CM frame the total energy can be expressed as,

$$E'_{tot} = \sqrt{s} = \sqrt{m_n^2 + \vec{P}'^2_{\pi^+}} + \sqrt{m_{\pi^+}^2 + \vec{P}'^2_{\pi^+}} \tag{B.3}$$

Solving for $|\vec{P}'_{\pi^+}|$ we get,

$$|\vec{P}'_{\pi^+}| = \sqrt{\frac{(s + m_n^2 - m_{\pi^+}^2)^2}{4s} - m_n^2} \tag{B.4}$$

Now we just have to apply the Lorentz transformation to the momentum of π^+ we calculated in the CM frame to find the momentum $\vec{P}_{\pi^+}$ in the lab frame. For this, we have to know the velocity of the lab frame, V_{lab}, with respect to the CM frame. Obviously the direction of the $\vec{V}_{lab}$ should be in the -Z direction. The CM frame with respect to the lab frame is traveling at a velocity V_{CM}

$$\vec{V}_{CM} = \frac{\vec{P}_{tot}}{E_{tot}} = \frac{E_\gamma}{E_\gamma + m_p}\hat{z} \tag{B.5}$$

Therefore,

$$\vec{V}_{lab} = -\frac{E_\gamma}{E_\gamma + m_p}\hat{z} \tag{B.6}$$

From Lorentz transformations, the momentum $|\vec{P}_{\pi^+}|$ can be written as,

$$|\vec{P}_{\pi^+}| = \gamma(|\vec{P}'_{\pi^+}| + |\vec{V}_{lab}|E'_{\pi^+}) \tag{B.7}$$

Where $\gamma = \sqrt{\frac{1}{1-V_{lab}^2}}$ and $E'_{\pi^+} = \sqrt{|\vec{P}'_{\pi^+}|^2 + m_{\pi^+}^2}$.
Similarly, the energy E'_{π^+} can be written as,

$$E_{\pi^+} = \gamma(E'_{\pi_+} + |\vec{V}_{lab}||\vec{P}'_{\pi^+}|) \tag{B.8}$$

B.2 Considering Reaction $p(\gamma, \pi^+)\pi^0 n$

The above same principles apply to this case. The resulting π^+'s momentum and energy will be maximized if both the neutron and the π^0 recoils in the opposite direction to the beam, in the lab frame. Therefore, we can treat the neutron and the π^0 as a composite object with mass m_{comps} and momentum $\vec{P}'_{comps}$ in the CM frame. Where,

$$m_{comps} = m_n + m_{\pi^0} \tag{B.9}$$

and,

$$\vec{P}'_{comps} + \vec{P}'_{\pi^+} = 0 \tag{B.10}$$

Now we can simply substitute m_n by m_{comps} in equation:B.4 to obtain the maximum possible momentum of π^+ in the reaction $\gamma(p, \pi^+)\pi^0 n$.

$$|\vec{P}'_{\pi^+}| = \sqrt{\frac{(s + m^2_{comps} - m^2_{\pi^+})^2}{4s} - m^2_{comps}} \tag{B.11}$$

The equation:B.7 and equation:B.8 can be used to find the maximum π^+ momentum and energy respectively.

B.3 When π^+ Ejects at a Polar Angle θ with Respect to the +Z (Beam Direction)

This is the case where actual experimental interests lies at, as our spectrometers are always placed at a non-zero polar angle ($0 < \theta < 90°$) and not along the down-stream beam direction ($\theta = 0$). All the calculations we did above in the CM frame (S′) should be still valid in this case, except for the fact that now we will have to account for the angle θ in the lab frame by giving a counterpart angle θ' in the CM frame, which however does not affect the calculations we have done within the CM frame itself.

The place where this non-zero polar angle changes things is when we try to Lorentz transform the momentum of π^+ in the CM frame, $\vec{P}'_{\pi^+}$, to the momentum in the lab frame, $\vec{P}_{\pi^+}$. The reason is that since now the π^+ momentum in the CM frame, $\vec{P}'_{\pi^+}$, is not entirely parallel to the Z/Z' axis, which is the axis the relative velocity of S and S′ frames with respect to each other is at, and only the momentum component $p'_{\pi^+,z}$ along that direction is subjected to the Lorentz transformation. The momentum

components along the X/X′ and Y/Y′ directions are completely unaffected and the lab frame observes the same components along those directions as in the CM frame. Figure:B.1 showcase the relative motion of the resulting scattered particles as observed in the two reference frames, for the case of non-zero polar angle of π^+.

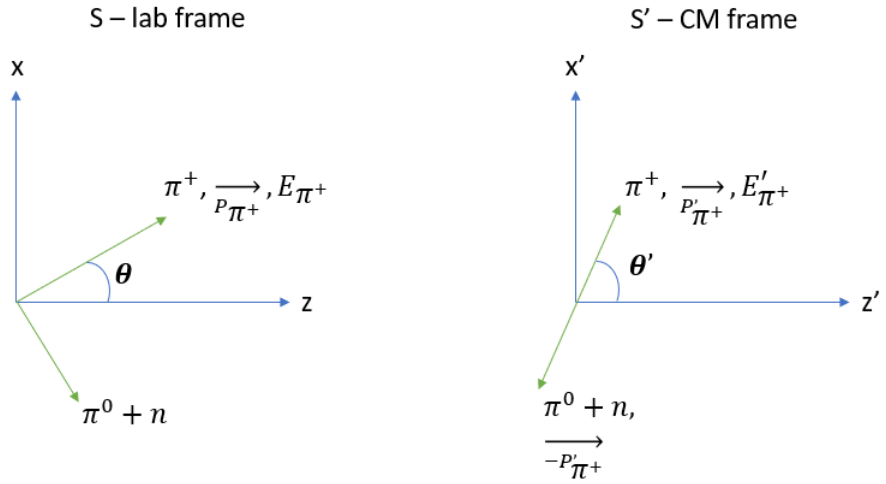

Figure B.1: Pion production at a non zero polar angle. The relative motion between the lab and CM mass frame is same as in the case where the pion production is along the +Z direction shown in equations B.5 and B.6.

The magnitude of $\vec{P}'_{\pi^+}$ is same as given by equation:B.11. What we want to find is the maximum possible magnitude of $\vec{P}_{\pi^+}$. In terms of the x,y,z components $|\vec{P}_{\pi^+}|$ can be expressed as,

$$|\vec{P}_{\pi^+}| = \sqrt{p^2_{\pi^+,x} + p^2_{\pi^+,y} + p^2_{\pi^+,z}} \tag{B.12}$$

But since we can choose the scattering plane to be perpendicular to the y axis, we can chose $p_{\pi^+,y} = 0$. The x component is straightforward and the z component can be obtained from the Lorentz transformations, respectively as,

$$p_{\pi^+,x} = p'_{\pi^+,x} = |\vec{P}'_{\pi^+}| \sin\theta' \tag{B.13}$$

$$p_{\pi^+,z} = \gamma(p'_z + vE'_{\pi^+}) = \gamma(|\vec{P}'_{\pi^+}| \cos\theta' + vE'_{\pi^+}) \tag{B.14}$$

Where $v = |\vec{V}_{lab}| = |\vec{V}_{CM}|$. By substituting into the equation:B.12 and after some algebraic work we get,

$$|\vec{P}_{\pi^+}| = \sqrt{(\gamma^2 - 1)|\vec{P}'_{\pi^+}|^2 \cos^2\theta' + 2\gamma^2 |\vec{P}'_{\pi^+}| v E'_{\pi^+} \cos\theta' + |\vec{P}'_{\pi^+}|^2 + \gamma^2 v^2 E'^2_{\pi^+}} \tag{B.15}$$

But we still need to express θ' in terms of the quantities we already know. The angle

θ counts as a quantity we know since we want to find the maximum possible π^+ momentum for a given scattering angle θ. Therefore, we can write,

$$\tan\theta = \frac{p_{\pi^+,x}}{p_{\pi^+,z}} = \frac{|\vec{P}'_{\pi^+}|\sin\theta'}{\gamma(|\vec{P}'_{\pi^+}|\cos\theta' + vE'_{\pi^+})} \tag{B.16}$$

From which we can obtain a quadratic equation of $\cos\theta'$,

$$[(\gamma^2\tan^2\theta+1)|\vec{P}'_{\pi^+}|^2]\cos^2\theta' + [2vE'_{\pi^+}|\vec{P}'_{\pi^+}|\gamma^2\tan^2\theta]\cos\theta' + [\gamma^2\tan^2\theta v^2 E'^2_{\pi^+} - |\vec{P}'_{\pi^+}|^2] = 0 \tag{B.17}$$

and solving for $\cos\theta'$ we get,

$$\cos\theta' = \frac{-vE'_{\pi^+}\gamma^2\tan^2\theta \pm \sqrt{\gamma^2\tan^2\theta(|\vec{P}'_{\pi^+}|^2 - v^2E'^2_{\pi^+}) + |\vec{P}'_{\pi^+}|^2}}{|\vec{P}'_{\pi^+}|(\gamma^2\tan^2\theta + 1)} \tag{B.18}$$

Substituting back into the equation:B.15, we can find $|\vec{P}'_{\pi^+}|$. Since it is not obvious for what solution of $\cos\theta'$ we get the largest value for $|\vec{P}'_{\pi^+}|$ for each θ (kinematic setting), both values to evaluate both values and see. In all the cases, the positive solution gave the larger value.

B.4 Finding E_γ^{min}

E_γ^{min} is the minimum photon energy required to produce π^+ above $E_\pi^{limit}(\gamma,\pi)$. According to the description given in the Section: 4.3.2,

$$E_\pi^{limit} = E_\pi^{max}(\gamma, 2\pi).(1 + 1.5\%) \tag{B.19}$$

Once you know the π^+ momentum in the lab frame, you can calculate the photon energy of the reaction $p(\gamma,\pi^+)n$ via first principles. Using the conservation of four-momentum, we can write:

$$p^\mu_\gamma + p^\mu_p = p^\mu_{\pi^+} + p^\mu_n \tag{B.20}$$

By solving for p^μ_n and taking the invariant dot product of both sides we get:

$$m_p^2 + 2E_\gamma m_p + m_{\pi^+}^2 - 2[E_\gamma E_{\pi^+} - E_\gamma p_{\pi^+}\cos\theta + E_{\pi^+}m_p] = m_n^2 \tag{B.21}$$

Then we can simply solve for the photon energy:

$$E_\gamma = \frac{2m_p E_{\pi^+} + m_n^2 - m_{\pi^+}^2 - m_p^2}{2(m_p + p_{\pi^+}\cos\theta - E_{\pi^+})} \tag{B.22}$$

Thus, when we know the π^+ track momentum from BigBite, we can find the photon energy for the reaction $p(\gamma, \pi^+)n$. This formula can be used to find E_γ^{min}.

Appendix C

Elastic Event Selection Cuts

Kinematic label	BigBite electron arm cuts				Elastic Cuts		Fiducial cut safety margins		Hadron arm (HCal) and electron arm (BigBite shower) coincidence time	Ad-hoc offsets used for the SIMC generated QE peaks (m)	
	Track momentum (GeV/c)	Vertex Z range (m)	Track χ^2/ndf	pre-shower energy (GeV)	W^2 range (GeV^2)	Delta y range (m)	x $\boldsymbol{\sigma}$	y $\boldsymbol{\sigma}$		D(e,e'n)p peak (m)	D(e,e'p)n peak (m)
SBS-4	> 1.9	$\lvert z\rvert < 0.075$	< 15.0	> 0.2	$0.4 < W^2 < 1.2$	$-0.5 < \Delta_y < 0.5$	1.5 $\boldsymbol{\sigma}$	1.5 $\boldsymbol{\sigma}$	Events within 4 $\boldsymbol{\sigma}$ from the mean	-0.04	-0.045
SBS-7	> 1.9	$\lvert z\rvert < 0.07$	< 15.0	> 0.2	$0.4 < W^2 < 1.2$	$-0.25 < \Delta_y < 0.15$	1.5 $\boldsymbol{\sigma}$	1.5 $\boldsymbol{\sigma}$	Events within 4 $\boldsymbol{\sigma}$ from the mean	-0.015	-0.015
SBS-11	> 2.0	$\lvert z\rvert < 0.07$	< 15.0	> 0.2	$0.35 < W^2 < 1.15$	$-0.25 < \Delta_y < 0.15$	1.5 $\boldsymbol{\sigma}$	1.5 $\boldsymbol{\sigma}$	Events within 4 $\boldsymbol{\sigma}$ from the mean	-0.01	0.015

Table C.1: Event-selection cut thresholds/regions for the SBS-4, SBS-7, and SBS-11 kinematic points.